

Applications of Dynamic nuclear polarisation in biological systems

By

Thomas Sandeep Deo

**Thesis submitted to the University of
Nottingham
for the degree of Doctor of Philosophy
November 2020**

Abstract

Cellular membrane disruption induced by the aggregation of amyloid beta ($A\beta$) peptide is considered a main mechanism responsible for neuronal death in Alzheimer's disease. However, the molecular basis of this toxicity, in particular the interaction of $A\beta$ and its aggregates with a cell membrane, remains unclear. Solid-state NMR (ssNMR) is a very well-suited technique for studies of the molecular basis of $A\beta$ peptide interactions with cell membranes, but low sensitivity limits such studies due to a large fraction of the sample volume being taken up by lipids. Dynamic Nuclear Polarisation (DNP) allows increasing the signals in ssNMR experiments, thus enabling measurements with lower amounts of protein material. In this work, the feasibility of structural ssNMR-DNP studies of $A\beta(1-40)$ peptide, at low concentration, interacting with biomimetic lipid bilayers was explored.

DNP enhancements of between 20-87 were observed for lipid and protein ^{13}C spins under a range of conditions. Sample conditions were optimised to give maximum signal strength under magic angle spinning (MAS) DNP conditions. The interaction between biradical and glycerol cryoprotectant, required for efficient DNP, and lipid vesicles was probed. Biradical was shown to have a significant interaction with lipid vesicles, with glycerol causing a partitioning effect into lipid vesicles, determined by paramagnetic relaxation enhancement (PRE) experiments. ^{31}P chemical shift anisotropy (CSA) patterns of lipid vesicles showed only slight changes on addition of biradical and glycerol, indicating no major changes in vesicle structure. Two-dimensional ^{13}C - ^{13}C (DARR) and ^{15}N - ^{13}C (NCA, NCACX) correlation experiments were possible in under 3 hours at lipid-to-peptide ratio (L:P) of 20:1. In order to reduce the contribution of signals from natural abundance ^{13}C of lipids we used double quantum (DQ) experiments. POST-C7 double-quantum single-quantum (DQSQ) correlation was shown to be feasible at L:P of 100:1 (70 nmol peptide) and 200:1 (35 nmol peptide) with well resolved cross-peaks in under 10 hours and under 20 hours, respectively. Structural $A\beta(1-40)$ information was also obtained in a complex mixture of membrane mimicking lipids, including the ganglioside GM1 and cholesterol, which have been shown to modulate both $A\beta$ and membrane properties. DNP enhancement of 87 was achieved for rat synaptic membrane extracts, and structural $A\beta(1-40)$ information was obtained following addition and incubation with the membrane extracts. Secondary chemical shifts at the uniformly labelled amino acids in the $A\beta(1-40)$ sequence agree with β -sheet conformation at these positions. This demonstrates that DNP enhanced ssNMR can be used to

probe structures of A β (1-40) which exist at low concentrations in a cell membrane environment, as well as in physiologically relevant samples where membranes have been extracted from mammalian cells. This will lead to a better understanding of mechanism of cell membrane disruption by A β . Additionally, DNP-enhanced ssNMR measurements were made of A β (1-40) at two timepoints following addition to synthetic lipids, showing the feasibility of tracking kinetic A β events by flash freezing and recording spectra at cryogenic temperatures at various points in the process.

Dissolution Dynamic Nuclear Polarisation (d-DNP) is another method for generating strong NMR signals, but in solutions rather than solids. This is achieved by polarizing nuclear spins using microwave irradiation, followed by a rapid dissolution with hot solvent. The d-DNP setup at the University of Nottingham is based on a dual iso-centre magnet with its top section (3.4 T) used for polarizing the sample at low temperatures (~ 1.8 K), and the bottom section (9.4 T) used for solution NMR measurements at room temperature. The system was optimized to achieve 300 ms dead time (time between start of dissolution process and recording a signal) during which the sample is dissolved and transferred into an NMR tube. Many protein folding, unfolding and aggregation events develop on a similar timescale. The refolding process of hen egg-white lysozyme was used as a model, to which ^{19}F -containing labels were introduced.

Maximum nuclear polarization was achieved with 40 mM water soluble TEMPOL as a polarizing agent in the glassy partially deuterated water/DMSO at the optimal microwave frequency of 94.05 GHz. Hen egg-white lysozyme was chemically modified to covalently attach trifluoroacetyl groups ($\text{CF}_3\text{CO}-$) to six surface exposed amines of lysine residues. The protein was dissolved in a matrix consisting of 60/30/10 v:v DMSO- d_6 /D $_2$ O/H $_2$ O with 40 mM TEMPOL polarizing agent and 100 mM 5-fluorouracil, presence of which is shown to improve the enhancements of lysozyme. 900 ms after the dissolution, the NMR signals were acquired using a 90° pulse. The signal enhancements for ^{19}F -nuclei of lysozyme and 5-fluorouracil were ~ 300 and ~ 1000 respectively, which show overall suitability of the approach. Polarisation of ^{19}F -labelled lysozyme under protein denaturing conditions followed by dissolution into protein folding conditions and acquisition of DNP enhanced protein signals shows the feasibility of tracking kinetic protein events using this methodology.

Contents

1. Introduction.....	8
2. NMR theory	11
2.1. Sample magnetisation.....	12
2.2. Effect of an RF pulse	14
2.3. Spin Interactions	15
2.4. Chemical shift anisotropy (CSA)	16
2.5. Dipolar coupling	18
2.6. Essential techniques in ssNMR	19
2.7. Dynamic Nuclear Polarisation (DNP)	24
2.8. Polarising agents.....	27
2.9. MAS DNP sample.....	29
2.10. MAS DNP hardware.....	30
2.11. Dissolution DNP Hardware	32
2.12. References.....	33
3. Optimising the membrane sample for DNP MAS experiments	38
3.1. Introduction	38
3.2. Methods.....	39
3.3. Results / discussion	46
3.4. Biradical position within a lipid bilayer	53
3.5. Lipid structure disruption by DNP dopants	62
3.6. Conclusion and Outlook	68
3.7. References	69
4. A β interactions with phospholipid bilayers	72
4.1. Protein structure determination by ssNMR	72
4.2. Sample preparation	74
4.3. Enhancement of protein by DNP in lipid environment.....	75
4.4. 2D measurements.....	76
4.5. Double-quantum single-quantum correlation.....	85
4.6. Conclusion and outlook.....	96
4.7. References	97
5. Characterisation of A β (1-40) in a membrane mimicking environment ...	100
5.1. Introduction	100
5.2. Methods.....	103
5.3. A β (1-40) associated with lipids at low concentration	106
5.4. A β (1-40) associated with a complex lipid mixture.....	113

5.5.	A β (1-40) associated with synaptic rat membrane	118
5.6.	External addition of A β (1-40) to lipids.....	123
5.7.	Discussion	133
5.8.	Conclusion and outlook.....	135
5.9.	References	138
6.	Enhancing ^{19}F NMR signals using d-DNP for lysozyme folding studies.	142
6.1.	Introduction	142
6.2.	The Nottingham dual-isocentre magnet.....	144
6.3.	Fluorine labelling of lysozyme.....	148
6.4.	Methods.....	153
6.5.	Optimising instrument conditions.....	155
6.6.	Optimization of d-DNP on small fluorinated molecules	159
6.7.	Dissolution-DNP with ^{19}F labelled lysozyme d-DNP	160
6.8.	^{19}F lysozyme under denaturing conditions.....	163
6.9.	Discussion	167
6.10.	Conclusion and outlook	168
6.11.	References.....	169
7.	Conclusion.....	171
8.	Appendices	173

Abbreviations

A β – Amyloid beta

AD- Alzheimer's disease

APP- amyloid precursor protein

IDP- intrinsically disordered protein

PDB- protein data bank

NMR – Nuclear magnetic resonance

ssNMR – Solid-state nuclear magnetic resonance

DNP- Dynamic Nuclear Polarisation

MAS- magic angle spinning

PRE – paramagnetic relaxation enhancement

CSA- chemical shift anisotropy

rf- radio frequency

ppm- parts per million

FWHM- full-width at half-maximum

TMS- trimethylsilane

CP- cross-polarisation

DARR- dipolar-assisted rotational resonance

PDS- proton-driven spin diffusion

DQ- double quantum

DQF- double quantum filtered

DQSQ- double quantum single quantum

d-DNP- dissolution Dynamic Nuclear Polarisation

TPPM- two-pulse phase-modulated

SPINAL-64- small phase incremental alteration with 64 steps

EPR- electron paramagnetic resonance

CE- cross effect

SE- solid effect

POPC- 1-palmitoyl-2-oleoyl-glycero-3-phosphocholine

POPG- 1-palmitoyl-2-oleoyl-sn-glycero-3-phospho-(1'-rac-glycerol)

DMPC- 1,2-Dimyristoyl-sn-glycero-3-phosphocholine

DMPG- 1,2-Dimyristoyl-sn-glycero-3-phosphoglycerol

PTFE- polytetrafluoroethylene
VT- variable temperature
VTI- variable temperature insert
ASR- absolute sensitivity ratio
TCE- trichloroethylene
HFIP- hexafluoro-2-propanol
REDOR- rotational echo double resonance
SPECIFIC CP- spectrally induced filtering in combination with cross polarization
SCP- SPECIFIC CP
POST-C7- Permutationally Offset Stabilized C7
SP-C5- Supercycled Permutationally Offset Stabilized C5
SR26- supercycled R26
CD- circular dichroism
BLM- black lipid membrane
BTLE- brain total lipid extract
SDS- sodium dodecyl sulphate
TEMPO- 2,2,6,6-tetramethylpiperidine 1-oxyl
DMSO- dimethyl sulfoxide
EM- electron microscopy
TEM- tunneling electron microscopy
NOE- nuclear Overhauser effect
NOESY- nuclear Overhauser effect spectroscopy
ZBD- zero bias detector
CIDNP- chemically induced dynamic nuclear polarization
SPM- Synaptosomal Plasma Membrane
RPM- revolutions per minute
RCF- relative centrifugal force

1. Introduction

Nuclear magnetic resonance (NMR) is a commonly used spectroscopic technique for probing molecular structure based on the interaction between certain nuclei and an external magnetic field. NMR has been applied in a huge range of disciplines including the determination of the structure of biomolecules. However, NMR has poor sensitivity compared to other types of spectroscopy due to the Boltzmann statistics that govern the percentage of a population of nuclear spins that align with the applied external magnetic field. Methods of improving sensitivity in NMR include using a stronger applied magnetic field and including a high concentration of the molecule under study in an NMR sample. For practical reasons, this is not always possible- superconducting materials have been continually developed to allow up to magnetic fields up to 25.9 Tesla for NMR applications at the time of writing, but increasing field strength further is extremely resource consuming. Using a high concentration of the molecule under study is not an option if that molecule is in short supply or if you wish to study a system in which one component is in low concentration relative to another. For this reason, techniques have been developed which alter the Boltzmann statistics in favour of having high signal. One of these is Dynamic Nuclear Polarisation (DNP), where electron spin polarisation is transferred to nuclear spins by irradiation of the electron paramagnetic resonance (EPR) spectrum using microwave irradiation followed by acquisition of an NMR signal.

The main application for DNP in this work is to enhance solid-state NMR studies of the protein amyloid beta ($A\beta$), a protein that is strongly associated with the development of Alzheimer's disease (AD). Alzheimer's disease is neurodegenerative and is the most accounts for 60-70 % of dementia cases, which effects 50 million people worldwide^[1]. The Amyloid cascade hypothesis links the pathology in AD to the dysregulation of production and clearance of $A\beta$ protein, leading to formation of amyloid aggregates, including fibrils which are the main component of $A\beta$ plaques found in the brain tissue of people suffering with AD. Cellular membrane disruption is one possible cause of cell death- biophysical and biological studies using a variety of techniques have aimed to determine the nature of the interaction between $A\beta$ and model membrane systems^{[2][3][4]}. Molecular level structural detail of $A\beta$ when associated with membrane is of importance when determining the mechanism by which cell death occurs. Solid-state NMR is an ideal candidate for doing this, with DNP enhancement providing signal increase in situations where the concentration of $A\beta$ in the sample is low.

The layout of the thesis is as follows-

Chapter 2 introduces relevant nuclear magnetic resonance (NMR) and Dynamic Nuclear polarisation (DNP) theory that is applied experimentally throughout.

Chapter 3 involves experiments in which hydrated lipid samples are optimised for maximum signal strength for DNP-enhanced ssNMR. The interaction of biradical and cryoprotectant molecules required for DNP with lipid vesicles was investigated, including the possibility of disruption of vesicle morphology.

Chapter 4 describes preliminary DNP-enhanced ssNMR experiments in which Amyloid beta (1-40) (A β (1-40)) protein was associated with lipid vesicles at a 20:1 lipid-to-protein ratio. A set of 2D ssNMR experiments were implemented and optimised, creating a methodology for gathering secondary chemical shifts and intra-residue cross peaks from uniformly ^{13}C , ^{15}N -labelled A β (1-40) positions.

Chapter 5 describes the implementation of the methodologies developed in Chapter 4 to explore A β (1-40) structure under various sample conditions:

1) Following pre-incorporation of A β (1-40) into POPC/POPG lipid vesicles at low protein concentrations relative to lipids, with lipid-to-protein ratios of 100:1 and 200:1. 2) Following pre-incorporation of A β (1-40) into vesicles made of a mixture of lipids, including ganglioside GM1, sphingomyelin and cholesterol. 3) Following addition and incubation of A β (1-40) with extracted synaptic rat cell membrane. 4) Following addition of A β (1-40) to POPG lipid vesicles, with measurements made before the incubation period and after 8 hours of incubation.

In chapter 6, a methodology for studying protein kinetics by using dissolution-DNP (d-DNP) using enhanced ^{19}F NMR signals is described. Lysozyme protein was labelled with ^{19}F spins, ^{19}F d-DNP was optimized on small fluorinated molecules, then d-DNP was demonstrated on ^{19}F labelled protein.

[1] <https://www.who.int/news-room/fact-sheets/detail/dementia>

[2] T. L. Williams, L. C. Serpell, *FEBS Journal*, 2011, **278**, 3905–3917

[3] D. A. Delgado, K. Doherty, Q. Cheng, H. Kim, D. Xu, H. Dong, C. Grewer, W. Qiang, *J. Biol. Chem.*, 2016, **291**, 12233–12244

[4] Q. Cheng, Z.-W. Hu, K. E. Doherty, Y. J. Tobin-Miyaji, W. Qiang, *Biochim. Biophys. Acta - Biomembr.*, 2018, **1860**, 1670–1680

2. NMR theory	11
2.1. Sample magnetisation	12
2.2. Effect of an RF pulse	14
2.3. Spin Interactions	15
2.4. Chemical shift	16
2.5. Dipolar coupling	18
2.6. Essential techniques in ssNMR	19
2.7. Dynamic Nuclear Polarisation (DNP)	24
2.8. Polarising agents	27
2.9. MAS DNP sample	29
2.10. MAS DNP hardware	30
2.11. Dissolution DNP Hardware	32
2.12. References	33

2. NMR theory

Nuclear magnetic resonance (NMR) is based on the fact that certain nuclei have an intrinsic property called nuclear spin, I . When placed in a magnetic field, the degenerate energy levels of a nuclei are split into $(2I + 1)$ non-degenerate energy levels, known as Zeeman splitting, illustrated in Figure 2.1. The gyromagnetic ratio, γ , of a nucleus describes the strength of its interaction with an external magnetic field. Table 2.1 summarizes the spin, natural abundance, gyromagnetic ratio and NMR frequency of a number of important isotopes that will feature in this thesis.

Isotope	Spin	Natural abundance / %	Gyromagnetic ratio $\gamma / 10^7 \text{ rad s}^{-1} \text{ T}^{-1}$	^1H NMR frequency @ 14.1 T / MHz	^1H NMR frequency @ 3.4 T / MHz
^1H	1/2	99.9885	26.75	600.1	144.7
^{13}C	1/2	1.07	6.73	150.9	36.4
^{15}N	1/2	0.36	-2.71	60.8	14.7
^{19}F	1/2	100.0	25.18	564.7	136.2
^{31}P	1/2	100.0	10.84	242.9	58.6

Table 2.1 Natural abundance, gyromagnetic ratio and Larmor frequency at relevant magnetic fields of nuclei that are mentioned in this thesis.

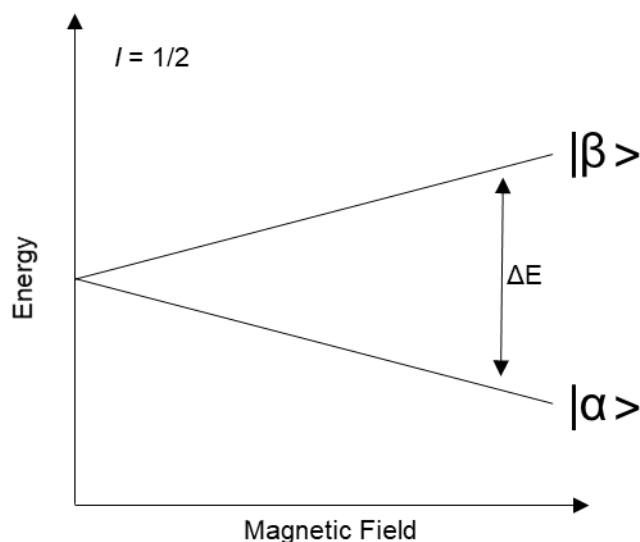


Figure 2.1 Diagram showing the Zeeman splitting of a spin = 1/2 nucleus in an external magnetic field.

The Zeeman interaction is represented by a Hamiltonian:

$$\hat{\mathcal{H}}_Z = -\gamma\hbar B_0 \hat{I}_Z \quad (2.1)$$

Where I_z is the vector of spin angular momentum parallel to the external magnetic field, B_0 . The difference in energy between Zeeman sublevels, ΔE , depends on the strength of the external magnetic field, B_0 , and the gyromagnetic ratio, γ , shown in Equation 2.2.

$$\Delta E = \gamma \hbar B_0 \quad (2.2)$$

Transitions between these energy levels can be achieved by applying electromagnetic irradiation with angular frequency, ω_0 , where

$$\hbar \omega_0 = \Delta E = -\gamma \hbar B_0 \quad (2.3)$$

The frequency $\omega_0/2\pi$ is known as the Larmor frequency- its value for nuclei under conditions relevant to this work is in the radiofrequency range, as shown in table 2.1. NMR is the spectroscopy of the nuclear Zeeman energy levels which is achieved by irradiating a sample containing spin active nuclei at close to the Larmor frequency in a strong external magnetic field.

2.1. Sample magnetisation

NMR measurements are made on samples which contain a large number of nuclear spins, the overall spin state of the ensemble of spins is termed the bulk magnetisation. The magnetic moments of individual molecules in the absence of magnetic field are randomly oriented as shown in Figure 2.2a. Applying an external magnetic field, leads to their partial alignment with respect to the magnetic field, thereby producing a non-zero net magnetization, as illustrated in Figure 2.2b. The polarization of the sample, can be calculated using a Boltzmann distribution-

$$P = \tanh \left(\frac{\Delta E}{2K_b T} \right) \quad (2.4)$$

where P is the polarisation of the sample, K_b is the Boltzmann constant and T is temperature. The strength of NMR signals is directly proportional to nuclear polarization. For this reason, performing experiments at higher fields and lower temperatures provides better sensitivity.

The polarization for electron spins, ^1H and ^{13}C nuclei as function of temperature is shown in Figure 2.3. As can be seen from the graph, at room temperature (298 K) the polarization is on the order of 10^{-4} for nuclear spins and 10^{-2} for electrons spins. Due to a much higher gyromagnetic ratio, unpaired electrons can achieve a polarization of 10^{-1} and 100 K and close to unity below 10 K, which can be employed for signal enhancements using DNP, where electron spin polarisation is transferred to nuclear spins.

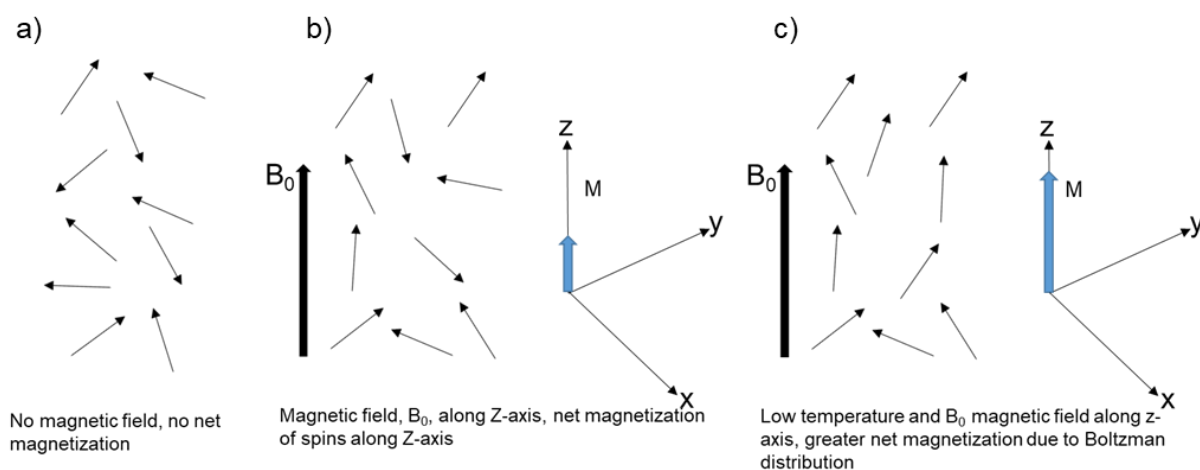


Figure 2.2 a) Classical model of bulk spin magnetization, shown in the absence of an external magnetic field where spin vector arrows are arranged randomly meaning that there is no net magnetization in the sample. b) In the presence of a magnetic field, spin vectors have a net alignment which causes bulk magnetisation of the sample in the direction of the applied field. c) Net magnetization of the sample is greater at low temperatures due to Boltzmann statistics.

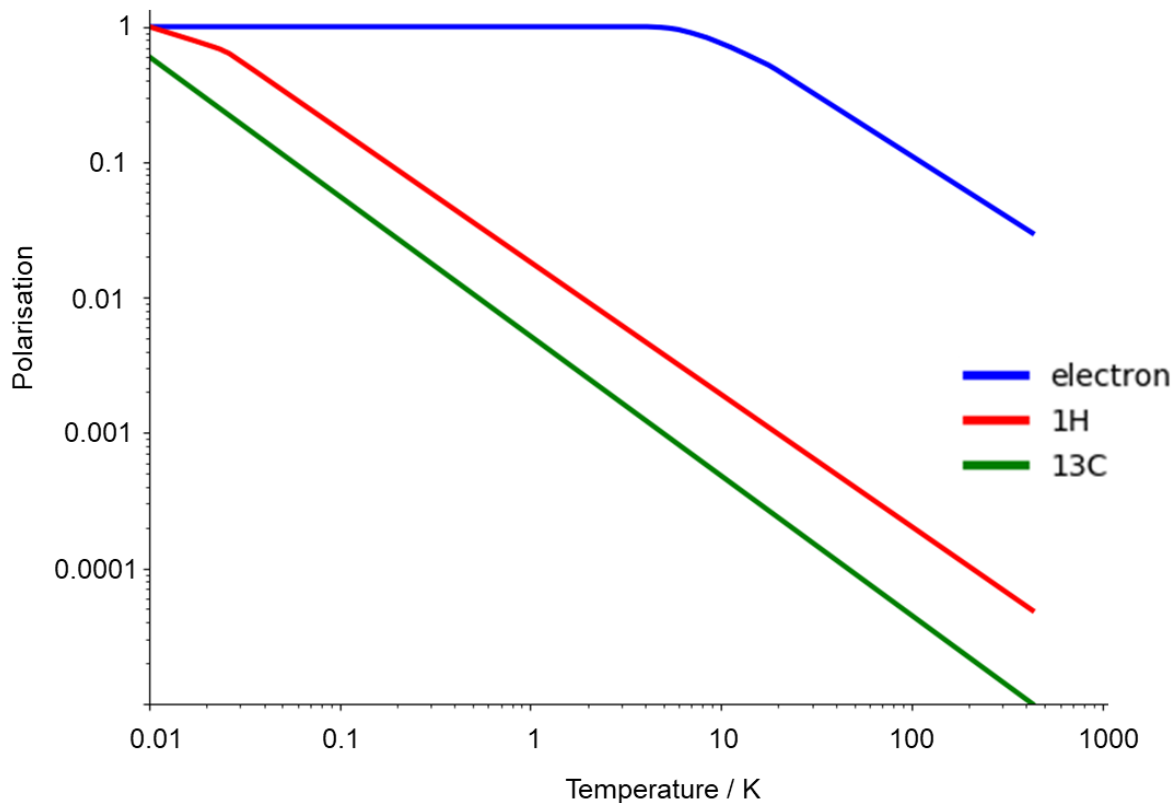


Figure 2.3 Graph showing the polarisation of electrons, ¹H nuclei and ¹³C nuclei as a function of temperature.

2.2. Effect of an RF pulse

In NMR experiments, the transitions between Zeeman split levels are induced by applying an oscillating magnetic field along the axis perpendicular to the direction of the main magnetic field, B_0 . Such an interaction is described by a Hamiltonian-

$$\mathcal{H}_{RF} = -\gamma\hbar B_1 \cos(\omega_{RF}t) I_x \quad (2.5)$$

Where ω_{RF} is the frequency of RF irradiation and B_1 is the strength of the perpendicular magnetic field. When ω_{RF} is on resonance- when it is equal to the Larmor frequency of a nucleus, the effect of this Hamiltonian is equivalent to a stationary magnetic field B_1 in the frame rotating with the Larmor frequency. If a pulse of a finite duration t_p is applied, this would rotate the magnetization around the x-axis by an angle:

$$\theta = \omega_1 t_p \quad (2.6)$$

This is visualised in figure 2.4.

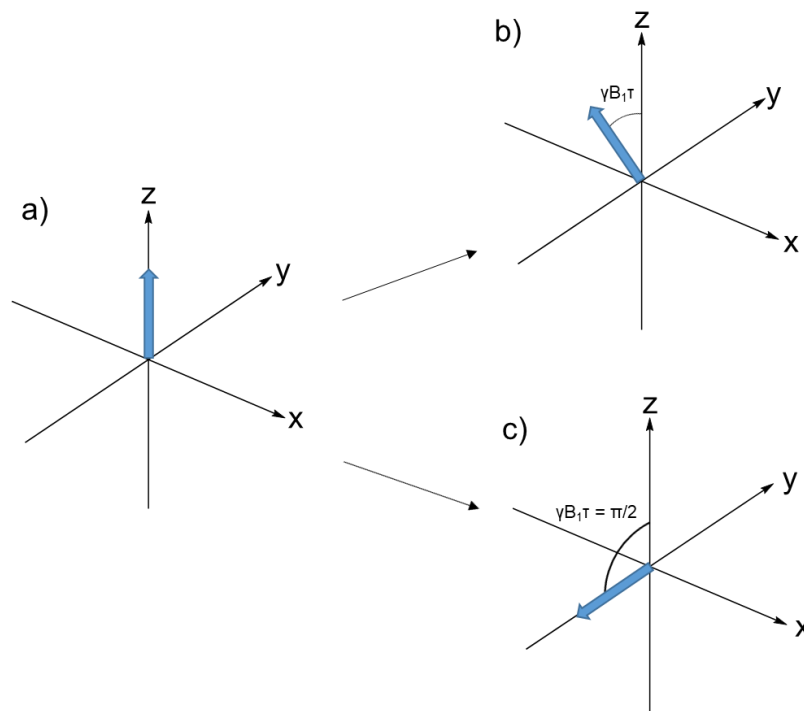


Figure 2.4 A schematic to show the effect of a radiofrequency (rf) pulse on a nuclear spin system. a) shows the system at thermal equilibrium in a magnetic field pointing along the z-axis, with the blue arrow representing the bulk magnetization of the sample. b) after a pulse of length τ , power γB_1 and phase γ (rotation about y axis), the bulk magnetization is rotated by angle $\gamma B_1 \tau$ away from the z-axis, leaving the magnetization vector in the xz plane. c) If $\gamma B_1 \tau = \pi/2$, the magnetization will be rotated to point along the -y-axis.

Maximum signal is acquired in an NMR experiment when the bulk magnetization vector is rotated 90° away from equilibrium position and into xy plane. In the laboratory frame, the magnetization precesses about the z-axis at the Larmor frequency. Such precession induces a voltage in a coil which surrounds the sample, which is detected by the NMR spectrometer electronic circuitry. Detection of this voltage followed by a Fourier transform leads to an NMR spectrum.

2.3. Spin Interactions

When placed in a strong magnetic field, nuclear spins experience a number of interactions with the external magnetic and with other nuclear and electronic spins. These interactions are classified as external and internal, respectively, and can be described using Hamiltonians (Equation 2.7).

$$\hat{\mathcal{H}} = \hat{\mathcal{H}}_{ext} + \hat{\mathcal{H}}_{int} \quad (2.7)$$

The external interactions are those between the spin system and the permanent, static magnetic field, known as the Zeeman interaction, \mathcal{H}_Z and with radiofrequency radiation, \mathcal{H}_{RF} .

$$\hat{\mathcal{H}}_{ext} = \hat{\mathcal{H}}_Z + \hat{\mathcal{H}}_{RF} \quad (2.8)$$

The internal interactions of the spin system describes the interactions between spins in the sample, including chemical shift, J-coupling, dipolar coupling, quadrupolar coupling and hyperfine coupling.

$$\hat{\mathcal{H}}_{int} = \hat{\mathcal{H}}_{CS} + \hat{\mathcal{H}}_J + \hat{\mathcal{H}}_{DD} + \hat{\mathcal{H}}_Q + \hat{\mathcal{H}}_{HF} \quad (2.9)$$

A brief overview of the interactions that are relevant to this thesis are provided.

2.4. Chemical shift

The Larmor frequency for nuclear spins varies slightly in different molecular environments due to the effect of electrons in the bonds that hold atoms together. When a molecule is placed in an external magnetic field, an electronic current is induced in the bonds that surround the nucleus. This induces a very weak magnetic field relative to the external field, which is added to or subtracted from the external field, known as shielding and deshielding, respectively. The chemical shift Hamiltonian is given by Equation 2.10, where the shielding constant, σ , accounts for the shielding effects in the molecule.

$$\mathcal{H}_{CS} = -\gamma\hbar\sigma B_0 I_z \quad (2.10)$$

The chemical shift depends on the orientation of the molecule with respect to the external magnetic field and is described by a CSA tensor. In a static solid state sample, broad lines are observed due to the anisotropic effects- spins in identical chemical environments experience different a slightly different local magnetic field. CSA powder patterns, shown in Figure 2.5, arise because of this effect. The shielding constant, σ in Equation 2.13, is a tensor with values $(\sigma_{xx}, \sigma_{yy}, \sigma_{zz})$. Three parameters using this tensor, which define the CSA of a nucleus. The isotropic chemical shift, σ_{iso} , anisotropy, σ_{aniso} , and asymmetry, η are defined as

$$\sigma_{iso} = \frac{1}{3}(\sigma_{xx} + \sigma_{yy} + \sigma_{zz}) \quad (2.13)$$

$$\sigma_{aniso} = \sigma_{zz} + \sigma_{iso} \quad (2.14)$$

$$\eta = \frac{\sigma_{yy} - \sigma_{xx}}{\sigma_{aniso}} \quad (2.15)$$

according to Haeberlen convention^[1].

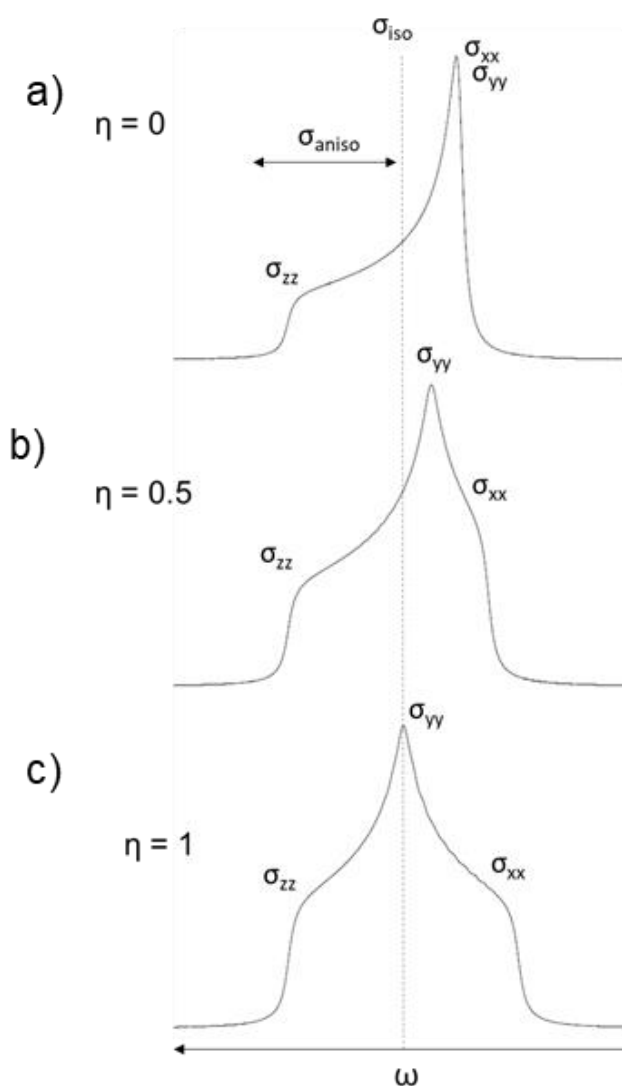


Figure 2.5 Simulated static ¹H spectra with varying asymmetry parameter, η, defined in equation 2.15 (a = 0, b = 0.5, c = 1) to show the effects of chemical shift anisotropy in a solid sample. Simulations were carried out using Simpson^[2].

Analysis of CSA patterns have a number of applications for obtaining information on local electronic environments, including reporting on hydrogen bonding interactions

in proteins^[65]. Effects of CSA are not observed in liquid state spectra due to the rapid tumbling of molecules, giving one time-averaged orientation with respect and the magnetic field for every molecule in the sample.

The effects of CSA in solid state samples can be negated by applying magic-angle spinning (MAS), described in **section 2.6**. This gives rise to narrow peaks at the isotropic chemical shift, which is used to give information about chemical environment. The chemical shift scale is defined based on a reference molecule which ideally contains a nucleus in the most deshielded environment relative to other molecules containing that type of nucleus. A typical reference compound is trimethylsilane (TMS) for ¹³C and ¹H NMR. Chemical shift is reported in parts per million (ppm), measured against this reference frequency, as shown in Equation 2.11.

$$\delta = 10^6 \left(\frac{\nu - \nu_{ref}}{\nu_{ref}} \right) \quad (2.11)$$

Chemical shift is dependent on the chemical environment of the atom, so can be used to determine local structure. The ¹³C chemical shifts of amino acids in a protein sequence have specific chemical shifts, which allow not only identification of the specific amino acid but also information about the secondary structure of the protein. Secondary chemical shift is defined as

$$\Delta\delta = \delta_{observed} - \delta_{random\ coil} \quad (2.12)$$

where $\delta_{observed}$ is the observed amino acid chemical shift and $\delta_{random\ coil}$ is the chemical shift of the same residue in a protein with random coil secondary structure^[3]. Negative CO and C_α and positive C_β $\Delta\delta$ values are characteristic of α -helical structures whereas positive CO and C_α and negative C_β indicate β -sheet structure. Also, some nuclei, such as ¹⁹F have chemical shifts that are particularly sensitive to nuclear environment. This can be employed in studies of molecular structure and dynamics.

2.5. Dipolar coupling

Dipolar coupling is a through space dipole-dipole interaction of two nuclear magnetic moments. The magnitude of the interaction depends on the distance between the interacting nuclei, making it a useful tool for measuring internuclear

distances in and between molecules. The Hamiltonian of two homonuclear spins coupled by dipolar coupling is:

$$\mathcal{H}_{DD} = \frac{1}{2} b_{jk} (1 - 3 \cos^2 \theta_{jk}) (3 I_{jz} I_{kz} - \mathbf{I}_j \cdot \mathbf{I}_k) \quad (2.16)$$

$$b_{jk} = \frac{\mu_0 \gamma_j \gamma_k \hbar}{4\pi r_{jk}^3} \quad (2.17)$$

where γ_j and γ_k are the gyromagnetic ratios of both spins, r_{jk} is the distance between the spins j and k and θ_{jk} is the angle between the external magnetic field and the vector that connects the two spins. For a $^{13}\text{C} - ^1\text{H}$ spin pair separated by 1.7 Å, the dipole-dipole coupling strength is 6150 Hz.

Heteronuclear dipolar coupling between ^1H and the nuclei under studies common in organic systems such as proteins and results in broadening of spectral peaks. These effects are combated using magic-angle spinning and high-power decoupling, which are described in the next section. The dipolar term plays an important role in this thesis, as techniques are applied to remove the effects of the interaction from spectra (MAS and heteronuclear decoupling), whilst cross polarisation (CP) including transfer from ^{15}N to ^{13}C and double quantum filtering make use of the dipolar interaction and are used to boost sensitivity, obtain structural protein information and remove unwanted background signals from spectra.

2.6. Essential techniques in ssNMR

NMR spectra of solids typically suffer from line broadening due to CSA and dipolar couplings, making interpretation of such spectra complicated. In order to produce spectra with good resolution and sensitivity, a number of techniques specific to solids have been developed. In particular we focus on magic angle spinning (MAS), high-power heteronuclear decoupling and cross-polarization.

Magic angle spinning (MAS)

A concept that dramatically improved the resolution possible in solid-state NMR experiments was magic angle spinning (MAS)^{[4][5][6]}. MAS removes the effects of CSA from ssNMR spectra as well as removing broadening due to dipolar coupling. In isotropic liquids, the effects of dipolar coupling and CSA are not present in spectra due to time averaging of the interactions with the external magnetic field as a result of molecular tumbling. MAS attempts to replicate this in solids by rapid rotation (up to 126 Hz at the time of writing^[7]) and a rotor angle of 54.74° with respect to the magnetic field. Dipolar coupling and CSA have a $(3\cos^2\theta - 1)$ dependence, so these interactions are averaged to zero at the magic angle. Typically, MAS spectra feature a main peak due to the isotropic chemical shift and several sidebands separated by the MAS rotation frequency ν_r . At low rotation frequencies the envelope of the sidebands reproduces the static NMR spectrum. With increasing spinning frequency the sideband intensities get smaller, and their position shifts further away from the isotropic peak. Spinning sidebands are observed in simulated spectra recorded under MAS, shown in Figure 2.7. Faster spinning results in sidebands reducing in intensity and moving further away from peaks of interest.

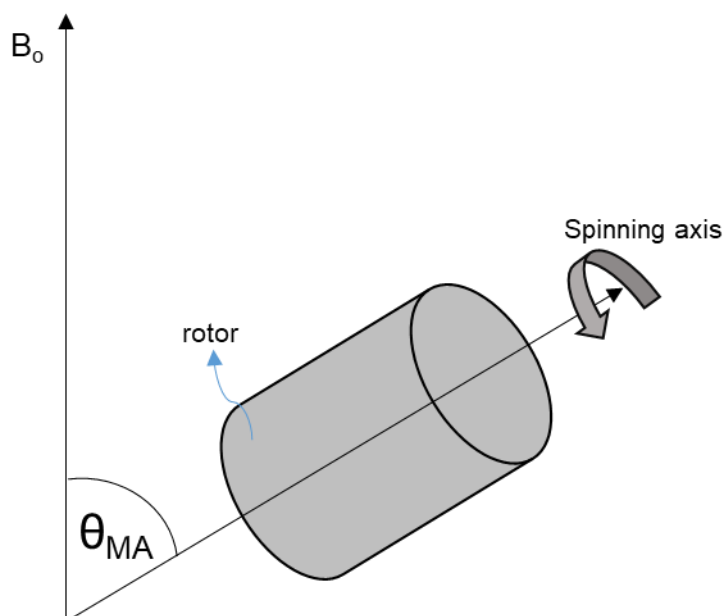


Figure 2.6 Diagram of a sample containing rotor oriented at $\theta_{MA} = 54.74^\circ$ with respect to the B_0 field.

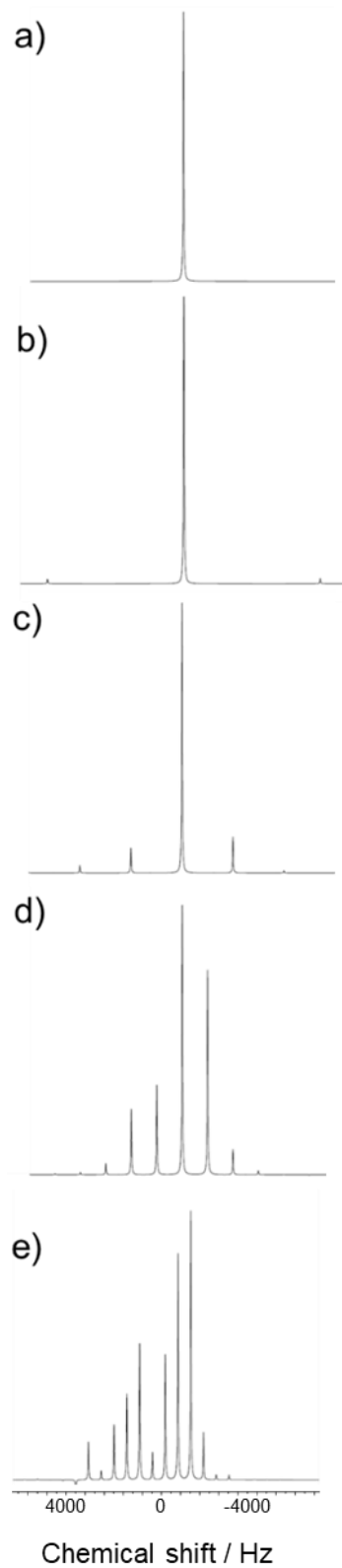


Figure 2.7 Simulated ^{13}C spectra at different spinning speeds (a) 10000 Hz, b) 5000 Hz, c) 2000 Hz, d) 1000 Hz, e) 500 Hz) in a 400 MHz ^1H Larmor frequency field. CSA in the simulation was 4000 Hz.

Heteronuclear high power decoupling

Quite commonly, MAS alone cannot entirely remove the effects of heteronuclear couplings with ^1H nuclei because of a rather significant strength of the proton couplings. This occurs in systems with extensive homonuclear dipolar couplings between abundant spins that which are coupled by a heteronuclear dipolar interaction with the nuclear spin which is being acquired, such as ^1H spins when acquiring ^{13}C signals in an organic species. Also, under DNP conditions spinning speeds are lower than for room temperature experiments (15 kHz for DNP versus 25 kHz at room temperature), meaning that the strength of dipolar interactions will be stronger than the MAS frequency. In order to get resolved spectra, heteronuclear decoupling^{[8][9]} is applied in many ssNMR experiments, pulse sequence shown in Figure 2.8.

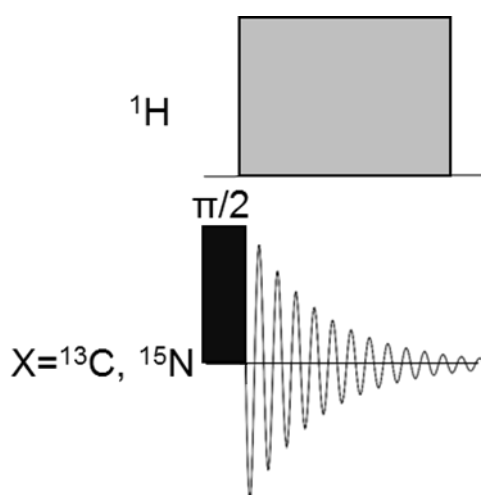


Figure 2.8 Pulse sequence showing a high power heteronuclear decoupling pulse which is applied during the acquisition time of the other channel.

The radiofrequency irradiation of ^1H nuclei causes repeated transitions between the Zeeman spin- $\frac{1}{2}$ $\alpha \leftrightarrow \beta$ energy levels at a rate determined by the amplitude of the applied pulse, $-\omega_1$. Provided that the frequency of transitions is fast relative to the ^1H -X dipolar coupling strength, the X nuclei experience a time-averaged dipolar coupling to ^1H , which averages to zero as the spin state of ^1H oscillates rapidly between $\pm\frac{1}{2}$. In modern ssNMR experiments, two-pulse phase-modulated decoupling (TPPM)^[10] and small phase incremental alteration with 64 steps (SPINAL-64)^[11] are two commonly used heteronuclear decoupling schemes that have been shown to be effective.

Cross-polarisation (CP)

Cross polarisation^[12] is a method of transferring magnetisation between nuclei of different types, enabled by the dipolar interaction. It is mainly used to boost the sensitivity of low γ nuclei by polarisation transfer from high γ nuclei- most commonly ^1H , but it can also be used to study nuclei that are close in space or for spectral editing^[13]. Figure 2.9 shows the pulse sequence for a CP experiment to increase the sensitivity of a low- γ nuclei.

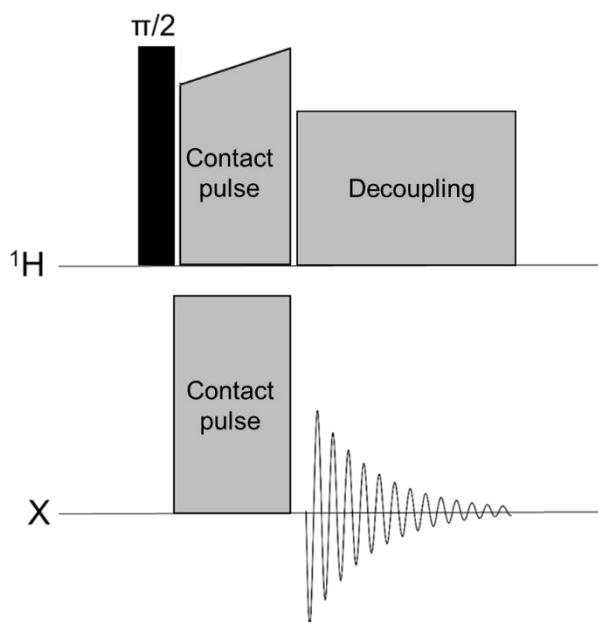


Figure 2.9 Pulse sequence for cross polarisation experiment from ^1H to a low γ nuclei. A 90° pulse is applied to bring ^1H magnetization into the transverse plane after which the contact pulses are applied to both channels in which magnetization is transferred from ^1H to X. An FID is then acquired on the X channel whilst a heteronuclear decoupling pulse is applied to the ^1H channel.

Since the thermal equilibrium polarization of ^1H is greater than the polarisation of low- γ nuclei, magnetisation transfer via cross-polarisation produces signal enhancement for the latter. In addition, the recovery delay between acquisitions is often reduced because ^1H relaxation times are typically faster than those of low- γ nuclei. This allows acquiring more scans per unit time of an experiment. In a CP experiment, the amplitudes of the contact pulses on the ^1H and X channels should satisfy the Hartman-Hahn matching condition^[14],

$$\gamma_H B_1(H) = \gamma_X B_1(X) \quad (2.18)$$

$B_1(H)$ and $B_1(X)$ are the applied magnetic field to both channels, so meeting this condition sets the energy gap between ^1H and X spin states to be equal. Under MAS conditions, the Hartman-Hahn condition becomes

$$\gamma_H B_1(H) = \gamma_X B_1(X) + n\omega_r \quad (2.19)$$

where ω_r is the MAS frequency and n is an integer number^[15]. A redistribution of energy occurs from the ^1H spin bath to X nuclei after flipping ^1H magnetization into the transverse plane, mediated by the dipolar coupling between ^1H and X.

2.7. Dynamic Nuclear Polarisation (DNP)

A more novel method of boosting sensitivity in high-field NMR experiments is Dynamic Nuclear Polarisation (DNP). This involves transferring electron magnetization to nuclei by irradiating electron paramagnetic resonance (EPR) transitions with microwave irradiation of appropriate frequency. The concept of DNP was introduced in 1953 by Overhauser^[16] and demonstrated experimentally by Carver and Slichter^[17]. Technological advances mean that DNP is now possible in both solid-state and liquid-state NMR, which will be reviewed in this section. There are a number of physical mechanisms by which DNP occurs, namely the Overhauser effect^{[18][19]}, thermal mixing^{[20][21]}, the cross effect (CE) and the solid effect (SE). The mechanisms most relevant to this work are the CE and SE, which will be discussed in detail.

Solid Effect

The solid effect (SE) DNP mechanism is a two spin model involving the interaction of one electron and one nucleus and makes use of narrow EPR line monoradical polarising agents^{[22][23]}. The hyperfine coupling between the electron and nucleus results in the mixed eigenstates shown in Figure 2.10. Microwave irradiation, $\omega_{\mu W}$ at the sum or difference of the nuclear Larmor frequency, ω_{0I} and electron Larmor frequency, ω_{0S}

$$\omega_{\mu W} = \omega_{0S} + \omega_{0I} \quad (2.20)$$

$$\omega_{\mu W} = \omega_{0S} - \omega_{0I} \quad (2.21)$$

causes saturation of forbidden double-quantum or zero-quantum transitions which results in a simultaneous flip of both the electron and nuclear spins leading to non-equilibrium nuclear magnetisation and either positive or negative enhancement. The drawback of optimising samples for SE DNP is that enhancement scales with B_0^{-2} , making this mechanism less applicable at high fields.

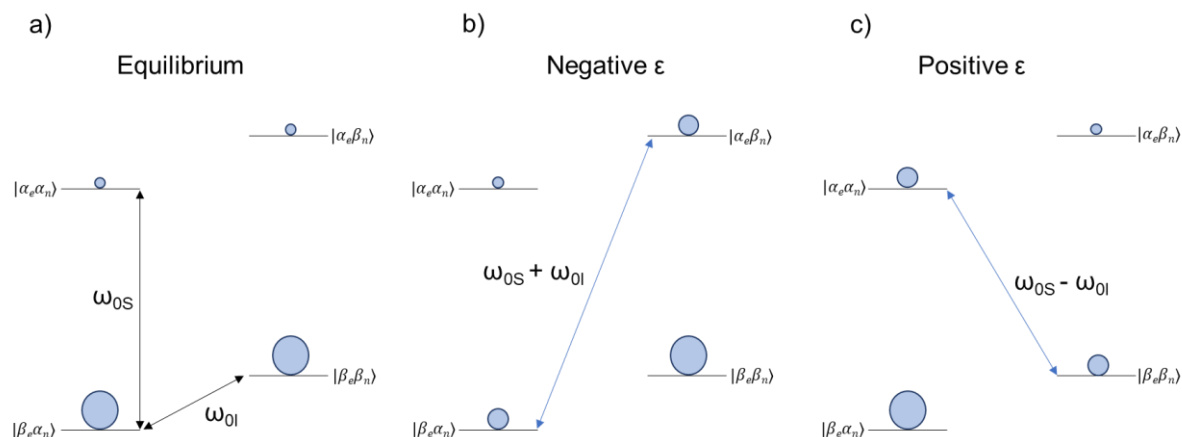


Figure 2.10 Energy level diagram showing the solid effect DNP mechanism. a) The four energy levels resulting from hyperfine coupling of an electron and a nucleus are shown at thermal equilibrium, with the size of the blue circles representing the population of the energy level. b) Microwave irradiation at the sum of the electron and nucleus Larmor frequency, $\omega_{0S} + \omega_{0I}$, results in equilibration of the populations of the $|\beta_e\alpha_n\rangle$ and $|\alpha_e\beta_n\rangle$ energy levels. Overall, such irradiation produces a non-equilibrium polarisation of $|\beta_n\rangle$ states giving a large negative polarisation of nuclear spins. In contrast, microwave irradiation at $\omega_{0S} - \omega_{0I}$ gives rise to positive nuclear enhancements.

Cross effect

Cross-effect^[24] (CE) DNP involves a three-spin system consisting of two electrons and a nucleus. The two electrons are introduced into the sample as a biradical, discussed in **section 2.11** which should have a large g-anisotropy causing a broad EPR linewidth. g-anisotropy is similar to CSA experienced by a nuclear spin- the anisotropic electronic environment surrounding the electron spin in a molecule with restricted molecular motion leads to electrons in different molecules experiencing different local magnetic fields, giving rise to a broad signal. The energy level diagram for the three spin CE is shown in Figure 2.11a). A condition for efficient CE is that

$$\omega_{0I} = \omega_{0S1} - \omega_{0S2} \quad (2.22)$$

where ω_{0I} is the nuclear Larmor frequency and ω_{0S1} and ω_{0S2} are the Larmor frequencies of the two biradical electrons. This means that the $|\alpha_1\beta_2\alpha_n\rangle$ and $|\beta_1\alpha_2\beta_n\rangle$ energy levels shown in Figure 2.11b) are degenerate, and the mutual action of dipole-dipole and hyperfine couplings leads to their mixing. Microwave irradiation at ω_{0S1} or ω_{0S2} causes an allowed single quantum transition of that electron and a simultaneous forbidden double quantum transition of the other. This results in a greater population difference in nuclear α and β states which gives a larger NMR signal. CE enhancement scales with B_0^{-1} so is often preferred to the SE for experiments at high field^[25].

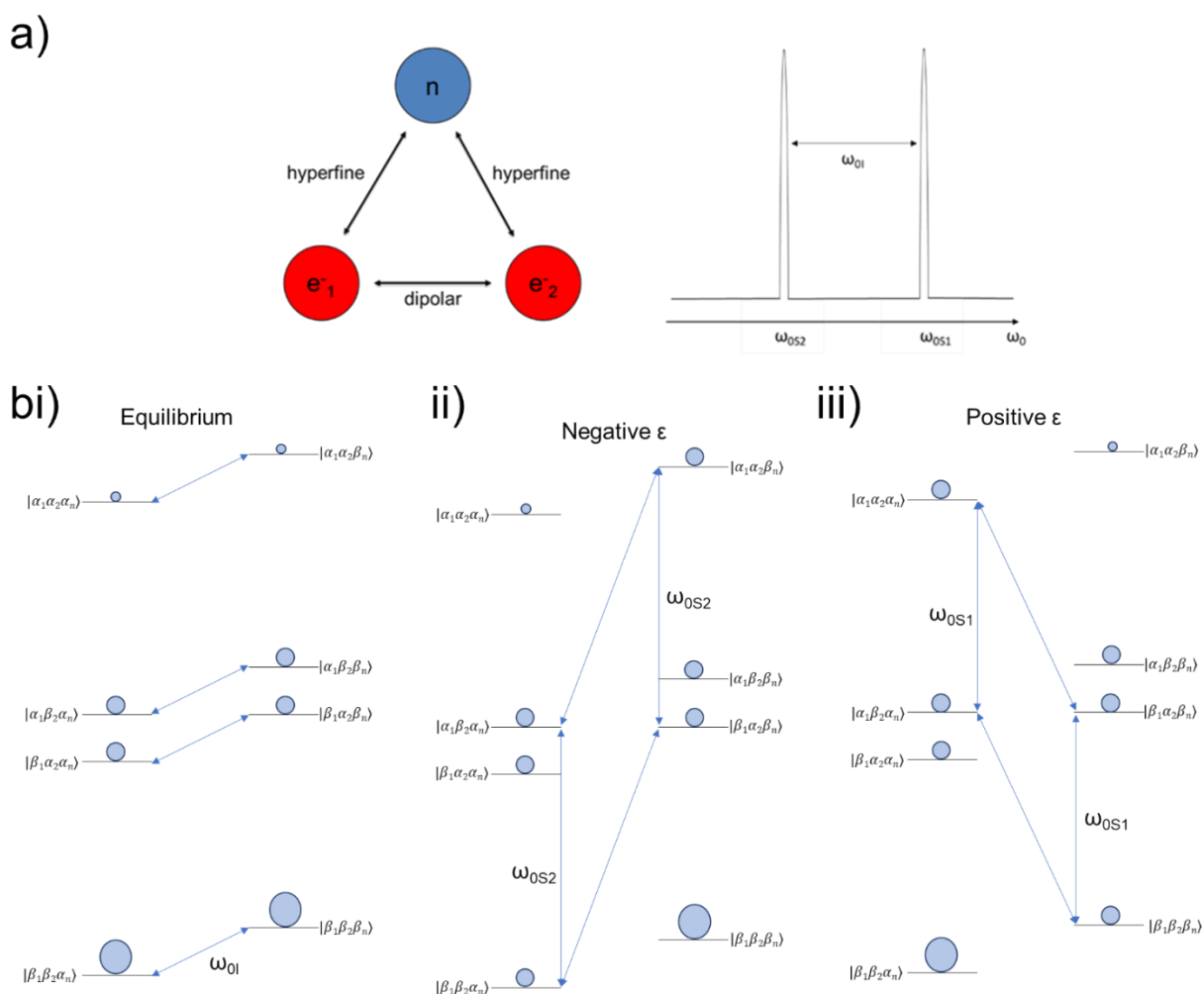


Figure 2.11 Energy level diagram showing the cross effect (CE) DNP mechanism. a) For efficient CE, the difference in Larmor frequency of dipolar coupled electrons should equal the Larmor frequency of the nucleus under study. b) Energy level diagram for the CE. i) The eight energy levels are present due to hyperfine (electron – nuclear) and dipolar (nuclear-nuclear) interactions are shown at equilibrium,

with the blue circles representing the population of the energy level. ii) Microwave irradiation at the Larmor frequency of electron 2, ω_{0S2} , causes the populations of the $|\beta_1\beta_2\alpha_n\rangle$, $|\alpha_1\beta_2\alpha_n\rangle$, $|\beta_1\alpha_2\alpha_n\rangle$ and $|\alpha_1\alpha_2\beta_n\rangle$ to equalise. This means that nuclear β energy levels have a much greater population than α levels which corresponds to negative DNP enhancement (middle). iii) Microwave irradiation at the Larmor frequency of electron 1, ω_{0S1} , causes an increase in nuclear α spin state population resulting in positive DNP enhancement.

CE under MAS

Under MAS conditions, the cross effect mechanism shown in Figure 2.11 is only valid at certain points of the rotor cycle, where the energy levels in a three-spin system cross with one another. As has been demonstrated previously^{[26][27]}, microwave irradiation excites one of the electrons, while level crossings happen over several rotor cycles causing three-spin flips leading to non-equilibrium nuclear polarization. One of the consequences of the CE under MAS conditions is nuclear depolarization, observed through a reduction of the NMR signal intensity under MAS in the presence of unpaired electrons without microwave irradiation^{[28][29]}. Numerical simulations show a relationship between depolarization effects and radical orientations- radical orientations that lead to strong enhancement also produce less depolarisation and *vice versa*^[28]. The standard method of calculating DNP enhancement is to compare signal strength with and without microwave irradiation. This does not take into account the depolarization effect in the microwave off spectra, so reported enhancements do not reflect the overall improvement in NMR signal-to-noise.

2.8. Polarising agents

CE radicals

The introduction of a biradical with rationally designed electronic properties increased the probability of the CE condition being met relative to adding a monoradical^[30]. The most efficient CE biradicals in use for MAS applications have a structure of two nitroxide radicals tethered together with a linker group, which determines the orientation of the two TEMPO nitroxide radical groups relative to one another and the distance between them. The linker also determines other important

properties such as solubility in a given solvent, so certain biradicals can be used depending on which solvent is compatible with the system under study. The electrons in the biradical should have a large EPR linewidth relative to nuclear Larmor frequencies, due to inhomogeneous broadening by g-anisotropy and long electron spin relaxation time, T_{1e} , which gives improved electron spin saturation leading to better DNP enhancement. Nitroxide radicals have been found to have a number of these favourable properties^[30]. TOTAPol is an important radical, designed for aqueous systems due to its relatively good solubility in an aqueous sample matrix and also showing good DNP enhancements^[31]. AMUPol was developed later and has improved solubility of water as well as producing greater enhancements^[32]. TEKPol is not water soluble but gives better enhancement than AMUPol when introduced into non-aqueous samples^[33] and has been shown to give enhancement in aqueous matrixes when introduced in surfactant vesicles^[34]. The chemical structures of these biradicals are shown in Figure 2.12.

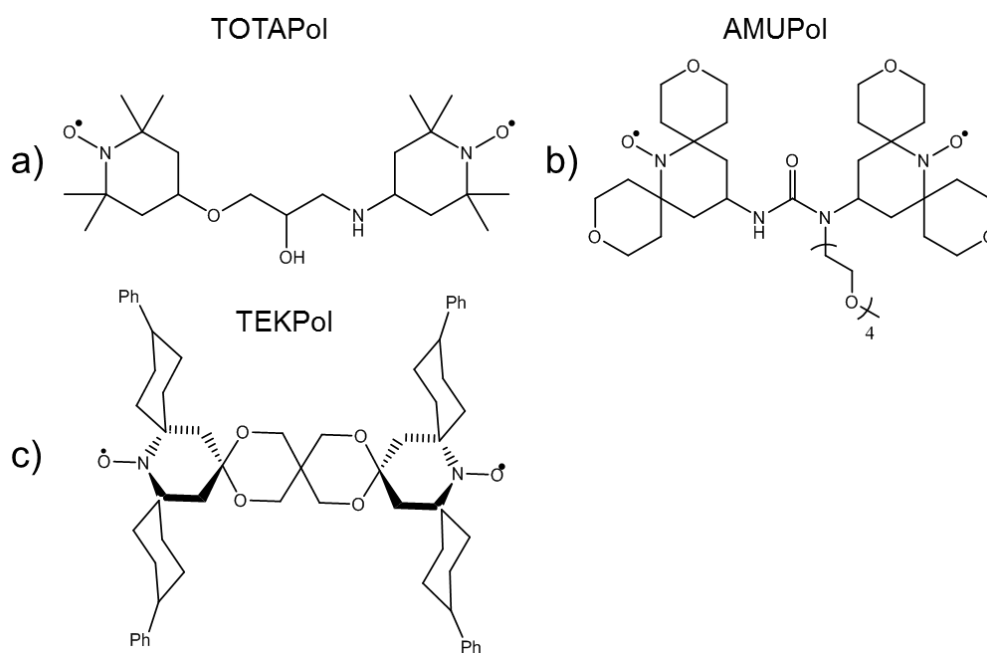


Figure 2.12 Chemical structures of biradicals used for MAS-DNP. a) TOTAPol was designed for solubility in an aqueous DNP sample matrix. b) AMUPol provides greater water solubility with improved overall enhancement, c) TEKPol gives better enhancement than both, but is insoluble in aqueous conditions.

For static cross effect DNP, TEMPO monoradical can be used. Addition of an alcohol group gives 4-hydroxy-TEMPO, known as TEMPOL, which makes the radical soluble in an aqueous DNP matrix. The structures are shown in Figure 2.13.

This radical is useful for ^1H - ^{19}F heteronuclear DNP as Larmor frequency of both nuclei falls within the large EPR linewidth of the radical electron^{[35][36]}.

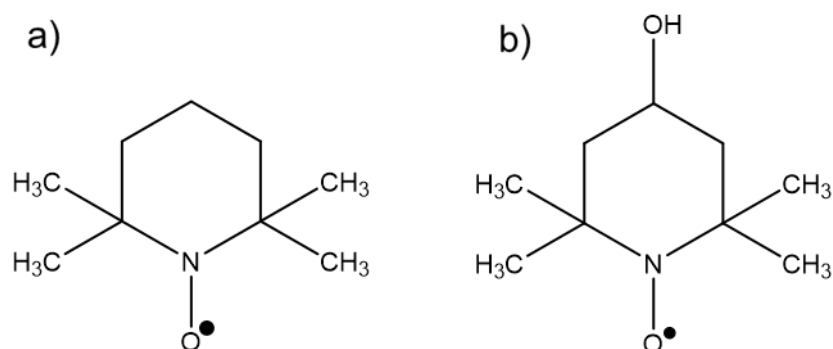


Figure 2.13 Chemical structure of TEMPO and TEMPOL, which have been shown to produce efficient heteronuclear DNP by the CE mechanism in static samples. TEMPOL has improved solubility in aqueous samples.

SE radicals

Radical polarizing agents should satisfy the condition for efficient SE (Equations 2.20, 2.21) and can be easily introduced into a relevant solvent system. The EPR linewidth of the radical electron should be narrower than the Larmor frequency of the nucleus that is being polarized. Examples of commonly used radicals to achieve SE DNP are trityl-OX063^[37], high-spin transition metal ions^[38] and BDPA^[39].

2.9. MAS DNP sample

As already discussed, a biradical polarising agent must be added to a MAS DNP sample to achieve enhancement. The concentration of biradical is an important property, as too much biradical leads to less overall sensitivity gain due to depolarization effects whilst a low biradical concentration leads to fewer nuclei being hyperpolarised leading to a fraction of the maximum enhancement. This has been shown experimentally for a number of sample types, including for biomembrane samples^[40] and has been simulated numerically^[41]. Cryoprotectant is required in DNP MAS samples to produce an amorphous glass sample rather than a sample with a crystalline structure. Ice has a distinct crystal structure at the cryogenic temperatures (~90 K) at which experiments are carried out. The ice crystals expel biradicals from the matrix, which causes regions of the sample to have clusters with high concentration of unpaired electrons. This clustering produces much faster

electron relaxation leading to reduced enhancement. Glycerol is often chosen as a cryoprotectant and has shown better performance to dimethyl sulfoxide (DMSO) for biomembrane samples^[40]. The cryoprotectant also protects the biological system at low temperature. Aqueous MAS DNP samples typically contain a high proportion of deuterated solvent, 90 % in the experiments presented. While a sufficiently high level of protonation is needed for efficient transfer of polarisation by spin diffusion, sample deuteration increase nuclear and electronic relaxation times leading to more DNP enhancement^[66].

2.10. MAS DNP hardware

MAS DNP requires a number of hardware components to be integrated together. These include a source of high-power microwave irradiation, cryogenic temperatures <180 K, MAS capability, control of DNP matching conditions and probe design to allow for cryogenic temperatures and transfer of microwaves to the sample.

DNP in solid state samples at high magnetic fields required development of microwave sources capable of generating microwaves of sufficient power and frequency to irradiate EPR transitions in large magnetic fields. The hardware to make this a possibility was developed by the Griffin group- the gyrotron is able to generate high power and high frequency microwaves compatible with magnetic fields, initially demonstrated at 5 T (140 GHz microwaves)^[42], and has since been demonstrated at higher fields^[43]. Bruker offers a number of commercial MAS DNP systems with gyrotrons operating at up to 527 GHz^[44]. Table 2.2 summarizes these systems.

Magnetic field / T	Microwave frequency / GHz	EPR wavelength / mm	¹H NMR frequency / MHz
9.4	263	1.14	400
14.1	395	0.76	600
18.8	527	0.57	800

Table 2.2 Properties of current commercially available Bruker MAS DNP systems

Other microwave sources for MAS DNP at high fields include extended interaction oscillators / klystron^[45], backward wave oscillators^[46] and solid-state sources^{[47][48]}.

Gyrotrons generate a fixed microwave frequency, so the magnetic field of the NMR magnet must be swept across a range of field strengths to meet DNP matching

conditions. This is achieved by including a sweepable superconducting coil in the magnet. Other hardware options for meeting DNP matching conditions at high field are tunable microwave sources^[49] and fast microwave frequency modulation^[50].

Integrating MAS with DNP NMR was first demonstrated at low field (~1.5 T) by Wind et al. using specially designed probes that allow microwave irradiation to reach the sample space^[51]. Low temperature are required to increase nuclear and electron T_1 relaxation times and to ensure a strongly dipolar-coupled spin system so that the various DNP mechanisms are efficient. A number of approaches have been used to achieve low temperatures (20 K – 180 K) in combination with MAS.

Temperatures of 100 K – 180 K can be achieved using evaporating nitrogen gas from a liquid nitrogen gas, which is pressurized and used in the bearing and drive gas lines that cause spinning by precisely directing gas flow onto fins at the bottom of the rotor. This is achieved by using heating copper coils surrounding a liquid nitrogen bath to produce gas at a desired rate to maintain the pressure of the MAS gas supply^[52]. Temperatures below 90 K in MAS DNP require helium gas cooling, which can be used to achieve sample temperatures of down to 20 K. Two methods have been devised to do this- using Helium as the MAS spinner gas^{[53][54][55]} or using the variable temperature gas line to supply helium gas to the sample, and using nitrogen as the spinner gas^{[56][57]}. To improve resolution in MAS DNP experiments, technical developments leading to faster MAS is important. Due to the higher viscosity of cold nitrogen gas, slower spinning speeds have been achieved than in room temperature ssNMR experiments. Integration of MAS DNP with smaller rotors (down to 1.3 mm) means that spinning speeds up to 40 KHz, which improves resolution and opens up the possibility of ^1H detected experiments^[58].

A number of probe designs have been presented to allow transmission of microwaves to the sample space and to operate at cryogenic temperatures^{[52][54]}. Microwaves are transmitted from the source to the sample space using a corrugated inner waveguide, which have been developed to cause very little microwave power attenuation^[59].

These technological developments- the combination of boosted sensitivity due to DNP at low temperature, with high field NMR and MAS has led to many applications within the fields of materials science and biology. Chapters 3, 4 and 5 describe measurements carried out on a MAS DNP system in which sample conditions and ssNMR experiments are optimised in order to study the structure of amyloid beta (1-40) ($\text{A}\beta(1-40)$) peptide in a lipid environment.

2.11. Dissolution DNP Hardware

DNP in liquid-state NMR has been achieved using dissolution DNP (d-DNP)^[60]. d-DNP involves microwave irradiation of a low temperature sample (1 K – 2 K) doped with polarizing radical and cryoprotectant followed by rapid dissolution using hot solvent after which an NMR signal is acquired. The pioneering experiment in this field was carried out by Ardenkjaer-Larsen et al. in 2003^[61]. Their set-up involved a modified 7 T polarising magnet with in-built dissolution equipment, manual transfer of the hyperpolarized sample in an NMR tube and signal acquisition in a high resolution 9.4 T magnet in a time of < 6 seconds after dissolution.

Rapid sample injection is important in d-DNP experiments, as the high polarisation achieved at cryogenic temperatures decays due to T_1 relaxation. Another consideration is bubbles in the sample tube following dissolution. A sample injection device, designed by Bowen et al., solved these problems by applying high pressure to the dissolved sample and using conductivity or optical sensors to trigger an automated system^{[62][63]}. Magnetic tunnels have also been used in d-DNP setups, which consist of a solenoid wrapped around the transfer line between the polarization magnet and the acquisition magnet, reducing polarization losses during the transfer time^[64].

In chapter 6, a d-DNP methodology is presented for a biological system with a much shorter transfer time which is useful for studying molecules with short t_1 times.

2.12. References

- [1] U. Haeberlen. *High Resolution NMR in Solids, Selective Averaging*, 1976.
- [2] M. Bak, J. T. Rasmussen, N. C. Nielsen, *J. Mag. Reson.*, 2000, **147**, 296-330
- [3] D. S. Wishart, C. G. Bigam, A. Holm, R. S. Hodges, B. D. Sykes, *J. Biomol. NMR*, 1995, **5**, 67-81
- [4] E. R. Andrew, R. G. Eades, *Discuss. Faraday Soc.*, 1962, **34**, 38-42
- [5] E. R. Andrew, *Prog. Nucl. Magn. Reson, Spectrosc.*, 1971, **8**, 1-39
- [6] S. Penzel, A. Oss, M.-L. Org, A. Samoson, A. Böckmann, M. Ernst, B. H. Meier, *J. Biomol. NMR*, 2019, **73**, 19–29
- [7] T. Polenova, R. Gupta, A. Goldbourt, *Anal. Chem.*, 2015, **87**, 5458–5469
- [8] A. I. Bloom, J. N. Shoolery, *Phys. Rev.*, 1955, **97**, 1261-1265
- [9] P. K. Madhu, *Isr. J. Chem.*, 2014, **54**, 25-38
- [10] A. E. Bennett, C. M. Rienstra, M. Auger, K. V. Lakshmi, R. G. Griffin, *J. Chem. Phys.*, 1995, **103**, 6951-6598
- [11] G. Comellas, J. J. Lopez, A. J. Nieuwkoop, L. R. Lemkau, C. M. Rienstra, *J. Magn. Reson.*, 2011, **209**, 131–135
- [12] A. Pines, M. G. Gibby, J. S. Waugh, *J. Chem. Phys.*, 1973, **59**, 569-590
- [13] M. J. Duer, *solid-state NMR spectroscopy*, 2004, 1st edition
- [14] S. R. Hartmann, E. L. Hahn, *Phys. Rev.*, 1962, **128**, 2042-205
- [15] S. Hediger, B. H. Meier, R. R. Ernst, *Chem. Phys. Lett.*, 1995, **240**, 449-456
- [16] A. W. Overhauser, *Phys. Rev.*, 1953, **92**, 411-415
- [17] T. R. Carver, C. P. Slichter. *Phys. Rev.*, 1953, **92**, 212-214
- [18] T. V. Can, M. A. Caporini, F. Mentink-Vigier, B. Corzilius, J. J. Walish, M. Rosay, W. E. Maas, M. Baldus, S. Vega, T. M. Swager, R. G. Griffin, *J. Chem. Phys.*, 2014, **141**, 064202
- [19] X. Ji, T. V. Can, F. Mentink-Vigier, A. Bornet, J. Milani, B. Vuichoud, M. A. Caporini, R. G. Griffin, S. Jannin, M. Goldman, G. Bodenhausen, *J. Magn. Reson.*, 2018, **286**, 138–142

- [20] A. Abragam, M. Goldman, *Rep. Prog. Phys.*, 1978, **41**, 395–467
- [21] V. A. Atsarkin, *Sov. Phys. Uspekhi*, 1978, **21**, 725-745
- [22] C. D. Jeffries, *Phys. Rev.*, 1957, **106**, 164-165
- [23] Y. Hovav, A. Feintuch, S. Vega, *J. Magn. Reson.*, 2010, **207**, 176-89
- [24] Y. Hovav, A. Feintuch, S. Vega, *J. Magn. Reson.*, 2012, **214**, 29–41
- [25] T.V. Can, Q.Z. Ni, R.G. Griffin, *J. Magn. Reson.*, 2015, **253**, 23–35
- [26] K. R. Thurber, R. Tycko, *J. Chem. Phys.*, 2012, **137**, 084508
- [27] F. Mentink-Vigier, U. Akbey, Y. Hovav, S. Vega, H. Oschkinat, A. Feintuch, *J. Magn. Reson.*, 2012, **224**, 13-21
- [28] F. Mentink-Vigier, S. Paul, D. Lee, A. Feintuch, S. Hediger, S. Vega, G. De Paëpe, *Phys. Chem. Chem. Phys.*, 2015, **17**, 21824-21836
- [29] K. R. Thurber, R. Tycko, *J. Chem. Phys.*, 2014, **140**, 184201
- [30] D. J. Kubicki, G. Casano, M. Schwarzwald, S. Abel, C. Sauvee, K. Ganesan, M. Yulikov, A. J. Rossini, G. Jeschke, C. Coperet, A. Lesage, P. Tordo, O. Ouari, L. Emsley, *Chem. Sci.*, 2016, **7**, 550–558
- [31] C. Song, K.-N. Hu, C.-G. Joo, T. M. Swager, R. G. Griffin, *J. Am. Chem. Soc.*, 2006, **128**, 11385-11390
- [32] C. Sauvée, M. Rosay, G. Casano, F. Aussenac, R. T. Weber, O. Ouari, P. Tordo, *Angew. Chem. Int. Ed.*, 2013, **52**, 10858 –10861
- [33] A. Zagdoun, G. Casano, O. Ouari, M. Schwarzwald, A. J. Rossini, F. Aussenac, M. Yulikov, G. Jeschke, C. Coperet, A. Lesage, P. Tordo, L. Emsley, *J. Am. Chem. Soc.*, 2013, **135**, 12790–12797
- [34] M. Lelli, A. J. Rossini, G. Casano, O. Ouari, P. Tordo, A. Lesage, L. Emsley, *Chem. Commun.*, 2014, **50**, 10198—10201
- [35] I. Kaminker, D. Shimon, Y. Hovav, A. Feintuch, S. Vega, *Phys. Chem. Chem. Phys.*, 2016, **18**, 11017-11041
- [36] A. Gennaro thesis, *19F Dynamic Nuclear Polarisation- Towards a novel method for studies of protein dynamics*, 2019
- [37] A. A. Smith, B. Corzilius, J. A. Bryant, R. De Rocher, P. P. Woskov, R. J. Temkin, R. G. Griffin, *J. Magn. Reson.*, 2012, **223**, 170–179

- [38] B. Corzilius, A. A. Smith, A. B. Barnes, C. Luchinat, I. Bertini, R. G. Griffin, *J. Am. Chem. Soc.*, 2011, **133**, 5648-5651
- [39] I. R. Becerra, G. J. Gerfen, B. F. Bellew, J. A. Bryant, D. A. Hall, S. J. Inati, R. T. Weber, S. Un, T. F. Prisner, A. E. McDermott, K. W. Fishbein, K. E. Kreisler, R. J. Temkin, D. J. Singel, R. G. Griffin, *J. Magn. Reson.*, 1995, **117**, 28-40
- [40] S. Y. Liao, M. Lee, T. Wang, I. V. Sergeev, M. Hong, *J. Biomol. NMR*, 2016, **64**, 223–237
- [41] F. Mentink-Vigier, S. Vega, G. De Paëpe, *Phys. Chem. Chem. Phys.*, 2017, **19**, 3506—3522
- [42] L. R. Becerra, G. J. Gerfen, R. J. Temkin, D. J. Singel, R. G. Griffin, *Phys. Rev. Lett.*, 1993, **71**, 3561–3564
- [43] V.S. Bajaj, M.K. Hornstein, K.E. Kreisler, J.R. Sirigiri, P.P. Woskov, M.L. Mak-Jurkauskas, J. Herzfeld, R.J. Temkin, R.G. Griffin, *J. Magn. Reson.*, 2007, **189**, 251-279
- [44] M. Rosay, M. Blank, F. Engelke, *J. Magn. Reson.*, 2016, **264**, 88-98
- [45] T.F. Kemp, H.R. Dannatt, N.S. Barrow, A. Watts, S.P. Brown, M.E. Newton, R. Dupree, *J. Magn. Reson.*, 2016, **265**, 77-82
- [46] V.L. Bratman, A.E. Fedotov, Y.K. Kalynov, P.B. Makhalov, A. Samoson, *J. Infrared Millim. Te.*, 2013, **34**, 837-846
- [47] T.A. Siaw, A. Leavesley, A. Lund, I. Kaminker, S. Han, *J. Magn. Reson.*, 2016, **264**, 131-153
- [48] K.R. Thurber, W.M. Yau, R. Tycko, *J. Magn. Reson.*, 2010, **204**, 303-313
- [49] A.C. Torrezan, S.T. Han, I. Mastovsky, M.A. Shapiro, J.R. Sirigiri, R.J. Temkin, A.B. Barnes, R.G. Griffin, *IEEE Trans. Plasma Sci.*, 2010, **38**, 1150-1159
- [50] T. Idehara, E.M. Khutoryan, Y. Tatematsu, Y. Yamaguchi, A.N. Kuleshov, O. Dumbrajs, Y. Matsuki, T. Fujiwara, *J. Infrared Millim. Te.*, 2015, **36**, 819-829
- [51] R.A. Wind, F.E. Anthonio, M.J. Duijvestijn, J. Smidt, J. Trommel, G.M.C. de Vette, *J. Magn. Reson.*, 1983, **52**, 424–434
- [52] A.B. Barnes, M.L. Mak-Jurkauskas, Y. Matsuki, V.S. Bajaj, P.C.A. van der Wel, R. DeRocher, J. Bryant, J.R. Sirigiri, R.J. Temkin, J. Lugtenburg, J. Herzfeld, R.G. Griffin, *J. Magn. Reson.*, 2009, **198**, 261-270

- [53] D.A. Hall, D.C. Maus, G.J. Gerfen, S.J. Inati, L.R. Becerra, F.W. Dahlquist, R.G. Griffin, *Science*, 1997, **276**, 930-932
- [54] D. Lee, E. Bouleau, P. Saint-Bonnet, S. Hediger, G. De Paëpe, *J. Magn. Reson.*, 2016, **264**, 116-124
- [55] Y. Matsuki, T. Idehara, J. Fukazawa and T. Fujiwara, *J. Magn. Reson.*, 2016, **264**, 107-111
- [56] K.R. Thurber, R. Tycko, *J. Magn. Reson.*, 2008, **195**, 179-186
- [57] K. Thurber, R. Tycko, *J. Magn. Reson.*, 2016, **264**, 99-106
- [58] S.R. Chaudhari, P. Berruyer, D. Gajan, C. Reiter, F. Engelke, D.L. Silverio, C. Coperet, M. Lelli, A. Lesage, L. Emsley, *Phys. Chem. Chem. Phys.*, 2016, **18**, 10616-10622
- [59] E.A. Nanni, S.K. Jawla, M.A. Shapiro, P.P. Woskov and R.J. Temkin, *J. Infrared Millim. Te.*, 2012, **33**, 695-714
- [60] E. Ravera C. Luchinat, G. Parigi, *J. Magn. Reson.*, 2016, **264**, 78–87
- [61] J. H. Ardenkjaer-Larsen, B. Fridlund, A. Gram, G. Hansson, L. Hansson, M. H. Lerche, R. Servin, M. Thaning, K. Golman, *Proc. Natl. Acad. Sci. U.S.A.*, 2003, **100**, 10158-10163
- [62] S. Bowen, C. Hilty, *Phys. Chem. Chem. Phys.*, 2010, **12**, 5766-5770
- [63] S. Bowen, C. Hilty, *Angew. Chem. Int. Ed.*, 2008, **47**, 5235-5237
- [64] J. Milani, B. Vuichoud, A. Bornet, P. Miéville, R. Mottier, S. Jannin, G. Bodenhausen, *Rev. Sci. Instrum.*, 2015, **86**, 024101
- [65] L. Yao, A. Grishaev, G. Cornilescu, A. Bax, *J. Am. Chem. Soc.*, 2010, **132**, 10866–10875
- [66] A. S. L. Thankamony, J. J. Wittmann, M. Kaushik, B. Corzilius, *Prog. NMR Spec.*, 2017, **102**, 120–195

3. Optimising the membrane sample for DNP MAS experiments	38
3.1. Introduction	38
3.2. Methods.....	39
3.3. Results / discussion	46
3.4. Biradical position within a lipid bilayer.....	53
3.5. Lipid structure disruption by DNP dopants.....	62
3.6. Conclusion and Outlook	68
3.7. References	69

3. Optimising the membrane sample for DNP MAS experiments

3.1. Introduction

To study membrane-protein systems using DNP MAS NMR, an appropriate solvent matrix that gives good signal enhancement and causes minimal disruption to the biological system is necessary. Figure 3.1 shows an illustration of a DNP MAS sample.

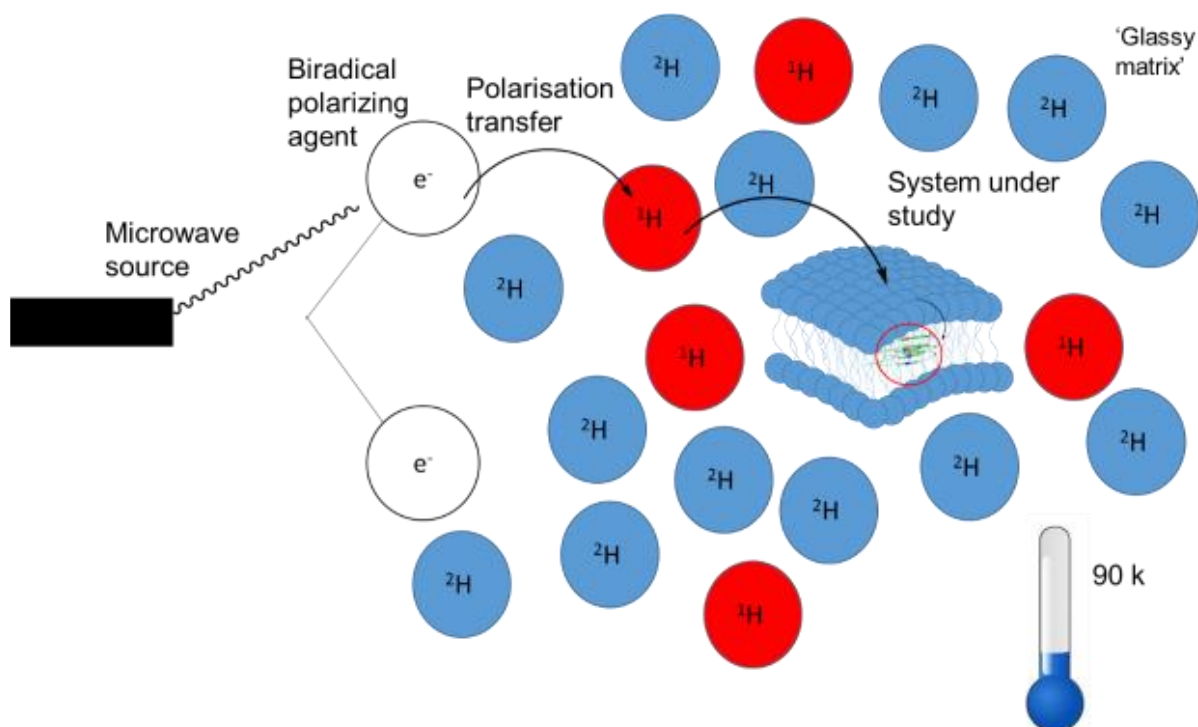


Figure 3.1 The DNP MAS glassy matrix, containing a cryoprotectant to ensure sample homogeneity at low temperature, a high level of deuteration for favourable DNP enhancement and relaxation properties and biradical polarising agent to transfer electron polarisation to nuclei upon microwave irradiation.

The aim of a membrane protein DNP sample is to transfer polarisation homogeneously around ^1H nuclear spins by spin diffusion following cross-effect DNP between the two biradical electron spins and a ^1H nuclear spin. The biological system should retain maximum physiological relevance despite interactions with cryoprotectant, biradical and 90 K temperatures required for efficient MAS DNP.

Hong and co-workers carried out experiments on a variety of lipid vesicle systems with associated peptides in order to achieve maximum DNP enhancement. The influence of the following factors was investigated- 1) the type of biradical used as a

polarising agent 2) the cryoprotectant, 3) the method for incorporating the polarising agent into the sample and 4) deuteration of the lipids^[1]. It was found that

- 1) AMUPol was shown to be a more efficient polarising agent than TOTAPol in a lipid sample, which agrees with studies on the majority of aqueous systems.
- 2) Glycerol was found to give better enhancement than DMSO, and is known to have less of a detrimental effect on some membrane systems^[2].
- 3) Titration of small aliquots of the biradical / cryoprotectant matrix directly into the membrane sample followed by thorough mixing was found to give improved enhancement compared with addition of the matrix followed by centrifugation. This was concluded to be due to more homogeneous mixing of the DNP dopants with the sample using the titration method as centrifugation causes the denser cryoprotectant to sit below the sample.

While these findings are useful, it is important to test other factors affecting the DNP performance. This chapter aims to systematically explore the effect of glycerol content, biradical concentration and freezing rate on the signal strength and relaxation times.

In addition, the room temperature NMR experiments help to establish how the polarizing agents (AMUPol, TEKPol) partition into the lipid bilayer and whether they disrupt its structure.

3.2. Methods

Sample preparation

An initial experiment was carried out to determine the enhancement in a chosen lipid system consisting of a 3:1 ratio of 1-palmitoyl-2-oleoyl-glycero-3-phosphocholine (POPC) / 1-palmitoyl-2-oleoyl-sn-glycero-3-phospho-(1'-rac-glycerol) (POPG). The sample preparation protocol was adapted from work by Qiang et al^[3]. These lipids were chosen to make experiments directly comparable to the work of collaborators who have used the same lipids in a number of A β (1-40) studies using other techniques^[3]. Mammalian cell membranes contain over 50 % Phosphatidylcholine (PC) type lipids, with a many other lipids making up the remaining composition^[25]. Negatively charged POPG was included to make the charge of the lipid mixture more similar to mammalian cell membranes.

POPC (2.60×10^{-2} mmol, 19.8 mg) and POPG (8.67×10^{-3} mmol, 6.8 mg) were dissolved in chloroform, the solvent was then removed using a nitrogen gas stream then lyophilised to remove any remaining chloroform. The mass of the lipid mixture was recorded to confirm CHCl_3 evaporation. The lipid film was hydrated using phosphate buffer (10 ml, 10 mM, pH 7.4) and agitated using a shaker for 1h at ambient temperature, 5 freeze-thaw cycles between liquid nitrogen and ambient temperature were carried out to give homogeneous vesicles. The lipid suspension was centrifuged (26000 rpm) and the remaining solvent removed to give a membrane pellet. The remaining H_2O in the sample was recorded. 5 μL aliquots of the d_8 -99.5% ^{12}C glycerol / D_2O / H_2O 6 / 3 / 1 stock solution containing 10 mM AMUPol were directly added into the membrane pellet (26 μL total) and stirred for 2 min after each aliquot using a vortex mixer, then for a further 5 min after addition of total matrix volume. H_2O / D_2O was removed by lyophilization until the sample is ~ 40 % hydrated by mass. The sample was loaded into a 3.2 mm sapphire rotor then flash frozen and stored in liquid nitrogen.

Pre-incorporation of TEKPol and AMUPol

POPC (2.60×10^{-2} mmol, 19.8 mg), POPG (8.67×10^{-3} mmol, 6.8 mg) and biradical (TEKPol- 3.2×10^{-3} , 0.29 mg AMUPol- 3.2×10^{-3} , 0.23 mg) were co-dissolved in chloroform, the solvent was then removed using a nitrogen gas stream. From here, the procedure is identical to sample preparation above.

Packing the sample into a DNP MAS rotor

The MAS DNP sample must be packed into the 3.2 mm sapphire rotor, shown in Figure 3.2, which is compatible with the commercial Bruker DNP system. The sample after the preparation protocol is a viscous membrane pellet so cannot be packed efficiently with Bruker supplied tools for solid powder samples or pipetted in the same way as a low viscosity liquid. In order to pack the membrane pellet, a polytetrafluoroethylene (PTFE) tool was designed and machined. The tool consists of two parts, the 3.2 mm rotor fits into the larger component and a smaller parts screws into it to hold the rotor in place, shown in Figure 3.2a. The membrane pellet is then scrapped from a centrifuge tube using a spatula and placed in a conical space at the top of the large part, which has a small hole leading to the open top of the rotor (Figure 3.2b). The tool fits into a Beckman Coulter centrifuge rotor (Figure 3.2c). Centrifugation at relatively slow speeds of ~3000 RPM for short times (~10 seconds) forces the membrane pellet into the rotor without separating sample components by centrifugation.

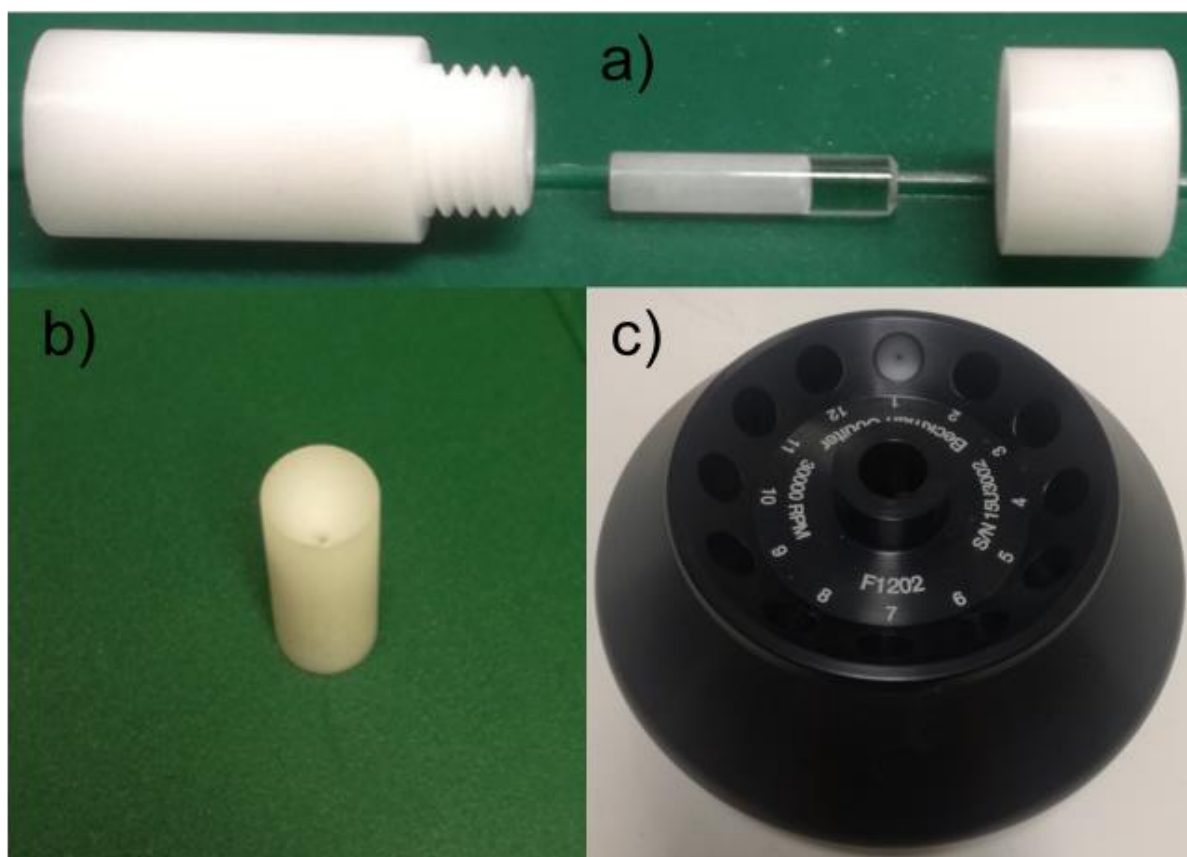


Figure 3.2 Home-built tool used to pack membrane pellet samples into an NMR rotor. a) the rotor fits into a cavity inside the larger part, the smaller part screws onto the bottom to hold the rotor in place. b) The membrane pellet is placed in the conical space at the top of the large component which has a hole above the open end of the rotor. c) The tool fits inside a centrifuge rotor, centrifugation causes the sample to move into the NMR rotor.

Variable freezing rate

Three methods of freezing were tested-

- i) Slow freezing- The rotor was placed into the sample catcher of the DNP probe at room temperature, then injected into the probe and cooled slowly by the MAS and variable temperature (VT) nitrogen gas supply.
- ii) Liquid nitrogen flash freezing- The sample was frozen by holding the rotor in liquid nitrogen from room temperature.
- iii) Isopentane freezing- The sample was frozen by holding the rotor in isopentane, which was placed in a copper cup and cooled by partially submerging it in a liquid nitrogen bath. Figure 3.3 shows the design of the copper cup used for this experiment.

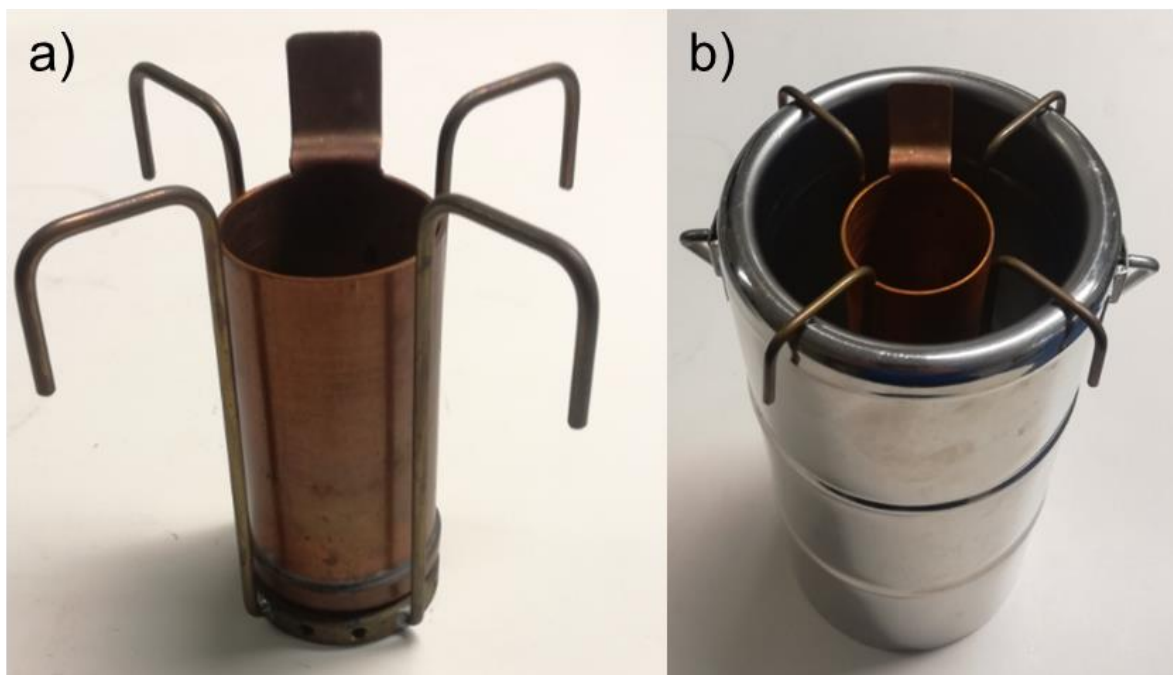


Figure 3.3 a) Image of specially designed copper container to freeze DNP samples quickly, b) designed to be partially submerged in liquid nitrogen. Copper has good thermal conductivity so can be used to cool isopentane to liquid nitrogen temperatures.

Hardware

All DNP-enhanced ssNMR experiments described were carried out on the Nottingham MAS DNP NMR system using a 3.2 mm sapphire rotor, shown in Figure 3.4. It is a commercially available Bruker system consisting of a 600 MHz ^1H Larmor frequency NMR magnet with a sweep coil, a 7.2 T gyrotron which emits 395 GHz microwaves at 5 W power and a MAS chiller unit.

A waveguide transmits microwaves emitted from the gyrotron to a spinning sample rotor in an NMR probe. The sweep coils in the NMR magnet allow adjustment of the magnetic field to achieve the maximum DNP enhancement. The chiller unit produces pressurized nitrogen gas which is used to drive MAS and to chill the sample to cryogenic temperature (90 – 100 K). Spinning speeds up to 15 KHz are achievable when using a 3.2 mm probe. The sample is loaded into 3.2 mm sapphire rotor, stored in liquid nitrogen until the time of the experiment then loaded into a sample catcher and inserted into the probe using a pressurized nitrogen gas line connected to the chiller unit. Condensation is quickly removed from the outside of the rotor during transfer to the base of the probe, using a lint free tissue, to reduce the probability of a rotor crash.

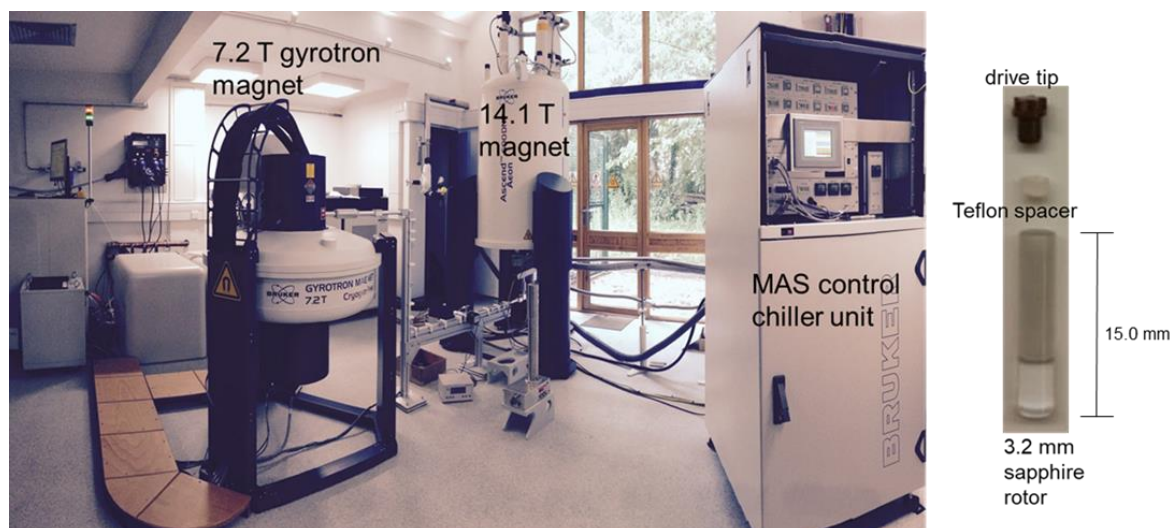


Figure 3.4 Picture of the Nottingham MAS DNP facility. A 7.2 T gyrotron generates 395 GHz high-power microwaves which are transferred to the sample space by a waveguide. Enhanced NMR signals are acquired in a 14.1 T Avance III Bruker magnet. Sample temperature and MAS are controlled by the MAS chiller unit. The sample is packed into a 3.2 mm microwave transparent sapphire rotor.

MAS DNP ssNMR

Lipid samples were packed into 3.2 mm sapphire rotor using the home built packing tool and stored in liquid nitrogen until experiments were performed. DNP microwave-on and microwave-off ^1H - ^{13}C cross-polarisation experiments were performed with 16 scans to measure enhancement. Room temperature ^1H - ^{13}C cross-polarisation experiments were performed with 1024 scans using a conventional 600 MHz ssNMR system. All experiments were carried out at 8 KHz MAS frequency.

Room temperature experiments

sample preparation

POPC (60 mg) or POPG (60 mg) were dissolved in chloroform, the solvent was then removed using a nitrogen gas stream then lyophilised to ensure complete removal of chloroform. The lipid film was hydrated using phosphate buffer (20 ml, 10 mM, pH 7.4) and agitated using a shaker for 1 h at ambient temperature, 5 freeze-thaw cycles between liquid nitrogen and ambient temperature were carried out to give homogeneous vesicles. The lipid suspensions were centrifuged (26000 rpm) and the remaining solvent removed by a pipette to give a membrane pellet. The remaining H_2O in the sample was recorded. The lipid suspension was split into three identical aliquots before addition of DNP dopants. AMUPol (10 mM), TEKPol (10 mM) and AMUPol (10mM) + glycerol (60 % by volume) was added to samples. The

samples were vortexed for 10 min to ensure thorough mixing of the additives with lipid vesicles. The reference sample was not altered. Hydration level in all samples was reduced to ~40 % using a lyophiliser. The sample was packed into a spherical sample space with to ~20 μL volume inside a 4 mm rotor with an 80 μL volume using home-built rotor inserts.

ssNMR

ssNMR experiments were carried out using Bruker 600 MHz avance III spectrometer with a 4 mm ^1H and ^{13}C tuned probe. The $^1\text{H}\rightarrow^{13}\text{C}$ cross-polarisation (CP) experiment was carried out with an MAS rate was 8000 Hz, 1024 acquisitions and an 8 s recycle delay.

^{31}P NMR CSA measurements

Sample preparation

POPC (2.60×10^{-2} mmol, 19.8 mg) and POPG (8.67×10^{-3} mmol, 6.8 mg) were dissolved in chloroform, the solvent was then removed using a nitrogen gas stream then lyophilised to ensure complete removal of chloroform. The lipid film was hydrated using Tris-HCL buffer (20 ml, 10 mM, pH 7.4) and agitated using a shaker for 1h at ambient temperature, 5 freeze-thaw cycles between liquid nitrogen and ambient temperature were carried out to give homogeneous vesicles. The lipid suspension was separated into four equal 5 ml aliquots in volume and centrifuged (26000 rpm), the remaining solvent removed by a pipette to give a membrane pellet. The remaining H_2O in the sample was recorded. To samples b) and d), AMUPol (0.18 mg) was added to give a concentration of 10 mM after dehydration. To samples c) and d), glycerol (14.1 mg) was added to give a glycerol / H_2O ratio of 60 : 40 v / v after dehydration. The samples were vortexed for 10 min to ensure thorough mixing of the additives with lipid vesicles. The reference sample a) was not altered. Hydration level in all samples was reduced to ~40 % using a lyophiliser.

^{31}P ssNMR

NMR measurements were carried out using 2.5 mm rotors in a H / X / Y probe in a Bruker Avance 600 MHz ^1H Larmor frequency magnet. MAS experiments were recorded with a spinning rate was 10 KHz, 1024 acquisitions and SPINAL-64 ^1H decoupling was applied during acquisition. For static experiments, 81920 acquisitions were recorded with SPINAL-64^[26] ^1H decoupling during acquisition.

Effect of sample preparation on DNP Enhancement

The effect of the sample preparation procedure is assessed using the enhancements and relaxation times, which are the most important factors that determine whether a particular DNP-enhanced experiment is feasible.

The DNP enhancement, $\epsilon_{on/off}$, is measured by recording one spectrum with microwaves being transmitted to the rotor from the gyrotron and another without microwave irradiation. $\epsilon_{on/off}$ is defined as

$$\epsilon_{on/off} = \frac{S_{on}}{S_{off}} \quad (3.1)$$

where S_{on} is signal strength with microwave irradiation and S_{off} is signal strength without microwave irradiation.

The overall gain from using DNP is therefore not as simple as the $\epsilon_{on/off}$ measurement. A protocol has been established to analyse the absolute sensitivity gain from DNP enhanced MAS NMR compared to conventional acquisition based on eight factors. This protocol involves making three samples and taking four measurements- 1) microwave on DNP NMR experiment, 2) microwave off NMR experiment at cryogenic temperatures, 3) sample mixed with radical using conventional ssNMR at room temperature, 4) sample without radical recorded using conventional ssNMR^{[4][5]}. Analysis of the signal intensity and resolution in these four samples can be used to calculate the absolute sensitivity ratio (ASR), which has the following contributions-

$$ASR = \epsilon_{DNP} \cdot \epsilon_T \cdot \eta_{T1} \cdot \chi_{bleach} \cdot \chi_{LW} \cdot \chi_{weight} \cdot \chi_{seq} \cdot \chi_{ex} \quad (3.2)$$

where ϵ_{DNP} is the DNP enhancement, ϵ_T is the polarisation gain due to low temperature, η_{T1} is the difference in T_1 and therefore repetition times at low temperature vs room temperature, with T_1 being longer at lower temperatures. χ_{bleach} is the signal bleaching effect due to the paramagnetic biradical, χ_{LW} takes into account differences in linewidths, χ_{weight} is the difference in sample weight in the sample, χ_{seq} is the difference in effective magnetization after decays during the pulse sequence and χ_{ex} takes into account any other differences such as the probe used and magnetic field strength^{[4][5]}. This laborious protocol was not followed in these experiments as the overarching aim of the research is to detect a membrane bound protein at low concentration rather than to exactly quantify sensitivity gain

due to each individual factor. Instead a focus is on the overall signal strength, which the most important experimental parameter for our purposes.

Freezing rate of sample

Large variations in DNP-enhancements have been reported in the literature for seemingly identical samples. In the experimental work described, variations in DNP enhancement have been observed for the same sample when it is stored in liquid nitrogen between experiments. A possible reason for this is the nature of the freezing process of the sample. The effect of varying the method of freezing on the DNP enhancement and other properties was investigated. Removing oxygen dissolved in the sample has been shown to improve DNP enhancement in some systems^[27], this is a possible reason for variations in enhancement.

3.3. Results / discussion

The glassy matrix for this initial experiment was performed using a matrix consisting of a 60 : 30 : 10 d₈- glycerol / D₂O / H₂O containing 10 mM AMUPol biradical, which is a commonly used DNP matrix for aqueous compatible samples^[6]. This was therefore a logical starting point before optimization of sample conditions.

Figure 3.5 shows a comparison of DNP-enhanced and non-enhanced ¹³C-CP spectra of a 3 : 1 POPC / POPG sample at cryogenic temperatures and a hydrated lipid sample containing POPC vesicles at the same magnetic field .

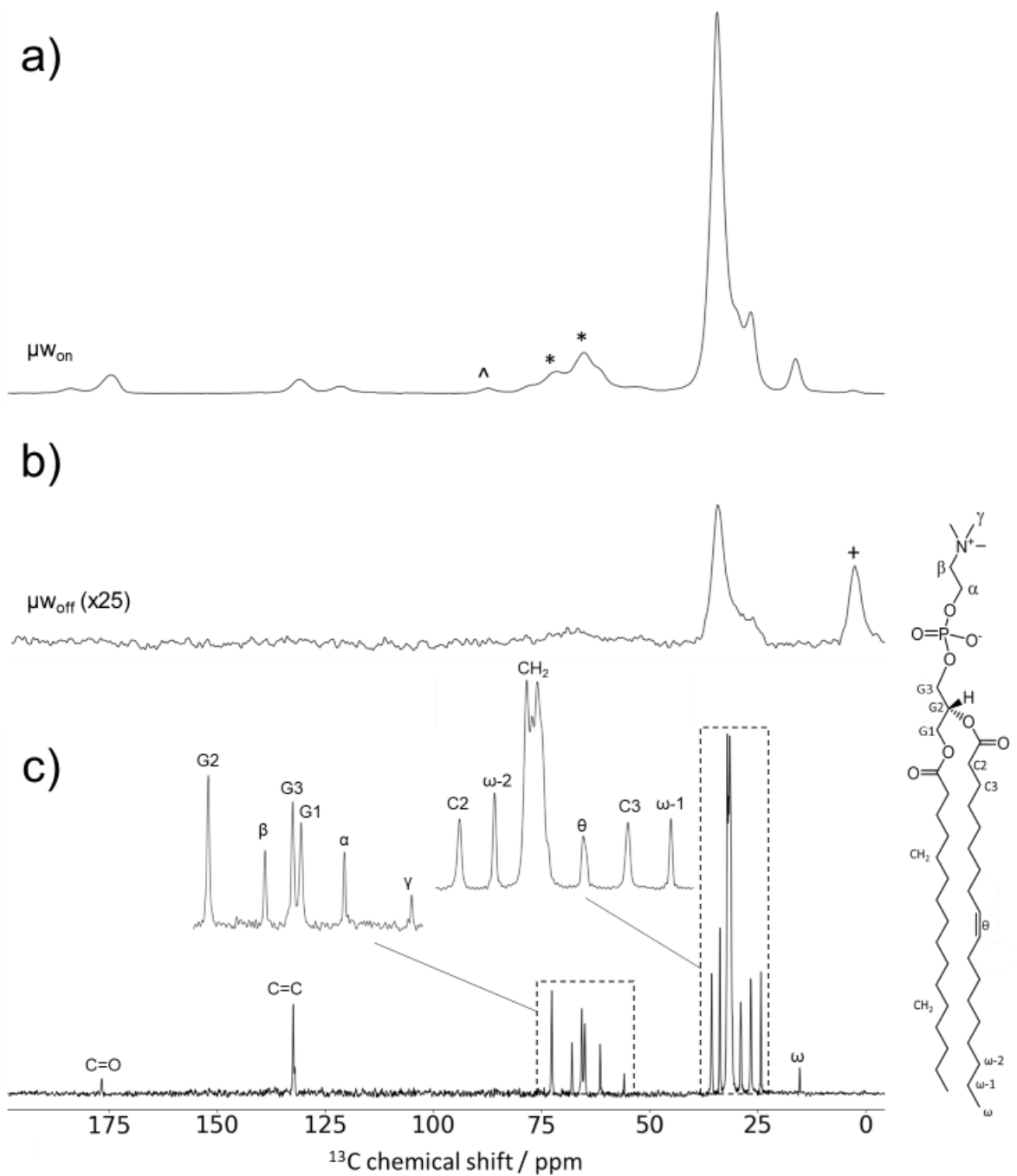


Figure 3.5 ^{13}C cross-polarisation spectra of a lipid sample containing 3:1 POPC/POPG. a) DNP enhanced microwave-on spectrum of the lipid sample in a DNP matrix consisting of 60:30:10 d_8 -glycerol/ $\text{D}_2\text{O}/\text{H}_2\text{O}$. b) The same sample recorded under the same conditions but with microwaves-off. These spectra were compared to quantify DNP enhanced, which was 54 for this sample. $*$ shows glycerol peaks, which are in the same region as the lipid peaks found in the 50-75 ppm range, \wedge denotes spinning sidebands and the $+$ symbol shows a peak due to a polymer stopper placed between the rotor cap and sample. c) an assigned^[7] spectrum of a sample containing hydrated POPC vesicles sample at room temperature using a conventional 600 MHz NMR spectrometer (not to scale in terms of signal intensity).

This demonstrates the sacrifice in resolution that must be taken when working at the cryogenic temperatures (90 – 100 K) required for efficient MAS DNP. The CH₂ lipid tail at 33 ppm is the main feature of the DNP enhanced spectrum. The broad lines at cryogenic temperatures, caused by restricted molecular motions, causes several nearby peaks to be included in this one. The ω, C=C and C=O peaks are also well defined in the DNP enhanced spectrum. Glycerol resonates close to the lipid peaks between 50 ppm and 75 ppm, so these peaks are not clearly defined in the DNP lipid spectrum. Identifying the peaks that come from lipids was important in later experiments when protein was included in the sample. This sample contained 10 mg glycerol (sample 2 in table 3.1).

Glycerol content

DNP is performed at low temperatures to achieve sufficiently long electron (100-1000 μs) and nuclear longitudinal relaxation times to allow for efficient DNP. In the Nottingham DNP MAS system, evaporating gas from a liquid nitrogen supply is used to give sample temperatures of 90 -100 K during experiments. This means that a cryoprotectant is required in aqueous samples to form a homogeneous glassy matrix at low temperature. The crystalline structure formed when water freezes excludes soluble radicals from the sample bulk, causing aggregation of the radical. Glycerol and DMSO are examples of cryoprotectants commonly used in biological DNP samples. Experimental and computational modelling data shows that in aqueous samples containing a high mole fraction of glycerol, glycerol-glycerol and water-glycerol hydrogen bonding is prominent but water-water hydrogen bonding interactions are perturbed, with water molecules preferring to exist as monomers, preventing the formation of large ice crystals at low temperatures^{[8][9]}. Glycerol has also been shown to protect lipid unilamellar vesicles from the negative effects of freezing water. The altered hydrogen bonding properties of water when mixed with glycerol means that the vesicle surface is not strained by water crystallization^[2].

Glycerol content was varied to in further samples to assess differences in enhancement, T₁ and T₂, displayed in table 3.1.

Sample reference	Glycerol content / mg	$\epsilon_{on/off}$				Relative signal intensity / A. U.	T_1 / s	T_2^* / ms
		CO	C=C	CH ₂	Glyc.			
1	0	14	14	11	-	16	3.9	7.38
2	10	-	-	53	60	100	12.8	7.76
3	20	26	-	30	32	45	12.2	6.84

Table 3.1 $\epsilon_{on/off}$, relative signal intensity (relative to **sample 2**), build-up time and T_2^* for lipid samples with varying glycerol content. – indicates that signal-to-noise in the microwave-off CP spectrum was not sufficient to calculate enhancement.

Sample **1** was prepared without glycerol to test whether the synthetic membrane would act as a cryoprotectant in a MAS DNP experiment. Less enhancement was observed than when glycerol is included in samples **2** and **3**, suggesting a limited ability of lipids to solubilise and ensure a homogeneous distribution of radical. The shorter T_1 relaxation time indicates that the nature of the sample is different from the cryoprotected samples at cryogenic temperatures, and possibly suggest clustering of biradical molecules. A higher glycerol content in sample **3** gave a lower enhancement than sample **2**, which could be due to a lower ^1H concentration across the sample causing polarisation transfer by spin diffusion across the sample to become less efficient. Also, more of the rotor volume is occupied by cryoprotectant rather than sample which subtracts from overall signal intensity.

Biradical concentration

The concentration of biradical is an important property. A high concentration of biradical leads to high DNP enhancement, $\epsilon_{on/off}$, and reduces T_1 and therefore the repetition time required between scan acquisitions, which serve to increase overall sensitivity. However, paramagnetic bleaching and depolarization are also more significant at high biradical concentrations which lead to a decrease in overall sensitivity. A lower biradical concentration results in lower $\epsilon_{on/off}$ and longer T_1 but leads to a reduction in depolarization and paramagnetic relaxation. The optimum concentration is found by balancing this factors to give the greatest overall sensitivity and resolution. Biradical concentration has the subject of studies after the installation of commercial Bruker DNP systems^[10].

Table 3.2 shows lipid samples with different AMUPol biradical concentrations.

Sample reference	[AMUPol] / mM	$\epsilon_{on/off}$				relative signal intensity	Build-up time / s	T_2^* / ms
		CO	C=C	CH ₂	Glyc.			
4	5	44	28	37	34	128	11.4	5.91
2	10	-	-	53	60	100	12.8	7.76
5	30	28	-	26	22	70	3.3	5.14

Table 3.2 $\epsilon_{on/off}$, relative signal intensity, build-up time and T_2^* for lipid samples with varying AMUPol biradical

5 mM and 30 mM AMUPol content in samples **4** and **5** show reduced $\epsilon_{on/off}$ compared sample **2**, but it is important to note the short build-up time in sample **5** and the relative signal intensity in sample **4**. Short build-up time in sample **5** is consistent with there being a high concentration of paramagnetic relaxation agent in the sample means that there would be more signal per time when acquiring an experiment with a high number of scans. However, high concentrations of biradical also leads to line broadening and therefore reduced resolution which could make protein assignments difficult in later experiments. Sample **4** with 5 mM shows improved relative signal intensity (not dependant on enhancement) compared to sample **2**. This could be due to depolarization effects in the microwave-off spectrum at 10 mM AMUPol.

As sample **2** gave the greatest overall enhancement, the prevalence of using 10 mM AMUPol biradical in the literature and the fact that differences in relative signal enhancement could also be due to differences in the amount of lipids that were present in the rotor means that 10 mM was the chosen biradical concentration for protein containing samples.

AMUPol and TEKPol pre-incorporation

TEKPol is known not to be water soluble but shows better enhancement than AMUPol in systems compatible with an organic solvent, commonly trichloroethylene (TCE). However, TEKPol has been shown to provide good enhancement in aqueous samples when solubilised in an appropriate surfactant^[11]. We tested the hypothesis that TEKPol would sit in the membrane vesicles, which would act in the same way as surfactant vesicles and provide good enhancement to the membrane system. For this experiment, TEKPol biradical molecules were pre-incorporated into the membrane vesicles during sample preparation in the same way as A β (1-40), described in the methods section of the next chapter.

Table 3.3 shows the shows the properties of DNP samples prepared with pre-incorporation of TEKPol and AMUPol in lipid vesicles.

Sample reference	[TEKPol] / mM	$\varepsilon_{on/off}$				relative signal intensity	T_1 / s	T_2^* / ms
		CO	C=C	CH ₂	Glyc.			
6	5	6	5	8	5	37	11.45	6.42
7	10	10	12	14	10	32	7.82	6.14
8	20	5	-	8	4	9	9.65	5.01
9	5	3	3	3	3	14	4.88	3.81
10	10	5	4	6	6	14	11.76	3.81

Table 3.3 $\varepsilon_{on/off}$, relative signal intensity, build-up time and T_2^* for lipid samples with pre-incorporated TEKPol (samples **6**, **7** and **8**) and AMPol (sample **9** and **10**) at varied concentrations.

The enhancements using TEKPol show the same variation with varying concentration as with AMUPol, shown in Table 3.3, with sample **7** (10 mM biradical) showing the greatest enhancement, albeit significantly lower than the enhancement factors observed for AMUPol.

Interestingly, TEKPol shows higher enhancements than AMUPol when the biradicals are incorporated into membrane vesicles but a significantly lower enhancement than when AMUPol is mixed with membrane after vesicle formation. This suggests that AMUPol is a more efficient polarizing agent when dissolved in the bulk solvent, rather than when closely associated with lipid molecules.

TEKPol and AMUPol biradicals are possibly being solubilised in lipid vesicles by a similar mechanism to what has been observed in aqueous samples in which detergents have been introduced, where TEKPol molecules have been shown to provide DNP enhancements when solubilised in a variety of surfactants^[11]. If this is the case, TEKPol has been shown to provide better enhancement than AMUPol when samples are prepared in this way. The relative signal intensities show that the low biradical concentrations in samples **6** and **9** are favoured when samples are mixed in this way, as weak microwave-off signals are observed with this method of adding the biradical. This is likely due to depolarization effects due to the proximity of biradical paramagnetic centres to lipid nuclear spins. The lipid T_2 is shorter for pre-incorporated AMUPol than for pre-incorporated TEKPol or for exogenously added AMUPol.

Freezing rate of sample

Large variations in DNP-enhancements have been reported in the literature for seemingly identical samples. Han and co-workers have shown that this may be due to glass polymorphism at different sample freezing rates^[12]. In the experimental work described, variations in DNP enhancement have been observed for the same sample after being stored in liquid nitrogen between experiments. A possible reason for this is the nature of the freezing process of the sample, which may differ depending on slight variations in the time taken to transfer the sample containing rotor from a liquid nitrogen dewar and into the 90-100 K sample space in the NMR probe. The effect of varying the method of freezing on the DNP enhancement and other properties was investigated.

Table 3.4 shows the properties of lipid DNP samples with different freezing protocols.

Sample reference	Freezing method	$\epsilon_{on/off}$				relative signal intensity	T_1 / s	T_2^* / ms
		CO	C=C	CH ₂	Glyc			
11	Isopentane 1	27	27	32	45	81	7.71	4.22
12	Liquid nitrogen 1	45	32	45	53	110	8.62	4.58
13	Isopentane 2	27	38	32	42	53	10.71	4.34
14	Liquid nitrogen 2	-	35	26	45	41	7.62	4.47
15	N ₂ gas stream	23	20	19	20	65	6.48	4.72
16	Liquid nitrogen	32	27	28	27	92	13.33	4.30

Table 3.4 $\epsilon_{on/off}$, relative signal intensity, build-up time and T_2^* for lipid samples with different methods of freezing the sample in samples containing 10 mM AMUpol.

Submerging a sample in liquid nitrogen cooled isopentane results in faster cooling than flash freezing in liquid nitrogen because isopentane has a higher specific heat capacity. When room temperature materials are placed in liquid nitrogen, insulating gas is produced which surrounds the material and creates a buffer to the liquid, slowing the rate of freezing. For the glassy matrix of a MAS DNP sample, this means faster cooling to cryogenic temperature, which is likely to have a significant effect on the final sample morphology^[13].

Samples **11** and **12** show a difference in lipid peak enhancements due to freezing rate, with freezing with liquid nitrogen giving a greater enhancement than with

isopentane. However, Samples **13** and **14** give a contradictory result with respect to freezing rate. Samples **15** and **16** suggest that liquid nitrogen freezing produces greater enhancement than slow freezing using the liquid nitrogen MAS gas supply. These results show the large variability in DNP enhancement for the same sample when frozen at a different rate. The different results on repeating the experiment show that this effect is not specifically due to the rate of freezing, but due to another factor that determines the final morphology of the glassy matrix on going from room temperature to cryogenic temperature. An experiment to determine exactly what the cause of these differences is would be interesting, although it is hard to think of what this could be.

T₁ and T₂ relaxation

T₁ and T₂ relaxation were measured for the lipid CH₂ as this signal gave the best signal to noise. T₁ relaxation determines the recycle delay before each NMR acquisition so is an important factor when considering the time taken to perform experiments. The low temperature used in MAS DNP experiments results in longer relaxation times than at room temperature, but the paramagnetic centres of biradicals result in faster T₁ relaxation of proximal spins. T₂ is reduced when working at cryogenic temperatures compared to room temperature, and is an important property because it is a limiting factor for dipolar recoupling experiments (discussed in detail in **chapter 4**) as well as dipolar dephasing experiments such as REDOR^{[14][15]}. Overall we discovered a slight variation around 5-7 ms upon changing AMUPol concentration and little variation under other conditions. That means that T₂ is not so dramatically limited by the presence of a paramagnetic species.

3.4. Biradical position within a lipid bilayer

Accurately determining the position of biradicals in the sample could prove useful for optimising sample conditions. To further characterise the synthetic membrane interaction with the biradical and glycerol required for DNP, paramagnetic relaxation enhancement (PRE) experiments were performed^{[16][17]}. PRE occurs due to magnetic hyperfine interactions between unpaired radical electron spins and nuclear spins, which has an r^{-6} distance dependence meaning that distances between paramagnetic centres and nuclei can be investigated. A wide range of applications have been found for PRE in biological samples, including synthetic lipid systems. C.

Hilty et al. showed that the orientation of lipid head groups in a membrane-protein system can be determined using a combination of lipophilic and polar paramagnetic probes^[18]. Another study involving nitroxide labelling of amyloid fibrils and long range PRE measurements revealed protein folding that could not be determined by ssNMR measurements^[19].

In this study, the paramagnetic centres on AMUPol and TEKPol were used to measure distances between biradicals and lipid vesicle nuclei in order to better characterise this interaction. The effect of glycerol on radical insertion depth into lipid vesicles was also investigated.

The methodology for analysing PREs along the lipid chain was adapted from a similar study from the Hong group^[1]. The relative PRE at each lipid position is given by

$$\frac{S}{S_0} \quad (3.2)$$

where S_0 is the signal strength of the lipid resonance in a hydrated sample without DNP additives and S is the signal strength of attenuated lipid resonance in a sample containing DNP dopants. Signal strength was determined using Topspin integration software. The alkyl ω -1 is taken as a reference for normalisation- S is normalised so that expression 3.2 equals 1 for this peak, to compensate for slight differences in lipid quantities in the samples, as PRE at this insertion depth is assumed to be close to zero. This peak is well resolved and has better signal intensity than the methyl ω , so error is reduced. There is likely to be some attenuation of this signal which would lead to systematic error in all of the other peaks, but this remains a good qualitative measurement of which lipid positions are attenuated more than others.

Lipid assignments for POPC lipids and POPG lipids are shown in Figure 3.6, respectively^{[1][7][20]}. Mixed 3:1 POPC / POPG vesicles were not used for these experiments because signals from each lipid type would overlap making assignments and PRE calculations difficult.

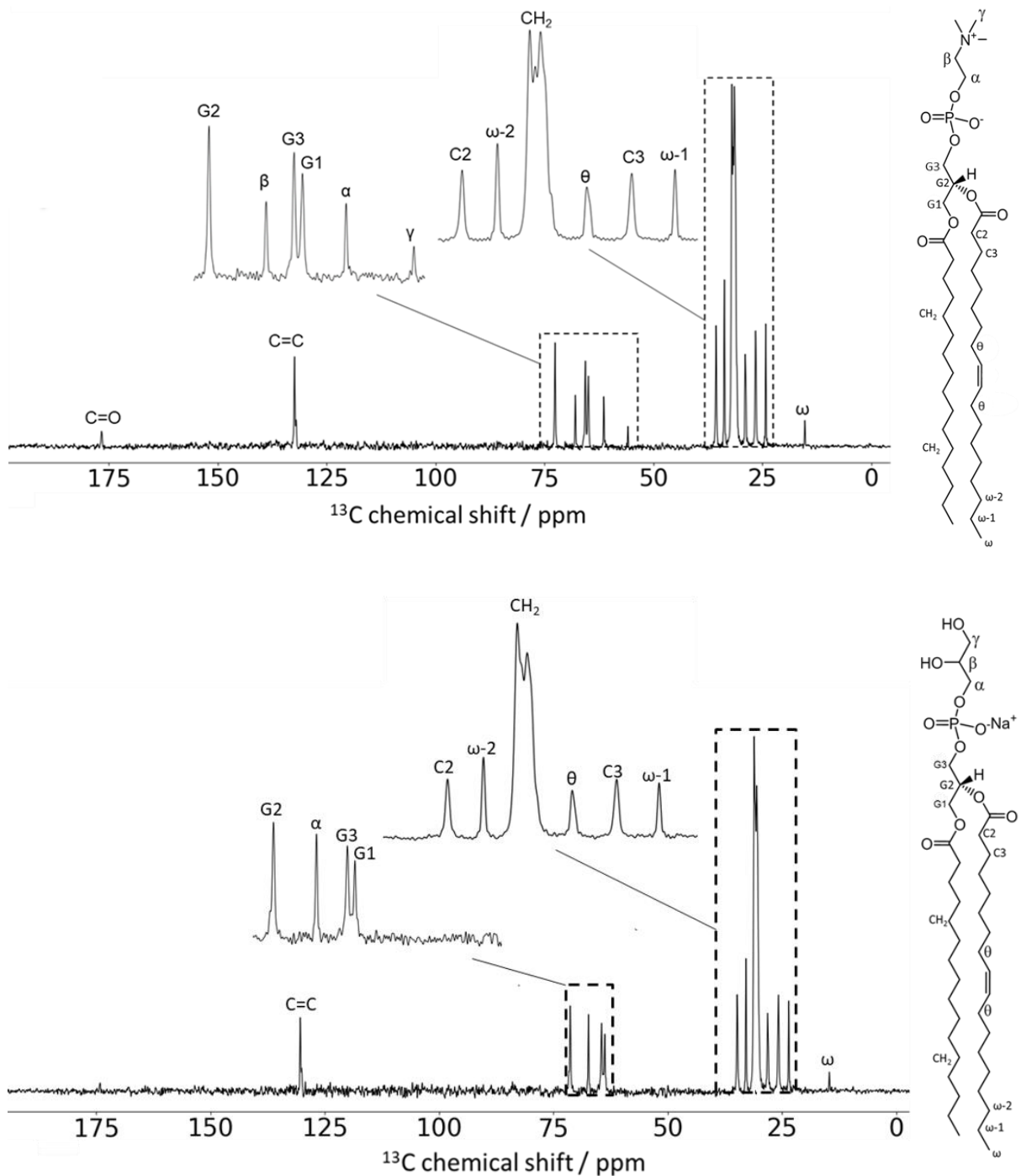


Figure 3.6 ^{13}C CP spectrum showing assignments of a) POPC lipid ^{13}C peaks and b) POPG ^{13}C peaks

An assignment of POPG lipids was not found in the literature, but only the head group positions differ from the molecular structure of POPC. The only unique headgroup POPG peak observed is at ~ 70 ppm and is assigned as α but could be due to the β or γ position. The missing headgroup peaks are possibly obscured by other peaks.

AMUPol insertion in the presence of glycerol

The interaction of glycerol with synthetic lipid vesicles and membrane systems has been the subject of several studies. In the context of a membrane MAS DNP sample, this could be an important interaction in terms of the DNP enhancement achieved for membrane nuclear spins and proteins embedded in the membrane. Insertion of AMUPol biradical was investigated with and without glycerol present in uniform POPC and POPG vesicles. Figure 3.7 shows signal attenuation in lipid samples due to paramagnetic AMUPol polarising agent, with and without glycerol in POPC vesicles.

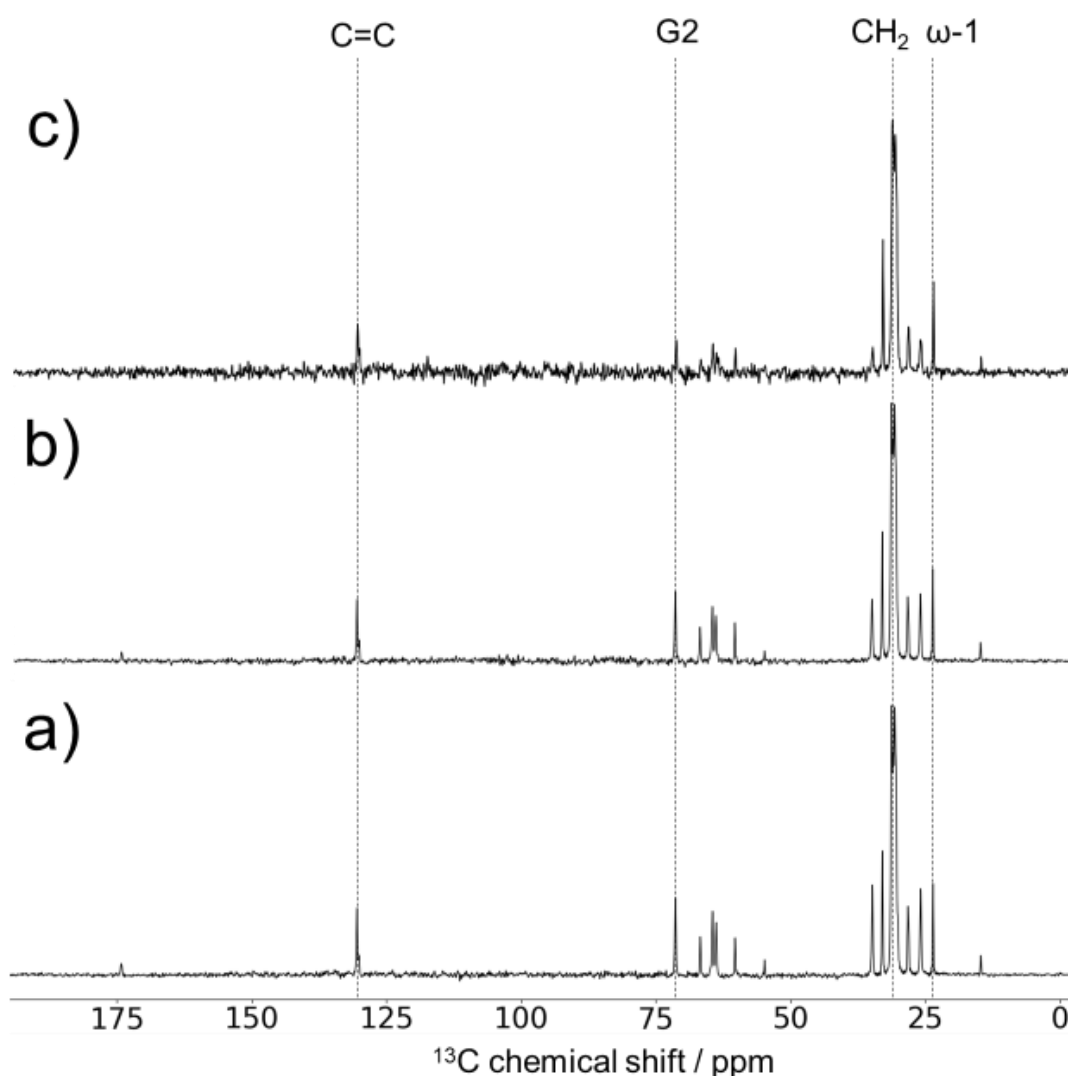


Figure 3.7 ^{13}C CP spectra for estimating PRE. a) Reference spectrum, S_0 , of POPC vesicles in buffer. b) Spectrum of POPC vesicles in buffer with 10 mM AMUPol, c) a sample containing POPC vesicles in buffer, 10 mM AMUPol and 60 % glycerol in the matrix.

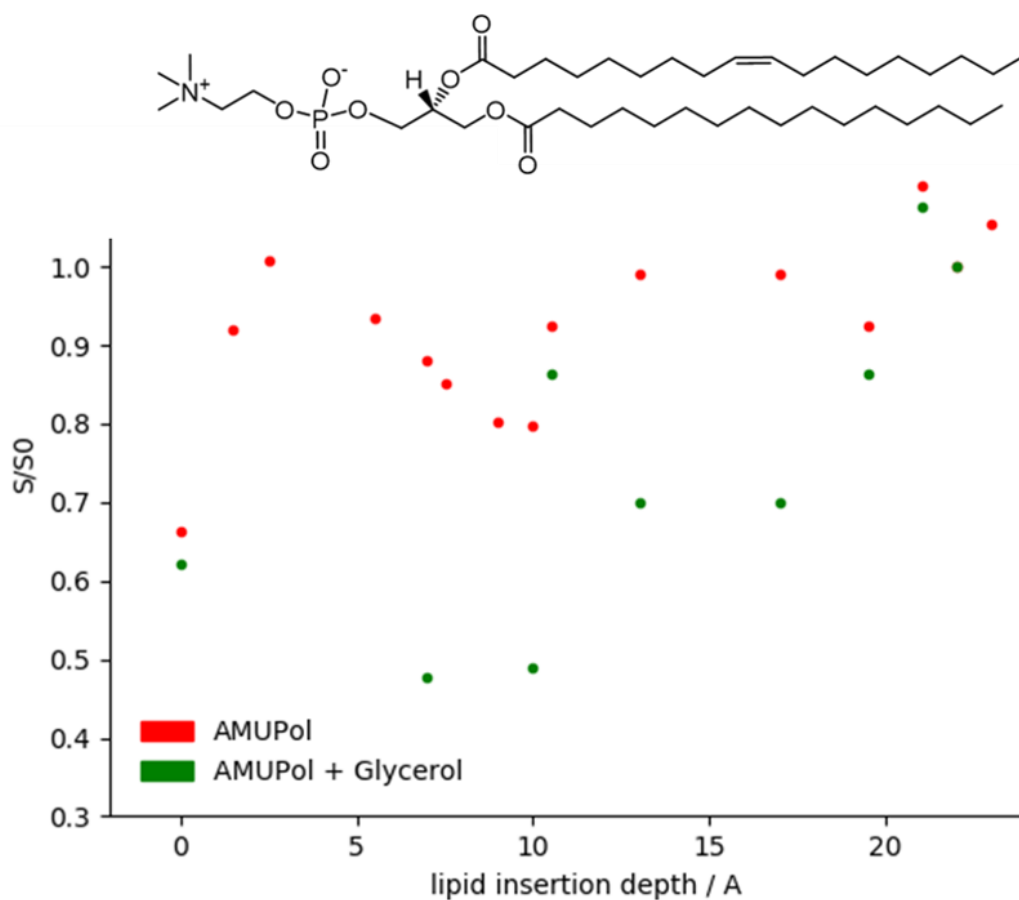


Figure 3.8 Plotted S/S_0 data for POPC vesicle samples containing 10 mM AMUPol (red) and 10 mM AMUPol and 60 % glycerol in the buffer (green). The values were normalised with respect to the $\omega-1$ peak, which is the second to last point in the plot.

Figure 3.8 shows the length down the lipid chain of the signals observed vs PRE, again based previous x-ray and neutron diffraction studies^[21]. In the sample containing lipid vesicles and 10 mM AMUPol biradical, a characteristic decrease in PRE is observed from first head group resonance, γ , to the last headgroup resonance, α , which is consistent with the previous study of this type, which investigated insertion in DMPC and POPC / cholesterol lipid vesicles^[1]. This is attributed to the interaction of biradical molecules in the bulk solvent with the lipid head. A local minima is observed at the C2 position in the POPC and POPG lipid vesicles. This can be explained by a model in which the biradical anchors into the lipid vesicle, with one of the nitroxides causing signal attenuation in this region.

Glycerol is shown to have a large effect on the signal attenuation of lipid positions in the headgroup region of the POPC lipid vesicles and at the θ positions in the lipid tail. G1, G3, β , γ and ω positions are not shown because signal-to-noise was too

poor for integration of peak area in the glycerol sample, shown in Figure 3.7c. This is consistent with glycerol partitioning into the vesicles, which allows a closer interaction with biradical molecules and greater PRE. A strong hydrogen bonding interactions is likely between the nitroxide N-O and the glycerol alcohol groups, which would explain how the glycerol transports the nitroxides into close contact with certain lipid positions. Alternatively, AMUPol could be less soluble in a matrix containing 60 % glycerol, meaning that it is more energetically favourable for the biradical to be solubilised in lipids under these conditions. This has consequences for the observed improved enhancements in glycerol cyroprotected lipid DNP samples- the higher enhancements may be due the partitioning effect of glycerol, allowing biradical molecules to sit closer to nuclear spins in the lipid vesicle system, in combination with the cyroprotective properties of glycerol.

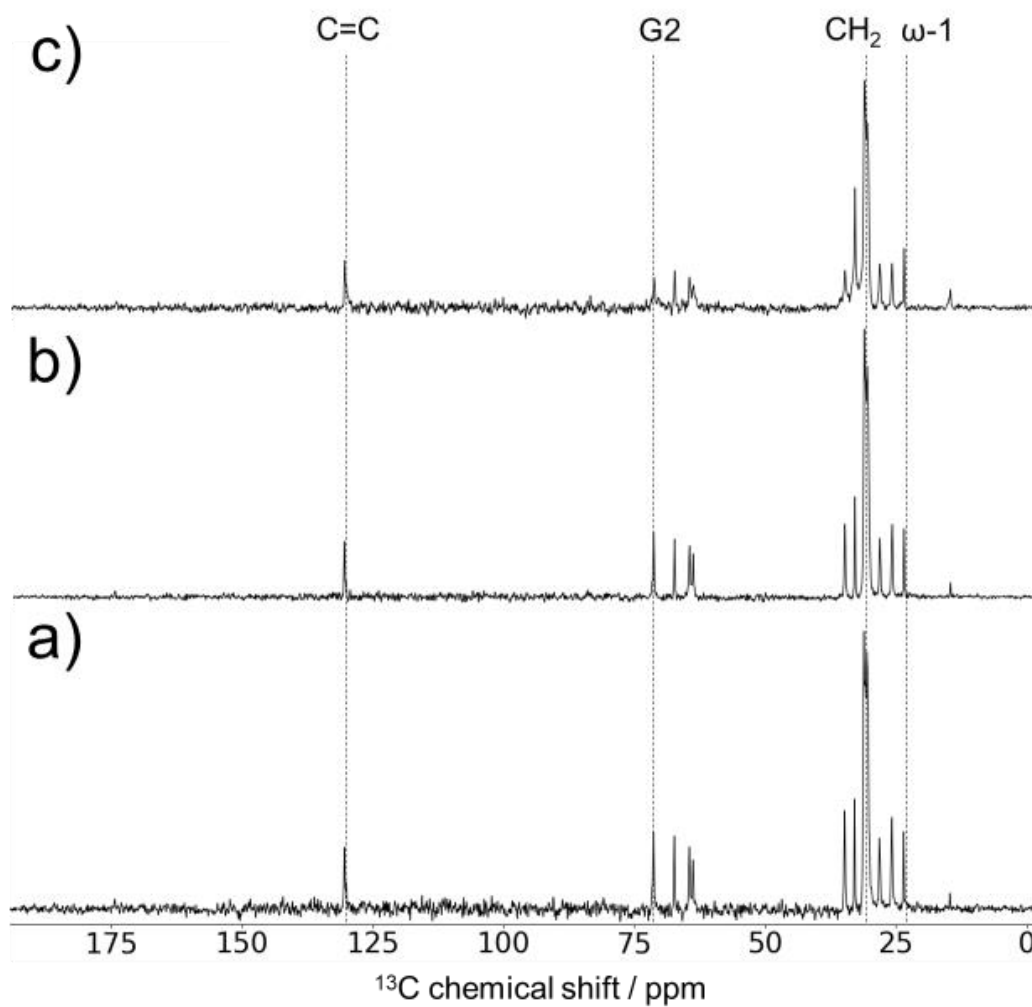


Figure 3.9 ^{13}C CP spectra for estimating PRE. a) Reference spectrum, S_0 , of POPG vesicles in buffer. b) Spectrum of POPG vesicles in buffer with 10 mM AMUPol, c) a sample containing POPG vesicles in buffer, 10 mM AMUPol and 60 % glycerol in the matrix.

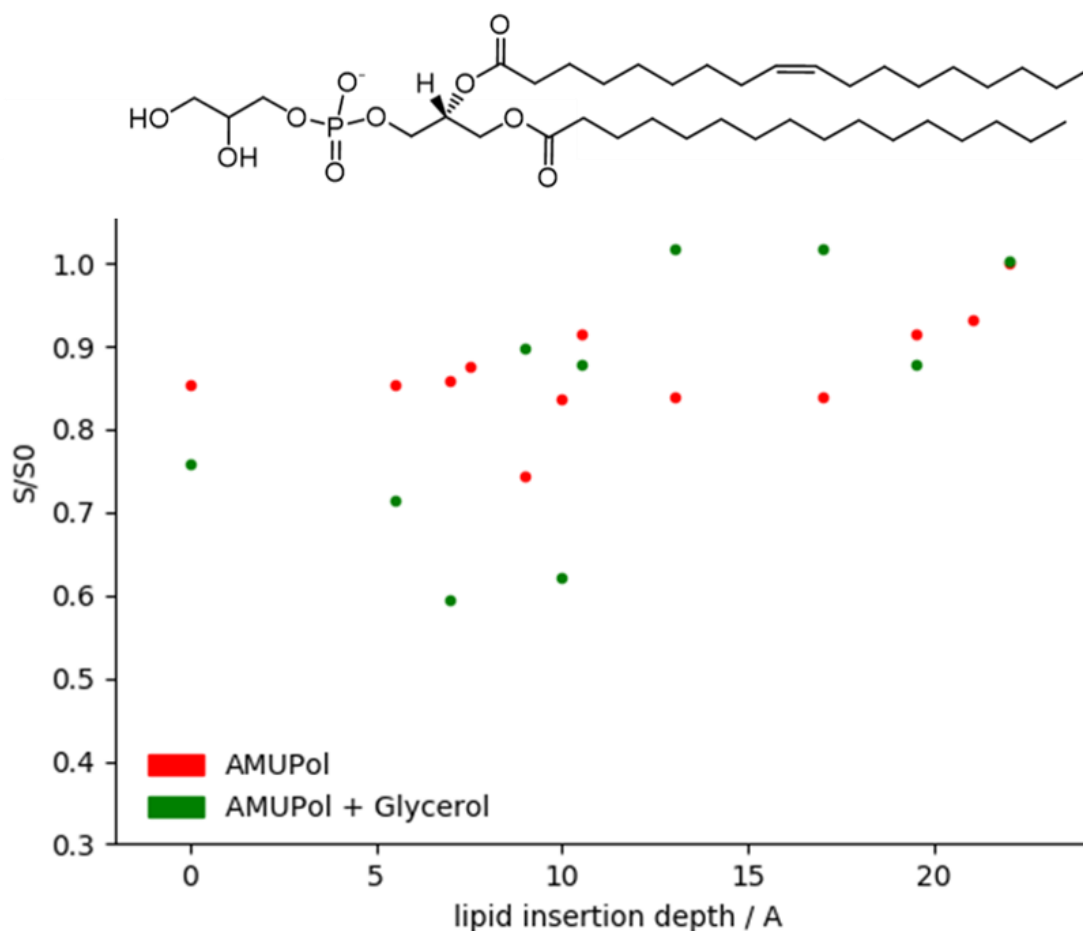


Figure 3.10 Plotted S / S_0 data for POPG vesicle samples containing 10 mM AMUPol (red) and 10 mM AMUPol and 60 % glycerol in the buffer (green). The values were normalised with respect to the $\omega - 1$ peak, which is the second to last point in the plot.

The experiment was also carried out in POPG lipid vesicles, with S / S_0 as a function of lipid insertion depth shown in Figure 3.10. POPG does not have a charged headgroup, leading to distinct properties to POPC in interacting with small molecules. Figure 3.9 shows the stacked POPG vesicle sample spectra showing signal attenuation due to paramagnetic biradical. The $\omega - 2$ and C2 peak were not considered in the sample containing glycerol due to overlap with the CH_2 lipid tail peak, making integration inaccurate, and the ω peak was also not considered due to poor signal-to-noise shown in Figure 3.9c.

Only one of the resonances in the headgroup region is resolved, there is no evidence for a dramatically different interaction with the uncharged diol group compared to the charged POPC tertiary amine. A similar interaction is observed as for POPC, with lipid head signals more attenuated than tail signals. The major difference is at the θ position, where no signal attenuation is observed in the glycerol containing sample.

^1H acquisition and ^{13}C direct polarisation experiments were also carried out to assess PRE. ^1H spectra resulted in significant overlap of many of the peaks and ^{13}C DP experiments took a prohibitively long time to produce enough signal-to-noise for reliable S / S_0 data.

TEKPol vs AMUPol insertion

TEKPol vs AMUPol insertion was probed in POPC lipid vesicles. The results in **section 3.3** for TEKPol in a lipid environment suggest that solubilisation in lipids may be the cause of the observed enhancement, as clustering of TEKPol molecules has been observed in aqueous DNP matrixes leading to unfavourable enhancement and relaxation properties. Figure 3.11 shows AMUPol and TEKPol insertion depth in POPC lipid vesicles.

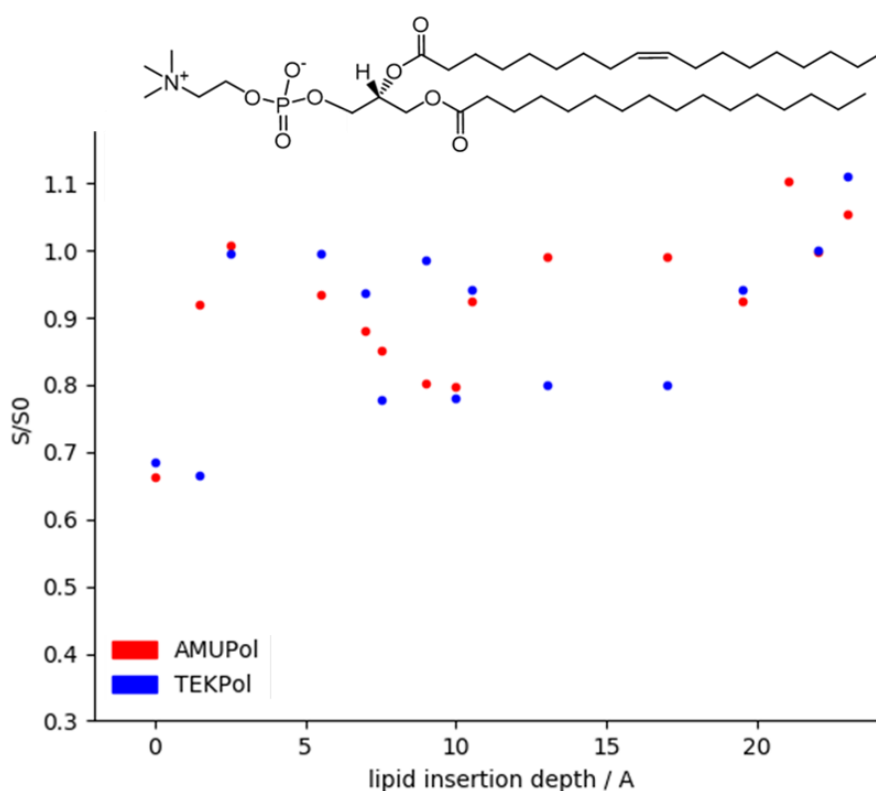


Figure 3.11 Plotted S / S_0 data for POPC vesicle samples containing 10 mM AMUPol (red) and 10 mM TEKPol (blue). The values were normalised with respect to the ω peak, which is the last point in the plot.

TEKPol is shown to have a differing PRE than AMUPol at several positions, most notably the β head group position, where attenuation in the TEKPol sample is significantly stronger than for the AMUPol sample, and at the C2 position, where the opposite is observed. The general trend for both samples is that attenuation is more

pronounced in the lipid head region than the tail region, with a local minimum close to the carbonyl group, with stronger attenuation in the TEKPol sample at the θ position suggesting TEKPol penetration further into the vesicles. Apart from the positions mentioned, all other peaks demonstrate similar PREs. The enhancement results of TEKPol and AMUPol, where TEKPol shows more enhancement than AMUPol when both are solubilised within the lipid molecules coupled with the studies showing good enhancement of insoluble biradicals when combined with lipid-like surfactants in an aqueous system suggests that there may be applications for insoluble radicals such as TEKPol in DNP studies of membrane systems.

3.5. Lipid structure disruption by DNP dopants

Phospholipids consist of a hydrophilic, phosphate containing head group and a hydrophobic diglyceride tail containing either a saturated or unsaturated alanyl chain. The amphipathic character of the hydrophobic and hydrophilic components results in self-assembly to lipid vesicles in an aqueous environment. Cellular membranes are made up of these lipid bilayers as well as an array of membrane proteins and other lipids. The ^{31}P chemical shift anisotropy (CSA) patterns arising from PO_4^- groups are highly sensitive to changes in the structure and dynamics of phospholipid vesicles^[22]. Glycerol is known to interact with lipid vesicles and PRE data indicates that there is also an interaction with AMUPol biradical. Several different phospholipid structures are possible under different sample conditions such as temperature and solvent. Isotropic chemical shifts, as well as CSA, can also provide information about lipid structure- the phase behaviour of the lipid bilayer. A study using a soluble paramagnetic shift reagent showed that the interior and exterior lipid vesicle ^{31}P containing head groups could be observed due to binding of the shift reagent to the outside of the vesicles^[23]. This was used to investigate the time dependant interaction of the lipid vesicles with the shift reagent in different buffers. The lipid vesicle interaction with paramagnetic DNP biradicals can be investigated using the same methodology.

In this study, ^{31}P CSA patterns and isotropic chemical shift changes were analysed to determine the extent of lipid vesicle disruption by glycerol and biradicals in a membrane DNP sample.

CSA

The CSA patterns recorded for hydrated 3 : 1 POPC / POPG lipid vesicles with and without lipid vesicles are shown in Figure 3.12. All spectra show a similar characteristic CSA pattern, which indicates a lamellar vesicle structure^[22]. Table 3.5 shows CSA parameters of each of the lipid samples following fitting of the CSA lineshapes. There are minor differences in the observed CSA patterns and the parameters produced by fitting the CSA patterns with Dmfit^[24]. This shows that the additives required for MAS DNP do not have a strong structural effect on lipid vesicle structure which has important implications when trying to study membrane proteins under conditions that mimic cell physiology as closely as possible. As there are two superimposed powder patterns, the fitting is not quantitative, but the similar lineshapes and CSA parameters support the conclusions given. Further experiments comparing ³¹P CSA lineshapes at 100 K and room temperature are needed to see whether there is a phase change on moving to cryogenic temperatures.

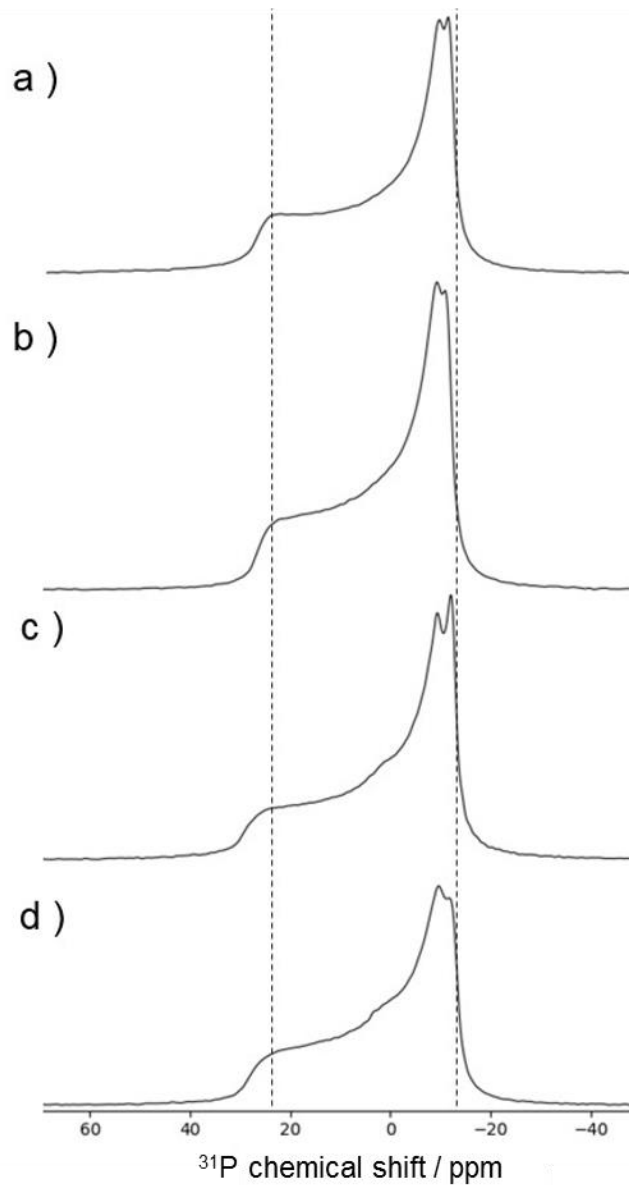


Figure 3.12 a) ^{31}P spectrum of a sample containing hydrated 3:1 POPC/POPG vesicles, b) hydrated 3:1 POPC/POPG vesicles and 10mM AMUPol, c) a sample containing hydrated 3:1 POPC/POPG with 60% glycerol and d) a sample containing hydrated 3:1 POPC/POPG with 10mM AMUPol and 60% glycerol. Spectra were recorded under static conditions with 81920 acquisitions and SPINAL-64 ^1H decoupling during acquisition.

Sample	$\sigma_{zz} - \sigma_{iso}$ / ppm	$\sigma_{xx} - \sigma_{iso}$ / ppm	$\sigma_{yy} - \sigma_{iso}$ / ppm	σ_{iso} / ppm	Linewidth / ppm
POPC / POPG 3:1	28.1	-13.9	-9.8	1.47	42.0
POPC / POPG + AMUPol	28.2	-13.4	-11.7	1.03	41.6
POPC / POPG + glycerol	26.6	-12.7	-10.1	1.27	39.2
POPC / POPG + glycerol and AMUPol	28.3	-12.5	-10.7	1.70	40.1

Table 3.5 ³¹P CSA parameters of samples containing 3:1 POPC/POPG and the dopants required for DNP.

CSA parameter definitions from Dmfit-

- Principal values $|\sigma_{zz} - \sigma_{iso}| > |\sigma_{xx} - \sigma_{iso}| > |\sigma_{yy} - \sigma_{iso}|$
- σ_{iso} is the isotropic chemical shift defined as $\frac{1}{3}(\sigma_{zz} + \sigma_{yy} + \sigma_{xx})$

MAS spectra

³¹P signals recorded under 10 KHz MAS show some interesting variations on addition of glycerol and AMUPol, shown in Figure 3.13.

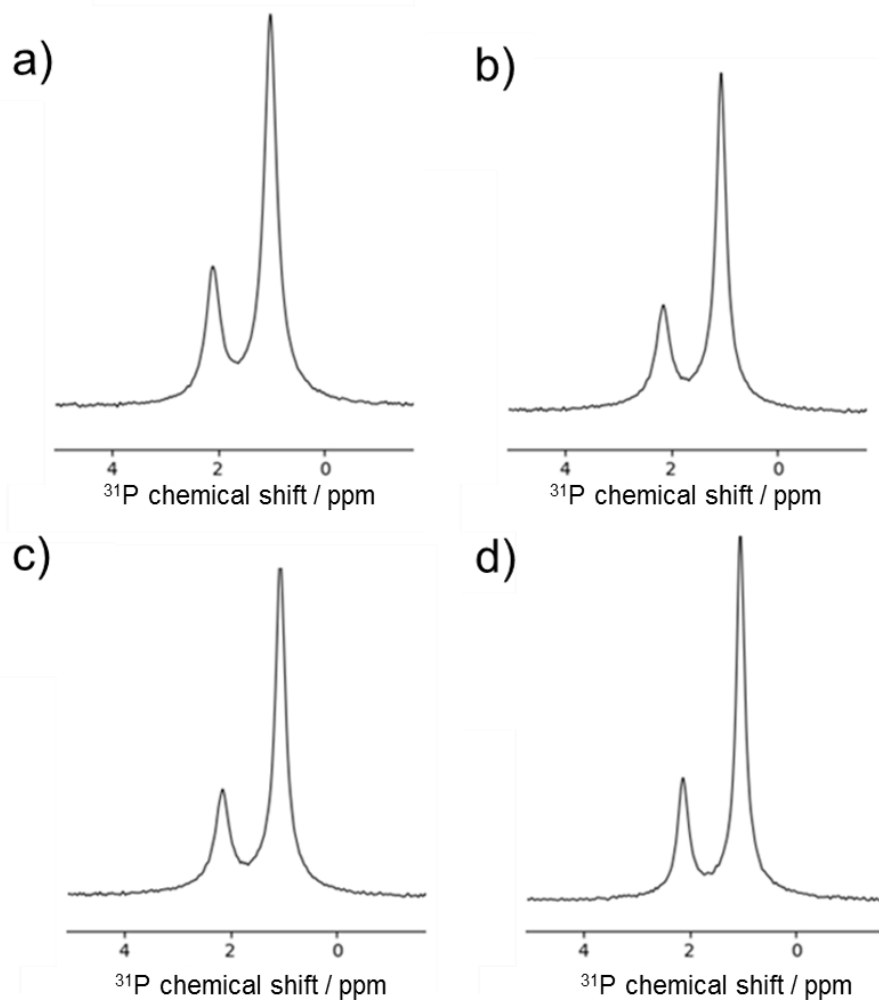


Figure 3.13 a) ^{31}P MAS spectrum of a sample containing hydrated 3:1 POPC/POPG vesicles, b) hydrated 3:1 POPC/POPG vesicles and 10mM AMUPol, c) a sample containing hydrated 3:1 POPC/POPG with 60% glycerol and d) a sample containing hydrated 3:1 POPC/POPG with 10mM AMUPol and 60% glycerol. Spectra were recorded with 10 KHz MAS, 1024 acquisitions and SPINAL-64 ^1H decoupling during acquisition.

Sample	POPC linewidth / Hz	POPG linewidth / Hz	POPC C_{iso} / ppm	POPG C_{iso} / ppm
a) POPC / POPG 3:1	45.9	62.3	1.06	2.14
b) POPC / POPG + AMUPol	54.9	84.1	1.08	2.16
c) POPC / POPG + glycerol	57.4	66.2	1.02	2.10
d) POPC / POPG + glycerol and AMUPol	69.3	84.5	1.04	2.12

Table 3.6 Linewidths and isotropic chemical shifts of lipid phosphate groups in 3:1 POPC/POPG vesicles containing the dopants required for DNP.

Table 3.6 shows linewidths and isotropic chemical shifts of lipid ³¹P resonances in POPC and POPG lipids after addition of DNP additives. Addition of radical and glycerol individually to lipid vesicles, shown in Figures 3.13b and 3.13c, caused line broadening in both POPC and POPG peaks. AMUPol caused the POPC and POPG linewidths to be broadened by 9 Hz and 22 Hz, respectively. This suggests a more significant interaction between the radical and POPG than POPC, possibly due to a hydrogen bonding interaction between the AMUPol tetrahydropyran group and the POPG alcohol groups. Glycerol caused an 11 Hz linebroadening for POPC and a 4 Hz linebroadening in POPG, suggesting a stronger interaction with the neutral POPC head group. This was attributed to reduced vesicle motion due to the higher viscosity of buffer that the vesicles are suspended in.

POPC and POPG both show a 0.02 ppm downfield shift on addition of AMUPol and a 0.04 ppm upfield shift on addition of glycerol. The cumulative effects of both interactions are observed in the lipid sample containing both AMUPol and glycerol- the sample containing both glycerol and AMUPol has the broadest ³¹P signals and the chemical shift differences compared to the reference sample are between those observed the AMUPol and glycerol are added individually.

The paramagnetic radical did not cause a dramatic chemical shift change or result in the observation of two distinct peaks for each head group type, as was observed when using paramagnetic shift reagents in a lipid sample^[23]. In this case, a paramagnetic molecule interacts strongly with phosphate headgroups on the outside of the vesicles but does not interact with headgroups on the inside, causing two distinct ³¹P signals.

3.6. Conclusion and Outlook

A protocol was established to produce a synthetic lipid sample with good enhancement and the tools were built to introduce it into a MAS DNP rotor. The sample with the greatest enhancement was selected for experiments going forward- 10 mg glycerol and 10 mM AMUPol biradical added using the pre-incorporation method. Liquid nitrogen freezing was used as the fast-freezing experiments were inconclusive.

PRE results when AMUPol and glycerol are present together indicate a membrane partitioning effect due to glycerol which allows greater penetration into the lipid vesicle by AMUPol biradical. Increased line broadening of ^{31}P lipid head group resonances under these sample conditions are consistent with this observation.

The most important conclusion from the ^{31}P CSA patterns of membrane DNP samples is that the additives do not cause a significant change to lipid vesicle morphology, but the effect of cryogenic temperatures used in DNP experiments has to be taken into account when comparisons are made with conventional NMR and other room temperature measurements.

Further work on probing these interactions could lead to an improved understanding of how polarisation is transferred to protein nuclei in a membrane protein system, leading to further adapting sample conditions to give improved enhancements.

3.7. References

- [1] S. Y. Liao, M. Lee, T. Wang, I. V. Sergeev, M. Hong, *J. Biomol. NMR*, 2016, **64**, 223–237
- [2] A. M. Schrader, C.-Y. Cheng, J. N. Israelachvili, S. Han, *J. Chem. Phys.*, 2016, **145**, 041101
- [3] W. Qiang, W.-M. Yau, J. Schulte, *Biochim. Biophys. Acta*, 2015, **1848**, 266–276
- [4] H. Takahashi, C. F. de-Alba, D. Lee, V. Maurel, S. Gambarelli, M. Bardet, S. Hediger, A.-L. Barrab, G. De Paëpe, *J. Magn. Reson.*, 2014, **239**, 91–99
- [5] H. Takahashi, D. Lee, L. Dubois, M. Bardet, S. Hediger and G. De Paëpe, *Angew. Chem. Int. Ed.*, 2012, **51**, 11766–11769
- [6] G. J. Gerfen, L. R. Becerra, D. A. Hall, R. G. Griffin, R. J. Temkin, and D. J. Singel, *J. Chem. Phys.*, 1995, **102**, 9494–9497
- [7] K. Nomura, M. Lintuluoto, K. Morigaki, *J. Phys. Chem. B*, 2011, **115**, 14991–15001
- [8] J. J. Towey, A. K. Soper, L. Dougan, *J. Phys. Chem. B*, 2011, **115**, 7799–7807
- [9] A. Mudalige, J. E. Pemberton, *Vib. Spectrosc.*, 2007, **45**, 27
- [10] S. Lange, A. H. Linden, Ü. Akbey, W. T. Franks, N. M. Loening, B. J. van Rossum, H. Oschkinat, *J. Magn. Reson.*, 2012, **216**, 209–212
- [11] M. Lelli, A. J. Rossini, G. Casano, O. Ouari, P. Tordo, A. Lesage, L. Emsley, *Chem. Commun.*, 2014, **50**, 10198–10201
- [12] A. Leavesley, C. B. Wilson, M. Sherwin, S. Han, *Phys. Chem. Chem. Phys.*, 2018, **20**, 9897–9903
- [13] S. R. Peters, *A Practical Guide to Frozen Section Technique*, 1st edition, 2010
- [14] T. Gullion, J. Schaefer, *Adv. Magn. Reson.*, 1989, **13**, 57–58
- [15] T. Gullion, J. Schaefer, *J. Magn. Reson.*, 1989, **81**, 196–200
- [16] I. Solomon, *Phys. Rev.*, 1955, **99**, 559–566
- [17] G. M. Clore, J. Iwahara, *Chem. Rev.*, 2009, **109**, 4108–4136
- [18] C. Hilty, G. Wider, C. Fernandez, K. Wuthrich, *Chem. Bio. Chem.*, 2004, **5**, 467–473

- [19] T. Theint, Y. Xia, P. S. Nadaud, D. Mukhopadhyay, C. D. Schwieters, K. Surewicz, W. K. Surewicz, C. P. Jaroniec, *J. Am. Chem. Soc.*, 2018, **140**, 13161–13166
- [20] A. Leftin, T. R. Molugu, C. Job, K. Beyer, M. F. Brown, *Biophys. J.*, 2014, **107**, 2274-2286
- [21] S. H. White, W. C. Wimley, *Annu. Rev. Biophys. Biomol. Struct.* 1999, **28**, 319–365
- [22] J. Seelig, *Biochim. Biophys. Acta.*, 1978, **515**, 105-140
- [23] R. E. Joyce, T. L. Williams, L. C. Serpell, I. J. Day, *Chem. Phys. Lett.*, 2016, **648**, 124-129
- [24] D. Massiot, F. Fayon, M. Capron, I. King, S. Le Calve, Bruno Alonso,1 Jean-Olivier Durand, Bruno Bujoli, Z. Gan, G. Hoatson, *Magn. Reson. Chem.*, 2002, **40**, 70–76
- [25] G. van Meer, A. I. P. M. de Kroon, *J. Cell Sci.*, 2011, **124**, 5-8
- [26] B. M. Fung, A. K. Khitrin, K. Ermolaev, *J. Mag. Res.*, 2000, **142**, 97–101
- [27] D. Le, F. Ziarelli, T. N. T. Phan, G. Mollica, P. Thureau, F. Aussenac, O. Ouari, D. Gigmes, P. Tordo, S. Viel, *Macromol. Rapid Commun.*, 2015, **36**, 1416–142

4.	Aβ interactions with phospholipid bilayers	72
4.1.	Protein structure determination by ssNMR	72
4.2.	Sample preparation	74
4.3.	Enhancement of protein by DNP in lipid environment.....	75
4.4.	2D measurements.....	76
4.5.	Double-quantum single-quantum correlation.....	85
4.6.	Conclusion and outlook.....	96
4.7.	References	97

4. A β interactions with phospholipid bilayers

4.1. Protein structure determination by ssNMR

NMR is a useful non-invasive tool in structural biology. Liquid-state NMR is used for soluble protein samples, leading to complete structural assignments due to high resolution in rapidly tumbling molecules in liquid samples. The first protein structure determination by solution NMR was carried out by the group of Kurt Wüthrich using distant restraints from ^1H NOESY and a distance geometry program^{[1][2]}.

However, insoluble protein aggregates and fibrils, as well as large macromolecular systems require MAS ssNMR in order to achieve appropriate resolution.

Development of ssNMR hardware, such as going to higher magnetic field, advances in probe technology and the introduction of DNP, as well as improved understanding of magnetic resonance under MAS conditions means that ssNMR is now a powerful tool for structural biology studies^[4].

1D direct acquisition or cross polarisation (CP) experiments provide a simple spectrum with chemical shifts of all resonances in the sample, but lead to crowded spectra if many different chemical environments are present in the sample. 2D NMR experiments are needed in many circumstances to achieve informative spectra, as two spin interactions are correlated to show nuclear spins that are close in space leading to spectra are far less crowded than their 1D equivalents. A simple 2D NMR experiment and spectrum is shown in Figure 4.1.

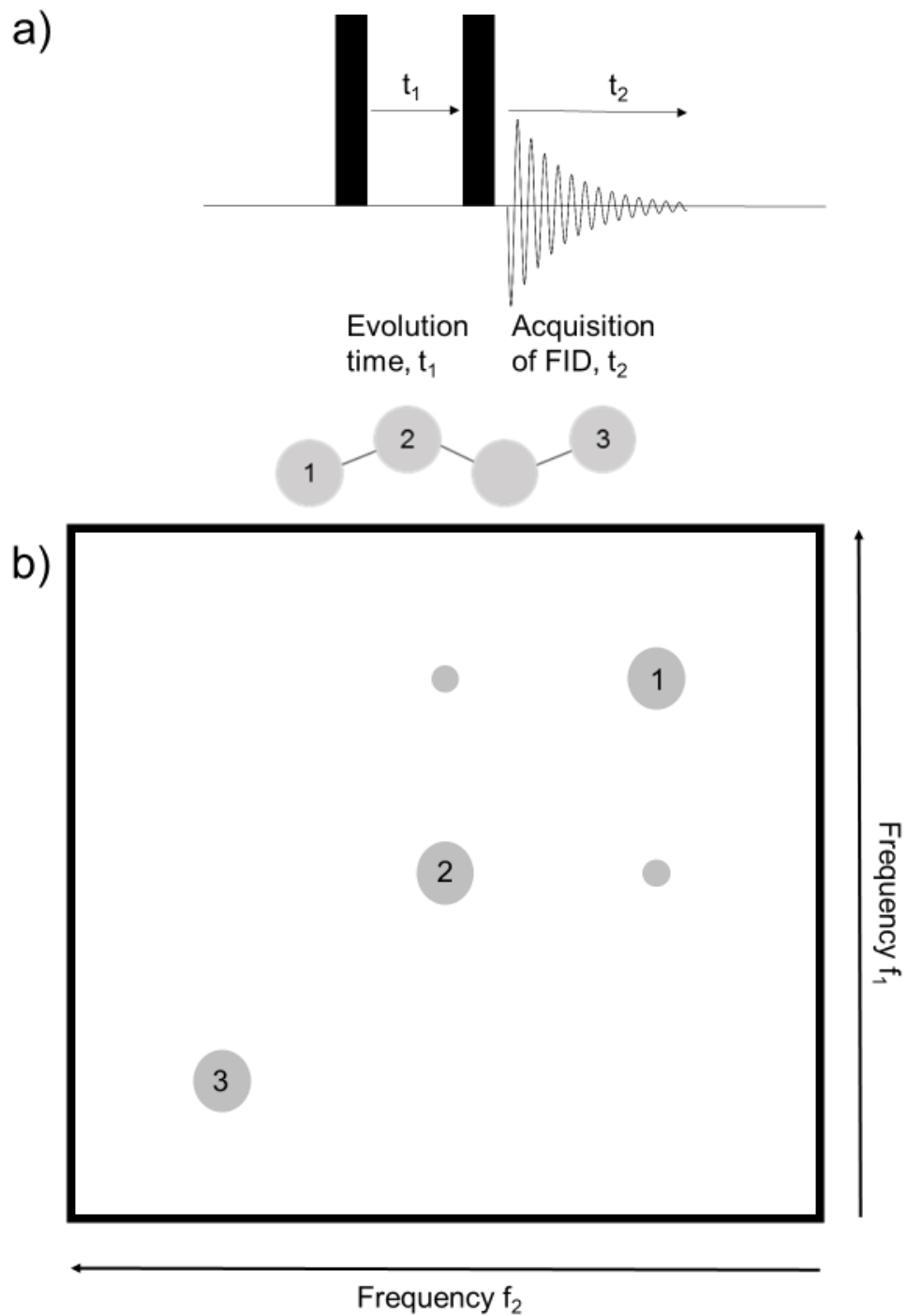


Figure 4.1 a) Schematic showing a basic pulse sequence for a 2D experiment. A pulse is applied which causes nuclear spins to evolve under a specific interaction, after which there is an incremented mixing time, t_1 . Another pulse is applied which brings magnetisation into the transverse plane and an FID is recorded in the time period t_2 . Two-dimensional Fourier transform leads to a spectrum such as the one shown in 1b), where correlations between spins in non-equivalent environments are shown by off-diagonal peaks due to spin interactions. A model molecule is shown above the spectrum. In this case, an interaction between resonances 1 and 2 produces cross-peaks, due to their closeness in space or a through bond interaction, at the frequency of these resonances in the f_1 and f_2 dimensions.

In this chapter, a number of 1D and 2D ssNMR experiments are applied to a A β (1-40) sample pre-incorporated into synthetic lipid vesicles. The aim was to find optimal experiments to obtain A β (1-40) structural information in a membrane environment under DNP MAS conditions and to overcome problems arising from cryogenic temperatures and background signals.

4.2. Sample preparation

A protocol for pre-incorporating A β (1-40) into lipid vesicles was adapted from a procedure by the Qiang group^[5]. After the sample pellet is prepared, the DNP sample is made as described in “methods” section of **chapter 3**.

Preparation of Protein / lipid samples with ^{13}C depleted d_8 -glycerol

POPC (8.67×10^{-3} mmol, 6.59 mg) and POPG (2.89×10^{-3} mmol, 2.23 mg) were dissolved in chloroform, the solvent was then removed by a nitrogen gas stream. Purified and lyophilized A β (1-40) peptide (1.15×10^{-4} mmol, 0.5 mg) and the phospholipid mixture were co-dissolved in hexafluoro-2-propanol (HFIP, 2 ml). The solution was sonicated in a water bath for 5 min to ensure the complete dissolving and then the solvent was removed by an N₂ gas stream followed by lyophilisation. The remaining lipid / peptide film was hydrated using phosphate buffer (6 ml, 10 mM, pH 7.4). Peptide concentration was kept at 25 μM to avoid the formation of large aggregates during the time period of vesicle preparation. Re-suspended lipid / peptide Mixture was agitated for 1 h at ambient temperature, 5 freeze-thaw cycles between liquid nitrogen and ambient temperature were carried out to give homogeneous vesicles. The vesicle solution was centrifuged (26000 rpm, 10 hours) and the remaining supernatant removed by a pipette to give a membrane pellet. The weight of buffer solution in the membrane pellet was recorded. A stock solution of D₈-99.5% ^{13}C glycerol / D₂O / H₂O in a 6 : 3 : 1 ratio containing 10 mM of dissolved AMUPol biradical was made. 5 μL aliquots of the stock solution were directly titrated added to the membrane pellets followed by 2 minutes of vortexing in the centrifuge tube. This was repeated 5 times to give total volume of added matrix stock of 25 μL . This was followed by 5 minutes of vortexing to ensure a uniform distribution of the radicals. The sample was then lyophilised until the total hydration level of the membrane pellet was ~ 40 % w/w. The sample was then added to a 3.2 mm sapphire rotor using the home built packing tool (**section 3.2**) and stored in liquid nitrogen until NMR experiments were performed.

Protein labelling

Uniformly ^{13}C , ^{15}N -labelled A β (1-40) was synthesized manually using routine Fmoc solid-phase peptide synthesis protocols by Qinghui Cheng at Binghamton University, State University of New York. For DNP MAS applications, uniform labelling of the entire protein is not useful due to broad linewidths (1.5 – 5 ppm in our experiments), which would result in poor spectral resolution. Therefore, labels in the protein are placed at a few specific important locations along the protein length.

4.3. Enhancement of protein by DNP in lipid environment

Following on from phospholipid sample enhancement optimization, the first step for phospholipid associated A β (1-40) was to confirm that the polarization transferred to lipids by spin diffusion could be further transferred to the peptide. Figure 4.2 shows a CP spectrum of A β (1-40) associated with the phospholipid mixture at 20 : 1 molar lipid-to-protein ratio. This high protein : lipid ratio was chosen. Enhancements for protein positions are shown in Table 4.1.

L : P ratio	Lipid composition	ϵ_{DNP} enhancement					
		CO	C $_{\alpha}$	C $_{\beta}$	C $_{\text{alkyl}}$	C $_{\text{aromatic}}$	Lipid CH $_2$
20 : 1	3 : 1 POPC / POPG	40	33	33	40	40	46

Table 4.1 DNP enhancements for protein peaks in 20 : 1 lipid-to-protein ratio sample

Enhancements for the protein positions are shown to be 33-40. This value is less than the observed enhancement of 46 for the CH $_2$ lipid peak in this sample. Less efficient polarisation transfer by spin diffusion from the DNP matrix to lipid embedded A β (1-40) than to the lipid positions is likely to be the cause of this drop in enhancement. Polarisation transfer is shown to be most efficient in 90 % deuterated samples, so losses as polarisation is transferred through lipids which contain 100 % ^1H nuclei are to be expected^[3]. A possible solution for this would be to use perdeuterated lipids in protein – lipid samples where the protein concentration is at the limit of NMR sensitivity as some studies suggest this leads to more efficient transfer of polarisation^[6]. However, other studies suggest that there is no benefit to lipid deuteration due to a reduction in CP efficiency because of the lack of ^1H spins^[7]. All ^{13}C spectra were referenced using adamantane^[31], and 11 W of microwave power from the gyrotron out of a possible 17 W to limit sample heating.

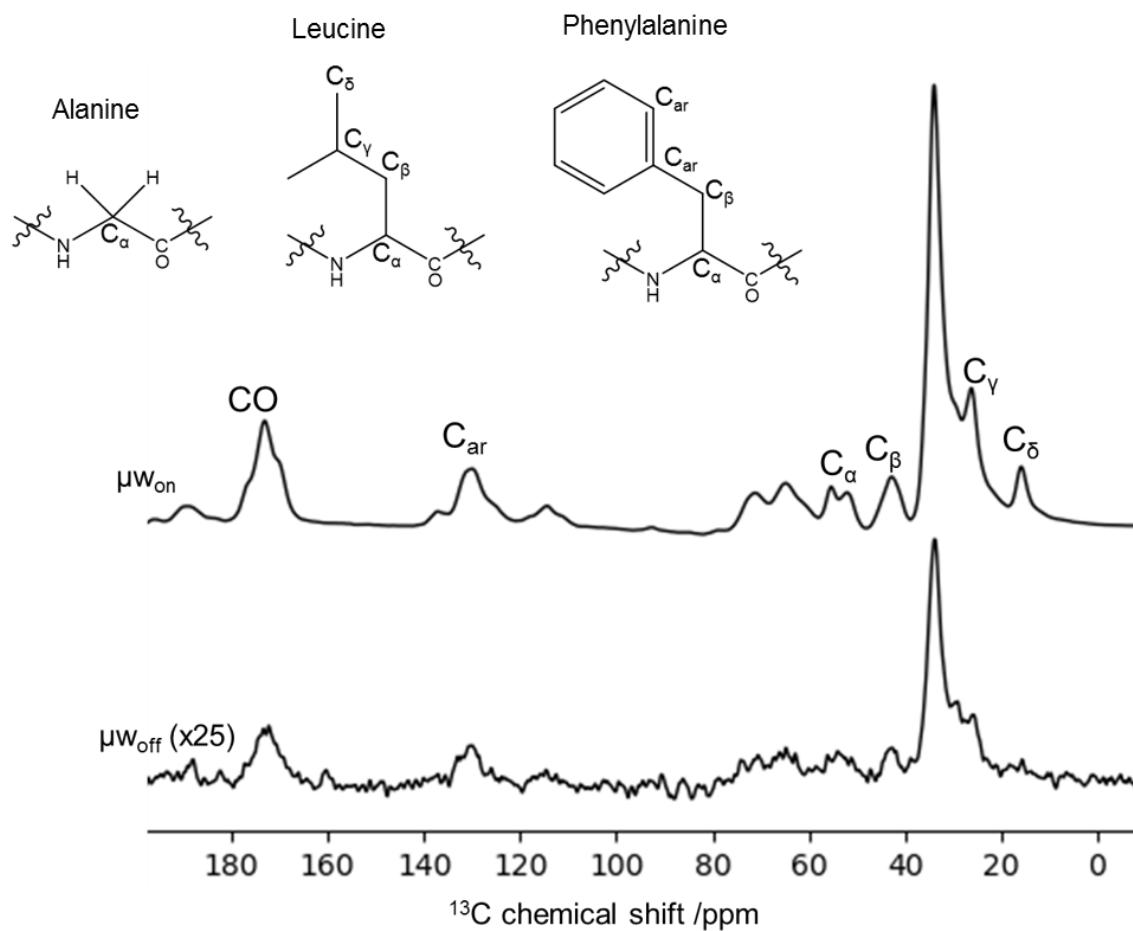


Figure 4.2 ^{13}C CP spectrum of a sample containing uniformly ^{13}C , ^{15}N -labelled F19, L34 and G38 labelled $\text{A}\beta(1-40)$ pre-incorporated in POPC / POPG 3:1 lipid vesicles. CP measurements were carried out with 16 scans in both cases. Protein positions are roughly labelled but peaks cannot be assigned to specific amino acids due to broad linewidths at cryogenic temperatures in 1D spectra.

4.4. 2D measurements

To obtain any useful information from biological samples under MAS DNP condition, 2D experiments are required due to large linewidths and overlapping background signals from the glassy matrix, and in this case background lipid signals. Several experiments were performed to check which one gives the best resolution of chemical shift information from protein signals without too much spectral disruption from background signals. Secondary chemical shifts^[8] (discussed in **section 2.4**) provide a method for assessing the secondary structure by comparison to the chemical shift index of reference protein chemical shifts, introduced by Wishart et al.^{[9][10]}.

Dipolar assisted rotational resonance (DARR)

The DARR experiment involves a CP step followed by magnetization being exchanged between ^{13}C nuclei that are close in space during an exchange time, t_{ex} , in which continuous wave irradiation is applied to ^1H nuclei at the same power as the rotation rate^{[11][12]}, shown in Figure 4.3. This is similar to the pre-cursor proton driven spin diffusion (PDSD) experiment, which is identical apart from lacking the continuous wave ^1H pulse during exchange time^[13]. The DARR pulse on the ^1H channel causes recoupling of the ^1H - ^{13}C dipolar interaction, so ^{13}C spins that are close in space exchange magnetization via ^1H spins. The exchange time, t_{ex} , is set to induce magnetization transfer of differing distances via the dipolar interaction- a short t_{ex} will lead to a dipolar interaction between ^{13}C nuclei that are close in space whereas a longer t_{ex} will lead to transfer between more distant spins.

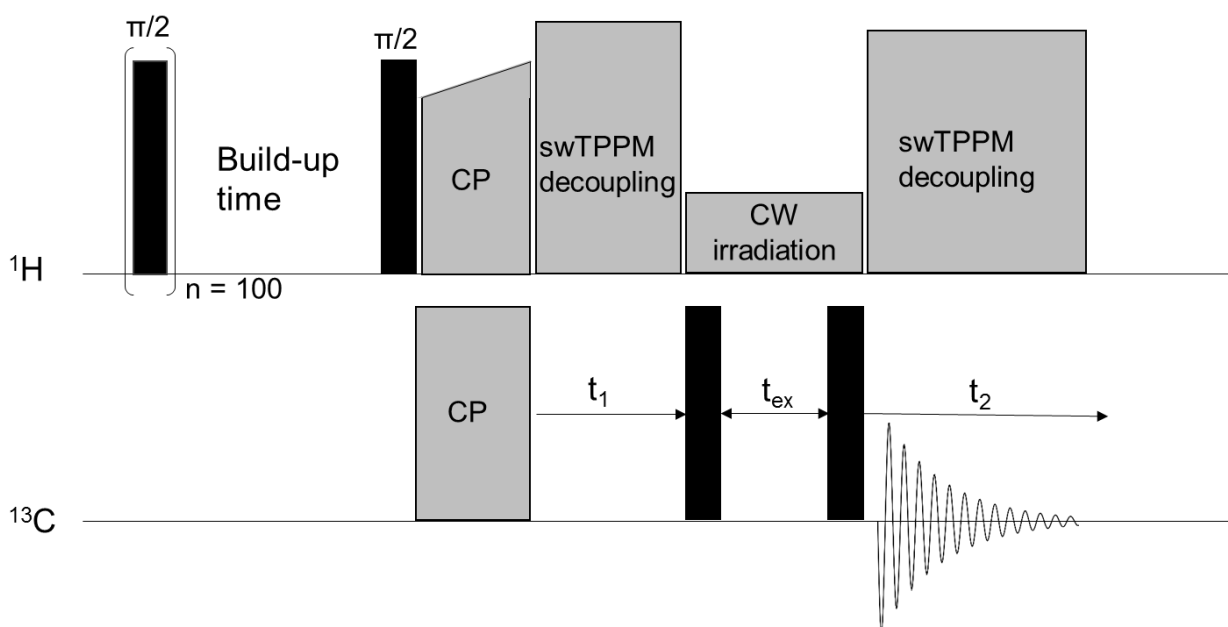


Figure 4.3 Pulse sequence for dipolar assisted rotational resonance (DARR) experiment. A CP step is followed by incremented t_1 time. Magnetization exchange between ^{13}C nuclei occurs during t_{ex} , during which time continuous wave irradiation is applied to the ^1H at a power level equivalent to the rotation rate of MAS.

DARR spectra of a sample containing 20 : 1 lipid-to-protein ratio is shown in Figure 4.4a and 4.4b for DARR mixing times of 0.25 s and 1 s, respectively. The long mixing time of 1 s was used to look for evidence inter-amino acid cross-peaks, specifically a an interaction between labelled ^{13}C spins in F19 and L34.

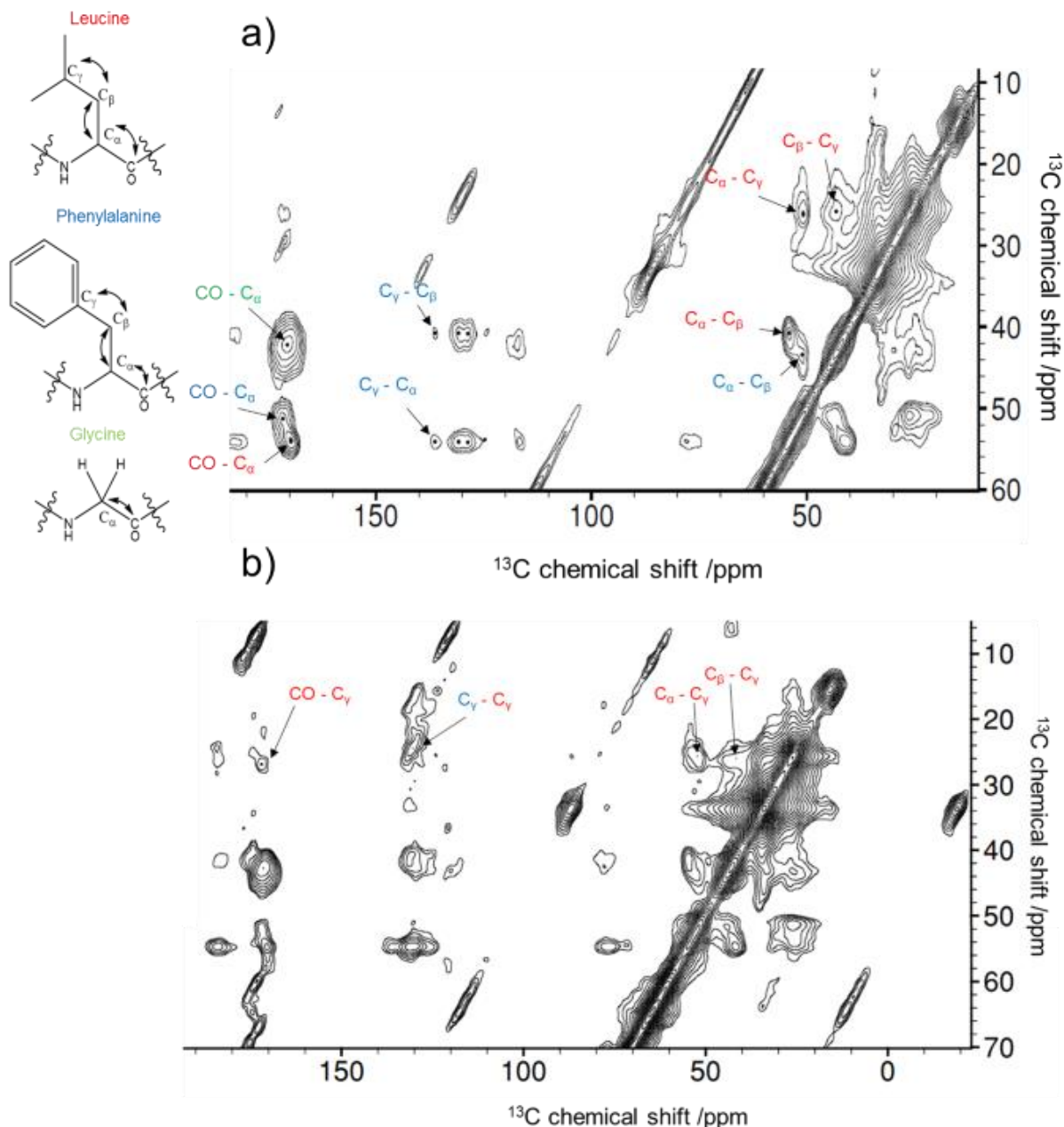


Figure 4.4 DARR spectrum of $A\beta(1-40)$ uniformly labelled at F19, L34 and G38 pre-incorporated in 3:1 POPC / POGP lipid vesicles at a lipid-to-protein ratio of 20 : 1. 8.5 kHz mas was used and 2000 μ S CP, with a) 25 ms DARR giving predominately one-bond correlations (32 acquisitions, 300 t_1 increments) and b) 1 s DARR mixing, giving inter-residue correlations (32 acquisitions, 200 t_1 increments). The inter-residue cross-peak between F19 and L34 C_γ will be discussed in more detail in chapter 5.

This spectrum shows useful assignments for carbonyl and aromatic labels correlated with C_α and C_β . DARR mixing time was set to 25 ms to excite mainly one-bond inter-residue correlations, although the leucine and phenylalanine two and three bond correlations are also present with good signal-to-noise. Previous studies had shown a correlation between F19 and L34 labelled positions due to a close

proximity of these residues in fibril samples due to double layered, parallel cross- β motifs which stabilises monomer units when they come into contact with the existing fibrillar structure, which is why the labels are in these positions^[14]. The cross-peak is visible in the spectrum recorded with 1 s of DARR mixing, indicating that the monomer A β (1-40) monomer units adopt a similar structure to those observed in fibrils when pre-incorporated in lipids. The significance of this cross-peak will be further explored in **chapter 5**.

1D slices were extracted at leucine chemical shifts in the indirect, at the methyl, C β and C α chemical shifts (27 ppm, 43 ppm and 54 ppm, respectively) with phenylalanine positions highlighted by horizontal lines, shown in Figures 4.5a and 4.5b which correspond to 0.25 s and 1 s DARR mixing times, respectively.

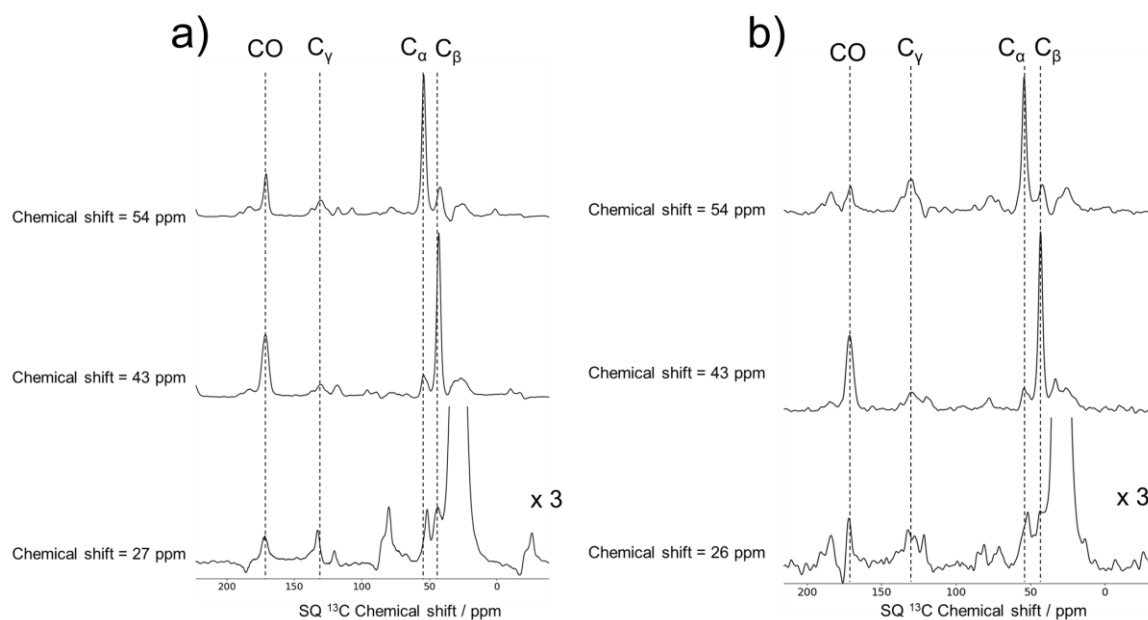


Figure 4.5 1D slices from 2D DARR spectra at leucine chemical shifts in the indirect with phenylalanine positions highlighted by horizontal lines. a) 0.25 s DARR mixing, b) 1 s DARR mixing.

A spinning side band is found close to the F19-L34 cross-peak at 8000 Hz MAS, but an additional peak is visible in the 1D leucine slice at 26 ppm in the 1 s mixing time spectrum, which appears at the F19 aromatic ^{13}C chemical shift at ~ 135 ppm. Linewidths of 1.5 – 4 ppm compare favourably with comparable DNP studies on similarly labelled A β (1-40) carried out on a DNP system operating at 25 K^{[15][16]}, which is to be expected as lower temperatures result in less molecular motion in the sample and therefore more anisotropy.

$^{15}\text{N} \rightarrow ^{13}\text{C}$ SPECIFIC CP

The drawbacks of the DARR experiment on this type of samples under cryogenic MAS DNP conditions are the strong background signals of glycerol and lipids and associated t_1 noise in 2D spectra. t_1 noise appears in vertical streaks in 2D spectra and is more visible in long experiments when the concentration of the molecule under study is low. It is attributed to instrument and temperature instability^[17], which are likely to be more pronounced in DNP-enhanced ssNMR compared to conventional ssNMR due to the increased complexity of the system and the number of components which must remain stable over time. Fluctuations in temperature over time will result in slightly different enhancements due to DNP which could contribute to more t_1 noise. This makes unambiguous assignments of C_α , C_β and aliphatic side chain resonances difficult as experiments start to focus on $A\beta(1-40)$ in low concentration relative to lipids. Spectra in which a lot of t_1 noise was present-DARR experiments at low concentration are not presented but were recorded.

The fact that the labelled amino acids contain 100 % ^{15}N means that experiments involving polarisation transfer from ^{15}N to ^{13}C result in spectra with no background signals from the glassy matrix or lipids, which do not contain any ^{15}N atoms. This requires a spectrally induced filtering in combination with cross polarization (SPECIFIC CP) step, which involves transferring magnetization from ^{15}N to ^{13}C following cross polarisation from hyperpolarized ^1H to ^{15}N ^[18]. The pulse sequence is shown in Figure 4.6.

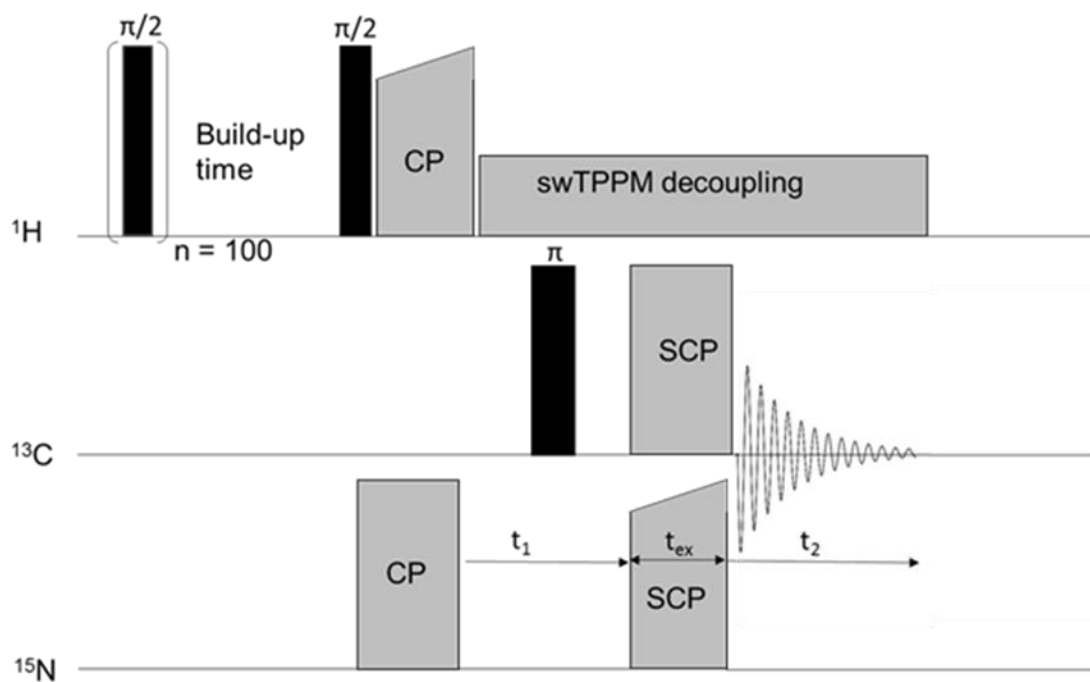


Figure 4.6 Diagram showing the pulse sequence elements for a 2D NCA experiment. A 90° pulse is followed by CP from ^1H to ^{15}N . During the incremented t_1 time, ^{15}N chemical shifts are allowed to evolve and a refocusing 180° pulse is applied to the ^{13}C channel. SPECIFIC CP (SCP) from ^{15}N to ^{13}C is then carried out for exchange time t_{ex} , corresponding to the length of SCP pulses on ^{13}C and ^{15}N . An FID is then detected on the ^{13}C channel during t_2 .

Figure 4.7a shows a DNP enhanced ^{15}N CP spectrum acquired using a triple tuned HXY probe..

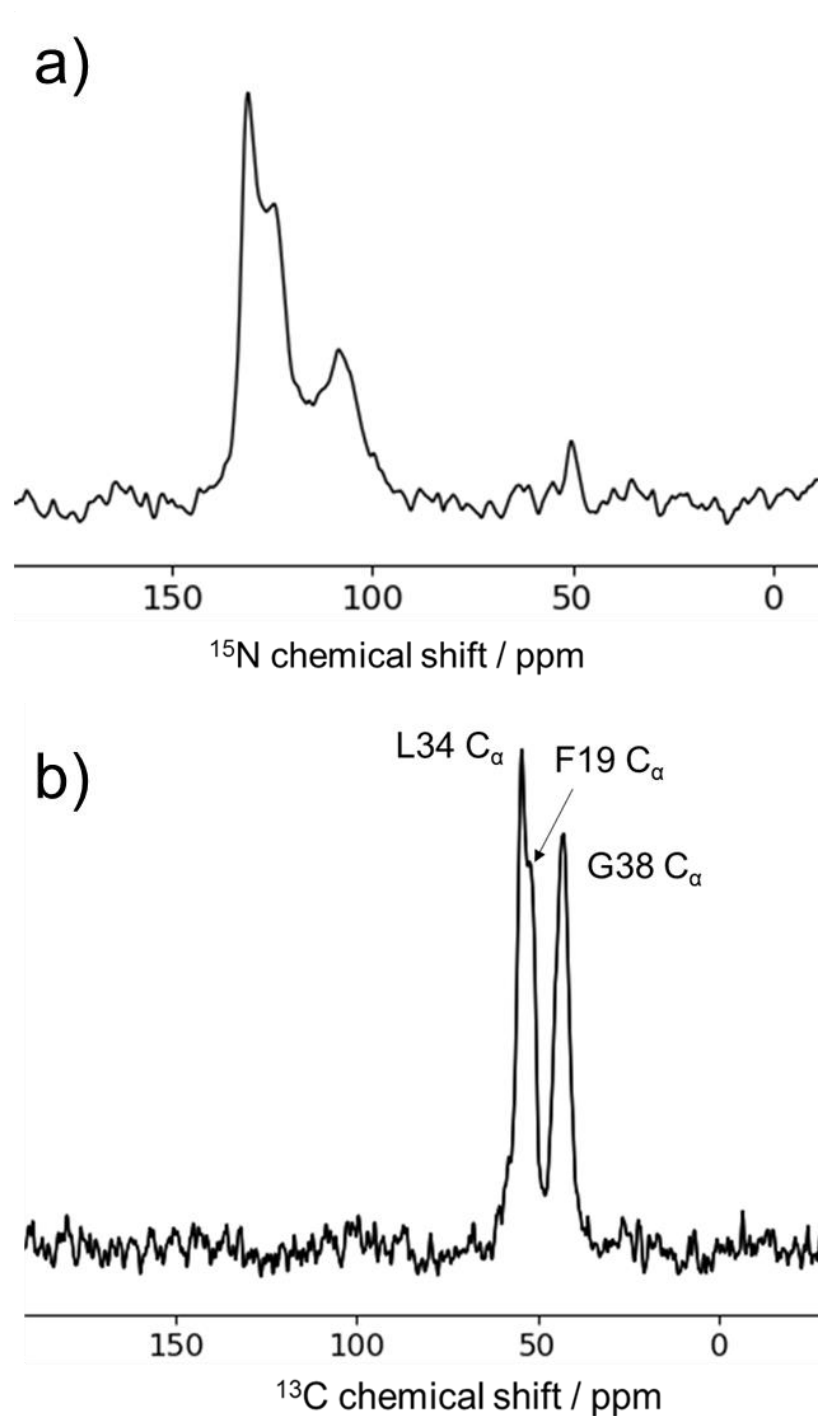


Figure 4.7 a) ^{15}N CP spectrum of $\text{A}\beta(1-40)$ pre-incorporated into 3:1 POPC / POPG vesicles. The experiment was performed with 8 acquisitions, using a $2000 \mu\text{s}$ CP contact pulse. 100 Hz linebroadening with an exponential function was applied. b) $^{15}\text{N} \rightarrow ^{13}\text{C}$ SCP spectrum performed with 8 acquisitions, using a $2000 \mu\text{s}$ CP contact pulse and a $9000 \mu\text{s}$ SCP contact pulse. 100 Hz linebroadening with an exponential function was applied.

Peaks are observed at 140 ppm, 156 ppm and 163 ppm corresponding to the labelled ^{15}N in F19, L34 and G38. The ^{15}N carrier frequency for SPECIFIC CP (SCP) is set based on the positions of these peaks. SCP was optimised using a

series of 1D experiments and 9000 μs was found to be the optimal length for the contact pulse. Three ^{13}C peaks were observed corresponding to the labelled ^{13}C C_α positions in F19, L34 and G38, shown in Figure 4.7b, assigned based on literature amino acid chemical shifts^[10].

Assignments of ^{15}N and ^{13}C resonances required 2D NCA and NCACX experiments, shown in Figures 4.8 and 4.9, respectively. The NCA spectrum shows correlations between the nitrogen in the amide backbone and C_α for the labelled amino acids in this sample. C_β - NH correlations are also observed due to longer range magnetization exchange, albeit with lower intensity. No contribution from lipids or glycerol are present in the spectrum.

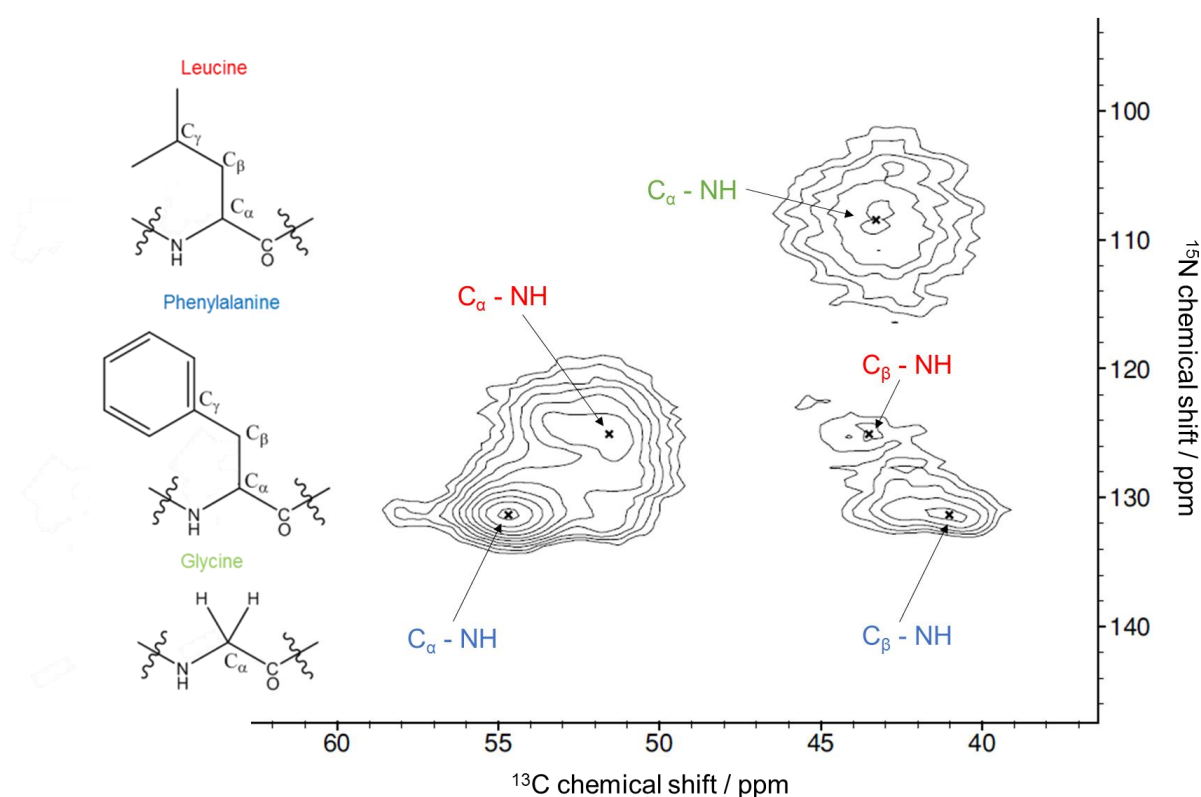


Figure 4.8 2D NCA spectrum showing correlations between proximal ^{15}N and ^{13}C nuclear spins in $\text{A}\beta(1-40)$ containing uniformly labelled F19, L34 and G38. ssNMR experiments were acquired with 8 acquisitions in the direct dimension, 128 increments in the indirect dimension and a 9000 μs SCP pulse. 100 Hz line broadening was applied in the direct dimension and 30 Hz was applied in the indirect dimension, both with an exponential function.

NCACX (N to C_α to proximal ^{13}C nuclei in the amino acid) were recorded and are shown in figure 4.9. After the SCP, a 90° pulse is applied to the ^{13}C channel and the dipolar interaction is allowed to evolve for a DARR mixing period, in this case for 25 ms, after which a second 90° ^{13}C pulse is applied bringing magnetization into the transverse plane and an FID is acquired. This experiment is more useful compared

with NCA as more correlated ^{13}C resonances are observed, so assignments can be made based on observed cross-peaks with reference to literature protein chemical shift values. The aromatic ^{13}C spins in F19 appear at ~ 136 ppm, therefore the F19 ^{15}N is assigned as the peak at ~ 130 ppm. A similar assignment of the L34 can be made as the C_γ and C_δ appear at 20 – 25 ppm, meaning that cross-peak at this ^{13}C chemical shift can only be due to the L34 ^{15}N .

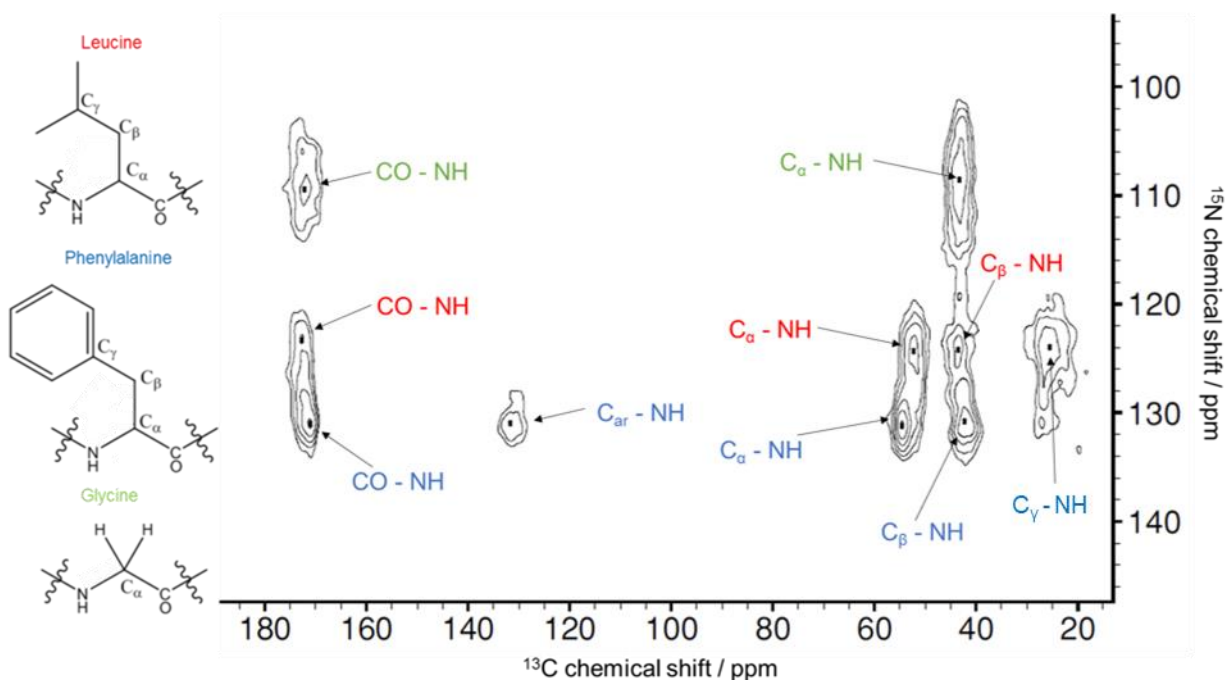


Figure 4.9 Assigned spectrum of $\text{A}\beta(1-40)$ using NCACX pulse sequence. ssNMR experiments were acquired with 8 acquisitions in the direct dimension, 128 increments in the indirect dimension and a $9000 \mu\text{s}$ SCP pulse. 100 Hz exponential line broadening and 100 Hz Gaussian line broadening was applied in the direct dimension and 80 Hz exponential linebroadening was applied in the indirect dimension.

The signal-to-noise for ^{15}N - ^{13}C correlation spectroscopy under DNP MAS conditions is demonstrated by leucine 1D slices from these spectra in Figure 4.10.

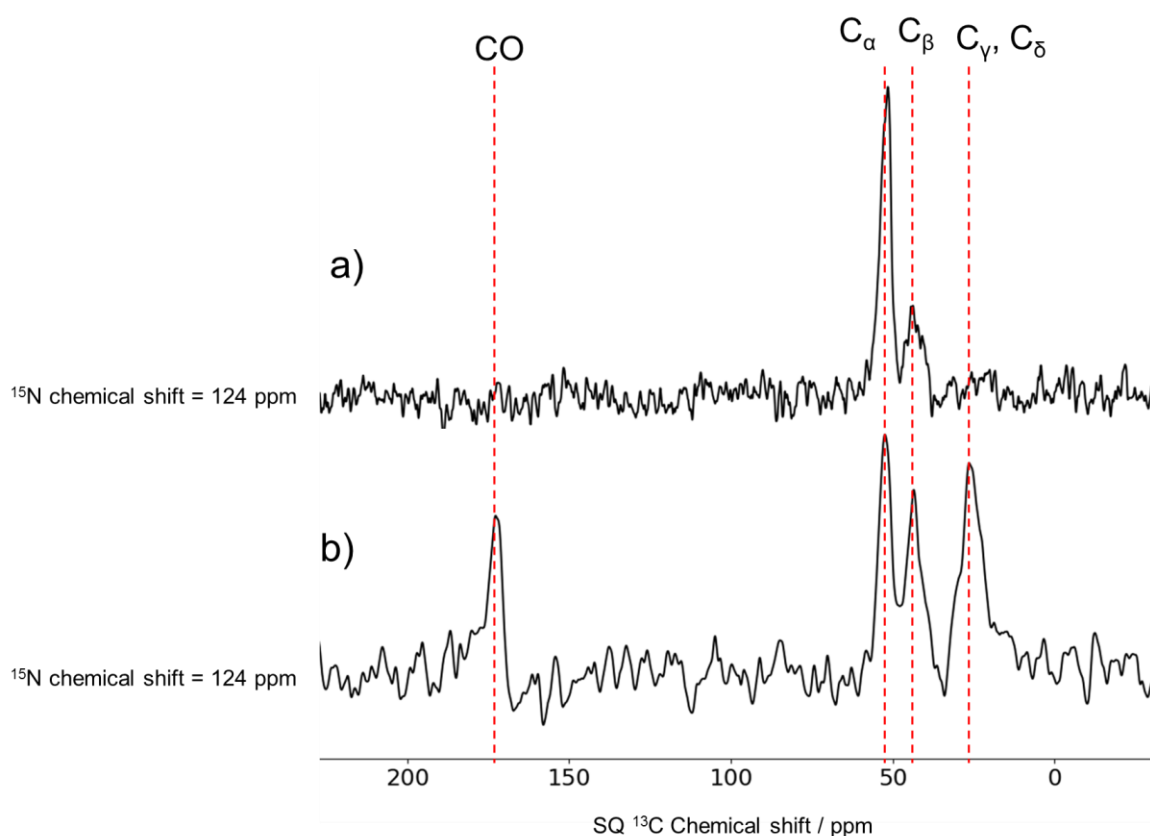


Figure 4.10 1D slices from a) NCA and b) NCACX at leucine ^{15}N chemical shifts.

The linewidths resulting from G38 correlations are broader than the F19 and L34, which is two amino acids away from the C-terminus of the protein. This could be due to the end of the protein having more conformational freedom than the core resonances resulting in slight differences in molecular environment of the nuclear spins for different monomers. The broad lines and relatively narrow ^{15}N chemical shift range means that cross-peaks in the spectra are overlapping. In protein samples where a greater number of A β (1-40) are labelled, spectral assignments will become difficult due to a cluttered spectrum. However, this method is shown to be successful in resolving chemical shift information for A β (1-40) in a lipid environment under MAS DNP conditions for a sparsely labelled sample without contributions from lipid or glycerol signals.

4.5. Double-quantum single-quantum correlation

Another way of removing lipid and glycerol background signals shown in the DARR experiment was to use double quantum filtered (DQF) and double-quantum single-quantum (DQSQ) correlation experiments. These experiments involve the build-up of magnetisation between two ^{13}C spins, which is ~ 10000 times more likely for the

labelled amino acids than for lipids, where ^{13}C abundance is 1.1 %. Room temperature experiments were carried out on a uniformly labelled tyrosine amino acid sample to determine the most efficient DQF method for samples containing labelled protein. DQF and DQSQ have been previously demonstrated to be effective on biological samples under MAS DNP conditions.

Comparison of 1 bond dipolar recoupling sequences

A number of symmetry based double quantum excitation sequences have been developed, each with different advantages depending on the spin system under study^[19]. Four symmetry based DQ exciting pulse sequences, POST-C7, SP-C5, SR26 and R20₂⁹, were analysed on the amino acid tyrosine to determine which one would be optimal for one bond DQ excitation in the labelled amino acids of A β (1-40).

Tyrosine is an amino acid that contains both aliphatic and phenyl carbon positions, so the same challenges that need to be overcome by the pulse sequence are similar to labelled amino acid positions in proteins, for example the enhanced chemical shift anisotropy at phenyl carbons due to restricted motion, and the difference in nutation frequencies between carbonyl, aromatic and aliphatic positions.

The C7 pulse element is an example of a double quantum (DQ) homonuclear dipolar recoupling using Levitt's symmetry based pulse sequences^[20], which was improved by Permutationally Offset Stabilized (POST) pulse elements to give POST-C7^[21]. The POST-C7 pulse sequence is shown in Figure 4.11. The sequence consists of a DQ excitation and reconversion period which contain the POST-C7 pulse elements. The B_1 field for ^{13}C , ω_1 , is set to $7 \omega_r$, where ω_r is the MAS rotation frequency, so that seven POST-C7 pulse elements fit into exactly two rotor cycles. The excitation and reconversion blocks are repeated L_0 times, where L_0 is a multiple of 7. With each repeat of the basic sequence element, the phase is incremented by $2\pi / 7$ so that after L_0 loops the phase cycle is reset.

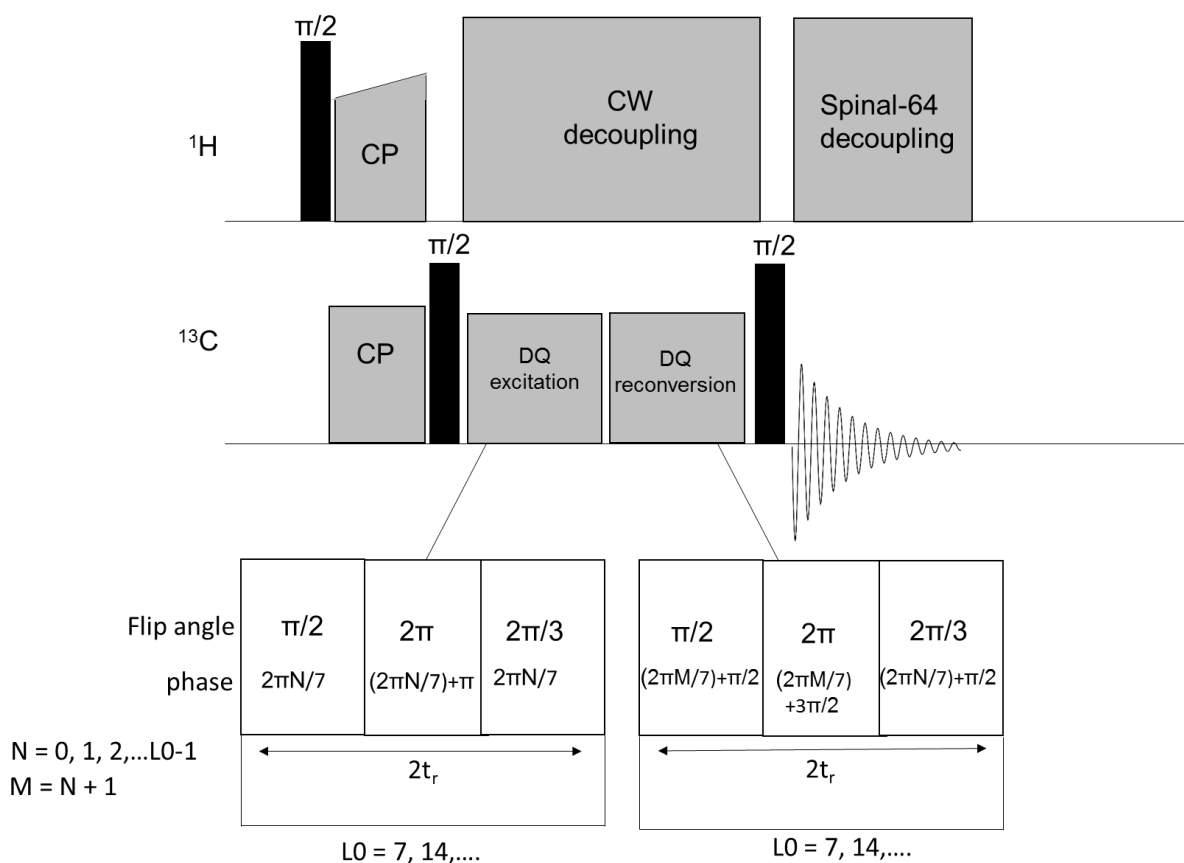


Figure 4.11 POSTC7 pulse sequence. The double-quantum (DQ) excitation and reconversion are looped L_0 times, which is set to a multiple of 7. The phase is incremented by $2\pi/7$ after each loop. The nutation frequency is set to seven times the MAS frequency so that one DQ loop takes exactly two rotor periods.

The length of the excitation and reconversion blocks are set depending on the separation, and therefore dipolar coupling strength, between spins under study. Short excitation periods are chosen if one bond ^{13}C interactions are being studied. Supercycled POST-C5 (SP-C5)^[22] is similar to POST-C7, but with five elements in the DQ excitation and reconversion loops. This means that field strength of the pulse applied to the ^{13}C channel, ω_1 is set to $5\omega_r$ rather than $7\omega_r$, so ^1H decoupling is more efficient during the DQ excitation and reconversion loops as ^1H decoupling power is most efficient at three times of that applied to the observe channel^[23].

$\text{R}20_2^9$ is an R-symmetry sequence, with promising results observed for powder solids without ^{13}C labelling^[24]. Unlike the previously described experiments, high power ^1H decoupling is not required during the recoupling blocks so optimisation of the pulse sequence requires only the ^{13}C 90° flip angle, which makes optimisation of the experiment easier. $\text{SR}26$ ^[25] has been used for weak homonuclear dipolar

interactions, with distances between spins of up to 8 Å^[26]. The literature DQ efficiency of the four pulse sequences analysed are summarised in table 4.2.

Sequence	Mixing time / μS	Experimental DQ efficiency	powder	MAS rate / Hz	Theoretical DQ efficiency	Ref.
POST-C7	714	61 %	1,2- ¹³ C - oxalate hemihydrate	5710	70 %	[21]
	357	35 %	2,3- ¹³ C-diammonium fumarate	5602	-	
	400	25 %	[U- ¹³ C]- α -glycine	10000	57 %	[24]
SP-C5	664	55 %	1,2- ¹³ C labeled diammonium oxalate	12000	73 %	[22]
	400	28 %	[U- ¹³ C]- α -glycine	10000	48 %	[24]
R20 ₂ ⁹	400	49 %	[U- ¹³ C]- α -glycine	10000	64 %	[24]
SR26	10800	38 %	[1,4- ¹³ C]-fumarate	5923	-	[25]
	5400	20 %	[15,20- ¹³ C]-all-E-retinal	5923	52 %	

Table 4.2 Literature double quantum efficiencies of homonuclear dipolar recoupling sequences.

Experimental DQ efficiencies are determined by comparison of signal intensity in DQF spectra with signal intensity in a CP experiment, displayed in Figure 4.12.

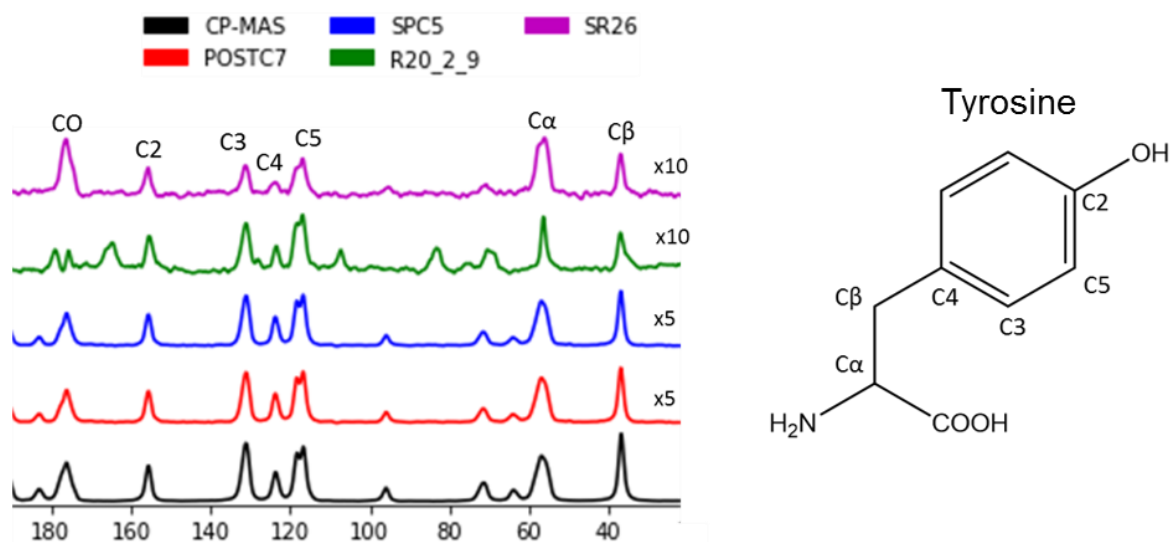


Figure 4.12 A cross-polarization (CP) spectrum for comparison with spectra acquired using double-quantum filtered (DQF) sequences. The signal intensity of peaks in a powder sample of labelled tyrosine were analysed to assess double quantum filtering efficiency for different peak positions. Magic angle spinning frequency was 9000 Hz in all experiments except for R20₂⁹ (7246 Hz). These experiments were recorded on a 600 MHz magnet at room temperature and without DNP.

Sequence	Mixing time / μ S	MAS frequency / Hz	Experimental DQ efficiency						
			CO	C $_{\alpha}$	C $_{\beta}$	C5	C4	C3	C2
POST-C7	444	9000	18 %	20 %	16 %	19 %	19 %	16 %	16 %
POST-C7	222	9000	16 %	15 %	14 %	17 %	16 %	15 %	14 %
SP-C5	444	9000	18 %	20 %	21 %	16 %	23 %	14 %	17 %
SP-C5	222	9000	9 %	9 %	6 %	6 %	8 %	5 %	5 %
R20 ₂ ⁹	552	7246	3 %	5 %	2 %	6 %	4 %	4 %	4 %
SR26	14222	9000	3 %	7 %	9 %	4 %	2 %	3 %	4 %

Table 4.3 Experimental double quantum efficiencies of homonuclear dipolar recoupling sequences on labelled tyrosine.

Table 4.3 shows experimental DQ efficiencies for the labelled tyrosine powder. POST-C7 and SP-C5 perform best with DQ efficiency of ~20 % at 444 μ S mixing time, corresponding to two blocks of the dipolar recoupling sequence. The C $_{\alpha}$ and C $_{\beta}$ show greater efficiency of ¹H decoupling in the case of SP-C5 due to higher power of decoupling relative to the power applied to the ¹³C nuclei. Two loops of excitation gives the best recoupling efficiency, one loop is too short a time to allow for maximum build-up of dipolar magnetization, but more than two results in signal

loss because of dipolar truncation due to dipolar coupling of remote labelled ^{13}C spins.

The DQF experiment using the R20₂⁹ produced weak DQ efficiency compared to the value stated in the literature. This pulse sequence requires transmitted power to be ten times that of the MAS frequency used in the experiment in order to maintain rotor synchronisation. The maximum power that can be safely applied to the transmitter coil in the probe used for these experiments is 75 kHz corresponding to MAS of 7.5 kHz, whereas the literature source was able to use 100 kHz ^{13}C power (10 kHz MAS). At these high powers, decoupling of strongly dipolar coupled nuclei is not required^[27] so no ^1H decoupling is applied during the mixing time in the literature pulse sequence. The experimental pulse sequence was modified to include ^1H decoupling during the mixing time, but this did not result in improved DQ efficiency. When applied to DNP enhanced ssNMR investigations, the R20₂⁹ sequence could still be valuable as experiments are carried out at cryogenic temperatures of 90 - 100 K and more power can be applied to the probe.

The SR26 sequence also shows weak DQ efficiency when applied to uniformly labelled tyrosine. It should be noted that the literature values stated for this sequence were recorded on systems where the only labelled positions four bonds away from one another. In the fully labelled tyrosine system, dipolar truncation occurs- the build-up of magnetisation from remote dipolar coupled nuclei is disrupted by closer nuclei.

2D double-quantum single-quantum (DQSQ) correlation experiments POST-C7^[21], shown in Figure 4.13, SP-C5 and SR26 were shown to be possible in under 1 day of experimental time on ~5 mg of labelled tyrosine. Single-quantum chemical shift information is encoded in the direct dimension and double-quantum chemical shift information in the indirect dimension. The cross-peaks in the indirect dimension appear at the sums of single-quantum (SQ) chemical shifts of the spins which are exchanging magnetization via the dipolar interaction. For example, the $\text{C}_\alpha - \text{C}_\beta$ cross-peaks appear at the SQ chemical shifts of each nuclei (56 ppm and 38 ppm, respectively) in the direct dimension and at the sum of these shifts (56 ppm + 38 ppm = 94 ppm) in the indirect dimension. This allows for assignment walks in one-bond correlation experiments with short homonuclear dipolar recoupling times leading to unambiguous assignments of cross peaks.

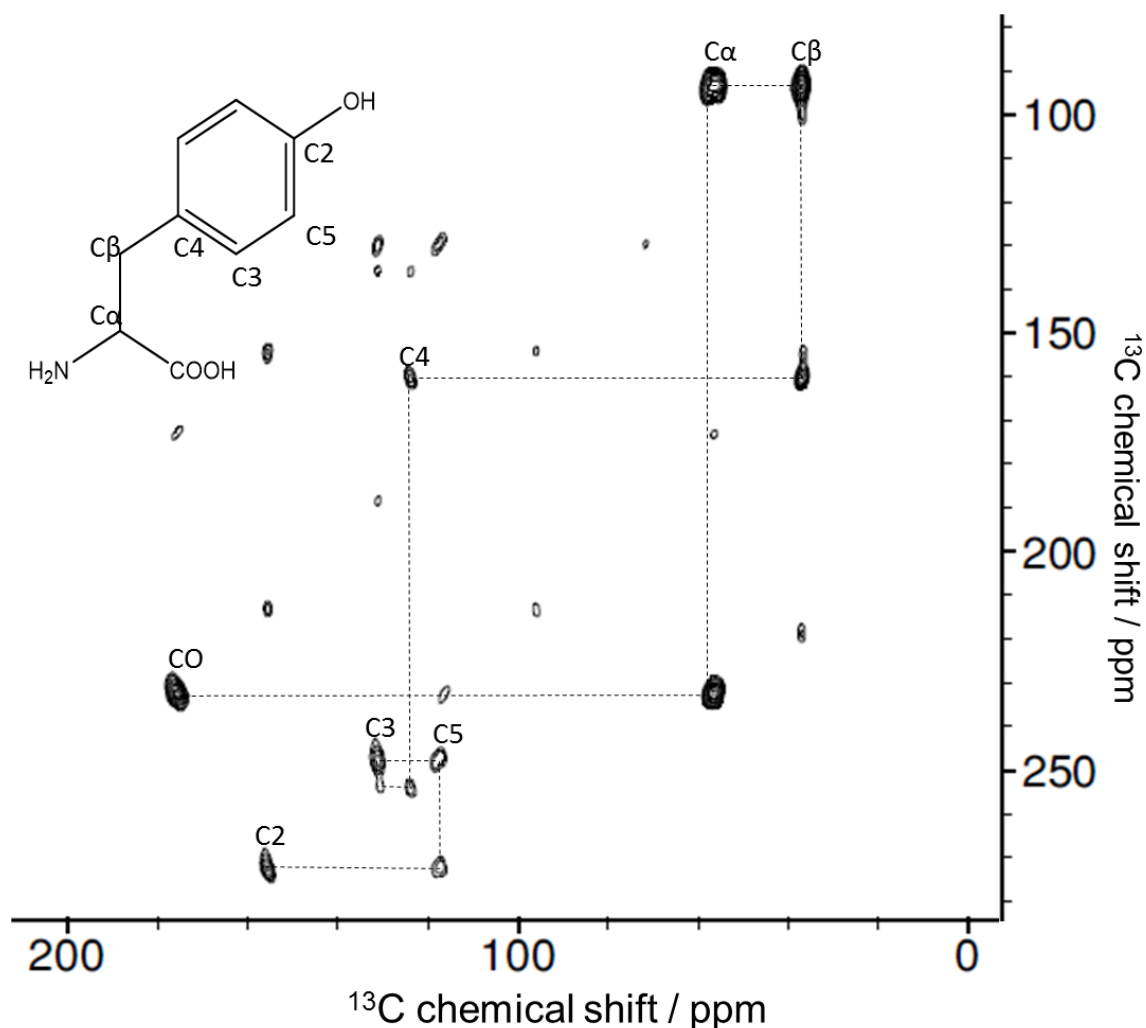


Figure 4.13 POST-C7 DQSQ correlation spectrum of tyrosine with 16 acquisitions in the direct dimension, 128 increments in the indirect dimension and a recycle delay of 30 s giving total experimental time of 17 h. The double-quantum excitation and reconversion blocks were 444 μ S, which is two loops of the composite pulse block, giving rise to predominantly one bond correlations. Assignments are given in the direct dimension showing the single-quantum chemical shifts, cross-peaks appear in the indirect dimension at the sums of the single-quantum chemical shifts that exchange magnetization.

Double-quantum filtering of A β (1-40) sample

POST-C7 and SP-C5 showed similar DQF efficiency. POST-C7 was chosen for DNP experiments on the 20:1 lipid-to-A β (1-40) sample. Figure 4.14 shows a POST-C7 DQF spectrum overlaid with microwave-on and microwave-off CP spectra. This shows the power of using double-quantum methods for membrane A β (1-40) samples, as the ratio of spectral intensity of lipids and glycerol compared to protein is dramatically reduced. This is because double-quantum magnetisation only builds up between ^{13}C nuclei that are separated by a distance equivalent to one bond

length, which is many times more likely for the labelled A β (1-40) amino acid residues compared to lipids and ^{13}C depleted glycerol- ^{13}C is 100 % abundant in labelled protein compared to 1.1 % in lipids, so a one bond separation between two ^{13}C nuclear spins is ~ 10000 times more likely in the protein than the lipid. The lipid peak at 34 ppm is the most intense peak in CP experiments (Figure 4.15b and c) but does not appear in the DQF spectrum (Figure 4.15a).

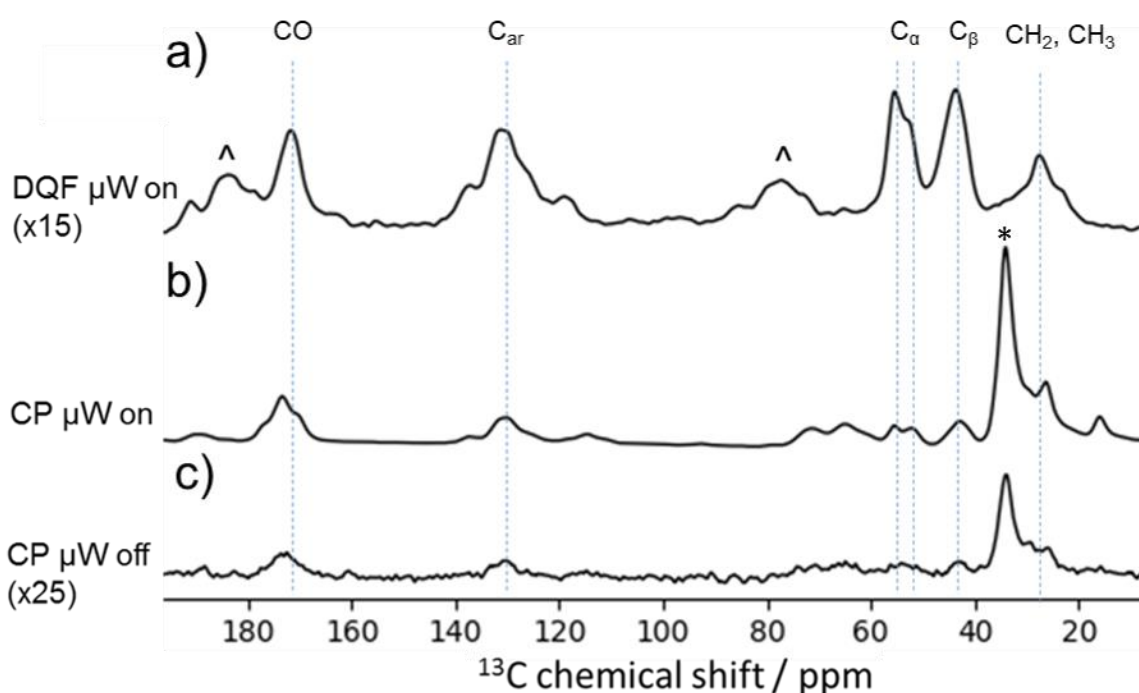


Figure 4.14 a) DQF POST-C7 spectrum of 20:1 POPC / POPG lipids and A β (1-40) sample compared with b) CP with microwaves and c) CP without microwaves. The dashed blue lines show labelled protein positions- carbonyls at ~ 175 ppm, F19 aromatic carbons at ~ 135 ppm, C $_{\alpha}$ of F19 and L34 at 51-55 ppm, C $_{\beta}$ of F19 and L34 and C $_{\alpha}$ of G38 at 42-45 ppm and alkyl ^{13}C labels in L34. * denotes the lipid peak, which is not visible in the DQF spectrum, ^ denotes spinning sidebands.

2D DQSQ experiments were required to assign peaks and better resolve resonances in order to make accurate calculations of secondary chemical shift.

Double-quantum single-quantum (DQSQ) correlation

DQSQ correlation experiments were carried out using the POST-C7 pulse sequence. As discussed previously, this gives a characteristic pattern of cross-peaks which appear at the chemical shift value in the direct dimension and at the sum of the single-quantum chemical shifts in the indirect dimension, shown in Figure 4.15. 1D slices at leucine correlation DQ chemical shifts are shown in Figure 4.16 to demonstrate the signal-to-noise that was achieved.

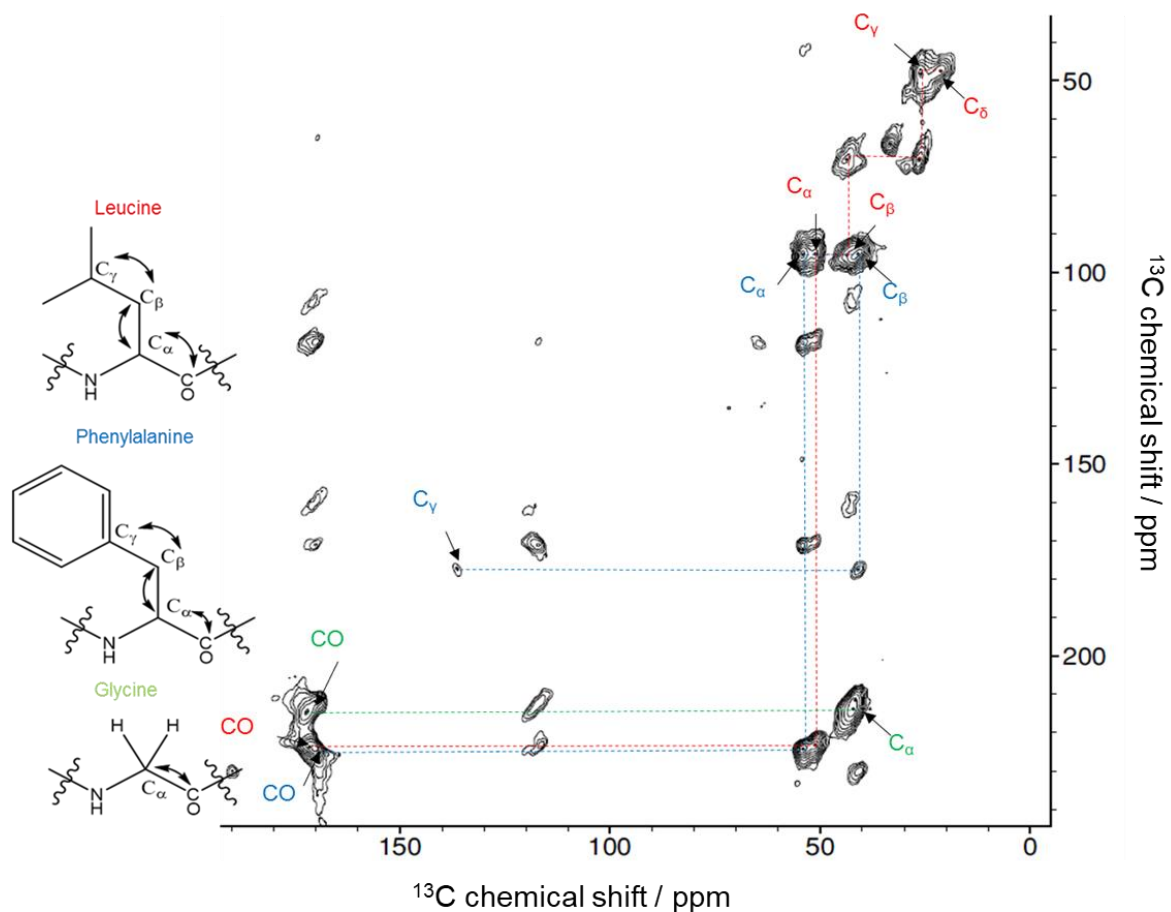


Figure 4.15 Assigned DQSQ experiment acquired with 16 scans in the direct dimension, 256 points in the indirect dimension and a recycle delay of 8 s giving an experimental time of ~9 h. 2 loops of POST-C7 DQ excitation and reconversion pulse were used, corresponding to 444 μs of excitation and reconversion.

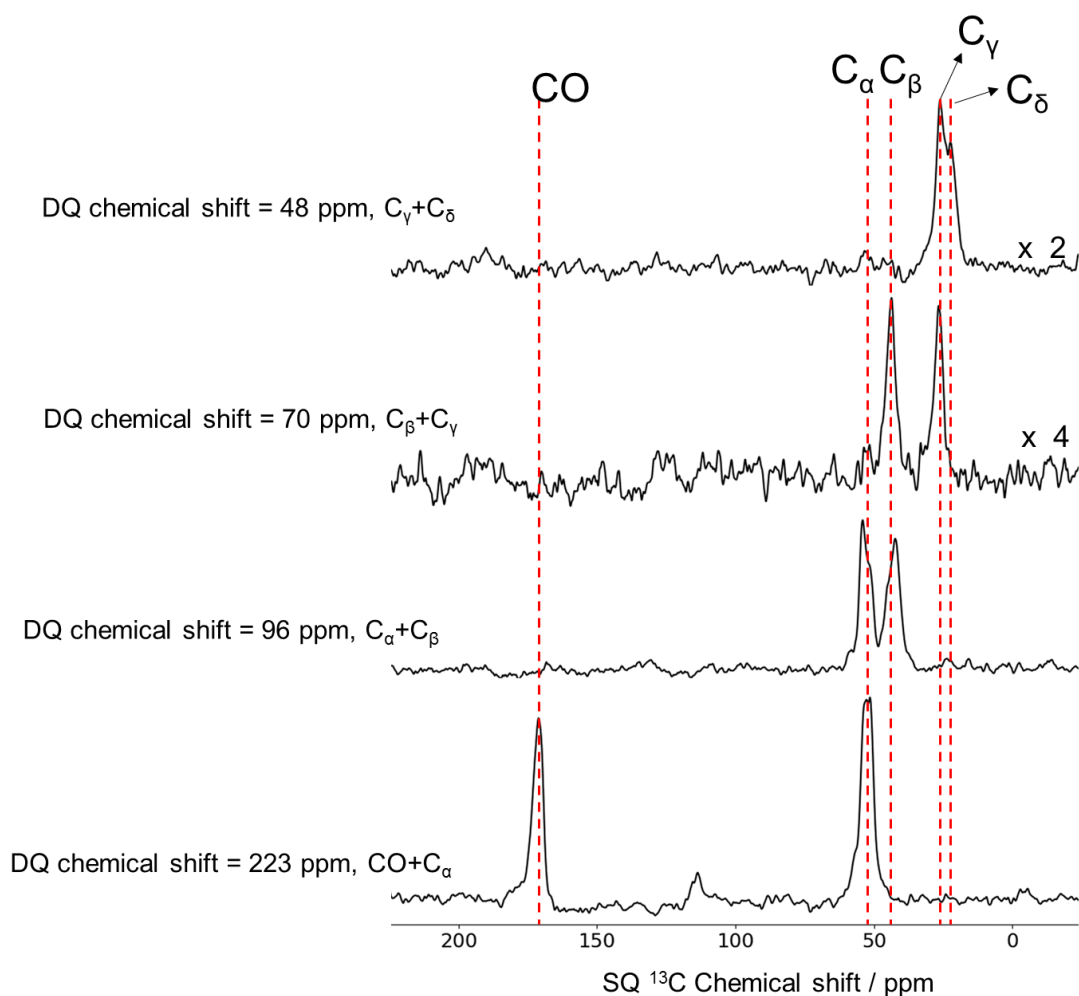


Figure 4.16 1D slices of leucine cross-peaks at DQ chemical shift of the sum of the SQ chemical shifts of the interacting spins.

G38 is clearly distinguishable in the DQSQ spectrum because the C_{α} is ~ 10 ppm from the C_{α} of F19 and L34, which gives a significant cross-peak separation in the double-quantum (DQ) axis. Resonances of F19 and L34 can also be unambiguously assigned from analysis of correlations with the side chain resonances- the C_{β} - C_{γ} L34 correlations give the chemical shift of the L34 C_{β} in the single-quantum (SQ) dimension, which is subtracted from the DQ chemical shift of the C_{α} - C_{β} cross-peaks. As the C_{α} SQ chemical shift is known, the chemical shift of CO can be determined by subtraction of this value from the DQ chemical shift of the CO - C_{α} cross-peaks. A similar procedure was carried out for F19 starting from the cross-peaks of the aromatic phenyl ring and C_{β} , which are clearly resolved in the spectrum at ~ 175 ppm in the DQ axis.

The spectrum was left to run overnight with 256 scans in the indirect dimension giving an experimental time of ~ 9 h, although the FID had fully decayed after ~ 160

points so the same spectrum could be collected in ~5.5 hrs. Signal-to-noise ratio increases as the square root of the number of scans and therefore as the square root of time.

Secondary chemical shifts at 20:1 lipid-to-protein ratio

The secondary chemical shifts for the 20 : 1 lipid-to-protein ratio sample are shown in Figure 4.17a, compared with A β (1-40) under DNP conditions after a variety of treatments, shown in Figure 4.17b^[14].

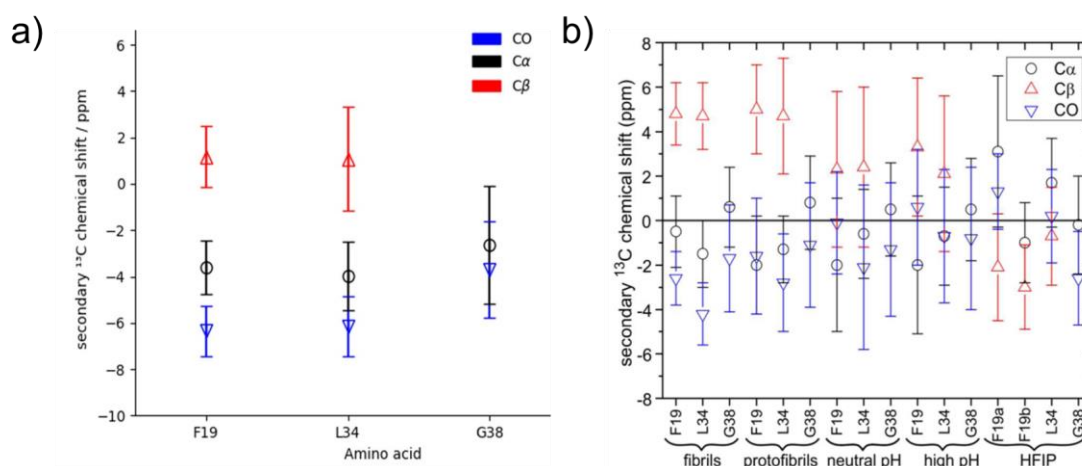


Figure 4.17 a) Graph showing the secondary chemical shifts of F19, L34 and G38 in A β (1-40) in the 20:1 lipid-to-protein sample. Negative CO and C α values and positive C β are indicative of β -sheet structure. Error bars indicate the linewidths of peaks in the DQSQ spectrum. b) secondary chemical shifts of A β (1-40) in fibrils, protofibrils, neutral pH, high pH and HFIP with the same labelling scheme. The section of protein where the labels adopt a β -sheet structure under all conditions apart from in hexafluoro-2-propanol (HFIP), which is known to break up aggregates, in which secondary chemical shifts suggest a α -helical structure. Figure reproduced with permission from [14].

The observed negative ¹³C chemical shifts for CO and C α and positive C β indicate that the labelled positions have a β -sheet structure, as explained in **section 2.4**. A previous study using DNP-enhanced ssNMR showed that α -helical secondary structure is observed in HFIP, which is known to break up A β aggregates and pre-aggregates, leaving the protein in its monomeric form^[28]. This has implications for studies on A β (1-40) at low concentration suspended in lipids, as this may induce an α -helical structure due to A β (1-40) monomers not interacting with one another and being retained in the lipid bilayer. α -helical protein structures are associated with a number of membrane disruption mechanisms as they have the ability to span membrane bilayers due to stabilisation of the helical structure by favourable hydrogen bonding, resulting in disruption of ion exchange across the cell membrane. This is explored in the next chapter, as well as the implications of this

structural information relative to the literature on A β associated with membrane mimics. The error bars presented in plots of secondary chemical shift correspond to the FWHM linewidth peaks taken from 1D slices of the 2D DQSQ correlation spectrum.

4.6. Conclusion and outlook

DNP enhancements, ϵ_{DNP} , were shown to be ~ 40 for protein peaks, in agreement with lipid sample optimization experiments outlined in **Chapter 3**.

Double-quantum filtering and double-quantum single-quantum correlation has been identified as a good method for unambiguously assigning labelled amino acid residues and removing background signals from spectra. Considerably better resolution was achieved using DQSQ compared to DARR and spectra are less crowded by natural abundance diagonal and cross-peaks. POST-C7 and SP-C5 showed very similar performance in preliminary studies on labelled tyrosine, POST-C7 was selected for experiments under MAS DNP conditions. DQSQ correlation spectra have better resolution than single quantum techniques and significantly less overlap due to natural abundance background signals.

Secondary chemical shifts of the labelled positions in A β (1-40) suggest a β -sheet secondary structure when associated with this lipid mixture. The next chapter discusses in detail the expected secondary structure of A β under different conditions and probes A β structure at low lipid-to-protein ratio, using synthetic lipids with synthetic membrane components which better mimic biological membrane and probe the structure of labelled A β (1-40) associated with synaptic rat membrane.

Selective labelling so that only one ^{13}C is labelled per amino acid will overcome dipolar truncation problems arising due to uniform labelling. This will allow long distance measurements between amino acid positions that give clues about overall structure. The SR26 pulse sequence has been shown to quantify distances of nuclear spins in samples that do not suffer from dipolar truncation^[29].

Another promising possibility is ^{31}P filtered and $^{13}\text{C} - ^{31}\text{P}$ correlation experiments between the phospholipid phosphate group and labelled A β (1-40) amino acid positions^[30]. This will show which protein positions are close in space to the headgroup region of the bilayer, providing clues as to how the protein sits relative to the cell membrane.

4.7. References

- [1] M.P. Williamson, T.F. Havel, K. Wuthrich, *J. Mol. Biol.*, 1985, **182**, 295–315
- [2] T.F. Havel, K. Wuthrich, *J. Mol. Biol.*, 1985, **182**, 281–294
- [3] A. Zagdoun, A. J. Rossini, M. P. Conley, W. R. Grüning, M. Schwarzwälder, M. Lelli, W. T. Franks, H. Oschkinat, C. Copéret, L. Emsley, A. Lesage, *Angew. Chem. Int. Ed.*, 2013, **52**, 1222–1225
- [4] Patrick C.A. van der Wel, *Emerg. Top. Life Sci.*, 2018, **2**, 57–67
- [5] W. Qiang, and K. E. Doherty, *Methods Mol Biol.*, 2018, **1777**, 355–367
- [6] S. Y. Liao, M. Lee, T. Wang, I. V. Sergeyev, M. Hong, *J. Biomol. NMR*, 2016, **64**, 223–237
- [7] E. S. Salnikov, S. Abel, G. Karthikeyan, H. Karoui, F. Aussenac, P. Tordo, B. Bechinger, O. Ouari, *ChemPhysChem*, 2017, **18**, 2103 – 2113
- [8] J. L. Markley, D. H. Meadows, O. Jardetzky, *J. Biomol. NMR*, 1967, **27**, 25–40
- [9] D. S. Wishart, B. D. Sykes, F. M. Richards, *Biochemistry.*, 1992, **31**, 1647–1651
- [10] D. S. Wishart, B. D. Sykes, *J. Biomol. NMR*, 1994, **4**, 171–80
- [11] K. Takegoshi, S. Nakamura, T. Terao, *Chem. Phys. Lett.*, 2001, **344**, 631-637
- [12] K. Takegoshi, S. Nakamura, T. Terao, *J. Chem. Phys.*, 2003, **118**, 2325-2341
- [13] N. M. Szeverenyi, M. J. Sullivan, G. E. Maciel, *J. Magn. Reson.*, 1982, **47**, 462–475
- [14] A. Potapov, W.-M. Yau, R. Ghirlando, K. R. Thurber, R. Tycko, *J. Am. Chem. Soc.*, 2015, **137**, 8294–8307
- [15] K.R. Thurber, R. Tycko, *J. Magn. Reson.*, 2008, **195**, 179-186
- [16] K. Thurber, R. Tycko, *J. Magn. Reson.*, 2016, **264**, 99-106
- [17] A. F. Mehlkopf D. Korbee T. A. Tiggelman R. Freeman, *J. Mag. Reson.*, 1984, **58**, 315-323
- [18] M. Baldus, A. T. Petkova, J. Herzfeld, R. G. Griffin, *Mol. Phys.*, 1998, **95**, 1197-1207
- [19] Malcolm H. Levitt, *Encyclopedia of Nuclear Magnetic Resonance Volume 9: Advances in NMR*, 2002, **9**, 165-196

- [20] Y.K. Lee, N.D. Kurur, M. Helmle, O.G. Johannessen, N.C. Nielsen, M.H. Levitt, *Chem. Phys. Letts.*, 1995, **242**, 304-309
- [21] M. Hohwy, H. J. Jakobsen, M. Edén, M. H. Levitt, N. C. Nielsen, *J. Chem. Phys.*, 1998, **108**, 2686-2694
- [22] M. Hohwy, C. M. Rienstra, C. P. Jaroniec, R. G. Griffin, *J. Chem. Phys.*, 1999, **110**, 7893-7992
- [23] Y. Ishii, J. Ashida, T. Terao, *Chem. Phys. Letts.*, 1995, **246**, 439-445
- [24] M. Dekhil, G. Mollica, T. T. Bonniot, F. Ziarelli, P. Thureau, S. Viel, *Chem. Commun.*, 2016, **52**, 8565-8568
- [25] P. E. Kristiansen, M. Carravetta, W. C. Lai, M. H. Levitt, *Chem. Phys. Letts.*, 2004, **390**, 1-7
- [26] D. H. Brouwer, P. E. Kristiansen, C. A. Fyfe, M. H. Levitt, *J. Am. Chem. Soc.*, 2005, **127**, 542-543
- [27] C. E. Hughes, S. Luca, M. Baldus, *Chem. Phys. Letts*, 2004, **385**, 435-440
- [28] M. G. Zagorski, J. Yang, H. Shao, K. Ma, H. Zeng, A. Hong, *Methods Enzymol.*, 1999, **309**, 189-204
- [29] K. Märker, M. Pingret, J.-M. Mouesca, D. Gasparutto, S. Hediger, G. De Paëpe, *J. Am. Chem. Soc.*, 2015, **137**, 13796–13799
- [30] T. Wiegand, W.-C. Liao, T. C. Ong, A. Däpp, R. Cadalbert, C. Copéretb, A. Böckmann, B. H. Meier, *J. Biomol. NMR.*, 2017, **69**, 157-164
- [31] C. R. Morcombe, K. W. Zilm, *J. Mag. Res.*, 2003, **162**, 479-486

5.	Characterisation of Aβ(1-40) in a membrane mimicking environment ...	100
5.1.	Introduction	100
5.2.	Methods.....	103
5.3.	A β (1-40) associated with lipids at low concentration	106
5.4.	A β (1-40) associated with a complex lipid mixture.....	113
5.5.	A β (1-40) associated with synaptic rat membrane	118
5.6.	External addition of A β (1-40) to lipids.....	123
5.7.	Discussion	133
5.8.	Conclusion and outlook.....	135
5.9.	References	138

5. Characterisation of A β (1-40) in a membrane mimicking environment

5.1. Introduction

Amyloid-beta (A β) is a major pathological hallmark of Alzheimer's disease (AD). Many possible mechanisms have been proposed for the cause of brain cell death due to interactions with A β , but no consensus has been reached^[1]. The observation that A β readily forms amyloid fibrils which aggregate to plaques has led to a number of proposed mechanisms that involve these larger structures^[2]. However, the amount of fibrillar A β is not always an indicator of the progression or severity of AD, so the possibility that A β monomer or oligomer structures cause the death of neuronal cells is a key area of research.

Studying the interaction between A β structures and cell membrane is important for several reasons. First, many of the proposed mechanisms for A β toxicity involve the direct disruption of cell membrane. Second, membrane mimics have been shown to stabilise certain A β structures leading to fibrillation, and finally, the formation of A β protein results from cleavage from membrane bound amyloid-precursor protein (APP)^{[1][3]}.

A β interactions with cell membranes can be investigated using *in vitro* models. Such models mimic the composition of a real cell membrane and they typically consist of phospholipids and other membrane components such as cholesterol, sphingomyelins and gangliosides, structures are shown in Figure 5.1. Many of these individual components have their own structural effects on A β and modulate its interaction with the membrane. For example, cholesterol at high concentration reduces the fluidity of the membrane thereby prevents the insertion of A β ^[4], and the ganglioside, GM1, leads to a greater stabilisation of the membrane upon insertion of A β ^[5].

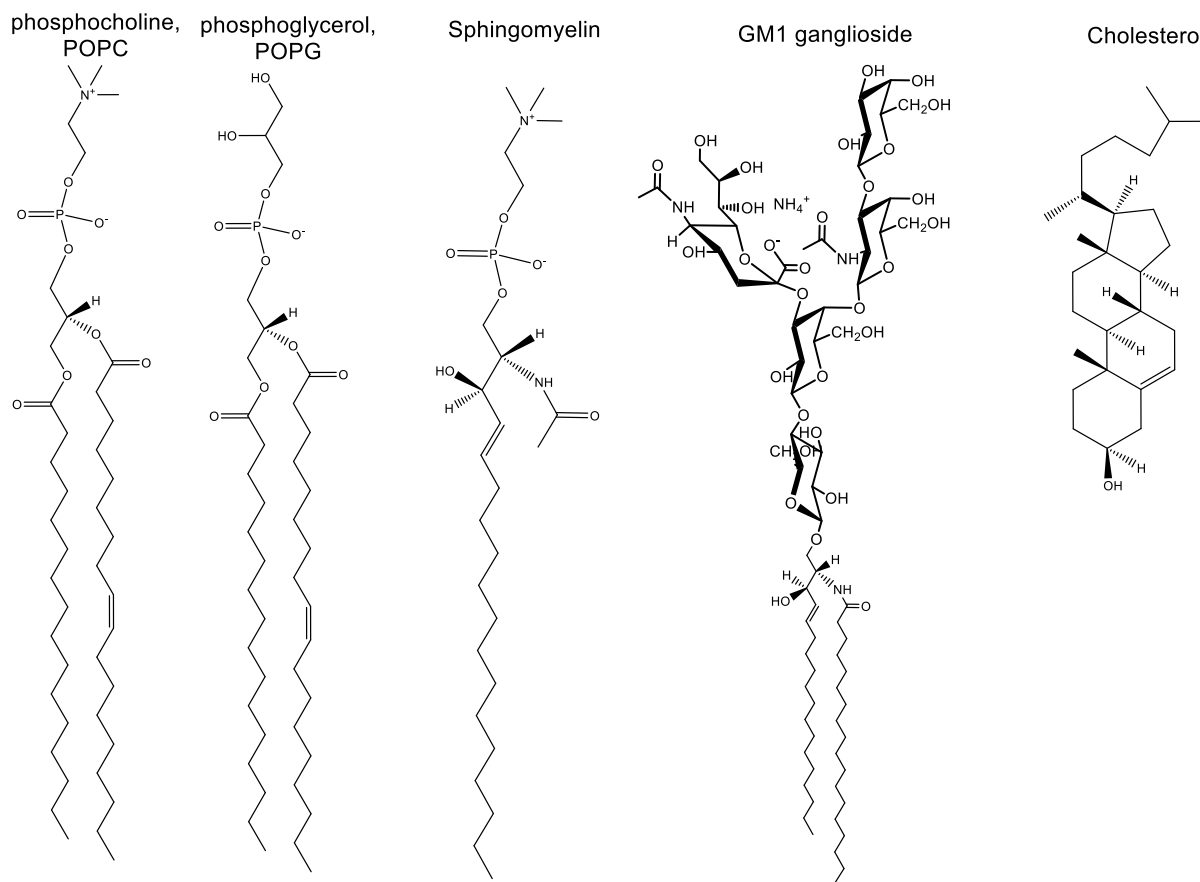


Figure 5.1 Synthetic membrane components for designing accurate replicas of a biological system.

Lipid charge affects the secondary structure of A β - more α -helical character is found in certain lipids due to being retained in the lipid, shown by the circular dichroism (CD) spectroscopy^[6]. Solution-state NMR has also shown a partially helical conformation on addition of A β (1-40) to zwitterionic lipids^[36]. α -helical membrane protein structures have been implicated in disruption of membrane functionality by causing strain to the curvature of the cell and by formation of ion pores when imbedded in the membrane^[7], so observing lipid-associated A β (1-40) in an α -helical conformation would therefore provide support to this mechanism of brain cell death.

Actual biological membrane bilayers are rather complex and are difficult to reproduce entirely using synthetic mimic systems. For that reason, some studies have focused on lipids extracted from living organisms. For example, AFM and black lipid membrane (BLM) electrical recording show differences in ion conductivity in brain total lipid extract (BTLE) compared with synthetic lipids in the presence of A β (1-42)^[8]. The size of A β oligomers has been demonstrated to have a significant effect on the nature of the interaction with BTLE. The fibrillation of large oligomers is accelerated by BTLE whereas smaller oligomers result in pore formation and destruction of the membrane^[9]. Recent studies have suggested that in excised

neuronal cells, A β (1-42) forms cytotoxic ion channels but A β (1-40) does not^[10]. These studies present useful information about possible mechanisms of cell destruction, but do not provide evidence about the molecular structure of A β when associated with membrane material at low concentration.

Structural studies of A β (1-40) at low concentrations are challenging due to the limited sensitivity of many spectroscopic techniques. However, such studies are needed for answering important questions about the A β -membrane interaction. For example, formation of ion channels by A β mentioned above is a potential mechanism of cell death. The presence of these channels is suggested to cause a dysregulation of the ionic homeostasis as confirmed in *in vitro* model by ionic conduction studies^{[11][12][13]}. However, formation of these ionic channels take place at relatively low A β -to-lipid ratios (<1:100). Circular dichroism, electron microscopy, atomic force microscopy etc. can provide information for such a low concentration, but, these techniques only give a general idea of overall secondary structure and the size of the formed oligomers. These techniques cannot capture atomic resolution level details of A β interaction with lipids.

Atomic resolution details can be obtained using nuclear magnetic resonance (NMR) spectroscopy. Solution state NMR has been carried out in apolar solvents that loosely mimic the electrostatic environment of a cell membrane. A β (1-40) and A β (1-42) have been shown to adopt a helical region between amino acids 8-25 and 28-38 in aqueous solution containing fluorinated alcohols^[14]. A similar observation was made in aqueous solution containing the surfactant sodium dodecyl sulphate (SDS)^[15]. Solution state NMR and x-ray crystallography cannot be used to study membrane associated A β . Membrane associated protein tumbles too slowly in solution for solution-state NMR, and cannot be crystallised easily, which is essential for x-ray diffraction. ssNMR studies of A β fibrils have resulted in structural models in which the protein adopts a U-shaped conformation which stack to form parallel, in-register cross- β structures^{[33][34]}. Structurally distinct polymorphs of A β (1-40) fibrils have been shown to form when grown with and without sample agitation^[35], showing the sensitivity of fibril structure to preparation conditions.

Membrane - A β samples can also be studied using ssNMR, with MAS providing sufficient resolution for investigation of the molecular structure of A β ^[16]. In particular, ssNMR can provide information both on A β conformation in lipids, and also on its insertion into the membrane, in a similar manner to what has been demonstrated for HIV fusion peptides^[17]. However, ssNMR rotors have a limited volume, much of

which is taken up by water and membrane rather than protein in an A β – membrane sample. This means that sensitivity of protein NMR signals is low meaning that conventional measurements take a prohibitively long time due to the signal averaging required.

Previously, 2D spectra using ssNMR of samples with A β -to-lipid ratio of 1 : 30 have been demonstrated^{[18][19]}, as well as in 1D measurements^[20], but probing structures at higher lipid-to-protein, closer to conditions found *in vivo*, is necessary in order to understand the mechanism of toxicity.

For this reason, DNP is applied to enhance the ssNMR signals from protein which is present in low concentration compared to membrane^[21]. Previously, DNP enabled the ssNMR signal increase sufficient for characterising several metastable A β 40 aggregate structures^[22]. For that reason, it is promising for studies of A β 40 interacting with lipids. This chapter shows the feasibility of the DNP-enhanced ssNMR measurements under conditions when the unenhanced A β (1-40) NMR signals are weak. Two scenarios were considered:

- 1) A β (1-40) is pre-incorporated into vesicles of POPC / POPG lipids mimics at high lipid-to-protein ratio. The amount of material, however, is sufficient to fill the entire 3.2 mm NMR rotor.
- 2) A β (1-40) is externally added to lipid vesicles made of synaptic lipids obtained from rat brains. The procedure for obtaining the lipid material yields small amounts of material, which is why the sample size is limited.

Finally, we apply DNP-enhanced ssNMR to probe the initial and final state of A β (1-40) aggregation after the peptide is externally added to POPG lipids, to show that this method can in principle be used to capture the time-progression of A β (1-40) aggregation.

5.2. Methods

Sample preparation protocols

A β (1-40) pre-incorporated into lipids

The sample preparation protocol is identical to the pre-incorporation protocol described in **section 4.2**. In the experiments described in this section, the A β (1-40) was pre-incorporated at various protein : lipid ratios either into a lipid mixture of POPC / POPG (3 : 1) or into a mixture containing POPC / POPG / cholesterol /

sphingomyelin / ganglioside GM1 (1 : 1 : 1.33 : 1 : 0.1). For experiments involving synaptic rat membrane, the protocol was modified-

Two aliquots of 1 mg lyophilized A β (1-40) were dissolved in 1 ml HFIP and sonicated in a water bath for 5 minutes to give a clear solution. HFIP was removed with an N₂ gas stream followed by overnight drying under vacuum. The peptide film was dissolved in 60 mM NaOH to a concentration of 200 μ M, the solution was vortexed to ensure complete dissolving. Synaptic rat membrane extraction was performed by Qinghui Cheng using a previously described protocol, described in Appendix 1. The two A β (1-40) aliquots were diluted using 4 mM HEPES buffer and mixed with synaptic rat membrane stocks, one extracted from a 12 month old rat and one from an 18 month old rat. The final solution was diluted such that A β (1-40) concentration was 10 μ M and peptide-to-total-lipid ratio 1 : 10. The solution was vortexed for 2 minutes the incubated quiescently at 37°C for 48 hours. The mixture was centrifuged at 80000 rpm using a Beckmann Ultracentrifuge with TLA100.4 rotor to collect the membrane pellet.

The resulting lipid – protein pellet was packed in a DNP rotor using the procedure described in **chapter 4**.

External addition of A β (1-40) to lipids

The external addition method was adapted from the method used earlier by the Qiang group in order to make a sample for DNP studies^[23].

Two aliquots of POPG (11.56 x 10⁻³ mmol, 8.6 mg) were dissolved in chloroform. The solutions were sonicated in a water bath for 5 min, solvent was removed with N₂ flow. The remaining lipid film was dried by lyophilisation and rehydrated using 10 mM phosphate buffer (12 ml, 10 mM, pH 7.4). The re-suspended lipid was agitated for 1 h at ambient temperature followed by 10 freeze thaw cycles and 10 cycles of extrusion with 300 nm pore size membranes. A solution of 1.25 mg A β (1-40) dissolved in 155 μ L DMSO was added to each of the aliquots of POPG to give a lipid-to-protein ratio of 40 : 1, of which one was incubated quiescently at 37 °C for 8 hrs. A β (1-40) concentration was quantified every hour during incubation by UV / vis spectroscopy using an analytical HPLC system. Both mixtures were then centrifuged at 28000 rpm using a Beckman centrifuge with a F1010 rotor to collect the membrane pellet. The resulting lipid – protein pellet was packed in a DNP rotor using the procedure described in **chapter 4**.

DNP MAS ssNMR

NMR parameters used in all the experiments in this chapter are summarized in table 5.1.

Sample	Experiment	MAS frequency / Hz	Mixing / excitation time / μS	Recycle delay / s	ns	np
100 : 1 POPC / POPG + A β (1-40)	POST-C7	8500	471	6.3	80	128
100 : 1 POPC / POPG + A β (1-40)	POST-C7	8500	471	8.3	64	128
30 : 1 complex lipid mixture + A β (1-40)	POST-C7	8500	471	9.0	32	256
150 : 1 complex lipid mixture + A β (1-40)	POST-C7	8000	500	12.0	64	128
10 : 1 Synaptic rat membrane + A β (1-40)	POST-C7	8000	500	6.0	512	64
10 : 1 Synaptic rat membrane + A β (1-40)	R20 ₂ ⁹	9000	444	7.0	256	64
40 : 1 POPG + A β (1-40) no incubation	POST-C7	8500	471	4.5	128	141
40 : 1 POPG + A β (1-40) no incubation	DARR	8500	2.5×10^5	4.5	16	300
40 : 1 POPG + A β (1-40) no incubation	PDSD	8500	2×10^6	4.5	28	300
40 : 1 POPG + A β (1-40) 8 hr incubation	POST-C7	8500	471	3.5	160	120
40 : 1 POPG + A β (1-40) 8 hr incubation	DARR	8500	2.5×10^5	3.5	28	300
40 : 1 POPG + A β (1-40) 8 hr incubation	PDSD	8500	2×10^6	3.5	28	300

Table 5.1 A summary of the NMR parameters used for experiments in this chapter. ns is the number of scans in the direct dimension, np is the number of points in the indirect dimension.

All experiments were performed with microwave irradiation from the 395 GHz gyrotron to give DNP enhancement. The recycle delay was set to 1.3 times $^1\text{H } T_1$ to achieve maximum signal-to-noise per unit time. All DQ dipolar recoupling experiments were performed using two blocks of excitation and reconversion, which was found to be optimal in **section 4.9**. The temperature in all experiments was between 95 K – 103 K. Some variation in temperature occurs due to the strength of the vacuum applied to the probe.

Data presentation

Secondary chemical shifts are shown on graphs for each sample, with error bars which are the linewidths of the peaks from which the chemical shift was recorded. The full-width at half maximum (FWHM) of the peaks were recorded from 1D slices at the chemical shifts in both axis at which cross-peaks appear in the 2D spectrum.

5.3. A β (1-40) associated with lipids at low concentration

POST-C7 DQSQ experiments were carried out on both the 100 : 1 and 200 : 1 samples, displayed in Figure 5.2 and 5.3. The samples were prepared using the pre-incorporation method described in **section 4.2**. An experimental issue for samples with low protein concentrations is that DQF takes a long time to optimise DQ excitation and reconversion pulse power, so this is optimised on an arginine sample which may have slightly different NMR pulse calibrations to membrane-protein samples.

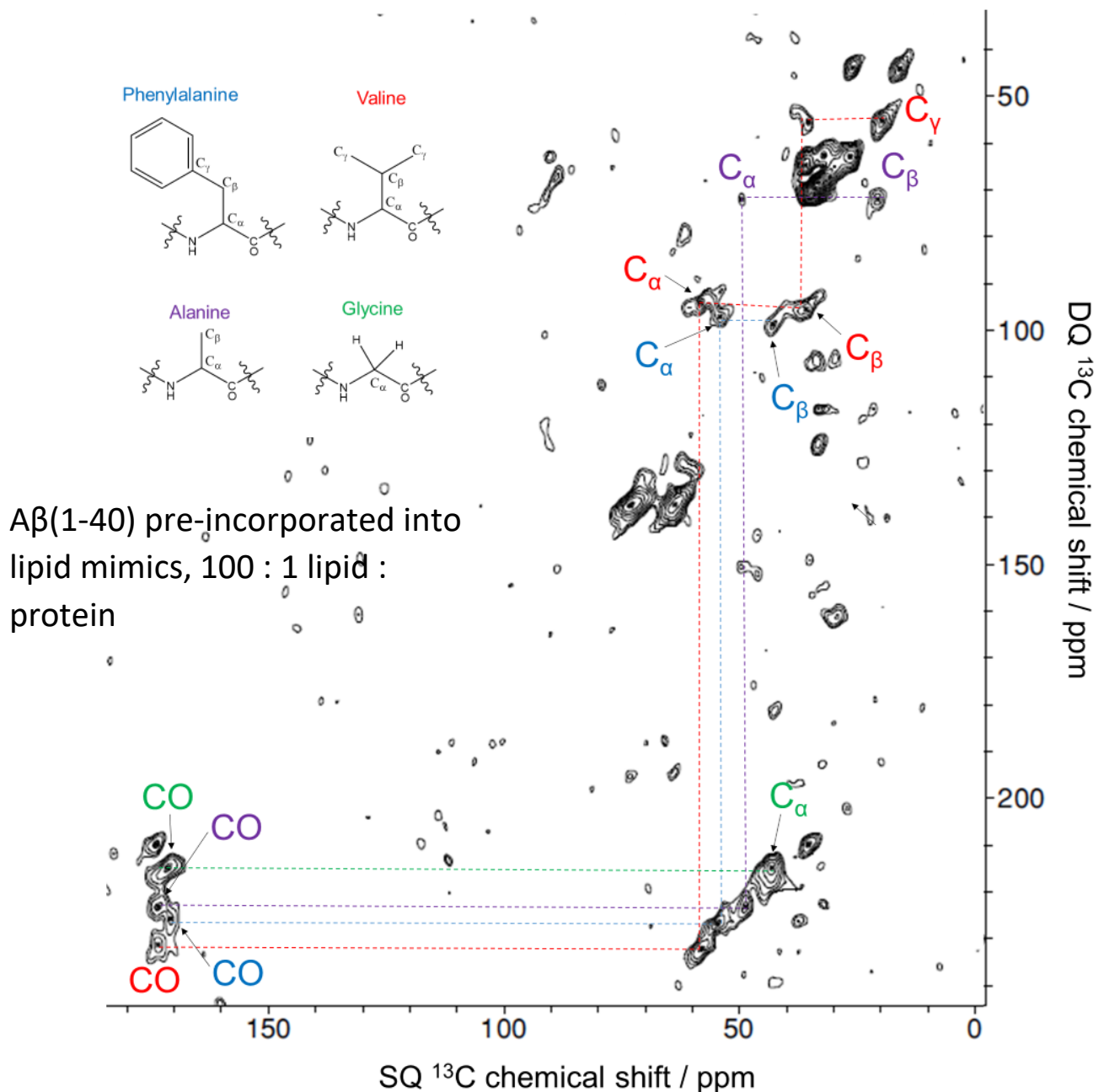
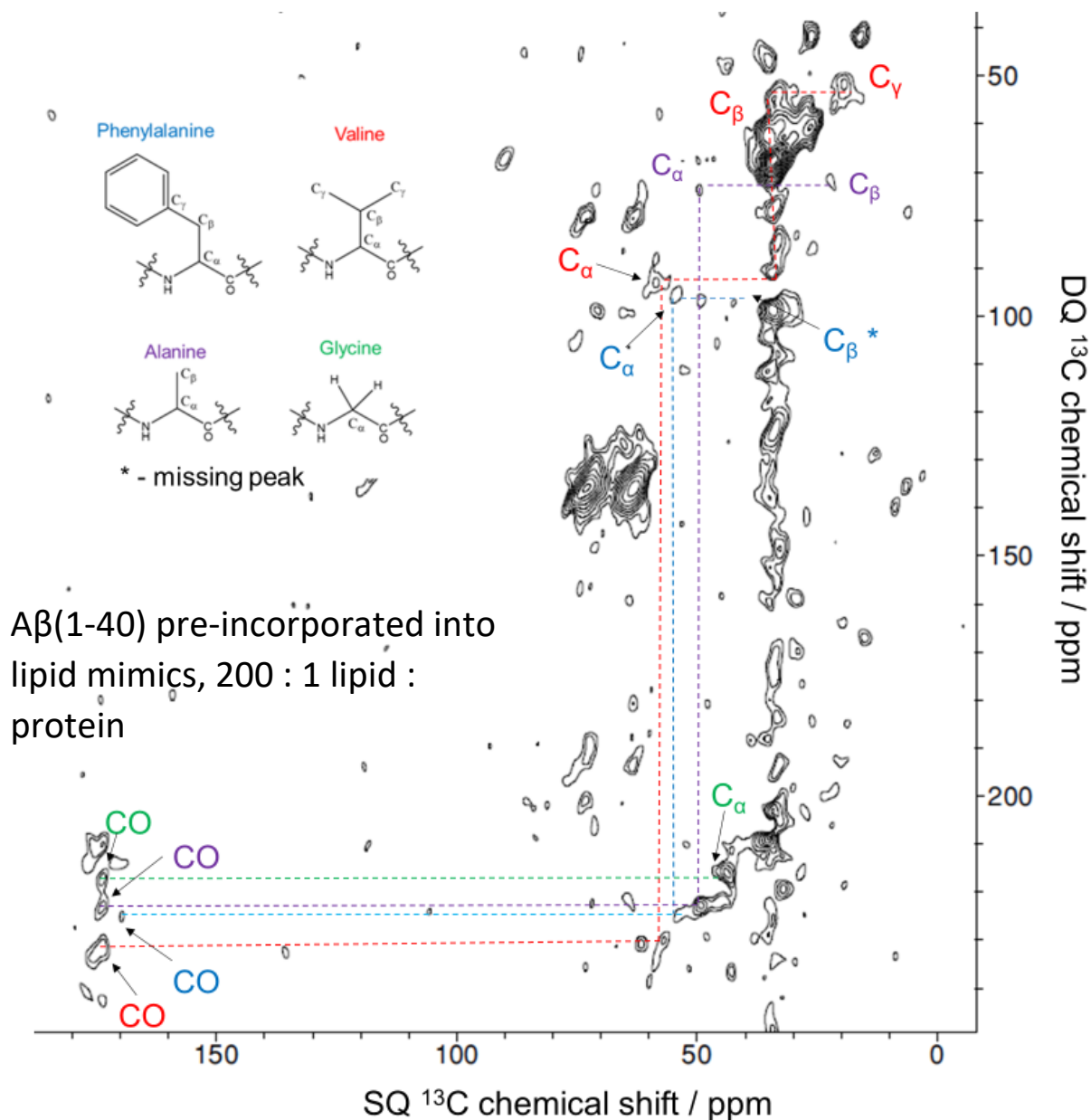


Figure 5.2 POST-C7 DQSQ spectrum of $\text{A}\beta(1-40)$ uniformly labelled at F20, A21, G31 and V36 pre-incorporated into POPC / POPG lipid vesicles at a lipid to protein ratio of 100 : 1. The spectrum was acquired with 80 scans in the direct dimension, 128 points in the indirect dimension and a recycle delay of 6.4 s giving an experimental time of 18 h.

All uniformly labelled positions are observed except for the $\text{C}_\gamma - \text{C}_\beta$ phenylalanine correlation due to poor efficiency of DQ excitation of aromatic residues because of increased chemical shift anisotropy. As is observed in many of the experiments presented in this chapter, this is the first correlation that is lost when moving to low protein concentration. In contrast to the 20 : 1 sample presented in the previous

chapter, lipid resonances are observed at high lipid-to-protein ratio due to double quantum build-up between natural abundance resonances- CO to C2 correlations are observed are ~173 ppm and ~37 ppm in the SQ axis and at 208 ppm in the DQ axis, a large number of correlations are observed between 30 - 40 ppm in the SQ axis and 60 - 75 ppm in the DQ axis due to correlations between various resonances in the lipid tail. The cross-peaks at ~25 ppm and ~12 ppm in the SQ axis and 40 in the DQ axis are due to alkyl tail and the ω methyl at the end of the lipid tail. The lipid molecule resonance assignments are presented in **section 3.11**.

A low enhancement of 22 was observed for the lipid CH₂ peak in this sample. A more commonly observed enhancement of 35-50 for DNP lipid samples would result in a shorter experimental time of 10-15 h, which shows the feasibility of analysing a large number of A β – membrane samples in a limited timeframe. This would be useful for experiments where A β structure is analysed at various timepoints in the presence of membrane mimics to track structure during a dynamic process such as aggregation or fibrillation or in a clinical setting, which has been explored for A β ssNMR studies without DNP enhancement^[24].



Aβ(1-40) pre-incorporated into lipid mimics, 200 : 1 lipid : protein

Figure 5.3 POST-C7 DQSQ spectrum of Aβ(1-40) uniformly labelled at F20, A21, G31 and V36 pre-incorporated into POPC / POPS lipid vesicles at a lipid to protein ratio of 200:1. The spectrum was acquired with 64 scans in the direct dimension, 128 points in the indirect dimension and a recycle delay of 8.3 s giving an experimental time of 19 h.

DNP enhancement was observed to be 57 for the 200 : 1 sample for the lipid CH₂ peak. This allowed acquisition of the spectrum shown in figure 5.3 in ~19 h, a similar time as for acquisition of the 100 : 1 experiment. This also demonstrates that DNP enhancement has a degree of variability with an identical sample preparation protocol. This is commonly reported in DNP enhanced ssNMR studies in water / glycerol matrixes, and studies have been carried out to explain this observation^[25]. The high lipid content relative to protein in the 200 : 1 sample lead to significant natural abundance lipid contributions to the 2D spectrum, including significant t₁

noise at between 30 - 40 ppm in the SQ axis, where lipid cross-peaks due to correlations between lipid tail resonances appear. The C_{β} phenylalanine cross-peak at $C_{\alpha} + C_{\beta}$ DQ chemical shift and C_{β} SQ chemical shift are lost below the level of noise, but can be determined by subtracting the C_{α} SQ frequency from the $C_{\alpha} + C_{\beta}$ DQ frequency. All other cross-peaks that were assigned in the 100 : 1 sample were identified in the 200 : 1, using the 100 : 1 POST-C7 spectrum as a guide.

The signal-to-noise and resolution that is achievable at these lipid-to-protein ratios are shown in the 1D slices of valine in Figure 5.4.

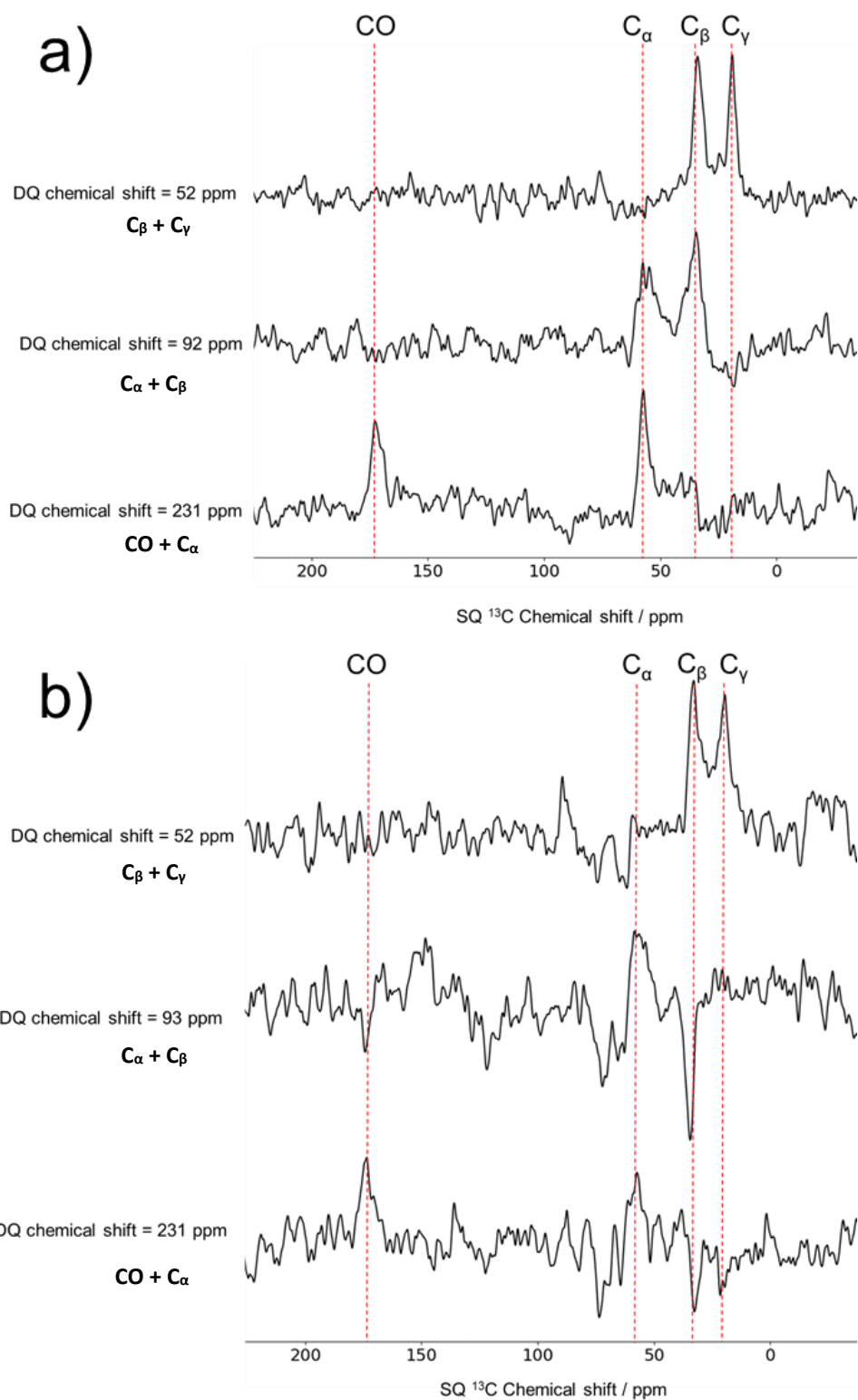


Figure 5.4 1D slices 2D DQSQ spectrum at DQ chemical shifts at which V36 intra-residue cross-peaks appear in the DQ axis. Lipid-to-protein ratio of a) 100 : 1 and b) 200 : 1.

Calculations of secondary chemical shifts are shown in Figure 5.5 for both the 100 : 1 and 200 : 1 A β (1-40) / lipid samples.

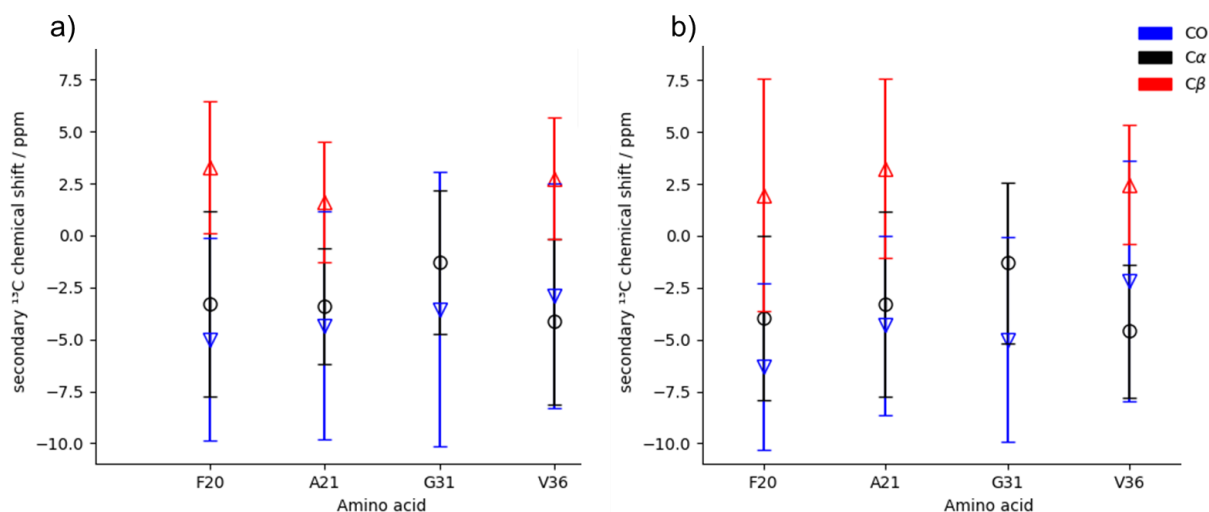


Figure 5.5 Secondary chemical shifts of F20, A21, G31 and V36 labelled positions in A β (1-40) pre-incorporated into 3 : 1 POPC / POPG lipid vesicles at a lipid-to-protein ratio of a) 100 : 1 and b) 200 : 1.

The secondary chemical shifts indicate β -sheet structure at the F20, A21, G31 and V36 labelled positions for monomer A β (1-40). This is consistent with the anti-parallel β -sheet conformation between residues 8-25 and 28-38 which is well documented at lower lipid-to-protein ratios by ssNMR^[26] and using CD^[6] and microscopy techniques^[27]. Pre-incorporating A β (1-40) at low concentration in this lipid composition does not induce a change to a different secondary structure than has been reported in similar samples at lower lipid-to-protein. The secondary chemical shifts at 200 : 1 also show β -sheet structure at the labelled position, no change from 20 : 1 and 100 : 1 protein to lipid ratios. This indicates that POPC / POPG 3:1 lipid vesicles stabilise A β (1-40) structures in a β -sheet when they are not interacting with other A β (1-40) units, which are known to stabilise a β -sheet conformation as monomers self-associate to form oligomers and eventually amyloid fibrils.

5.4. A β (1-40) associated with a complex lipid mixture

Complex lipid mixtures containing selectively added membrane components has been shown to induce differences in A β (1-40) structure. A lipid mixture consisting of 1 : 1 : 1.33 : 1 : 0.1 DMPC, POPG, cholesterol, Sphingomyelin and ganglioside GM1 was prepared by Qinghui Cheng of the Qiang lab, State University of New York, Binghamton and transported to Nottingham. A POST-C7 spectrum of 30 : 1 A β (1-40) pre-incorporated into the complex lipid mixture is shown in Figure 5.6.

A β (1-40) pre-incorporated into complex lipid mimics, 30 : 1 lipid : protein

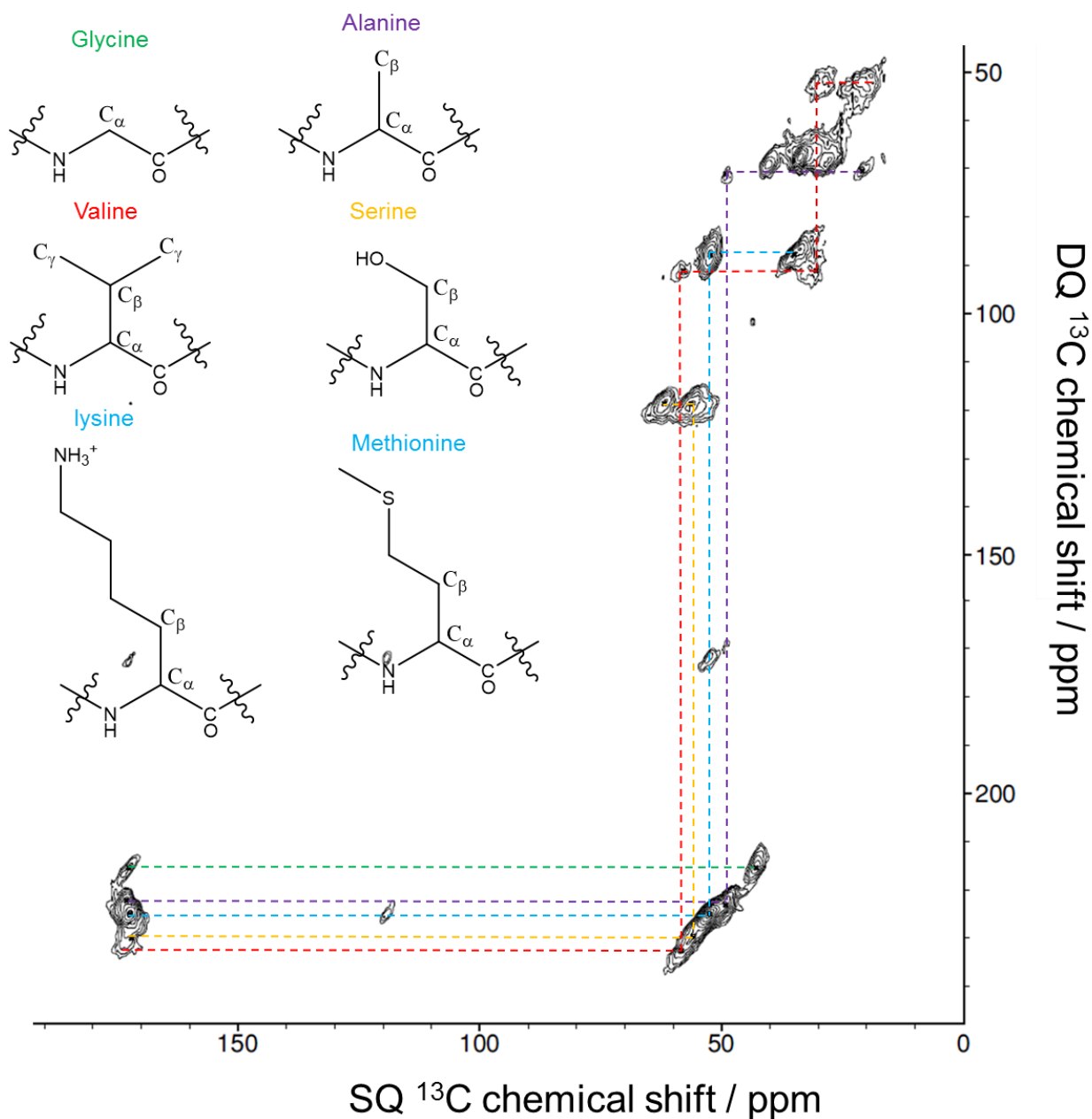


Figure 5.6 POST-C7 DQSQ spectrum of A β (1-40) uniformly labelled at G5, K16, A21, V24, S26 and M35 pre-incorporated into 1 : 1 : 1.33 : 1 : 0.1 DMPC, POPG, cholesterol, Sphingomyelin and ganglioside GM1 lipid vesicles at a lipid to protein ratio of 30:1. The spectrum was acquired with 32 scans in the direct dimension, 256 points in the indirect dimension and a recycle delay of 9 s giving an experimental time of 20 h.

The spectrum was acquired with 256 points in the indirect dimension, but the FID had fully decayed after 128 points so a spectrum with the same resolution could have been acquired in 10 h. The K16 and M35 labelled amino acids do not have a distinct set of cross peaks so are assumed to be overlapping due to the closeness

of their random coil chemical shifts, summarised in table 5.2. The 1D slices at the K16/M35 DQ chemical shifts are shown in Figure 5.7.

Amino acid	Random coil chemical shift / ppm		
	CO	C _α	C _β
K16	176.6	56.2	33.1
M35	176.3	55.4	32.9

Table 5.2 Comparison of lysine and methionine random coil chemical shifts.

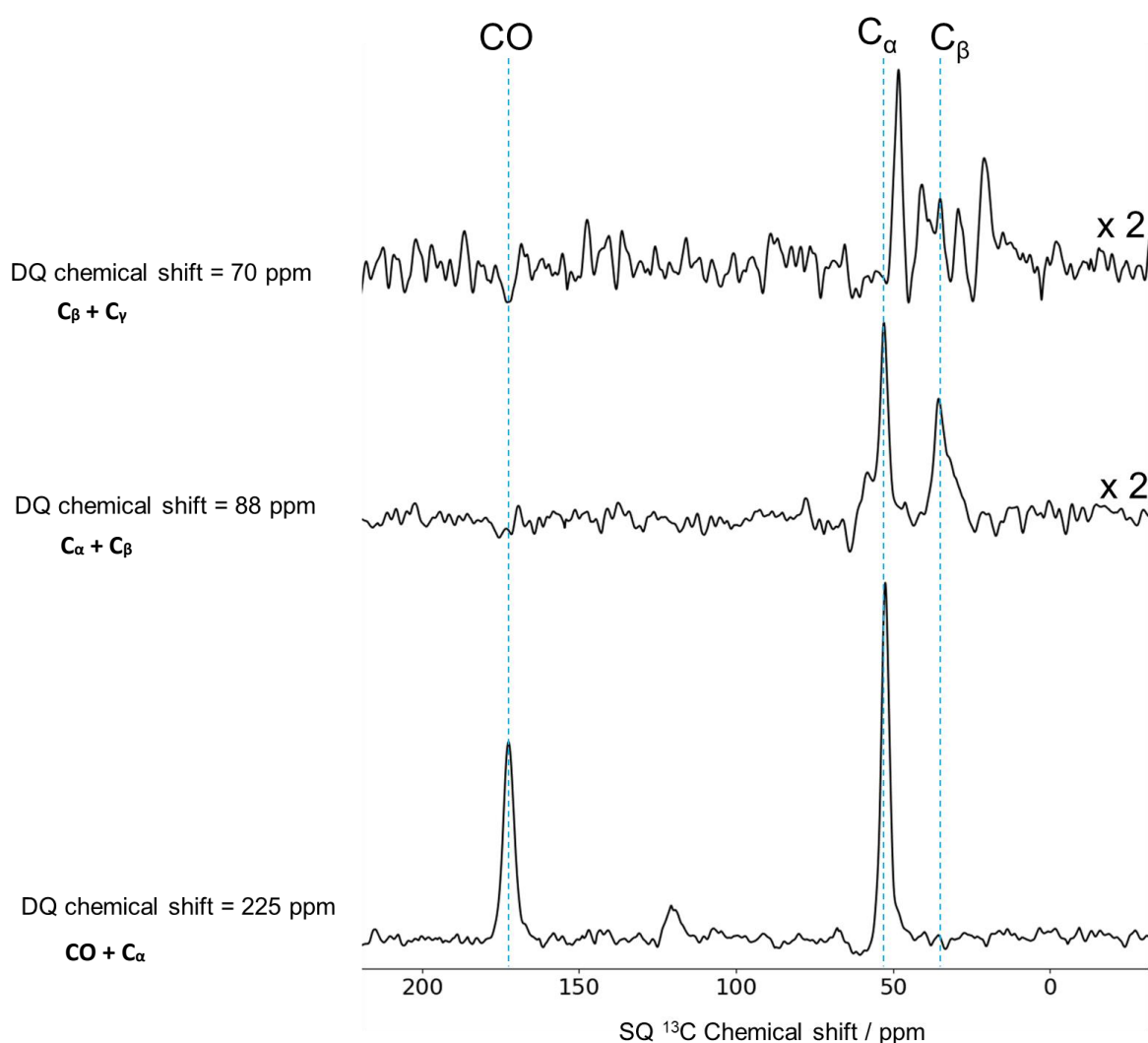


Figure 5.7 1D slices at K16/M35 DQ chemical. The resolution under DNP MAS conditions does not allow each to be distinguished.

This demonstrates the limitations of DNP enhanced ssNMR for these structural studies- six uniform labels are too many due to broad linewidths at low temperatures, causing the overlap of peaks and making assignments difficult. This

labelling scheme also shows the value in using selective labels with C_{α} and C_{β} chemical shifts that are away from the typical range of 50 – 57 ppm and 37 – 45 ppm, respectively. For example, serine C_{β} appears at ~60 ppm so the assignment pattern is clearly distinguishable. Alanine and glycine labels are often easily assigned under DNP conditions, whereas uniform labelling of a large number of alkyl and methyl R-groups makes the regions between 30 – 10 ppm in the SQ axis and 60 – 20 ppm in the DQ axis extremely cluttered. Enhancements were determined for protein and lipid positions in this sample and are discussed fully in **section 5.7**. Figure 5.8 shows F19 and L34 labelled $A\beta(1-40)$ pre-incorporated into vesicles made from the complex lipid mixture at a lipid-to-protein ratio of 150 : 1.

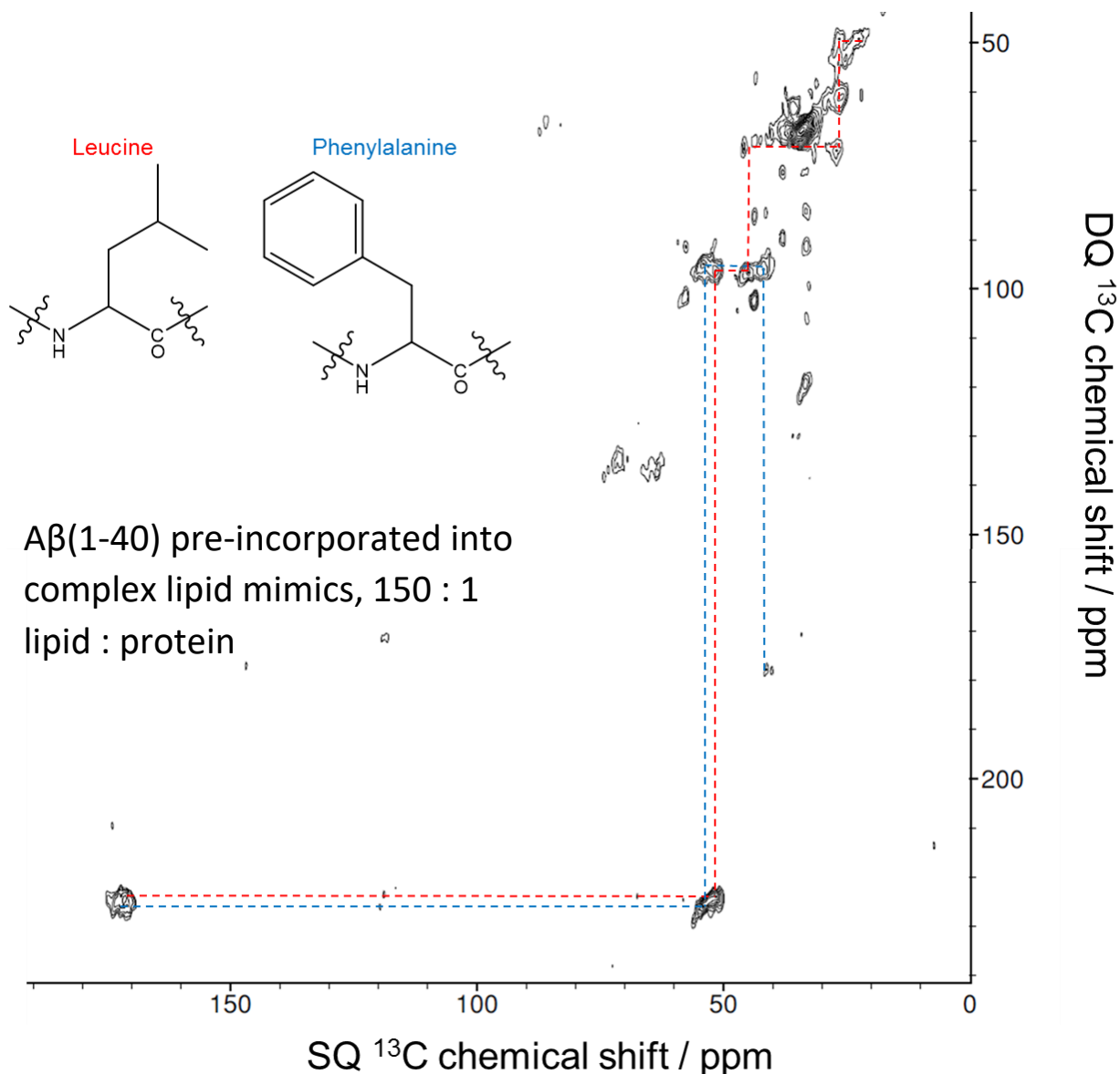


Figure 5.8 POST-C7 DQSQ spectrum of $A\beta(1-40)$ uniformly labelled at F19 and L34 pre-incorporated into 1 : 1 : 1.33 : 1 : 0.1 DMPC, POPG, cholesterol, Sphingomyelin and ganglioside GM1 lipid vesicles at a lipid-to-protein ratio of 150:1. The spectrum was acquired with 64 scans in the direct dimension, 128 points in the indirect dimension and a recycle delay of 12 s giving an experimental time of 27 h.

In both complex lipid spectra, the lipid peak at ~33 ppm in the SQ axis are larger than in previous experiments due to a greater number of resonances in this region. For the 150 : 1 spectra, all peaks were assigned, except for the F19 $C_\beta - C_\gamma$ cross peak, in an experimental time of 27 h, enhancement for the lipid tail CH_2 peak was 57. The T_1 was found to be 11.5 s, so a longer recycle delay was used resulting in a long experimental time. The secondary chemical shifts for $A\beta(1-40)$ pre-incorporated into the complex lipid mixture are plotted in Figure 5.9.

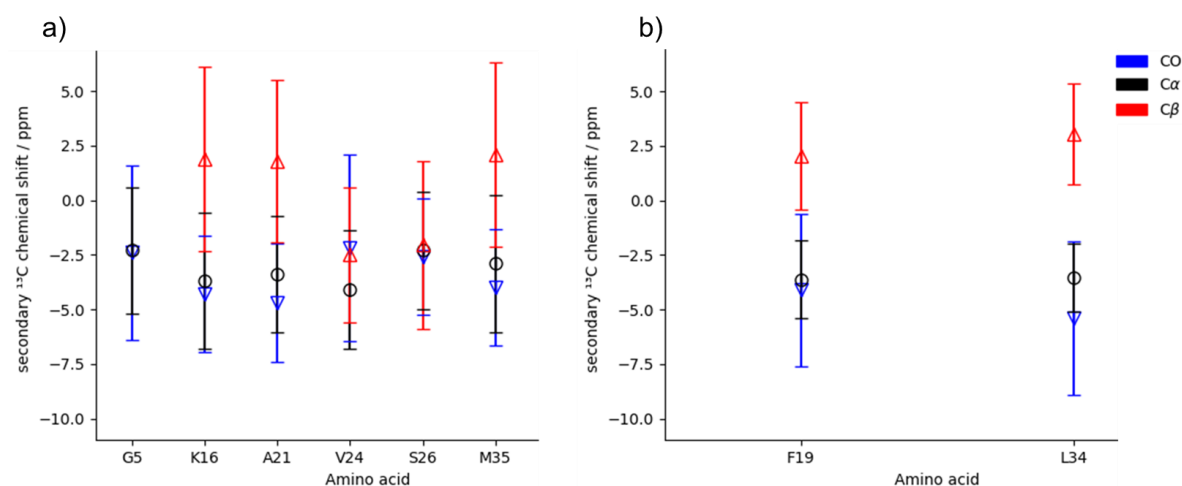


Figure 5.9 Graph showing the secondary chemical shifts of labelled in Aβ(1-40) after pre-incorporation into a complex lipid mixture. a) 30 : 1 lipid-to-protein ratio, b) 150 : 1 lipid-to-protein ratio. Error bars indicate the linewidths of peaks in the DQSQ spectrum.

The secondary shift pattern is again consistent with a β-sheet conformation in the regions containing labels. G5 occurs before the first expected β-sheet region but still show negative CO and C_α chemical shift values consistent with that secondary structure. This will be further explored in the discussion.

5.5. Aβ(1-40) associated with synaptic rat membrane

Moving towards experiments involving extracted biological membranes associated with Aβ(1-40) provides structural information with more physiological relevance than with synthetic lipid mimics. However, the complexity of a biological membrane coupled with the challenges in extracting them mean that controlled, repeatable experiments are difficult and resource consuming. Synaptic membrane was associated with Aβ(1-40) using an external addition protocol described in the **methods** section. Figure 5.10 shows 1D CP spectra with and without microwave irradiation.

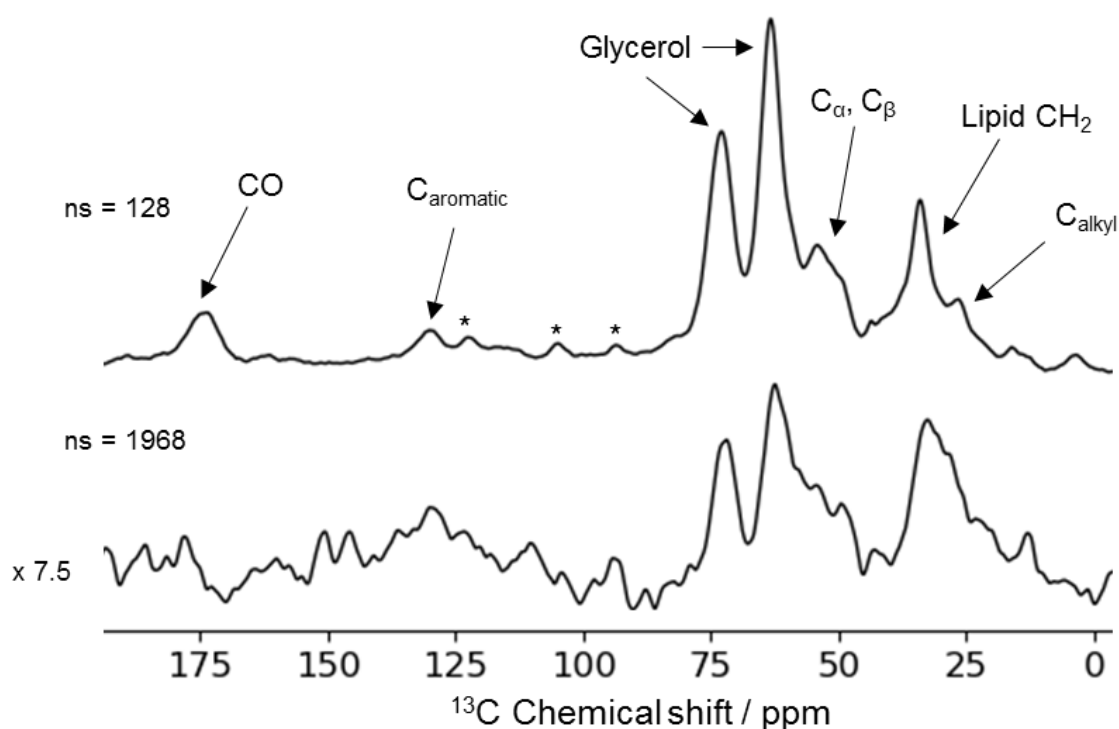


Figure 5.10 ^{13}C CP spectra of $\text{A}\beta(1-40)$ associated with synaptic rat membrane. The top spectrum was recorded with microwaves on and 128 scans, the bottom spectrum was recorded without microwaves, 1968 scans and was scaled 7.5 x for the purpose of the figure. * denotes spinning sidebands. Enhancement was found to be 87 for the lipid CH_2 peak, there was not enough signal intensity to estimate enhancement for protein positions.

Poor signal-to-noise was observed for protein and lipid signals despite a high ϵ_{DNP} of 87 for the lipid CH_2 peak. The theoretical lipid-to-protein ratio was 10 : 1, but it is unclear how much $\text{A}\beta$ binds to the rat membrane, and the total mass of the lipid pellet with bound $\text{A}\beta$ was only ~2.5 mg, which presented difficulties in packing the sample compared to in synthetic lipid samples which typically have a pellet mass of ~10 mg following centrifugation. Some sample is lost during the removal of the membrane-protein pellet from the centrifuge tube so the high protein content in the mixture means that a greater percentage is lost during the packing stage. Specially designed inserts, similar to those presented in **section 3.10**, were used to decrease the rotor volume and centre the sample in the middle of the rotor, and therefore in the middle of the NMR coil to give the maximum possible fill factor and increase signal intensity.

Figure 5.11 and 5.12 show POST-C7 and $\text{R}20_2^9$ DQSQ spectra for this sample. The 1D slices of isoleucine are presented in Figure 5.13 to demonstrate the signal-to-noise in the POST-C7 spectrum.

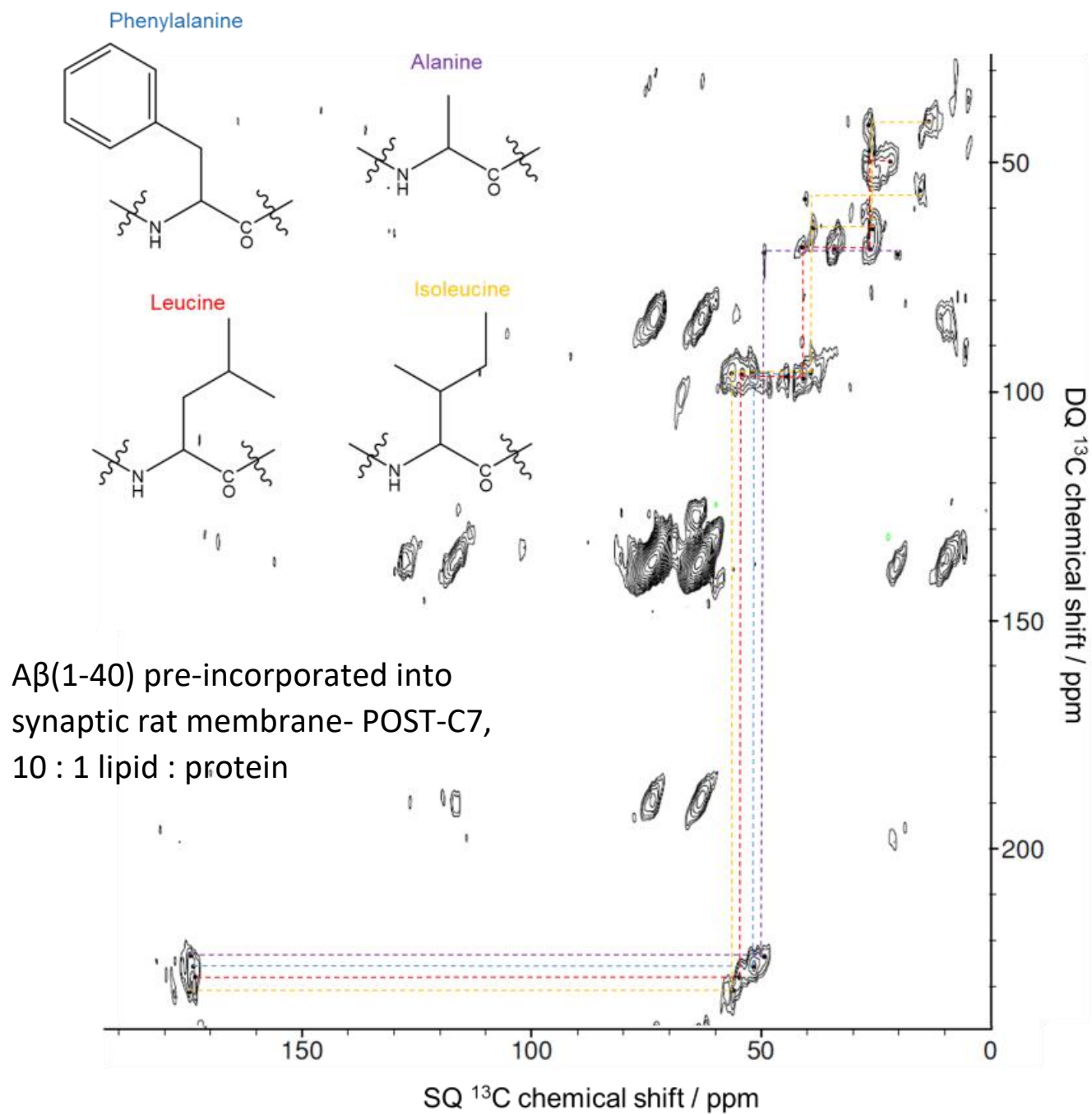
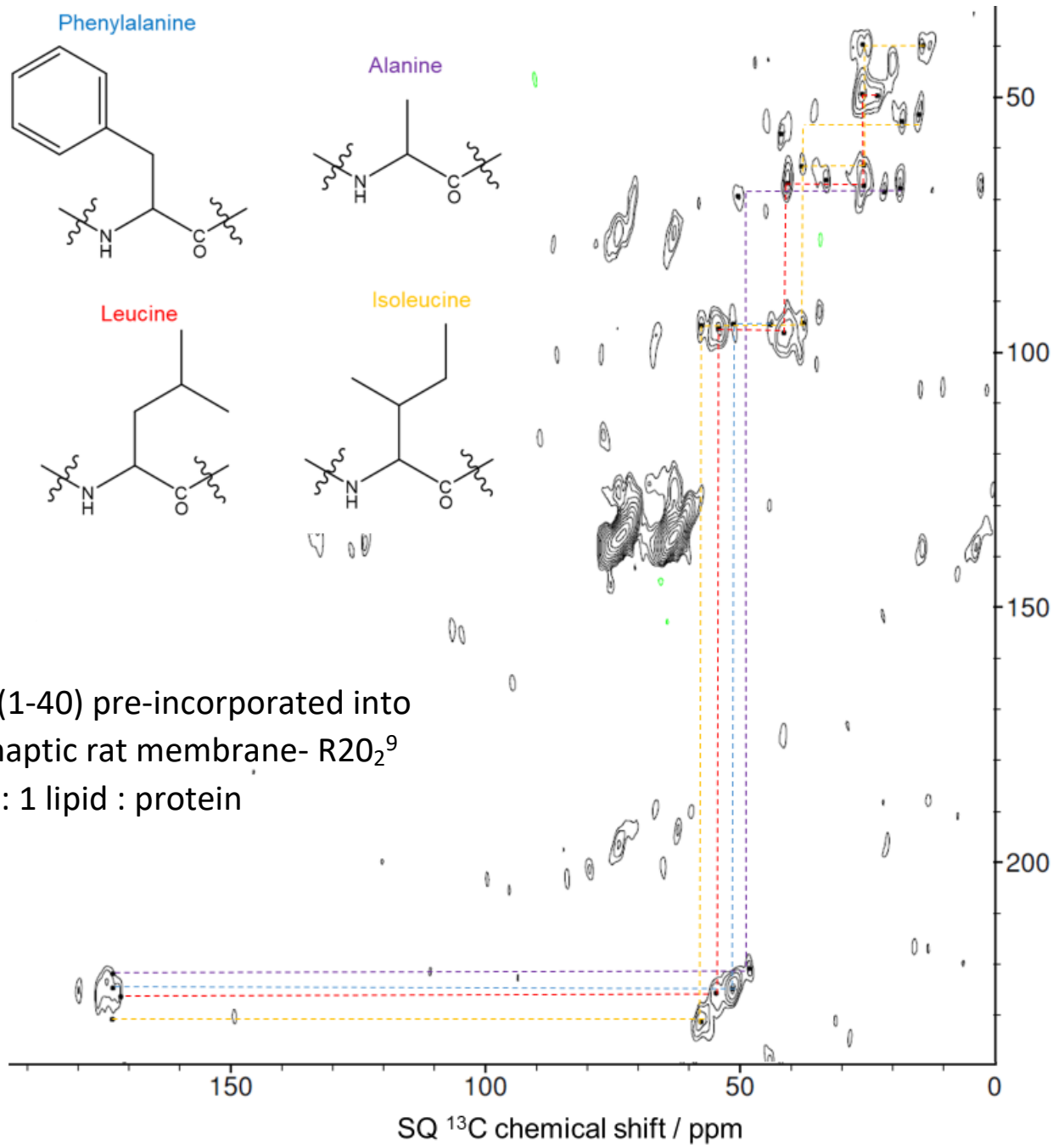


Figure 5.11 POST-C7 DQSQ spectrum of $\text{A}\beta(1-40)$ uniformly labelled at F19, A21, I32, L34 following external addition to rat synaptic membrane and 24 hrs incubation at 37 °C. The spectrum was acquired with 512 scans in the direct dimension, 64 points in the indirect dimension and a recycle delay of 6.0 s giving an experimental time of 55 h.



Aβ(1-40) pre-incorporated into synaptic rat membrane- R20₂⁹
 10 : 1 lipid : protein

Figure 5.12 R20₂⁹ DQSQ spectrum of Aβ(1-40) uniformly labelled at F19, A21, I32, L34 following external addition to rat synaptic membrane and 24 hrs incubation at 37 °C. The spectrum was acquired with 256 scans in the direct dimension, 64 points in the indirect dimension and a recycle delay of 7.0 s giving an experimental time of 32 h.

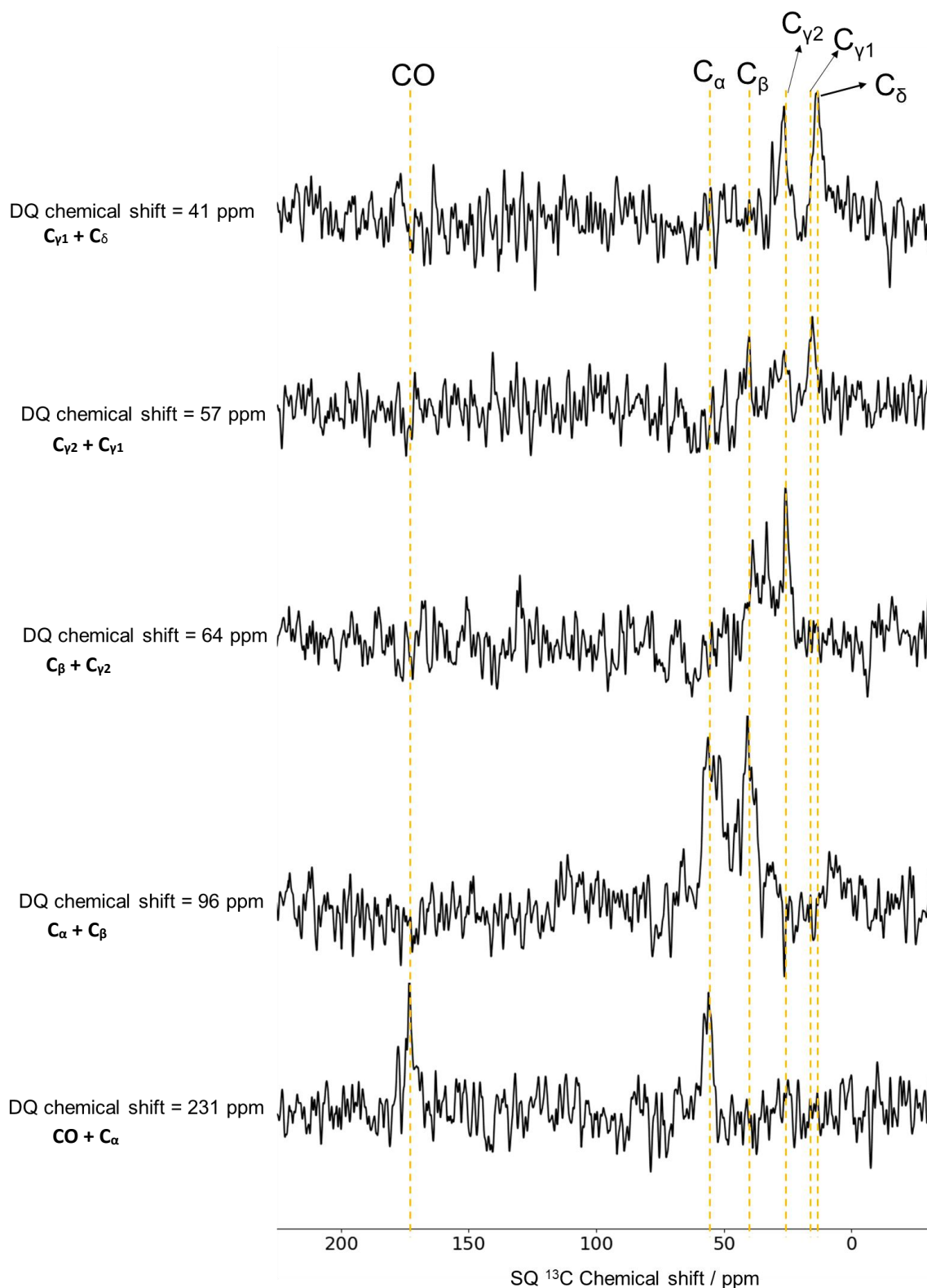


Figure 5.13 1D slices of isoleucine at DQ chemical shifts of intra-residue cross-peaks taken from the R20₂⁹ 2D experiment.

Due to the low signal intensity of protein in this sample 2D DQSQ took 55 h and 32 h for POST-C7 and R20₂⁹, respectively. R20₂⁹ was attempted to try to observe the

F19 $C_\beta - C_\gamma$ cross peak, which has low signal intensity due to the anisotropy of the aromatic group, to see if R20₂⁹ performed better in an anisotropic chemical environment. A peak was observed at SQ 41.4, DQ 174.9 ppm, which is consistent with the F19 $C_\beta - C_\gamma$, but its intensity is the same as some noise regions in the spectrum so the peak cannot be definitively identified. The protein secondary chemical shifts from this sample are displayed graphically in Figure 5.14.

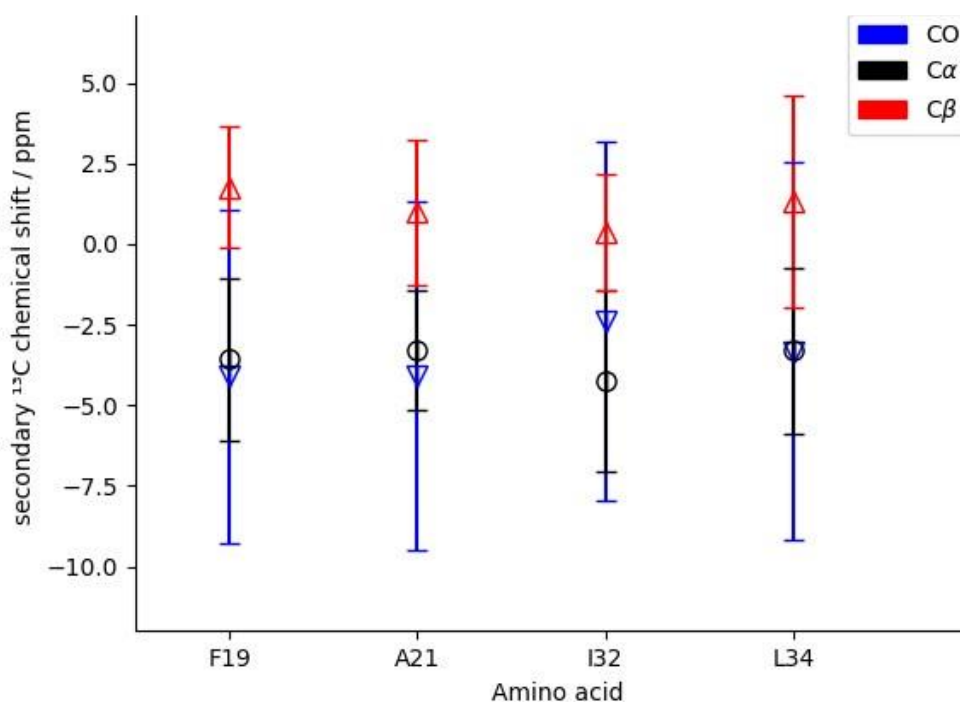


Figure 5.14 Graph showing the secondary chemical shifts of F19, A21, I32 and L34 in A β (1-40) after addition to synaptic rat membrane extracted from an 18 month old rat. Negative CO and C α values and positive C β are indicative of β -sheet structure. Error bars indicate the linewidths of peaks in the DQSQ spectrum.

5.6. External addition of A β (1-40) to lipids

Another method of studying A β (1-40) associated with lipid membrane mimics is the 'external addition' method used by the Qiang group^[23]. This involves addition of A β (1-40) to pre-formed lipid vesicles, so gives information on protein structure when the protein interacts with the lipid head region, and possibly inserts into lipid vesicles. POST-C7 spectra recorded with and without the 8 hour incubation are shown in Figure 5.15 and 5.16, secondary chemical shifts are plotted in Figure 5.17.

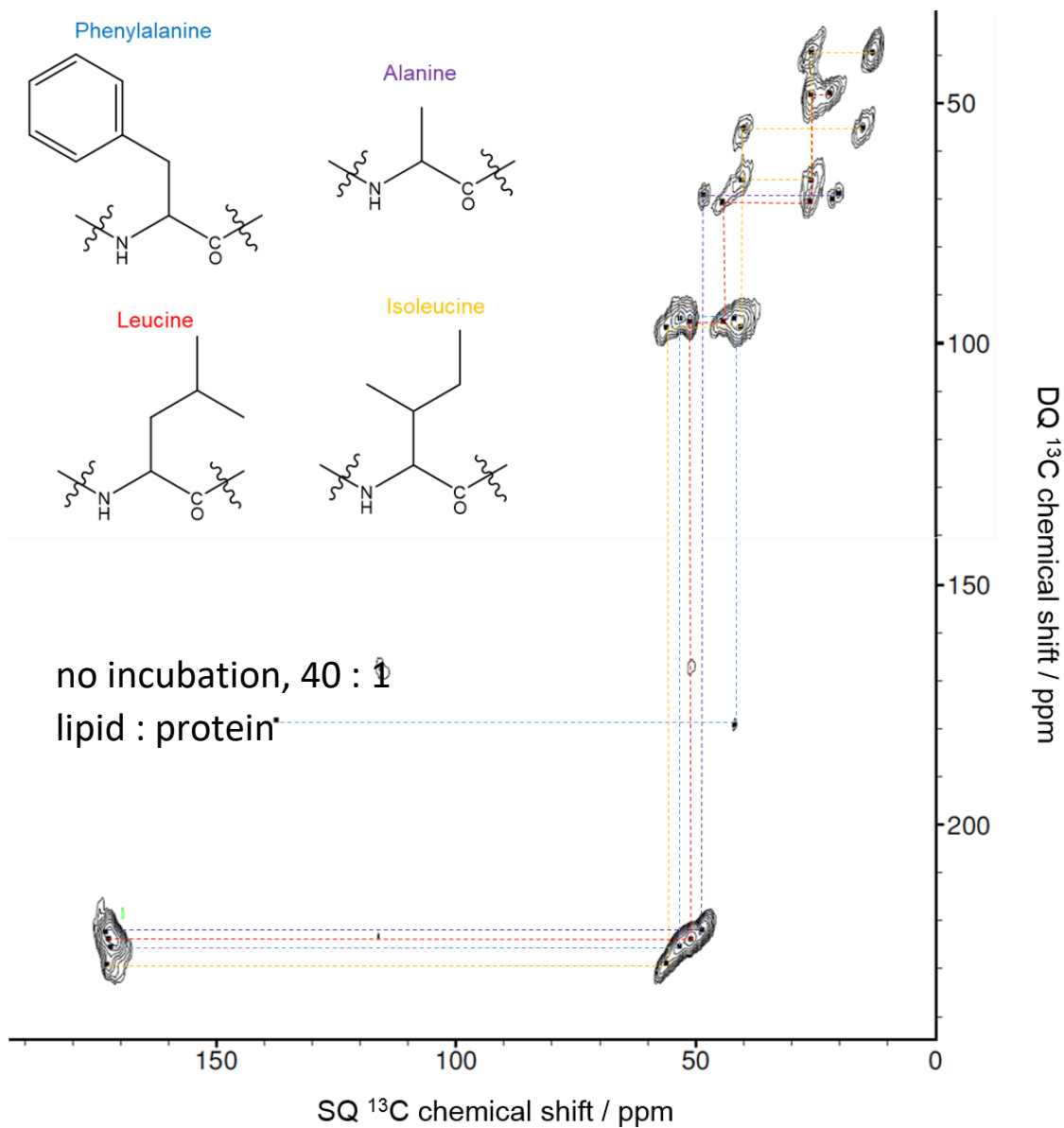


Figure 5.15 POST-C7 DQSQ spectrum of Aβ(1-40) uniformly labelled at F19, A21, I32, L34 following external addition to POPG lipid vesicles without an incubation period. The lipid to protein ratio was 40:1. The spectrum was acquired with 128 scans in the direct dimension, 141 points in the indirect dimension and a recycle delay of 4.5 s giving an experimental time of 22 h.

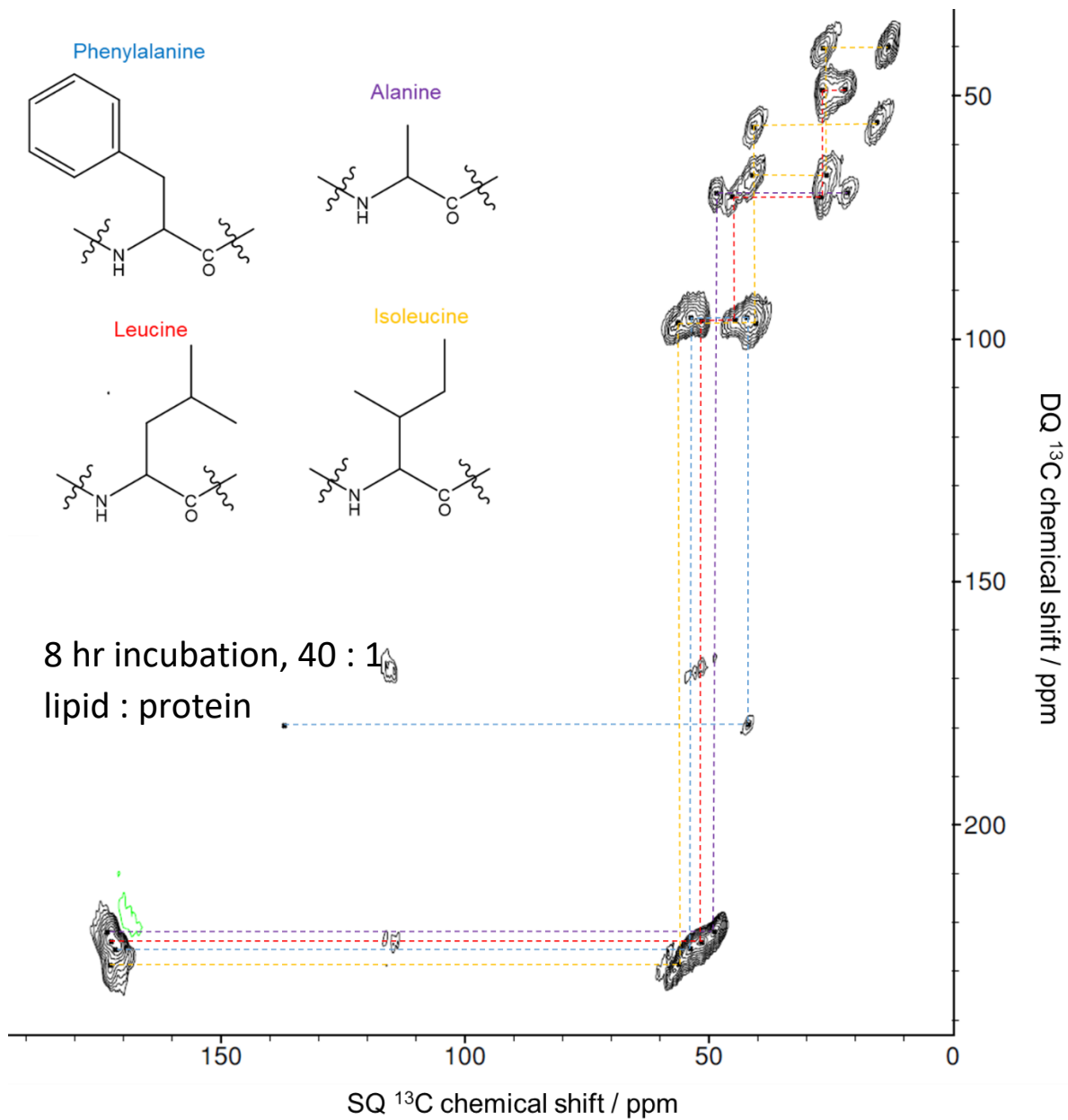


Figure 5.16 POST-C7 DQSQ spectrum of $\text{A}\beta(1-40)$ uniformly labelled at F19, A21, I32, L34 following external addition to POPG lipid vesicles and 8 hrs incubation at 37°C . The lipid to protein ratio was 40:1. The spectrum was acquired with 160 scans in the direct dimension, 120 points in the indirect dimension and a recycle delay of 3.5 s giving an experimental time of 19 h.

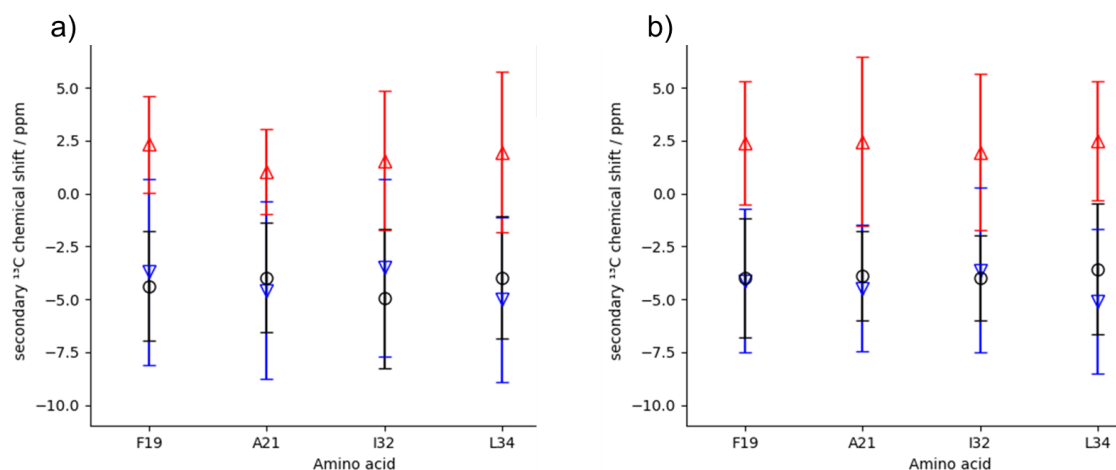


Figure 5.17 Graph showing the secondary chemical shifts of F19, A21, I32 and L34 in A β (1-40) after external addition at 40:1 lipid-to-protein ratio. a) Secondary chemical shifts without incubation following addition, b) shifts after 8 hrs incubation at 38°C. Negative C_{O} and C_{α} values and positive C_{β} are indicative of β -sheet structure. Error bars indicate the linewidths of peaks in the DQSQ spectrum.

The sample prepared directly after external addition as well as following 8 hours of incubation show characteristic β -sheet secondary chemical shifts. This demonstrates that β -sheet A β (1-40) structures are stabilised by both the outside and interior of lipid vesicles, observed in samples prepared using the external addition method and the pre-incorporation method. The lag phase to fibrillation of A β (1-40) was found to be 5-10 hours for a variety of lipid compositions at 30 : 1 L : P ratio (data not published). The aim of this set of experiments was to look for structural differences immediately after addition of A β and at the beginning of the fibrillation process. The β -sheet structure appears to be immediately stabilised by lipid vesicles after which the fibrillation process begins.

DMPG lipid vesicles (similar to POPG) have been shown to induce more α -helical character in A β (1-40) than DMPC (similar to POPC) following external addition^[6]. This was determined by membrane surface charge measurements, which showed 30 % α -helical character across the protein. α -helical structure was possibly adopted in other regions of the protein in these experiments so were not observed by NMR, or there was structural heterogeneity just after external addition which was not observed by NMR due to the relatively low percentage of expected α -helical structures.

Two distinct peaks are observed for the A21 C_{β} both without incubation and after 8 hours incubation, which are visible in the 1D slices displayed in Figure 5.18. This could be evidence of this structural heterogeneity, with one conformation adopting a β -sheet structure and a smaller population adopting a different structure.

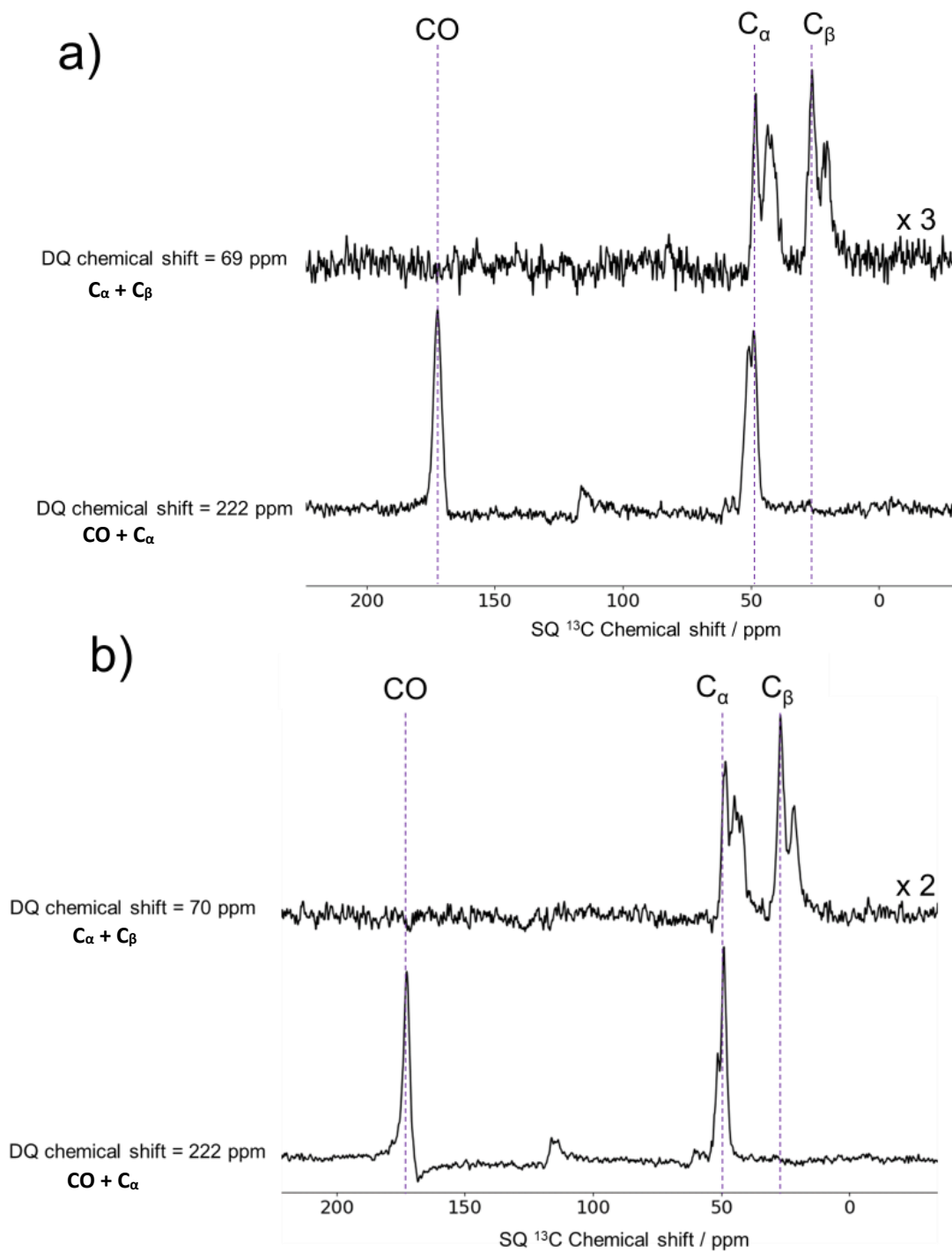


Figure 5.18 1D slices at the DQ chemical shifts where alanine appears, a) without incubation and b) after 8 hr incubation with POPG. In both cases, two distinct peaks at the DQ chemical shift corresponding to C_{α} - C_{β} correlation are observed.

Figures 5.19 and 5.20 show DARR and PDS spectra with and without 8 hours incubation of POPG with A β (1-40).

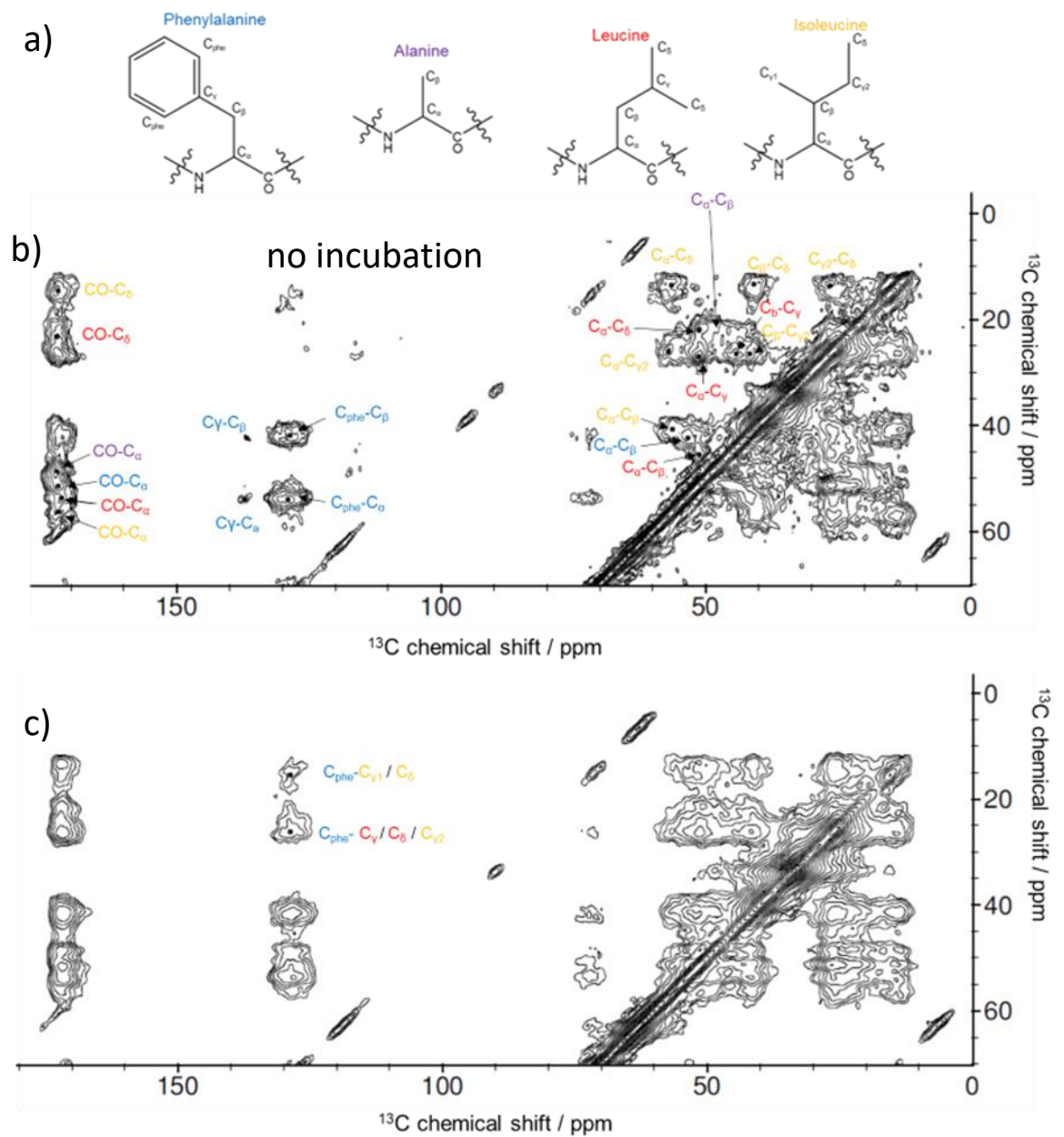


Figure 5.19 ^{13}C spin diffusion spectra on a sample of $\text{A}\beta(1-40)$ uniformly labelled at F19, A21, I32, L34 following external addition to POPG lipid vesicles and 8 hrs incubation at 38°C . The lipid to protein ratio was 40:1. a) chemical structures of labelled amino acid positions b) DARR experiment acquired with 0.25 s DARR mixing time, 16 scans in the direct dimension, 300 points in the indirect dimension, a recycle delay of 4.5 s giving an experimental time of 6 h. c) PDS experiment acquired with 2 s mixing time, 28 scans in the direct dimension, 300 points in the indirect dimension and a 4.5 s recycle delay giving an experimental time of 11 h.

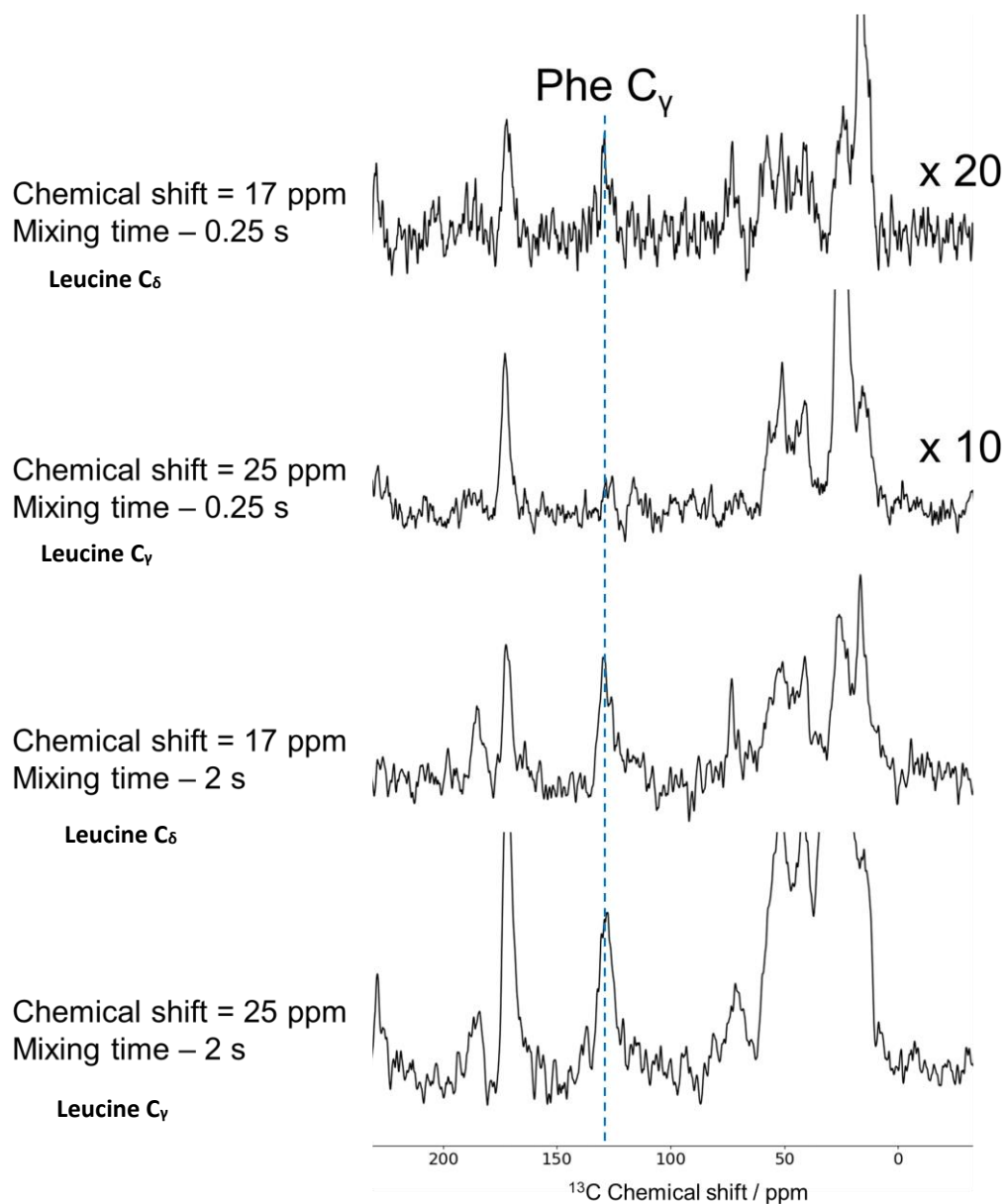


Figure 5.21 1D slices at the methyl chemical shift of I32 and L34 for the POPG + A β (1-40) sample with no incubation. Strong cross-peaks at observed with the F19 aromatic group when with 2 s PDSD mixing time.

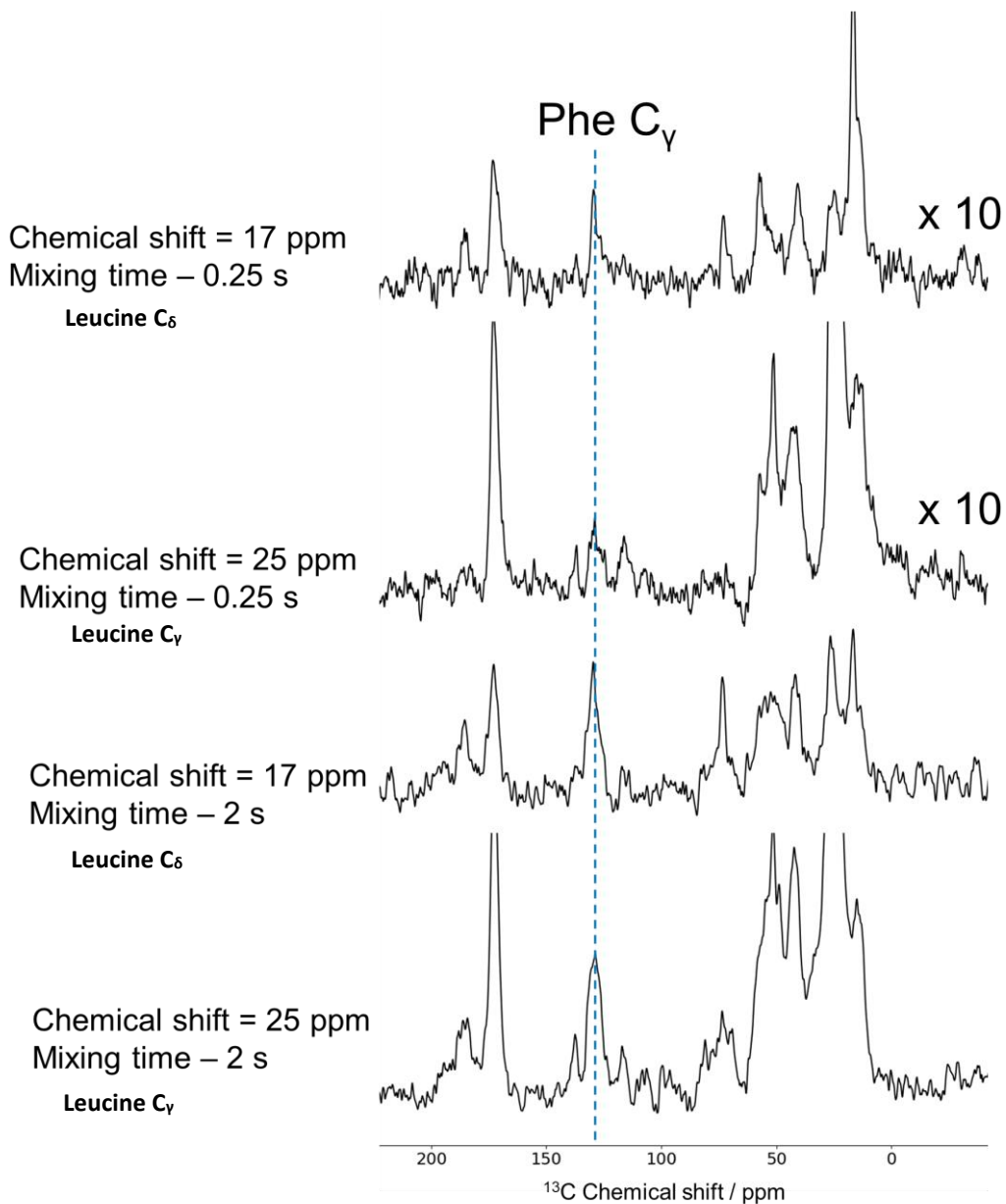


Figure 5.22 1D slices at the methyl chemical shift of I32 and L34 for the POPG + A β (1-40) sample with 8 hr incubation. Strong cross-peaks are observed with the F19 aromatic group when with 2 s PDSM mixing time.

The F19 - L34 cross peak has been previously observed in dissolved A β (1-40) fibrils under different pH conditions in DNP - enhanced ssNMR experiments^[22]. The observation that I32 also forms a cross peak with F19 is a useful additional distant constraint in determining A β (1-40) structure when associated with lipid vesicles. Both of these contacts, as well as an interaction between L17 and V36 cross-peaks have previously been observed on fibrils^[34]. There is some cross-peak intensity after 0.25 s due to magnetization exchange between I32 and L34. Figure 5.23 shows an A β (1-40) peptide chain with the labelled positions highlighted.

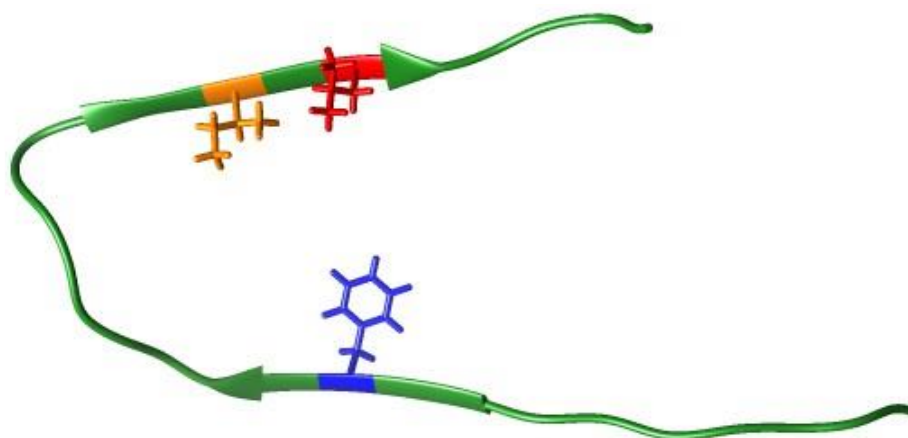


Figure 5.23 A β (1-40) peptide chain showing an antiparallel β -sheet conformation with phenylalanine, isoleucine and leucine (blue, orange and red) highlighted. PDB file 2LMQ, taken from a fibril model.

The F19 and I32 and L34 are shown to be in close proximity in this model based on the structure of A β (1-40) when they stack to form fibrils, found when they stack to form fibrils^{[28][34]}. The data presented suggests that a similar conformation is adopted in monomers prior to fibrillation, and the observation of some cross-peak intensity with 0.25 s of DARR mixing indicates that the two β -sheet regions may be closer together in space than previously thought. A β (1-40) fibrils seeded from brain extract of sufferers of AD have been shown to be very structurally homogeneous despite the polymorphism of A β fibrils^[33]. The structure form by the protein when it is stabilised in membrane is therefore an important detail, which we have demonstrated can be probed by enhancing ssNMR signals using DNP. A selective labelling scheme of the F19 aromatic region and I32 and L34 methyl group ¹³C's would be necessary to measure the exact distance between these two residues using an appropriate ¹³C-¹³C recoupling scheme^[29], as uniform labelling would result in many dipolar coupled ¹³C spins meaning that specific interactions could not be distinguished. Another option would be to use selective recoupling methods by applying RF irradiation at the frequencies of specific functional groups, for example F19 aromatic ¹³C spins and L34 alkyl ¹³C spins to investigate this interaction. Comparison of this result for A β (1-40) – membrane samples with high lipid-to-protein ratio would be interesting, but recording DARR spectra when lipid and glycerol signals are strong proved to be challenging.

5.7. Discussion

Table 5.3 summarizes observed enhancements for resolved labelled amino acid peaks in high I : P ratio samples. Different lipid vesicle compositions result in different enhancements for both the lipids and protein positions. Enhancement of protein peaks using the external addition is higher than that of the lipid CH₂ peak in contrast to the pre-incorporation method, which could be because the protein associates on the outside of the lipid vesicles in the case of external addition so are closer to the biradical in the DNP matrix. This results in less polarisation loss due to nuclear T₁ relaxation during spin diffusion than in a pre-incorporation sample were DNP polarisation must travel through ¹H nuclei in the lipids to reach the protein.

L:P ratio	Lipid composition	ε _{DNP} enhancement						
		C _O	C _α	C _β	C _{alkyl}	C _{aromatic}	Lipid CH ₂	Glycerol
20:1	3:1 POPC / POPG	40	33	33	40	40	46	-
30:1	Complex lipid (section 5.3)	24	20	20	-	-	38	34
40:1	POPG No incubation	20	20	41	20	20	20	31
40:1	POPG 8 hr incubation	32	21	35	20	24	16	-

Table 5.3 A summary of lipid and protein enhancements in low lipid-to-protein samples, in which 1D microwave-off CP experiments can be carried out without a prohibitively long experimental time.

Table 5.4 summarizes observed enhancements for resolved labelled amino acid peaks in high I : P ratio samples.

L:P ratio	Lipid composition	Lipid CH ₂	glycerol
100:1	3:1 POPC / POPG	22	19
200:1	3:1 POPC / POPG	53	54
150:1	Complex lipid (section 5.3)	57	34
10:1*	Synaptic rat membrane	87	137

Table 5.4 A summary of lipid and protein enhancements in high lipid-to-protein samples. Only the lipid CH₂ peak is analysed because 1D CP microwave-off peaks of protein positions do not have adequate signal-to-noise to measure enhancements.

The enhancement is recorded only of for the lipid CH₂ because protein peak signal-to-noise is not sufficient to record microwave-off spectra in a reasonable timeframe.

Good enhancements were achieved for all of the low protein content samples except for the 100:1 sample. The high enhancement for the synaptic rat membrane is attributed to the fact that a high fraction of the sample volume was taken up by optimised DNP matrix, which has been optimised to produce maximum DNP enhancement^[30], whereas the membrane-protein component of the sample has not.

Table 5.5 shows a comparison of secondary chemical shifts from amino acid labels that appear in several of the samples.

Lipid components	Lipid-to-protein ratio		Labelled amino acid													
			G5	K16	F19	F20	A21	V24	S26	G29	I32	L34	M35	V36	G38	
3 : 1 POPC / POPG	20 : 1	CO	-	-	-6.2	-	-	-	-	-	-	-6.2	-	-	-3.7	
		C _α	-	-	-4.0	-	-	-	-	-	-	-4.0	-	-	-2.6	
		C _β	-	-	1.1	-	-	-	-	-	-	1.1	-	-	-	
3 : 1 POPC / POPG	100 : 1	CO	-	-	-	-5.0	-4.3	-	-	-3.6	-	-	-	-2.9	-	
		C _α	-	-	-	-3.3	-3.4	-	-	-1.3	-	-	-	-4.2	-	
		C _β	-	-	-	3.3	1.6	-	-	-	-	-	-	2.8	-	
3 : 1 POPC / POPG	200 : 1	CO	-	-	-	-6.3	-4.3	-	-	-5.0	-	-	-	-2.2	-	
		C _α	-	-	-	-4.0	-3.3	-	-	-1.3	-	-	-	-4.6	-	
		C _β	-	-	-	2.0	3.3	-	-	-	-	-	-	2.5	-	
Complex lipid mixture	30 : 1	CO	-2.4	-4.3	-	-	-4.7	-2.2	-2.6	-	-	-	-4.0	-	-	
		C _α	-2.3	-3.7	-	-	-3.4	-4.1	-2.3	-	-	-	-2.9	-	-	
		C _β	-	1.9	-	-	1.8	-2.5	-2.1	-	-	-	2.1	-	-	
Complex lipid mixture	150 : 1	CO	-	-	-4.1	-	-	-	-	-	-	-5.4	-	-	-	
		C _α	-	-	-3.6	-	-	-	-	-	-	-3.5	-	-	-	-
		C _β	-	-	2.0	-	-	-	-	-	-	3.0	-	-	-	-
Synaptic rat membrane	10 : 1*	CO	-	-	-4.1	-	-4.1	-	-	-	-2.4	-3.3	-	-	-	
		C _α	-	-	-3.6	-	-3.3	-	-	-	-4.3	-3.3	-	-	-	-
		C _β	-	-	1.8	-	1.0	-	-	-	0.4	1.3	-	-	-	-
POPG no incubation	40 : 1	CO	-	-	-3.7	-	-4.6	-	-	-	-3.5	-5.2	-	-	-	
		C _α	-	-	-4.4	-	-4.0	-	-	-	-5.0	-4.0	-	-	-	-
		C _β	-	-	2.3	-	1.0	-	-	-	1.6	2.0	-	-	-	-
POPG 8 hr incubation	40 : 1	CO	-	-	-4.1	-	-4.5	-	-	-	-3.6	-5.1	-	-	-	
		C _α	-	-	-4.0	-	-3.9	-	-	-	-4.0	-3.6	-	-	-	-
		C _β	-	-	2.4	-	2.5	-	-	-	2.0	2.5	-	-	-	-
Threefold fibril [28]	na	CO	-	-3.1	-3.1	-3.5	-2.7	-0.2	-1.0	-3.3	-0.7	-4.4	-3.4	-2.0	-4.1	
		C _α	-	-1.9	-1.6	-1.7	-2.8	-2.2	-2.8	-0.4	-3.9	-0.9	-1.3	-3.1	-0.4	-
		C _β	-	2.9	2.6	3.3	3.0	1.2	1.6	-	3.6	3.4	3.5	1.7	-	-
Twofold fibril [31]	na	CO	-	-3.3	-3.9	-3.9	-3.4	-0.8	-	-0.8	-0.9	-4.9	-3.4	-2.8	-	
		C _α	-	-1.8	-0.7	-1.4	-1.6	-1.9	-	-3.8	-2.7	-1.3	-1.6	-1.7	-	-
		C _β	-	2.7	3.1	3.1	1.5	0.1	-	-	1.6	3.4	3.4	0.7	-	-
					5.7	3.6	1.6			3.1	4.1					

Table 5.5 Comparison of all A β (1-40) secondary chemical shifts recorded in a lipid environment using MAS DNP NMR.

There is a strong theme of a β -sheet conformation at all labelled positions. This is not an unexpected result- numerous ssNMR structural studies on A β (1-40) fibrils have shown the U-shaped structural feature, confirmed by the F19 – I32 / L34 cross-peaks in this work, with two anti-parallel β -sheet regions either side of it^{[28][31][32]}. We find that the pattern of secondary chemical shifts are similar to A β (1-40) fibrils with twofold-^[31] and threefold-^[28] symmetry about the fibril growth axis. In general, we observe more negative CO and C $_{\alpha}$, and smaller positive C $_{\beta}$ secondary chemical shifts. Generating a model for A β (1-40) monomers pre-incorporated in a lipid bilayer would require labelling of a maximum of 5 amino acids using DNP enhanced ssNMR due to the loss in resolution due to linebroadening at low temperatures. This would allow for a true comparison with the models provided for A β fibrils, leading to a better understanding of the early stages of the fibrillation process. This work shows that monomer structures that are not associated with other A β (1-40) units are stable in a similar secondary structure when associated with membrane mimics as in fibrils. Changing the lipid composition in ways which have been shown to alter A β (1-40) properties using non structurally specific techniques does not appear to correspond to a definitive change in A β (1-40) as observed using DNP-enhanced ssNMR.

Further DNP ssNMR studies are required on synaptic rat membrane + A β are needed to probe differences in structure in the presence of extracted lipids compared to synthetic lipids. The observation of only β -sheet chemical shifts in anionic POPG vesicles at relatively high lipid-to-protein ratio shows that negatively charged vesicles do not induce a change in secondary structure. A move to higher lipid-to-protein ratio with anionic lipids may induce a change in structure, as more α -helical character has been observed by CD which also provided evidence for structural heterogeneity across the sample or within the protein^[4].

5.8. Conclusion and outlook

The feasibility of experiments to probe A β structure when associated with membrane using DNP enhanced ssNMR has been demonstrated. 2D DQSQ correlation spectroscopy has been shown to be a good method of studying labelled proteins in samples where background signals from lipids and glycerol are abundant and under DNP conditions, where low temperature and presence of radicals results in poor resolution.

All lipid compositions and lipid-to-protein ratios tested suggest a β -sheet structure at labelled positions. This secondary structure appears to be very stable for A β (1-40), forms on addition of buffer to lyophilised protein on its own and on addition of buffer to dehydrated synthetic lipids and A β (1-40), and is not altered on addition to lipids or membrane at low protein.

Additionally, preliminary experiments involving A β (1-40) at different incubation times with lipid vesicles shows exciting possibilities for determining transient A β structures during a kinetic process such as fibrillation. This is possible because of the cryogenic nature of DNP NMR- intermediate species can be captured by flash freezing the sample at various time points followed by ssNMR structural analysis. Kinetic experiments which have been described extensively in the literature using CD, fluorescence and microscopy can be repeated using DNP-enhanced ssNMR, providing residue specific structural information rather than the overview of protein secondary structure that the other techniques provide.

The applications of DNP-enhanced ssNMR to A β – membrane systems have been demonstrated. However, complete protein structure determinations using this technique are not possible due to the broad lines at low temperatures meaning that only a limited number of labelled amino acid positions can be resolved in one sample, so multiple protein samples, each with 3 – 5 labelled amino acid positions are required. Dipolar truncation means that uniform labelling of amino acids prohibits distance measurements between remote positions, singly labelled amino acid positions would facilitate such distance measurements. For these reason, a multidisciplinary and integrative approach is required to determine fully A β structure in a membrane environment, which is a common goal of the BioNMR community^[28]. Electron microscopy (EM), including cyro – EM, is a powerful tool in structural biology. Figure 5.24 shows scanning electron microscopy images of A β (1-40) fibrils after 2 hrs incubation at 37°C with 3:1 POPC / POPG vesicles.

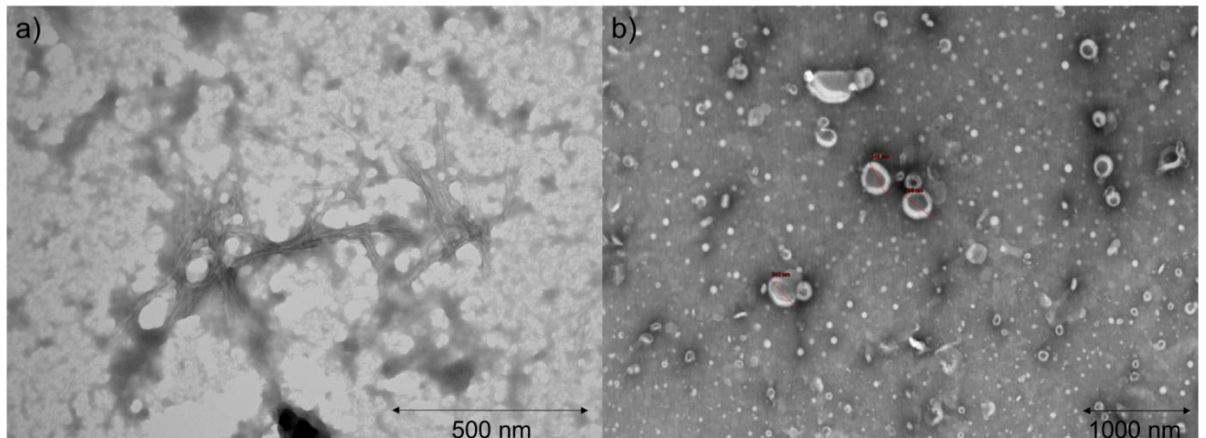


Figure 5.24 a) Tunnelling electron microscopy (TEM) image of A β (1-40) fibrils after 2 hrs incubation at 37°C in 10 mM pH 7.4 phosphate buffer. 2b) TEM image of 3:1 POPC / POPG lipid vesicles in 10 mM pH 7.4 phosphate buffer. Images were recorded by Caitlin Connolly.

Integrative, complementary studies in which results from both techniques are compared is the goal for future work, which can be done in-house, making use of the electron microscopy suite at the nanoscale and microscale research centre at the University of Nottingham

(www.nottingham.ac.uk/nmrc/facilities/emsuite/electronmicroscopysuite.aspx).

Circular dichroism (CD) is another complementary tool for A β secondary structure determination^[29] and UV detection during A β (1-40) incubation in the presence of membrane mimics will be used to determine the extent to which A β (1-40) binds to lipids^[30]. Many protein structure determination studies involving NMR also involve significant interplay between these and other techniques, including mature HIV-1 capsid structure^[31] and A β (1-42) fibril structure^[32].

5.9. References

- [1] T. L. Williams, I. J. Day, L. C. Serpell, *Langmuir*, 2010, **26**, 17260-17268
- [2] L.C. Serpell, *Biochim. Biophys. Acta*, 2000, **1502**, 16-30
- [3] J. Kang, H. G. Lemaire, A. Unterbeck, J. M. Salbaum, C. L. Masters, K. H. Grzeschik, G. Multhaup, K. Beyreuther, B. Müller-Hill, *Nature*, 1987, **325**, 733-736
- [4] P. T. Wong, J. A. Schauerte, K. C. Wisser, H. Ding, E. L. Lee, D. G. Steel, A. Gafni, *J. Mol. Biol.*, 2009, **386**, 81-96
- [5] M.-S. Lin, H.-M. Chiu, F.-J. Fan, H.-T. Tsai, S. S.-S. Wang, Y. Chang, W.-Y. Chen, *Colloids Surf. B*, 2007, **58**, 231-236
- [6] M. Bokvist, F. Lindstrom, A. Watts, G. Grobner, *J. Mol. Biol.*, 2004, **335**, 1039-1049
- [7] R. M. Epand, Y. Shai, J. P. Segrest, G.M. Anantharamaiah, *Biopolymers*, 1995, **37**, 319-338
- [8] J. Lee, Y. H. Kim, F. T. Arce, A. L. Gillman, H. Jang, B. L. Kagan, R. Nussinov, J. Yang, R. Lal, *ACS Chem. Neurosci.*, 2017, **8**, 1348–1357
- [9] D. Mrdenovic, M. Majewska, I. S. Pieta, P. Bernatowicz, R. Nowakowski, W. Kutner, J. Lipkowski, P. Pieta, *Langmuir*, 2019, **35**, 11940–11949
- [10] D. C. Bode, M. D. Baker, J. H. Viles, *J. Biol. Chem.*, 2017, **292**, 1404 –1413
- [11] A. Quist, I. Doudevski, H. Lin, R. Azimova, D. Ng, B. Frangione, B. Kagan, J. Ghiso, R. Lal, *Proc. Natl. Acad. Sci. U.S.A.*, 2005, **102**, 10427-10432
- [12] R. Lal, H. Lin, A. P. Quist, *Biochim. Biophys. Acta.*, 2007, **1768**, 1966–1975 - review
- [13] R. Capone, H. Jang, S. A. Kotler, L. Connelly, F. T. Arce, S. Ramachandran, B. L. Kagan, R. Nussinov, R. Lal, *J. Chem. Theory Comput.*, 2012, **8**, 1143–1152
- [14] O. Crescenzi, S. Tomaselli, R. Guerrini, S. Salvadori, A. M. D'Ursi, P. A. Temussi, D. Picone, *Eur. J. Biochem.*, 2002, **269**, 5642–5648
- [15] H. Shao, S. Jao, K. Ma, M. G. Zagorski, *J. Mol. Biol.*, 1999, **285**, 755–773
- [16] D. A. Delgado, K. Doherty, Q. Cheng, H. Kim, D. Xu, H. Dong, C. Grewer, W. Qiang, *J. Biol. Chem.*, 2016, **291**, 12233–12244

- [17] W. Qiang, J. Yang, D. P. Weliky, *Biochemistry.*, 2007, **46**, 4997–5008
- [18] R. D. Akinlolu, M. Nam, W. Qiang, *Biochemistry*, 2015, **54**, 3416–3419
- [19] Q. Cheng, Z.-W. Hu, K.E. Doherty, Y.J. Tobin-Miyaji, W. Qiang, *Biochim. Biophys. Acta - Biomembr.*, 2018, **1860**, 1670–1680
- [20] J.D. Gehman, C.C. O'Brien, F. Shabanpoor, J.D. Wade, F. Separovic, *Eur. Biophys. J.*, 2008, **37**, 333–344
- [21] M. L. Mak-Jurkauskas, V. S. Bajaj, M. K. Hornstein, M. Belenky, Robert G. Griffin, J. Herzfeld, *Proc. Natl. Acad. Sci. U.S.A.*, 2008, **105**, 883-888
- [22] A. Potapov, W.-M. Yau, R. Ghirlando, K. R. Thurber, R. Tycko, *J. Am. Chem. Soc.*, 2015, **137**, 25, 8294–8307
- [23] W. Qiang, K. E. Doherty, *Methods Mol. Biol.*, 2018, **1777**, 355–367
- [24] W. Qiang, W.-M. Yau, J.-X. Lu, J. Collinge, R. Tycko, *Nature*, 2017, **541**, 217–221
- [25] A. Leavesley, C. B. Wilson, M. Sherwin, S. Han, *Phys. Chem. Chem. Phys.*, 2018, **20**, 9897
- [26] W. Qiang, R. D. Akinlolu, M. Nam, N. Shu, *Biochemistry*, 2014, **53**, 7503-7514
- [27] H. Lin, R. Bhatia, R. Lal, *FASEB J.*, 2001, **15**, 2433–2444
- [28] A. K. Paravastu, R. D. Leapman, W.-M. Yau, R. Tycko, *Proc. Natl. Acad. Sci. U.S.A.*, 2008, **105**, 18349-18354
- [29] V. S. Mithu, S. Bakthavatsalam, P. K. Madhu, *PLoS ONE*, 2013, **8**, 1-10
- [30] G. J. Gerfen, L. R. Becerra, D. A. Hall, R. G. Griffin, R. J. Temkin, and D. J. Singel, *J. Chem. Phys.*, 1995, **102**, 9494-9497
- [31] A. T. Petkova, Y. Ishii, J. J. Balbach, O. N. Antzutkin, R. D. Leapman, F. Delaglio, R. Tycko, *Proc. Natl. Acad. Sci. U.S.A.*, 2008, **99**, 16742–16747
- [32] I. Bertini, L. Gonnelli, C. Luchinat, J. Mao, A. Nesi, A New Structural Model of A β 40 Fibrils, *J. Am. Chem. Soc.*, 2011, **133**, 16013–160
- [33] J. X. Lu, W. Qiang, W. M. Yau, C. D. Schwieters, S. C. Meredith, R. Tycko, *Cell*, 2013, **154**, 1257-1268
- [34] A. T. Petkova, W.-M. Yau, R. Tycko, *Biochemistry*, 2006, **45**, 498-512

[35] A. T. Petkova, R. D. Leapman, Z. H. Guo, W.-M. Yau, M. P. Mattson, R. Tycko, *Science*, 2005, **307**, 262-265

[36] K. J. Korshavn, A. Bhunia, M. H. Lim, A. Ramamoorthy, *Chem. Commun.*, 2016, **52**, 882–885

6.	Enhancing ^{19}F NMR signals using d-DNP for lysozyme folding studies.	142
6.1.	Introduction	142
6.2.	The Nottingham dual-isocentre magnet.....	144
6.3.	Fluorine labelling of lysozyme.....	148
6.4.	Materials.....	153
6.5.	Optimising instrument conditions.....	155
6.6.	Optimization of d-DNP on small fluorinated molecules	159
6.7.	Dissolution-DNP with ^{19}F labelled lysozyme d-DNP	160
6.8.	^{19}F lysozyme under denaturing conditions.....	163
6.9.	Discussion	167
6.10.	Conclusion and outlook	168
6.11.	References.....	169

6. Enhancing ^{19}F NMR signals using d-DNP for lysozyme folding studies

6.1. Introduction

Liquid-state NMR studies of proteins also suffer from low sensitivity already described for ssNMR in previous chapters. This means that obtaining sufficient signal-to-noise requires hours of signal averaging, which is not possible for many kinetic processes taking place on a faster timescale. Dissolution-DNP (d-DNP) is a method that helps in such kinetic studies, by boosting NMR signal in the liquid state by up to 5 orders of magnitude by using DNP at cryogenic sample temperatures, followed by rapid melting with a hot solvent and NMR acquisition at ambient temperature^[1]. Several applications of d-DNP have been demonstrated, including protein kinetics studies.

A promising method is currently being investigated by the groups of Frydman, Kurtzbaach and Hilty^[2]. The technique involves hyperpolarizing water, followed by d-DNP and mixing with buffered solution containing the protein of interest. The protein signals can get enhanced indirectly via cross-relaxation processes (NOEs) and chemical exchange with water molecules.

Frydman and co-workers have used this technique to collect enhanced 2D HMQC spectra of intrinsically disordered proteins (IDPs), making use of facile exchange of amide and amino acid side chain protons with hyperpolarized water. The d-DNP experimental set-up is capable of transferring the dissolved material from the polariser to 11.7 T magnet in 1 - 3 s. Under optimal conditions (1:1 v / v ratio of water / d_6 -DMSO and 25 mM TEMPO radical), a factor of ~3200 enhancement compared to thermal signals was achieved for ^1H in water. Upon transfer to the amino acid amides the enhancements drops to ~300 as measured in small model polypeptides, and to a factor of ~100 in the IDP α -synuclein.^{[3][4]} Differences in exchange rates due to differences in water accessibilities produces different polarization at different residue with some residues not enhanced at all^[5].

Kurtzbaach and co-workers have developed an analogous method for studying proteins by d-DNP using hyperpolarised water, and applied it to osteopontin, where similarly the polarization of individual residues varied due to chemical exchange rate and promiximity to hyperpolarised water^[6]. Dissolution DNP was then used to study structural adaptations of osteopontin upon herapin, an anticoagulant, using SOFAST

HMQC^[7]. This shows a unique advantage of d-DNP enhanced NMR compared to conventional NMR, as it enables to probe the dynamic events taking place on a short time scales. The group has also applied the method to a folded protein, ubiquitin, under physiological conditions^[8].

In all these works, the DNP-produced high polarization of the solvent is transferred to the protein. These methods rely on ultrafast 2D sequences^[9] requiring a sufficiently long magnetization lifetime, which is not possible for nuclear spins with fast relaxation times. Alternatively, one may apply only 1D techniques, such as done by Hilty and coworkers^[10]. By recording a number of 1D spectra in quick succession following dissolution, the ¹³C signals of labelled methyl isoleucine residues in ribosomal protein L23 upon refolding. However, the chemical shift resolution in such experiments is limited, producing spectra with a large number of overlapping resonances which are not easy to interpret^[10].

This chapter explores the feasibility of d-DNP-enhanced 1D NMR of ¹⁹F-labelled protein studies using lysozyme refolding as a model. Using ¹⁹F labels provides a number of advantages compared to studies with ¹³C labels^[10]. The chemical shifts of ¹⁹F nuclear spins are highly sensitive to local electronic environment so that changes in molecular structure are easily detected. In addition, ¹⁹F has a high gyromagnetic ratio (94 % of ¹H), and its 100% natural abundance leads to a better sensitivity compared to commonly used ¹³C and ¹⁵N and labels. Finally, ¹⁹F does not naturally occur in proteins and the vast majority of other biomolecules, so spectra of ¹⁹F-labelled proteins are free of background signals. Because of these favourable properties ¹⁹F NMR has already been widely used for conventional liquid-state NMR^{[11][12]}, but d-DNP-enhanced NMR of ¹⁹F has previously been applied only to studies of hyperpolarized ¹⁹F reporter ligands^[13]. Lysozyme is selected as a model because of a wealth of data on lysozyme folding^[14]. In addition, this protein is inexpensive and is commercially available in substantial amounts, which is important in the process of the technique development.

6.2. The Nottingham dual-isocentre magnet

For most d-DNP studies reported in the literature, experiments are carried out using commercial DNP machines, such as the Oxford instruments HyperSense or GE SPINlab, with pneumatic or manual transfer of the dissolved material from a separated polarization magnet to the acquisition magnet. Signal loss results from a relaxation taking place in the low magnetic field while the sample is transferred between the polarization magnet and the measurement magnet.

The University of Nottingham has a unique dual-isocentre magnet system for performing d-DNP experiments. This system reduces the transfer time by bringing the polarization magnet and acquisition magnet as close as possible to one another. This is achieved by housing both the polarization and acquisition magnets in the same container^[15]. Figure 6.1a shows both isocentres as well as the quasi-optic bench for microwave delivery to the sample. The DNP polarization is carried out in the top magnet at the magnetic field of ~3.4 T, whereas signal acquisition after the dissolution is done in the bottom magnet at the magnetic field of ~9.4 T.

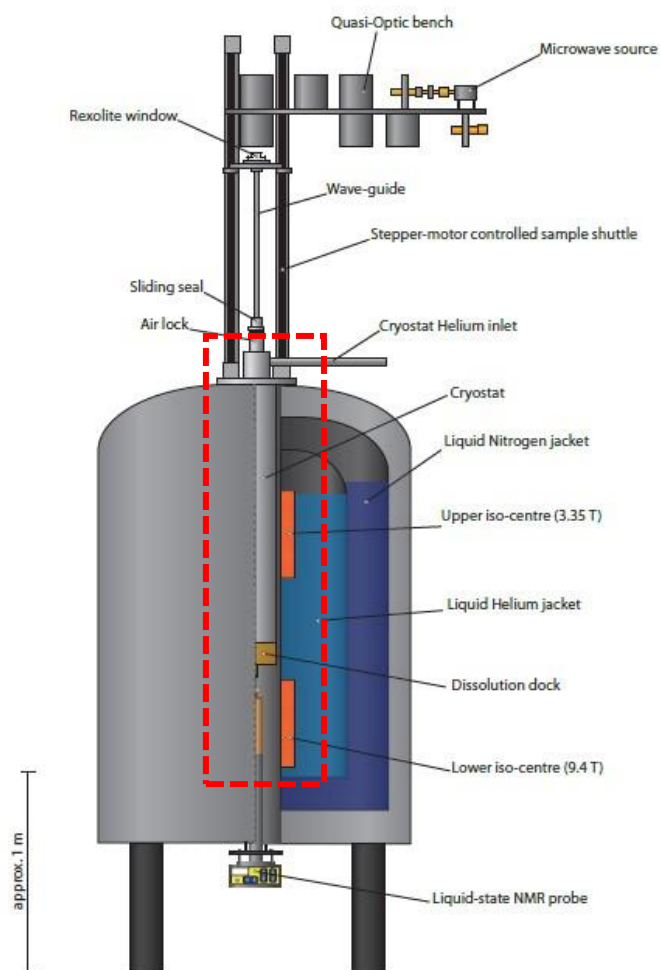
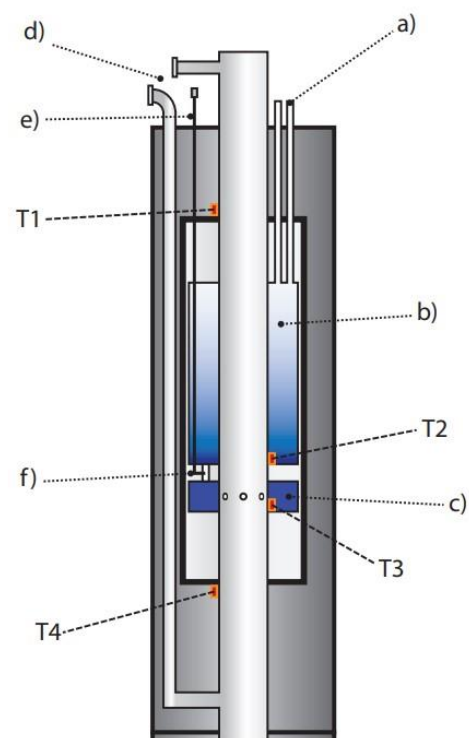
(a)**(b)**

Figure 6.1a) Dual-isocentre system. Microwaves transmitted by 400 mW power source at 95 GHz are directed to the sample in the upper magnet by the quasi-optic bench and a vertical waveguide. The sample is positioned at the end of a waveguide and is mechanically shuttled to the lower 9.4 T acquisition magnet in 700 ms. b) Schematic diagram of the variable temperature insert (VTI), highlighted using red dashed rectangle in (a). VTI is used for cooling the sample to ~ 1.8 K before polarising with MW. Liquid helium is inserted from an external dewar using a siphon inserted at opening labelled a), which fills the '4 K' pot, b). A needle valve (f), controlled from the top of the system (e) regulates helium flow into the '1 K' pot (c). Small holes in the bore allow helium gas flow into the sample space, which is kept at low pressure by vacuum pumps connected to top and bottom of the bore (d). Ceramic temperature sensors, T1, T2, T3 and T4 monitor the temperature at different parts of the system. Figures produced by Ben McGeorge-Henderson.

The relatively short distance of 80 cm between the top 3.4 T magnet and the bottom 9.4 T magnet centres allows fast shuttling of the sample from the region with

cryogenic temperature, where polarization is carried out, to the dissolution dock, where the sample is dissolved to produce a solution at ambient temperature suitable for a conventional NMR experiment. The sample is placed in a sample cup attached to the end of the waveguide which can be mechanically shuttled up and down the bore using a stepper-motor. The quasi-optic bench directs microwaves through a rexolite window at the top, along the waveguide down to the sample space. The microwave source is solid-state system providing 400 mW power output in a frequency range of 93.75 GHz to 94.25 GHz (ELVA-1 - St. Petersburg, Russia).

Figure 6.1b shows the variable temperature insert, capable of maintaining temperature of ~ 1.8 K in the sample space. During an experiment, the sample is inserted into the centre of the top 3.4 T magnet when the temperature reaches ~ 100 K recorded using the "T2" temperature sensor. This is achieved by filling the 4 K pot "b)" with liquid helium. The needle valve "f)" is fully opened when the "T2" sensor gets to ~ 20 K to start filling the 1 K pot "c)". When the "T3" sensor reaches ~ 4 K, the strength of the vacuum is increased by an additional vacuum pump attached to the top of the bore. The needle valve "f)" opening is reduced so that only a slight flow of helium occurs into the bore, which is maintained at low pressure by the vacuum pumps. These conditions result in Joule-Thompson expansion of the helium, cooling the sample space to the temperature of ~ 1.8 K.

After polarization is complete, the stepper-motor is used to shuttle the waveguide from the centre of the 3.4 T magnet to just above the centre of the 9.4 T acquisition magnet, and to dock the sample into the dissolution dock, which is a part of a hot solvent delivery system shown in Figure 6.2a. Solvent is pressurised using an N_2 gas cylinder, forcing it into the inside of a co-axial heating tube. The outer layer of the co-axial tube contain oil at 100°C , which heats solvent in the inside tube. The pneumatically driven 'dock' valve (Takasago Electric, Inc.) shortly followed by the 'line' valve are automatically triggered after the waveguide shuttles into the 'dock'. This results in pressurised hot solvent moving to the sample space, melting and dissolving the sample, then being drawn along the pressure gradient into the NMR probe.

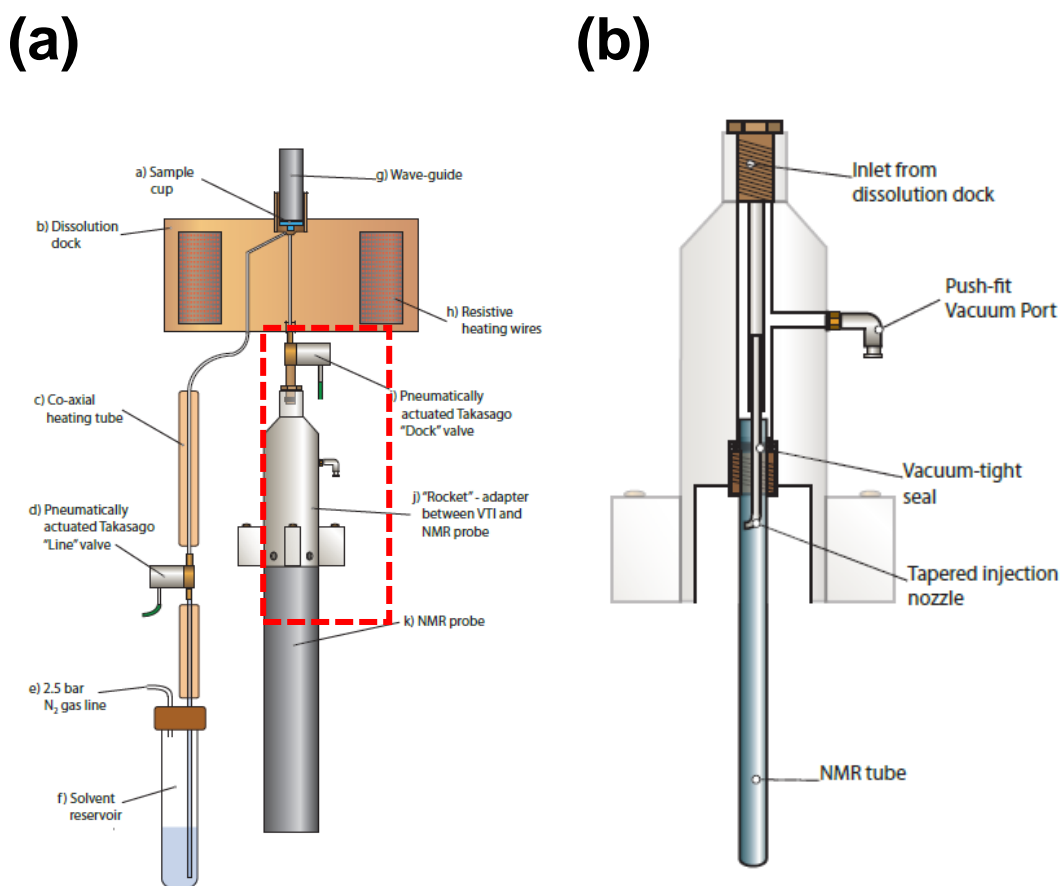


Figure 6.2a) Hot solvent delivery system. Pressurised solvent, heated by oil in a co-axial tube, is directed to the sample cavity following automatically activated 'line' and 'dock' pneumatically driven valves. The sample is drawn into an NMR tube at low pressure in the bottom magnet and, after a brief settling time, an NMR signal is acquired. Red dashed rectangle shows the adaptor for transferring the sample. b) Adaptor for transferring a dissolved sample into a sample tube sitting in the NMR probe. The inlet at the top fits tightly into bottom of the 'dock' valve so that no sample is lost due to spillage. A tapered injection nozzle is included so that the solvent flows down the side of the NMR tube to reduce air bubbles. The dissolved sample is drawn into a tube maintained at low pressure. Figures produced by Ben McGeorge-Henderson.

Figure 6.2b shows the design of the adapter used for the delivery of the dissolution sample to the NMR tube. A small vacuum pump is attached to push-fit vacuum pump to create low pressure in the NMR tube. The glass tube that introduces the dissolution mixture into the NMR tube is tapered such that the solvent flows down the edge of the NMR tube to reduce bubble formation. Due to the differences in the magnetic susceptibility of air and solvent the air bubbles formed right after the dissolution produce magnetic field inhomogeneities around them, leading to poor resolution^[16].

¹⁹F NMR signals were acquired using a ¹H, ¹³C Bruker solution NMR probe with standard 7 inch Bruker NMR tubes. The ¹H channel of the probe was tuned to ¹⁹F

frequency, however since this frequency is rather far off the optimal conditions for this probe, it was not possible to achieve good matching leading to some signal loss. Due to the limitations on the dissolution sample cup size, the measurements of NMR signals in the upper magnet at 3.4 T cannot be carried out right prior the dissolution. For that reason, the DNP build-up times and solid-state DNP enhancements were measured in a separate experiment, where the sample cup is modified with an additional saddle coil. The steps involved in a d-DNP experiment carried out using the dual-isocentre system are detailed in Appendix 2.

Some of the work presented in this chapter was carried out in collaboration with Antonio Gennaro, as the dual-isocentre DNP system requires a minimum of two people to be operated. The small molecule optimisation for ^{19}F d-DNP and the initial ^{19}F lysozyme d-DNP presented in this chapter were also presented in his thesis^[17].

6.3. Fluorine labelling of lysozyme

Lysozyme follows the procedure previously reported in ref.^[18]. The protein lysines are chemically modified with $-\text{COCF}_3$ groups as schematically shown in Figure 6.3a.

Hen white lysozyme and other reagents (Sigma-Aldrich) were used without additional purification. S-Ethyltrifluoroacetate (0.62 mmol, 98.8 mg) was added to lysozyme (60 mg, 4.20×10^{-3} mmol) dissolved in 8 ml water. A magnetic stir bar was used to mix the reactants. pH was maintained at 9.5-10 by dropwise addition of 1 M NaOH for 2 h, until base consumption ceased, which took ~2 h. The reaction was brought to pH 7 by addition of 0.1 M HCL, dialyzed against water and centrifuged for 1 h at 26,000 rpm.

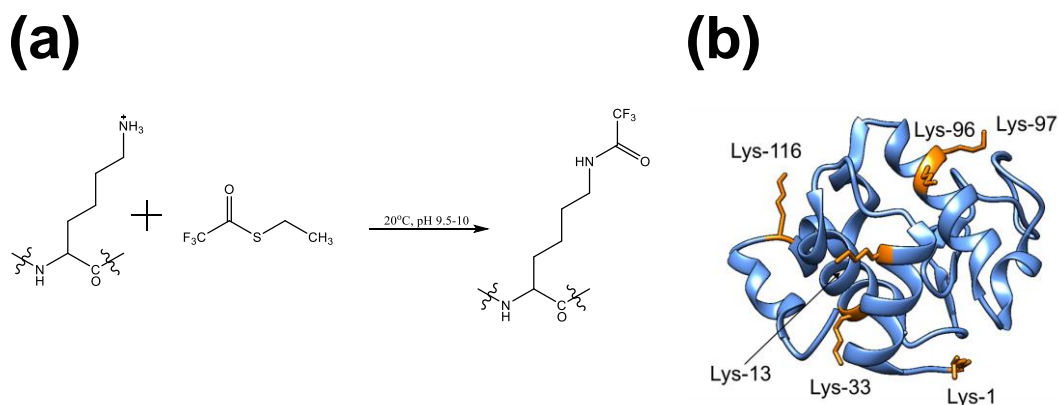


Figure 6.3a) Acetylation reaction scheme of lysine by S-Ethyltrifluoroacetate under basic conditions. b) Lysozyme structural model determined by X-ray ray crystallography (PDB ID: 4YMB). Lysines involved in ^{19}F -labelling are marked in yellow.

The supernatant was fractionated on a HiPrep CM FF 16 / 10 ion exchange column with a 6 % highly cross-linked agarose matrix with pH 7.3 0.05 M Tris / HCl buffer as eluent and a linear NaCl gradient of 0 - 0.175 M. Lysozyme contains a total of six lysine residue, all of them being surface exposed as shown in the structural model in Figure 6.3b.

The reaction mixture usually contains several products in which some a varying number of lysine residues undergo the reaction, denoted as LF6, LF5, LF4 and so on. These products contain differing amounts of positive charge so can be separated using ion exchange chromatography. The reaction product mixture was added to a cation exchanger column with an agarose sugar matrix and was eluted with pH 7.3 tris / HCL buffer with a linearly incremented NaCl gradient. The least positive LF6 has the weakest binding to the agarose matrix, therefore it elutes first at the lowest NaCl concentration, as shown in Figure 6.4. After chromatography, the collected fractions were dialysed twice more to remove NaCl used for ion exchange.

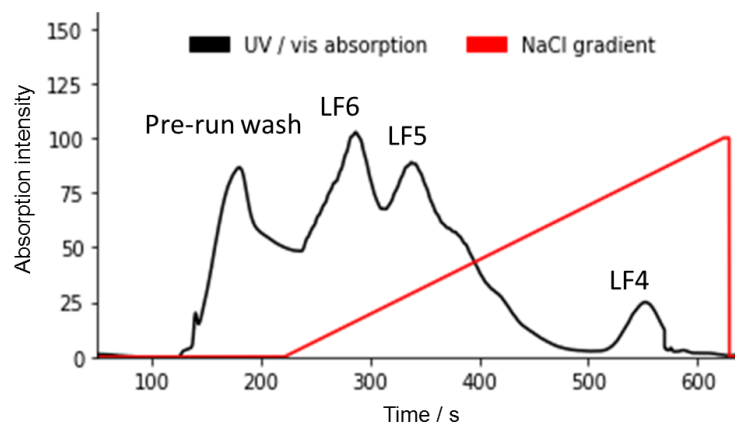


Figure 6.4 Graph showing the elution of ^{19}F labelled lysozyme using ion exchange chromatography tracked using UV / vis Absorption at 280 nm (black line) and ionic conductivity measurement (red line). NaCl gradient was linearly increased throughout the run to elute more positively charged eluents, which adhere more strongly to the column agarose matrix.

Figure 6.5 shows ^{19}F spectra of labelled lysozyme, with distinct peaks corresponding to the different labelled lysine environments, assigned based on previous studies^[18]. The peak shifts in spectra at different pH values are due to differences in the chemical environments of the $-\text{CF}_3$ groups. This shows the sensitivity of ^{19}F nuclear spins in labelled lysozyme to changes in experimental conditions so demonstrates its feasibility as a model system to optimize ^{19}F protein d-DNP.

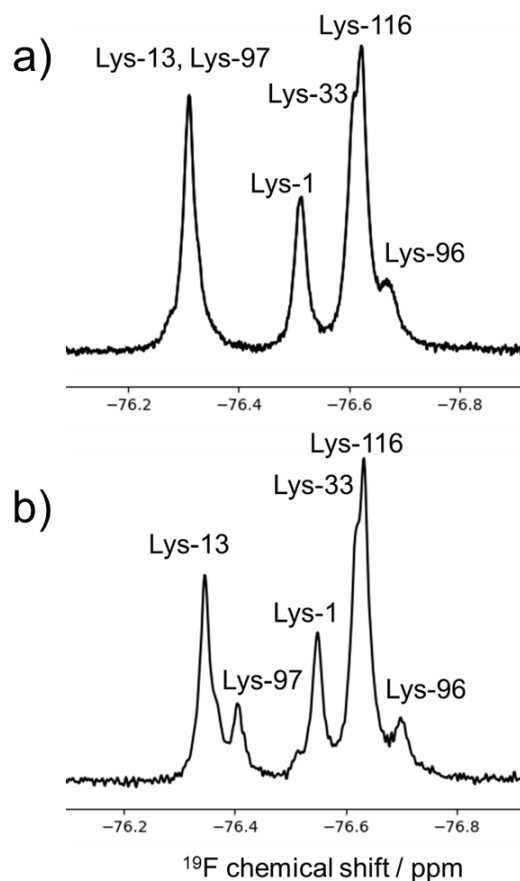


Figure 6.5 ^{19}F Spectra of fluorinated lysozyme in a) pH 5.5 glycine / HCL buffer and b) pH 3.5 acetate buffer. Spectra were recorded with 14848 scans (a) and 4600 scans (b) (not scaled for intensity) using a simple 90° pulse – acquire sequence. ^{19}F chemical shifts have good sensitivity to changes in chemical environment, so spectra change under different pH conditions due to changes in protein conformation.

In principle, the covalent attachment of $-(\text{CO})\text{CF}_3$ groups neutralizing the positively charge $-\text{NH}_3^+$ groups may result in an altered protein folding. To test this, 2D ^1H nuclear Overhauser effect spectroscopy (NOESY) experiments were carried out and some assignments were made based on previous studies^{[19][20]}, spectra are presented in Figure 6.6.

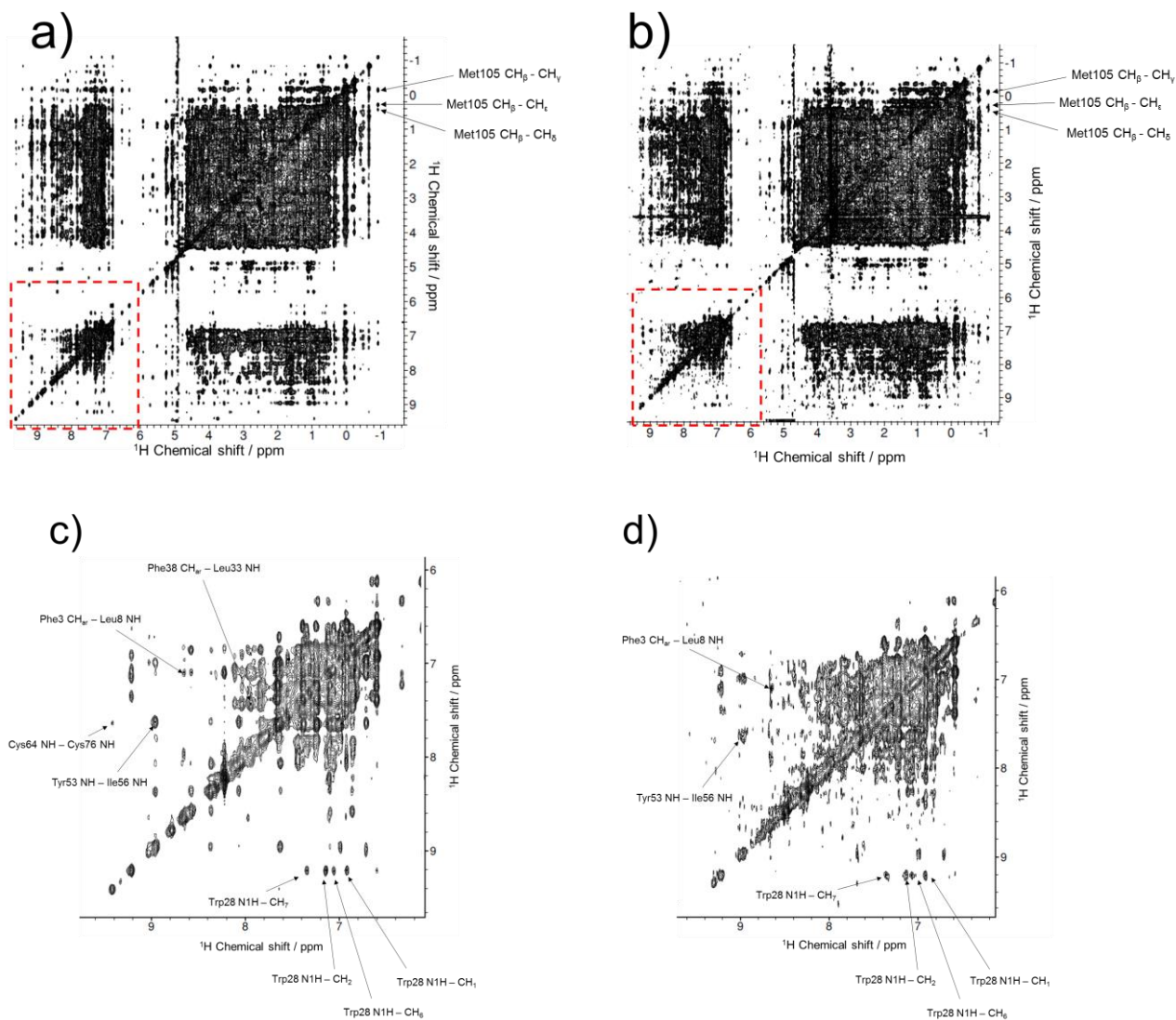


Figure 6.6 ^1H - ^1H NOESY spectrum, recorded at room temperature, of lysozyme a) without ^{19}F labels and b) with ^{19}F labels in pH 7.4 Tris-HCL buffer at 25 °C. NOE mixing time, $t_m = 250$ ms. Zoom of amide region, shown by red rectangle in top panel c) without ^{19}F labels and d) with ^{19}F labels.

A select number of prominent spectral peaks are chosen for analysis due to the crowded nature of the NOESY spectra. Met105 and Tyr28 show prominent inter-residue cross-peaks in the amide and methyl regions, respectively. The same cross-peak chemical shifts are within error for both the ^{19}F labelled and unlabelled sample and are also prominent in the literature spectra. Seven ^1H - ^1H correlations due to long range NOE interactions are identified in the literature assignment^{[19][20]}. Of these seven cross-peaks, four were identified in the non-labelled NOESY spectrum and 2 were observed in the ^{19}F labelled spectrum. A number of different experimental conditions should be noted which could account for the difference from the literature spectrum- the assigned literature NOESY experiment was carried at

35 °C and at pH 3.8 with an NOE mixing time, t_m , of 150 ms, the experimental spectrum was collected at 25 °C, pH 7.4 and with $t_m = 250$ ms. The temperature and pH differences are likely to lead to differences to some differences in folding leading to different $^1\text{H} - ^1\text{H}$ distances and differing cross-peak intensities, but the fact that 4 / 7 of the long range peaks are observed suggests similarities in the overall conformation. 2 / 4 of the intra-residue cross-peaks are observed in the ^{19}F labelled spectrum compared to the non-labelled sample. This provides evidence for both the retention of some tertiary structure but also for some minor structural changes due to addition of bulky and uncharged fluorinated acetyl groups to the lysine amine.

6.4. Materials / methods

Preparation of d-DNP samples

Small molecule



Figure 6.7 a) Chemical structure of trifluoroacetic acid (TFA), which contains three chemically identical ^{19}F nuclear spins that are prone to short T_1 times due to rapid rotation of the methyl group. b) Chemical structure of 5-fluorouracil.

Trifluoroacetic acid (100 mM) was dissolved in a 60/30/10 mixture of (Dimethyl sulfoxide) DMSO- d_6 , D_2O and H_2O containing 40 mM, 70 mM or 100 mM 4-Hydroxy-2,2,6,6-tetramethylpiperidine 1-oxyl (TEMPO) radical. After addition of TEMPO, the mixture was mixed using a vortexer for ~5 mins to ensure complete solvation and homogeneous distribution of the TEMPO monoradical. 30 μL of this mixture was pipetted into the d-DNP sample cup, which was attached to the bottom of the microwave waveguide. The sample was frozen by inserting the waveguide into the 'polarise' position- so that the sample sits at the centre of the 3.4 T magnet (Figure 6.1). This was done during the cool-down, when the temperature in the

sample space was ~130 K, and was left to cool down until microwaves were applied when the temperature reached 1.8 K.

Protein

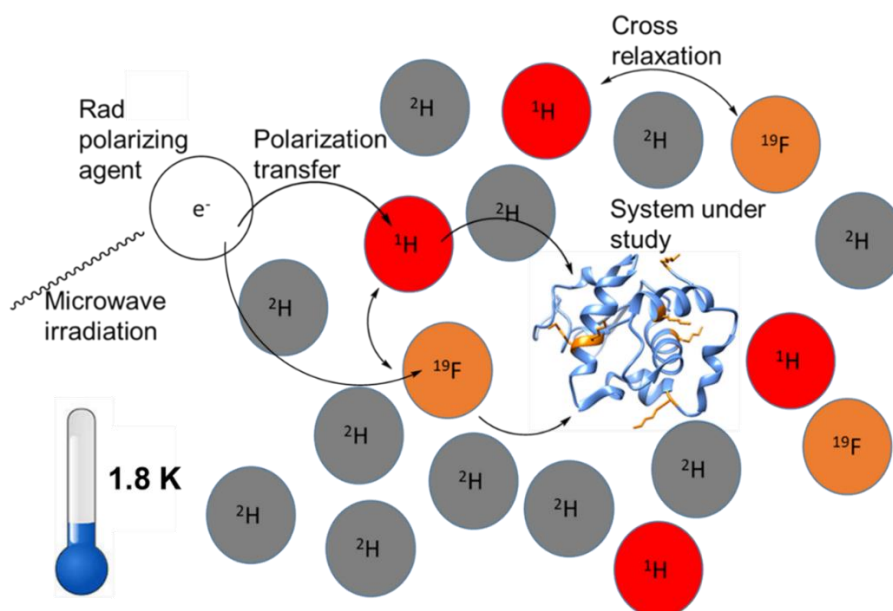


Figure 6.8 Illustration of hyperpolarization of fluorinated protein. Electron polarisation is transferred to nuclei and spreads through the sample by spin diffusion. Polarisation is transferred between ¹H nuclei and ¹⁹F nuclei by a cross relaxation mechanism.

¹⁹F labelled lysozyme (~70 mM) was dissolved in a 60/30/10 mixture of DMSO-d₆, D₂O and H₂O containing 40 mM TEMPOL radical. The sample also contains 100 mM of ¹⁹F-containing 5-fluorouracil, shown in Figure 6.7b, which serves two purposes: First, its presence increases the spin diffusion among ¹⁹F nuclei and thereby helps the DNP process, which was shown to depend on an interplay of a spin-diffusion dependent direct ¹⁹F polarization and a cross-polarization from ¹H nuclei as shown schematically in Figure 6.8^[17]. Also, ¹⁹F nucleus of 5-fluorouracil serves as a reference for comparing with CF₃- group signals of the labelled lysozyme. The same procedure for inserting and freezing the sample was used as for the small molecule sample.

Pulse Sequence

The NMR pulse sequence for ambient temperature acquisition following a d-DNP experiment is shown in Figure 6.9.

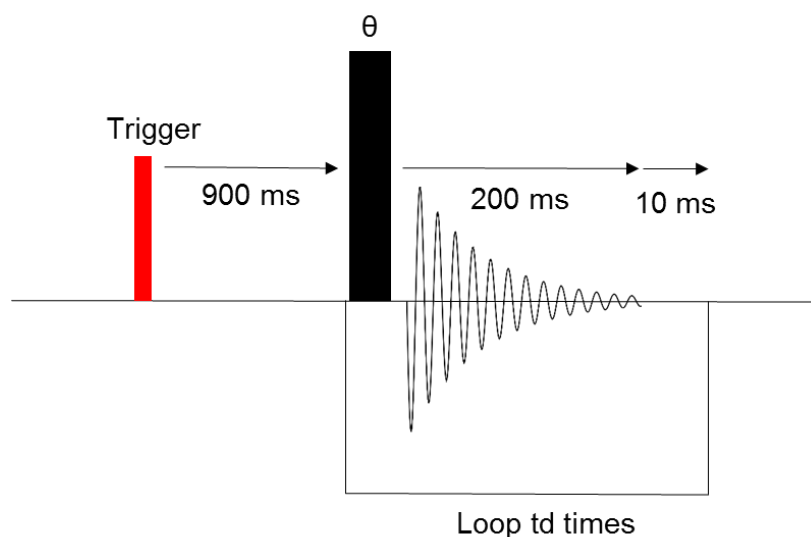


Figure 6.9 Pulse sequence for NMR acquisition in the d-DNP experiment. The pulse sequence is automatically triggered by the rapid movement of the waveguide to the 'dock position and activation of 'line' and 'dock' takasago valves. A delay of 900 ms is allowed for the sample to settle in the NMR tube followed by a pulse with flip angle θ and acquisition of an FID. The acquisition time was set to 200 ms, and an additional 10 ms delay was included to avoid an error message from the TopSpin acquisition software. After this, the pulse program loops back to the pulse to acquire subsequent FIDs. The pulse program loops td times- the number of time domain points in a pseudo-2D experiment so that multiple FIDs are acquired at 210 ms intervals following dissolution.

The trigger is activated by the rapid motion of the waveguide to the bottom position, where the sample sits in the 'dock'. The 900 ms delay gives time for the dissolution sample to settle following dissolution. While shorter delays of down to 300 ms are possible in principle, they result in line broadening in the NMR signal due to air bubbles formed during the dissolution process. After the initial 900 ms, FIDs are acquired using a pulse with flip angle θ at 210 ms intervals. The delay between signal acquisitions is the signal acquisition time plus an additional 10 ms delay, included so that the pulse program is compatible with the TopSpin acquisition software.

6.5. Optimising instrument conditions

In order to achieve maximum enhancement in the liquid state, several parameters were optimized to achieve maximum solid-state signal prior to dissolution. This was done by measuring ^1H and ^{19}F NMR signals in the 3.4 T polarisation magnet in a set of separate experiments using a specially designed sample cup equipped with a saddle coil. Such a sample cup is incompatible with the dissolution dock, which is why the acquisition on solid-state samples was not possible on the same sample

used for the dissolution. A sample of 60/30/10 DMSO-d₆, D₂O and H₂O containing 40 mM TEMPOL monoradical was used to optimise solid-state polarisation.

Microwave frequency

A microwave field sweep was carried out to determine the microwave frequency at which the combination of DNP mechanisms taking place are best satisfied. Figure 6.10a shows ¹H signal intensity within the frequency range that the microwave source is capable of operating. The time for which microwaves are applied to the sample before acquisition, termed the polarisation time, was 40 s for each acquisition. This was achieved using a LabView program to control the microwave source, which incremented the microwave frequency by 20 MHz every 40 s. This meant that there was a 40 s DNP build-up time before acquisition of each signal. A pseudo-2D pulse program was started at exactly the same time in which there is a delay of 40 s between each NMR acquisition, resulting an enhanced NMR spectrum after 40 s of polarisation at each incremented microwave frequency.

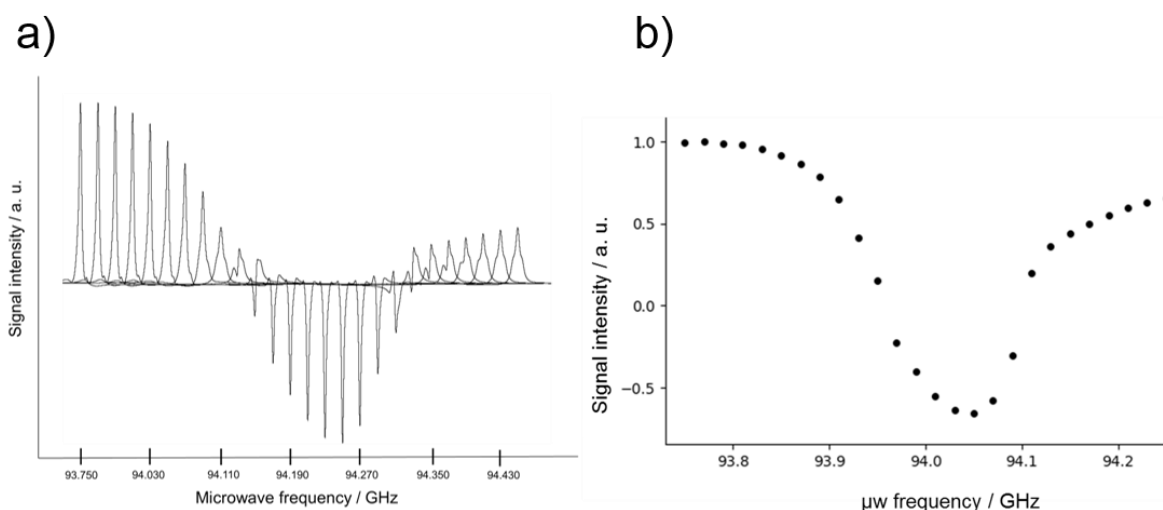


Figure 6.10a) ¹H spectra acquired at different microwave frequencies in the top 3.4 T dual-isocentre magnet. Spectra were recorded with a single acquisition, polarisation time was 40 s and microwave power was 200 mW. b) Graph showing ¹H solid-state signal intensity at different microwave frequencies at 3.4 T and 1.8 K. Maximum negative enhancement was at 94.050 GHz, which was used as the microwave frequency in dissolution experiments. The signal intensity was normalised by setting the intensity of the largest positive enhanced spectrum to 1.0.

Figure 6.10b shows a plot of normalised ¹H signal intensity at different microwave frequencies. The field sweep profiles of ¹H and ¹⁹F have been shown to be similar^[17], so the microwave frequency at which maximum enhancement is observed for ¹H can be safely assumed to be the same for ¹⁹F. ¹H acquisition is preferred to ¹⁹F because a large amount of fluorine is present in the plastics in the sample cup and

RF transmission line, leading to large ^{19}F background signals. The positive enhancement peak is close to the edge of the frequency range of the microwave source, so microwave frequency at which maximum negative enhancement was found was used for experiments. The positive enhancement was found to be significantly greater in magnitude than the negative enhancement, which is likely to be due to ^1H background signal from hardware materials that are close to the solid-state acquisition coil. The positive and negative enhancement peaks were previously both at higher microwave frequencies and the microwave frequency at the positive peak was used, but a quench of the 3.4 T magnet and subsequent recharge to a slightly different field led to the observed profile.

Microwave power

Microwave power was also optimized to give maximum enhancement and reasonable build-up time to maximum polarisation. Figure 6.11a) shows the build-up to maximum polarisation as a function of time at different microwave powers.

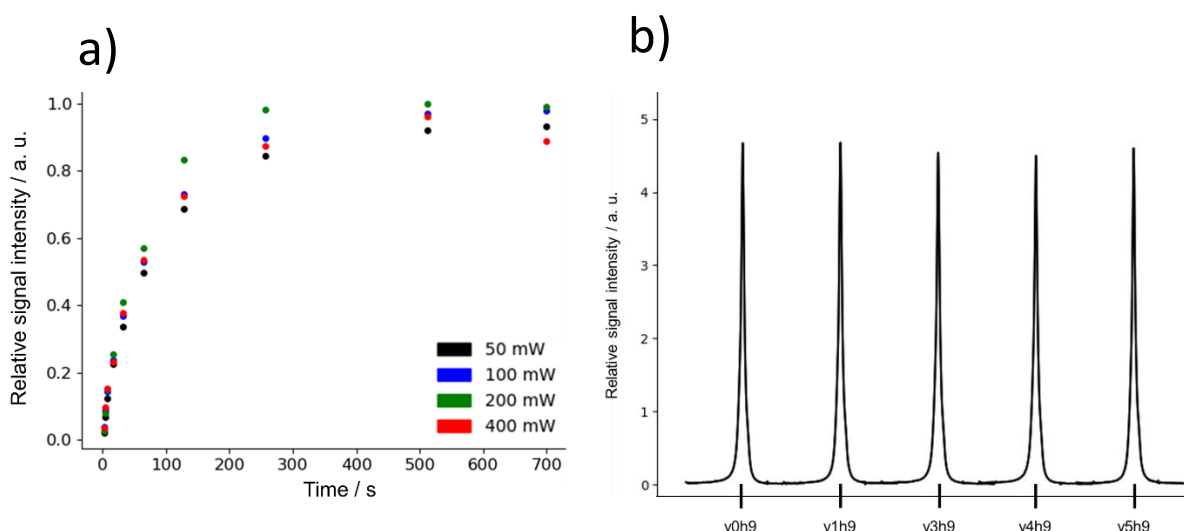


Figure 6.11a) Graph showing DNP-enhanced ^1H relative signal intensity at different polarisation times. This was repeated at a number of microwave powers- 50 mW (black), 100 mW (blue), 200 mW (green) and 400 mW (red) to ascertain which power level lead to optimal solid state polarisation. b) ^1H NMR spectra acquired on the top 3.4 T magnet at ~ 1.8 K at different positions of the quasi-optic bench. Similar intensities are shown, which suggests that precise positioning of the quasi-optic bench is not required in optimising solid state polarisation. v and h on the horizontal axis are the readings on the vertical and horizontal adjustment knobs on the quasi optic bench.

Previous studies have suggested that enhancement should increase as a function of microwave power^[21]. However, we observed greater enhancement at 200 mW than 400 mW, which is attributed to sample heating effects at high microwave powers and long polarisation times, resulting in faster electron spin relaxation, T_{1e} ,

leading to lower electron spin polarisation and therefore lower nuclear spin polarisation after spin diffusion. The final ^1H spectrum acquired at 400 mW after 700 s shows a significant dip in intensity relative to shorter polarisation times, which is consistent with heating of the sample due to exposure to long high power microwaves. Therefore, 200 mW was used for d-DNP experiments. The DNP build-up time was determined using Topspin dynamics analysis, are shown in Table 6.1.

Microwave power / mW	Build-up time / s	Maximum relative signal intensity / a. u.
50	74	0.93
100	77	0.98
200	66	1.00
400	66	0.96

Table 6.1 DNP build-up time and maximum relative signal intensity of ^1H spectra at different microwave powers.

The build-up time is shown to be shorter at higher microwaves powers, which would save experimental time for high sample throughput applications such as analysis of clinical extracts from patients, where multiple dissolutions are performed in a day.

Microwave alignment

The alignment of microwaves vertically down the waveguide was investigated by changing the position of the quasi-optic bench using micrometer screw gauges. Two methods were used to align microwaves

- 1) A mirror was placed at the bottom of the waveguide and the reflected microwave intensity was measured using a zero bias detector (ZBD). This approach did not prove to be informative, because the power of the reflected microwave beam measured in this manner, showed very strong sensitivity with respect to tiny alterations in the position of the quasi-optic bench. Most likely this arises due to a superposition of reflections produced at many locations within the microwave guiding system.
- 2) Alternatively, DNP enhanced ^1H signals as a function of the quasi-optic bench position. It was shown that, ^1H solid-state signals at different positions of the quasi-optic bench revealed very little difference in the signal intensity at different positions, as shown in Figure 6.11b.

There are slight variations in the observed enhancement, but this result suggests that good DNP enhancement can be achieved without precise alignment of the quasi-optic bench.

6.6. Optimization of d-DNP on small fluorinated molecules

As described in **chapter 3**, radical concentration is an important parameter for optimizing DNP enhancements- too little radical leads to not all of the nuclei in the sample being polarised, too much radical leads to fast electron relaxation time, T_{1e} , in the solid-state leading to inefficient DNP and also increases nuclear T_{1n} in the liquid state and causes signal bleaching due to paramagnetic centres in the liquid state following dissolution.

The concentration of TEMPOL radical in the sample was optimized to give maximum signal after dissolution. A DNP enhanced TFA sample and a thermal signal acquired with 344 scans are shown in Figure 6.12.

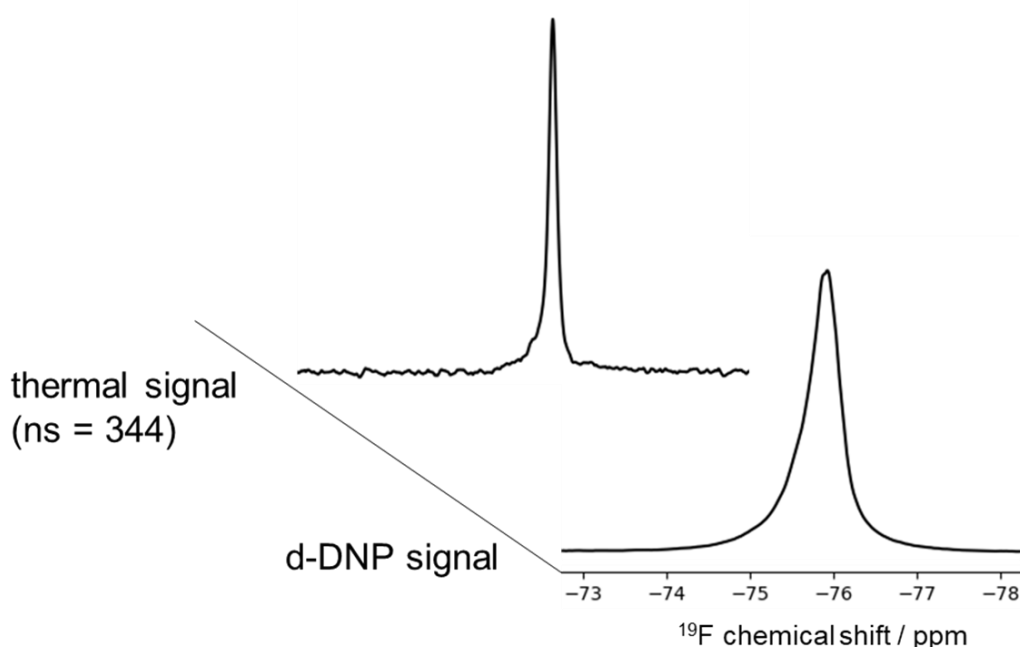


Figure 6.12 ^{19}F d-DNP spectrum of TFA compared with a thermal signal acquired with 344 scans. The DNP matrix was 60 / 30 / 10 (v : v : v) DMSO- d_6 , D_2O and H_2O with 100 mM TFA. Maximum enhancement was achieved when TEMPOL concentration was 40 mM.

Table 6.2 summarizes the liquid state enhancements following a d-DNP experiment at three TEMPOL concentrations. The longitudinal relaxation time of ^{19}F nuclei solutions with an equivalent TEMPOL concentration is also shown, which is an important factor in how much enhancement is observed in the liquid state.

[TEMPOL] / mM	Enhancement	TFA T ₁ / s
40	780	2.56
70	290	1.64
100	150	1.06

Table 6.2 ¹⁹F enhancements at different radical concentrations and T₁ in samples with equivalent radical concentrations. The largest enhancement and longest relaxation time was in the sample with 40 mM TEMPOL.

The greatest enhancement occurs at the lowest TEMPOL concentration of 40 mM in the solid-state sample giving a final concentration of 1-1.3 mM in the liquid state sample, as the dissolution factor is typically 30-40. This can be attributed to less signal loss due to T₁ relaxation which is caused by hyperfine coupling between the paramagnetic electron and ¹⁹F nuclei, which is demonstrated by the short T₁ time in a sample containing TFA and equivalent concentrations of TEMPOL radical following dissolution.

6.7. Dissolution-DNP with ¹⁹F labelled lysozyme d-DNP

To test that ¹⁹F signals of the protein can in principle be enhanced using dissolution DNP a dissolution experiment was first conducted with the lysozyme in dissolved in 60/30/10 DMSO-d₆, D₂O and H₂O containing 40 mM TEMPOL. Stacked spectra obtained using this method described are shown in Figure 6.13.

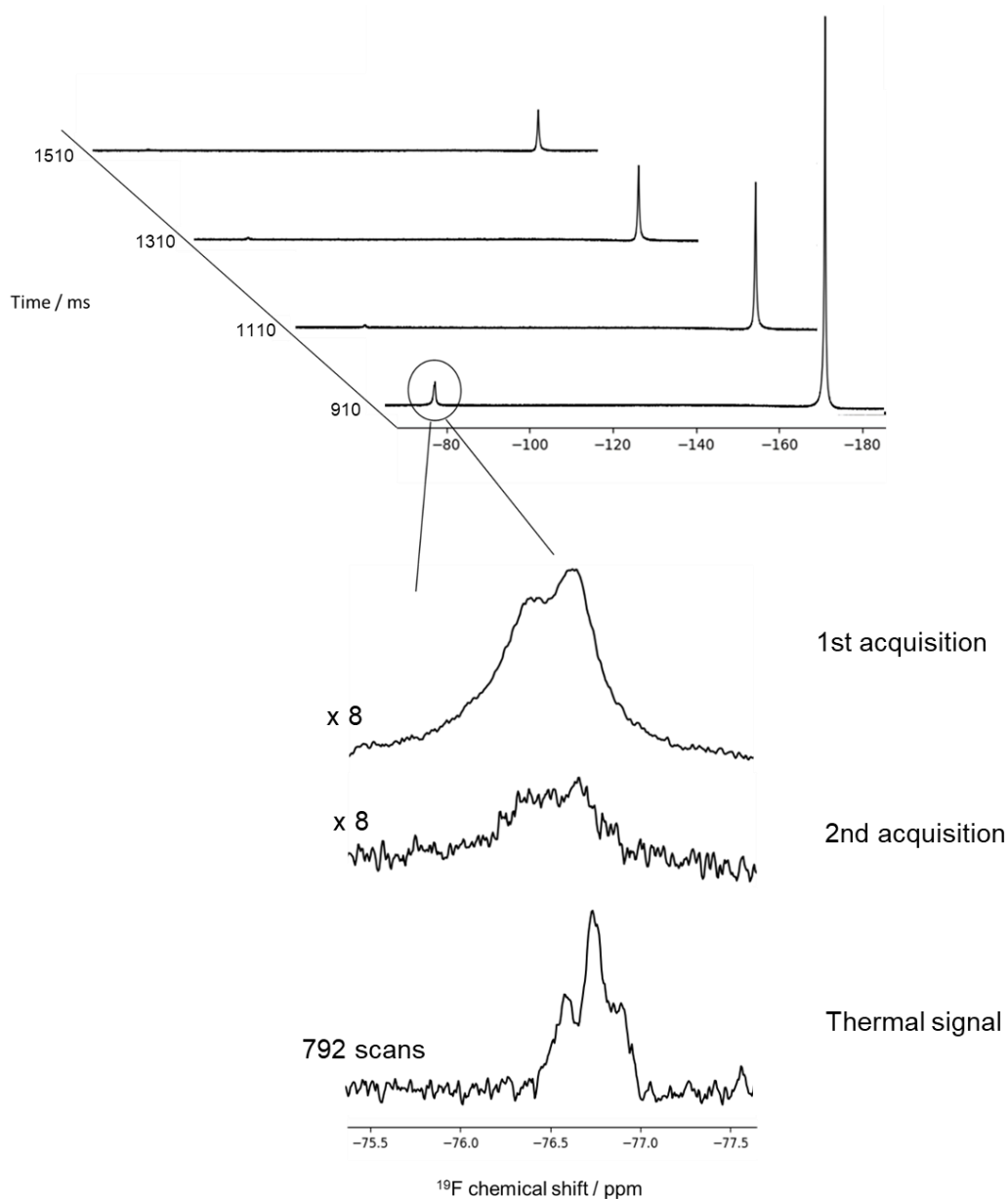


Figure 6.13 ^{19}F spectra acquired at 200 ms intervals following dissolution using a 90° flip angle pulse. The fluorinated Lysozyme peak is at -76 ppm and 5-fluorouracil peak is at -170 ppm relative to CFCl_3 . Signal intensity was observed after the first acquisition despite using a 90° pulse which suggests that the sample has not fully settled in the coil at the point that acquisition starts.

The observed enhancement following the dissolution experiment was 330 for labelled lysozyme and 1100 for 5-fluorouracil compared to a thermally acquired signal. This was determined by recording a sample at room temperature without hyperpolarizing with a large number of acquisitions and comparing the signal integral with that acquired during dissolution. Signal intensity was observed after the first acquisition despite a $\theta = 90^\circ$ pulse being applied, which is attributed to not all of

the sample having settled in the NMR tube after 900 ms, leaving hyperpolarized ^{19}F spins to be excited by the second 90° pulse.

The linewidths of ^{19}F signals from the molecules under study are presented under static and d-DNP conditions in Table 6.3.

Sample	Acquisition magnet	Acquisition conditions	Linewidth (FWHM) / Hz
^{19}F labelled lysozyme in pH 3.5 buffer	9.4 T wide-bore	thermal	7
^{19}F labelled lysozyme in H_2O + d-DNP matrix	9.4 T dual-isocentre bottom magnet	dissolution	210
TFA in H_2O	9.4 T wide-bore	thermal	3.5
TFA in H_2O + d-DNP matrix	9.4 T dual-isocentre bottom magnet	dissolution	160
5-Fluoruracil in H_2O + d-DNP matrix	9.4 T dual-isocentre bottom magnet	thermal	38
5-Fluoruracil in H_2O + d-DNP matrix	9.4 T dual-isocentre bottom magnet	dissolution	114

Table 6.3 Linewidths of fluorinated molecules using conventional acquisition and following d-DNP. The dilution factor in a d-DNP experiment is consistently between 30-40, so the d-DNP matrix components are in low concentration in the relevant samples.

The full width at half maximum (FWHM) of the lysozyme peak increased from 7 Hz acquired under static conditions when using conventional liquid state NMR to 210 Hz following dissolution. This is attributed to bubbles due to the rapid transfer of liquid during the dissolution process, which alter the magnetic susceptibility of the sample compared to standard acquisition. Also, the samples containing biradical with have increased linebroadening because of shorter T_2 due to proximity to paramagnetic centre. This compares with a loss in resolution for TFA- 3.5 Hz using conventional NMR, 160 Hz after d-DNP and for 5-fluorouracil, where linewidth increases from 38 Hz to 114 Hz. It should be noted that thermal acquisition using the bottom dual-isocentre magnet results in large linewidths due to the proximity of

the top 3.4 T, as is the case for 5-fluorouracil, a standalone 9.4 T wide-bore magnet provided better resolution. A possible solution to broad lines caused by bubbles be to apply methods used in other d-DNP systems to improve sample transfer to the NMR tube without bubbles, which have also been shown to increase nuclear T_1 , discussed in the **section 6.10**.

6.8. ^{19}F lysozyme under denaturing conditions

Next, an d-DNP experiment where the sample before the dissolution also contains 6 M of urea, ensuring the complete denaturation of the lysozyme^[22], while the dissolution is done using 10 mM phosphate buffer at pH 7.4

Stacked spectra following a d-DNP experiment are shown in Figure 6.14, the pulse sequence shown in Figure 6.9 was used with the flip angle, θ , set to 31° . The enhancement for 5-fluorouracil was found to be ~ 146 , considering the 31° flip angle used in the experiment. This calculation is based on the first spectrum collected following dissolution, and assumes that total magnetization in the transverse plane, M_x , is given by

$$M_x = M \sin(\theta) \tag{6.1}$$

Where θ is the flip angle of the pulse and M is the total magnetization. However, the total magnetization, M , has been shown not to be available to the NMR acquisition coil 900 ms after dissolution (Figure 6.13) due to the sample not settling in the NMR tube. This leads to significant error in the calculation of enhancement.

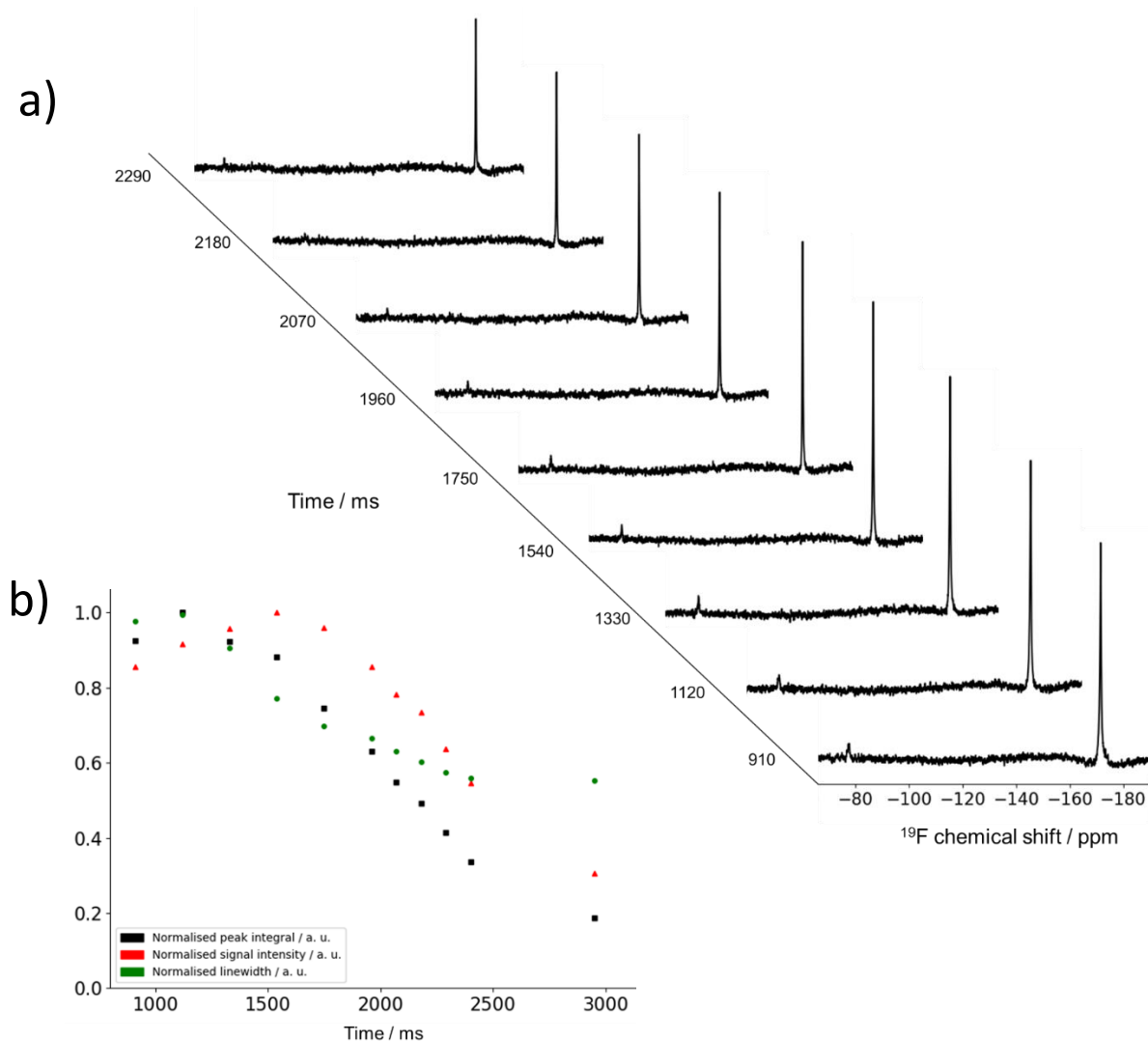


Figure 6.14a) Stacked ^{19}F spectra of labelled lysozyme at -76 ppm and 5-fluorouracil at -170 ppm. Acquisitions were made at 210 ms increments, with the first being 900 ms after dissolution with a small flip angle of 31° . A small flip angle was used to demonstrate the feasibility of tracking a dynamic event using this d-DNP method. 25 Hz of exponential linebroadening was applied to all spectra. b) Normalised peak integral, signal intensity and FWHM linewidth of 5-fluorouracil at time points following dissolution. Normalisation was carried out by dividing all values by the largest value. Signal intensity is defined as the highest point of the peak on the vertical intensity scale.

Analysis of the 5-fluorouracil peak at time points after dissolution is shown in table 6.4. This data is plotted in Figures 6.14b).

Time after dissolution / ms	Normalised peak integral / a. u.	Normalised signal intensity / a. u.	Linewidth / Hz
910	0.89	0.91	175
1120	1.00	0.96	179
1330	0.95	0.99	162
1540	0.68	1.00	138
1750	0.61	0.96	125
1960	0.44	0.85	119
2070	0.39	0.77	113
2180	0.29	0.71	108
2290	0.28	0.63	103
2400	0.23	0.53	100
2950	0.07	0.29	99

Table 6.4 Relative peak integral, relative peak intensity and linewidth of the 5-fluorouracil peak at different time points following a d-DNP experiment.

The linewidth of the 5-fluorouracil peak decreases with time following dissolution, which is consistent with the liquid sample settling in the NMR tube resulting in less sample motion and bubbles being forced out of the sample due to low pressure created by the small vacuum pump attached to the adaptor on top of the probe (Figure 6.2b). Maximum peak integral is observed at the second time point, despite the initial 31° pulse which left $M_z = M \cos(31) = 0.86 M$ of the total magnetization in the z- plane following the first acquisition, consistent with the TFA optimisation experiments, as more hyperpolarised spins become available to the NMR acquisition coil at some time point following dissolution. The maximum peak intensity increases until the fourth time point rather than the second due to the broad linewidths shortly after dissolution, then decreases at a rate close to that of the peak integral as the linewidth becomes narrower.

Figure 6.15 shows stacked zoomed spectra of the ^{19}F labelled lysozyme region at ~ 76 ppm.

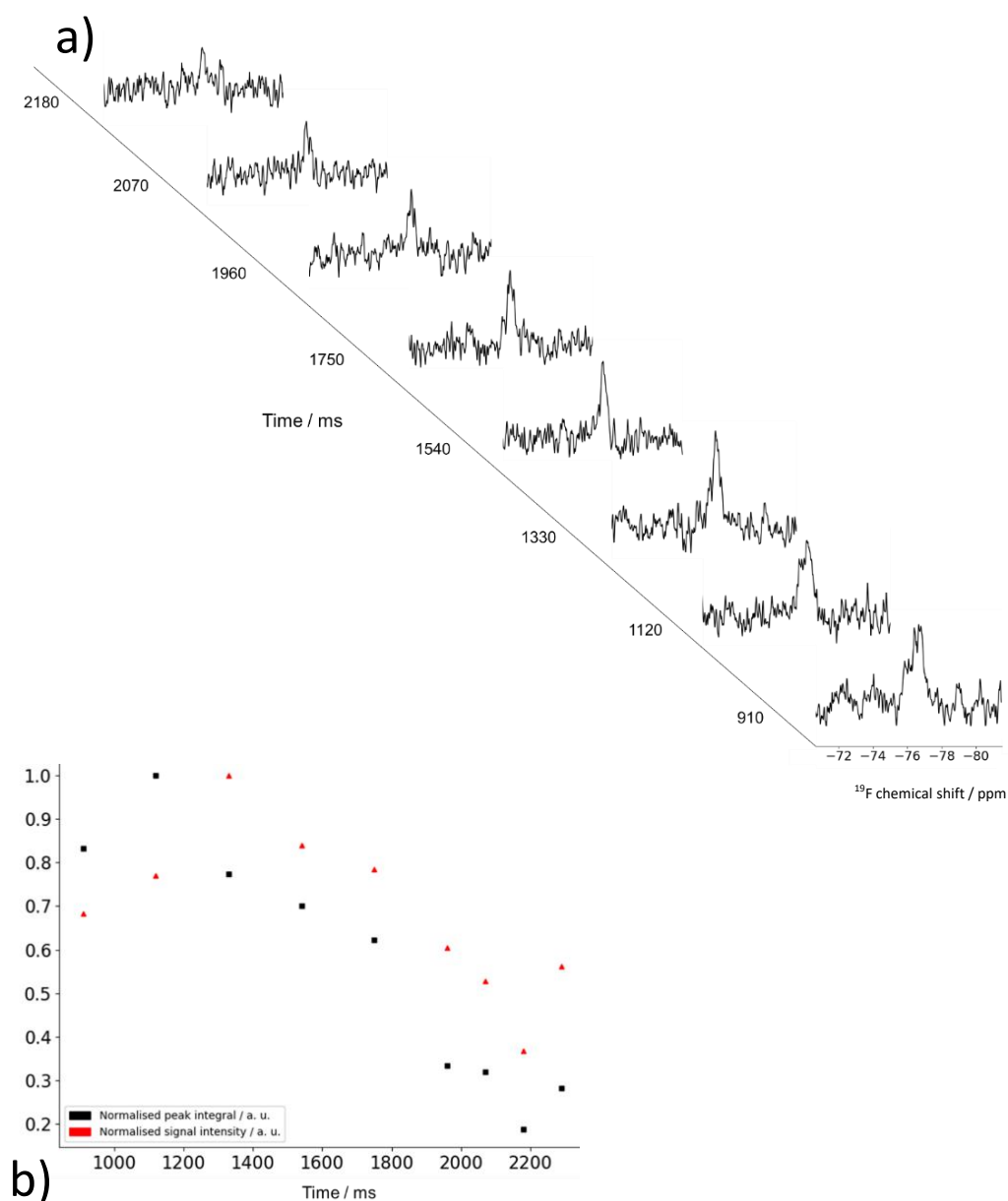


Figure 6.15a) Stacked spectra showing the labelled ^{19}F lysozyme peak following a d-DNP experiment in which the protein was prepared and polarised under denaturing conditions, after which NMR acquisition occurs under refolding conditions due to the dilution factor during dissolution. b) Graph showing normalised peak integrals and signal intensity of the ^{19}F lysozyme peak following dissolution. Normalisation was carried out by dividing all values by the largest value.

The observed enhancement for ^{19}F labelled lysozyme under refolding conditions was found to be ~ 20 . This value is significantly lower than the value observed without the addition of denaturant. This is attributed to the 6 M concentration of urea in the sample, which introduced a much higher concentration of ^1H nuclear spins into the solid-state sample than the samples on which the method was optimized. Optimising a dissolution sample containing denaturant is an interesting area of

future research. This has been shown to result in faster relaxation of electron spins, T_{1e} , in the sample^[23], resulting in lower solid state polarisation.

Normalised Peak integrals and signal intensity at time points after dissolution are plotted in Figure 6.15b. A similar pattern is observed in terms of peak integral and signal intensity as 5-fluorouracil, with the greatest peak integral at the second time point and maximum peak intensity after the third time point. Peak integral and intensity decays faster than the 5-fluorouracil peak due to the faster T_1 of the ^{19}F lysozyme labels. Deviations from the trend shown for the 5-fluorouracil peak are due to errors introduced by poor signal-to-noise of the ^{19}F lysozyme peak. Linewidths were not analysed due to large error as a result of poor signal to noise leading to low resolution.

6.9. Discussion

Overall, our experiments demonstrate the feasibility of a d-DNP experiment with small molecules such as TFA and 5-fluorouracil and ^{19}F labelled lysozyme. As demonstrated in the medium flip angle experiments, it is possible to collect dynamic information on a protein under selected conditions.

A problem with the d-DNP methodology for biological systems is the extreme temperature range that the sample is exposed to- firstly cryogenic freezing to 1.8 K followed by introduction of the dissolution solvent at 100 °C. In the presented work, lysozyme is not denatured by the dissolution solvent as there is more than one ^{19}F peak in the thermal signal and no white protein precipitate was present in the NMR tube following dissolution, which would be found in the case of if lysozyme was irreversibly denatured^[24]. A possible solution to the extreme temperature would be to perform dissolutions with temperatures below 100°C. This would result in less frozen hyperpolarized sample being melted and transferred to the NMR tube, but further optimizing efficient DNP and using a probe that is optimized for ^{19}F acquisition could result in sufficient signal-to-noise to compensate for this loss in signal intensity.

The observed broad linewidths following dissolution are a major problem with studying proteins with ^{19}F labelled methyl groups attached to lysine. The poor resolution following d-DNP means that studying a system with a larger chemical shift range in different ^{19}F environments would provide clearer biological information.

A suggested system would be ^{19}F labelling of tryptophan residues, which have larger differences in chemical shifts, for example of up to ~ 5 ppm^[24], equivalent to ~ 1880 Hz at 9.4 T, which would be clearly resolved even under the observed line broadening conditions of d-DNP. Another option to improve resolution would be to further reduce bubble formation following dissolution. This could be achieved with a flow injection system, such as the one used by the Hilty group in dissolution experiments^[26]. These experiments also include 10 % methanol in the DNP sample matrix, which was shown to reduce bubble formation. A DNP method to study protein folding has also been presented by Hore et al.^[27] Chemically induced dynamic nuclear polarization (CIDNP) was used to enhance ^1H nuclei in lysozyme resulting in spectra acquired at ~ 300 ms intervals, a similar timescale to the work described. The drawbacks of CIDNP are the need for high power light irradiation inside the NMR magnet, lack of uniform sample irradiation and accumulation of flavin in the NMR tube.

6.10. Conclusion and outlook

A d-DNP methodology for hyperpolarizing fluorinated biomolecules was developed. This is of relevance to a large range of chemical disciplines because ^{19}F nuclear spins are not found in many biological and material systems, so dynamic studies can be carried out following selective labelling without background signals and with unambiguous assignments.

Dynamic fluorinated biological, chemical and material systems with a wide chemical shift range can be studied using the presented methodology, resulting in 1D NMR spectra acquired at ~ 200 ms intervals with good signal-to-noise.

The presented methodology can be further improved by:

- Optimising delivery of the fluid into the NMR tube to reduce bubble formation and achieve faster settling of the liquid sample will allow high resolution studies of nuclei with short T_1 times. This could be achieved with a flow injection system, such as the one used by the Hilty group in dissolution experiments^[26].
- Using a probe that is optimised to ^{19}F acquisition would result in greater signal-to-noise due to better tuning to ^{19}F NMR frequency.

6.11. References

- [1] J. H. Ardenkjær-Larsen, B. Fridlund, A. Gram, G. Hansson, L. Hansson, M. H. Lerche, R. Servin, M. Thaning, K. Golman, *Proc. Natl. Acad. Sci. U.S.A.*, 2003, **100**, 10158–10163
- [2] J. Kim, R. Mandal, C. Hilty, *J. Phys. Chem. Lett.*, 2019, **10**, 5463–5467
- [3] T. Harris, O. Szekely, L. Frydman, *J. Phys. Chem. B*, 2014, **118**, 3281–3290
- [4] G. Olsen, E. Markhasin, O. Szekely, C. Bretschneider, L. Frydman, *J. Magn. Reson.*, 2016, **264**, 49–58
- [5] O. Szekely, G. L. Olsen, I. C. Felli, L. Frydman, *Anal. Chem.*, 2018, **90**, 10, 6169–6177
- [6] D. Kurzbach, E. Canet, A. G. Flamm, A. Jhajharia, E. M. M. Weber, R. Konrat, G. Bodenhausen, *Angew. Chem. Int. Ed.*, 2017, **56**, 389–392
- [7] P. Schanda, E. Kupče, B. Brutscher, *J. Biomol. NMR*, 2005, **33**, 199–211
- [8] P. Kaderavek, F. Ferrage, G. Bodenhausen, D. Kurzbach, *Chem. Eur. J.*, 2018, **24**, 13418–13423
- [9] L. Frydman, D. Blazina, *Nature Physics*, 2007, **3**, 415–419
- [10] H.-Y. Chen, M. Ragavan, C. Hilty, *Angew. Chem. Int. Ed.*, 2013, **52**, 9192 – 9195
- [11] E. N. G. Marsh, Y. Suzuki, *ACS Chem. Biol.*, 2014, **9**, 1242–1250
- [12] K. E. Arntson, W. C. K. Pomerantz, *J. Med. Chem.*, 2016, **59**, 5158–5171
- [13] Y. Lee, H. Zeng, S. Ruedisser, A. D. Gossert, C. Hilty, *J. Am. Chem. Soc.*, 2012, **134**, 17448–17451
- [14] Christopher M. Dobson, Philip A. Evans, Sheena E. Radford, *Trends Biochem. Sci.*, 1994, **19**, 31–37
- [15] J. Leggett, R. Hunter, J. Granwehr, R. Panek, A. J. Perez-Linde, A. J. Horsewill, J. McMaster, G. Smith, W. Köckenberger, *Phys. Chem. Chem. Phys.*, 2010, **12**, 5883–5892
- [16] B. P. McGeorge-Henderson, *Novel acquisition strategies for dissolution dynamic nuclear polarisation*, 2017

- [17] A. Gennaro, *¹⁹F Dynamic Nuclear Polarisation Towards a novel method for studies of protein dynamics*, 2019
- [18] P. Adriaensens, M. E. Box, H. I. Martens, E. Onkelinx, J. Put, j. Gelan, *Eur. J. Biochem.*, 1988, **177**, 383-94
- [19] C. Redfield, C. M. Dobson, *Biochemistry*, 1988, **27**, 122-136
- [20] C. Redfield, C. M. Dobson, *Biochemistry*, 1990, **29**, 7201-7214
- [21] Y. Matsuki, T. Maly, O. Ouari, H. Karoui, F. Le Moigne, E. Rizzato, S. Lyubenova, J. Herzfeld, T. Prisner, P. Tordo, R. G. Griffin, *Angew. Chem. Int. Ed.*, 2009, **48**, 4996–5000
- [22] F. R. Greene, C. N. Pace., *J. Biol. Chem.*, 1974, **949**, 5388-5393
- [23] B. Corzilius, A. A. Smith, R. G. Griffin, *J. Chem. Phys.*, 2012, **137**, 0542011-05420112
- [24] A. Schön, B. R. Clarkson, M. Jaime, E. Freire, *Proteins.*, 2017, **85**, 2009–2016
- [25] S. D. Hoeltzli, C. Frieden, *Biochemistry*, 1994, **33**, 5502-5509
- [26] H.-Y. Chen, C. Hilty, *ChemPhysChem*, 2015, **16**, 2646–2652
- [27] K. H. Mok, P. J. Hore, *Methods*, 2004, **34**, 75–87

7. Conclusion

Uniformly ^{13}C , ^{15}N labelled $\text{A}\beta(1-40)$ was shown to have strong DNP enhancement of up to 40 times the thermal signal when pre-incorporated in lipid vesicles, demonstrating that hyperpolarization can travel by spin diffusion efficiently through lipid ^1H spins and to the protein. 2D DQSQ correlation experiments have been demonstrated at high lipid to protein ratios of 100:1 and 200:1 in under 20 h of experimental time. DNP-enhanced ssNMR was applied to $\text{A}\beta(1-40)$ associated with extracted synaptic rat membrane for the first time, resulting in good enhancement and the determination of secondary chemical shifts under these conditions in under 2 days of experimental time.

Using ^{13}C – ^{15}N correlation experiments and double quantum filtering using the POST-C7 pulse sequence was used to produce ^{13}C spectra with greatly reduced spectral overlap from lipid peaks in a sample in which $\text{A}\beta(1-40)$ is pre-incorporated into lipid vesicles.

DNP-enhanced ssNMR was demonstrated as a method for analysing the structure of $\text{A}\beta(1-40)$ at various timepoints during incubation with membrane mimics as structures can be flash frozen and analysed. This means that kinetics can be observed by analysing secondary structure during a dynamic process. An inter-residue cross-peak between F19 and L34 was observed at 20:1 and 40:1 lipid-to-protein ratios, which has previously been identified in fibrillar structures and supports the anti-parallel β -sheet with a u-bend close to the middle of the sequence structure shown in Figure 5.23. Secondary chemical shifts collected at the labelled positions at low protein to lipid ratio also support this. Incubation of $\text{A}\beta(1-40)$ with POPG resulted in very similar spectra to those recorded without incubation, providing further evidence stable monomer structure when interacting with a lipid bilayer, which does not change dramatically as fibrillation starts. A valid question often raised about DNP enhanced ssNMR and associated low temperatures is whether the data is physiologically relevant. Some differences are very likely to occur, but in the case of $\text{A}\beta(1-40)$, the consistencies between room temperature fibrillar models and the experimental data presented means this is not a major problem.

The Nottingham dual isocentre d-DNP system was modified for acquisition of ^{19}F NMR signals, which was achieved without the need for purchasing specialised probes for ^{19}F acquisition. The highest ^{19}F DNP enhancement for TFA was achieved using 40 mM TEMPOL radical, concluded to be due to fast T_1 relaxation in the liquid

state following dissolution at higher radical concentrations. DNP enhanced ^{19}F signals were observed following polarization in protein denaturing sample conditions and dissolution into protein refolding conditions using a 30° flip angle pulse at 200 ms intervals. This demonstrates the feasibility of tracking dynamic protein events using ^{19}F d-DNP and the Nottingham dual isocentre, which benefits from a short transfer time between polarizing conditions and liquid state NMR acquisition.

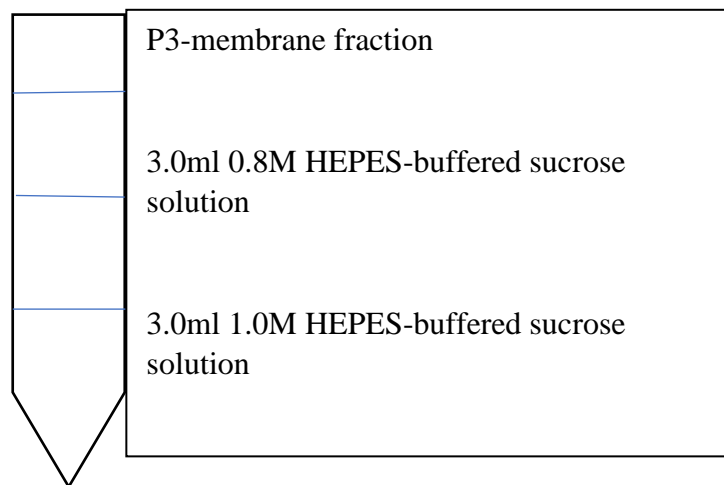
8. Appendices

Appendix 1

Fractionation of the Synaptosomal Plasma Membrane (SPM)

1. Weigh out selected tissue (50-100 mg) and homogenize it in 4 ml of 0.32 M HEPES-buffered sucrose solution.
2. Centrifuge at 900 xg for 10min at 4 °C to remove the nuclear pellet(P1)
3. Transfer the supernatant from this spin (S1) to a new tube. Spin at 10,000 xg for 15 min at 4 °C to remove the supernatant (S2).
4. Resuspend the remaining crude synaptosomal fraction pellet(P2) in 1 ml 0.32 M HEPES-buffered sucrose and then add another 3 ml 0.32 M HEPES-buffered sucrose solution.
5. Centrifuge at 10,000 xg for 15 min at 4 °C to remove the supernatant (S2'). Save the washed crude synaptosomal pellet(P2') in the polypropylene tube.
6. Lyse the crude synaptosomal pellet(P2') in the polypropylene tube by resuspending it in 1ml ddH₂O, and then add another 3 ml of ddH₂O, and then transfer to a glass-Teflon homogenizer to homogenize with 3 strokes by hand. Transfer samples back into the same 13 ml polypropylene tube and rapidly adjust the sample back to 4 mM HEPES with 16 μ l 1M HEPES solution, invert to mix. Rotate samples at 4 °C for 30min to ensure complete lysing.
7. Centrifuge at 25,000 xg for 20min at 4 °C to remove supernatant(S3) and resuspend membrane fraction(P3) in 1 ml 0.32M HEPES-buffered sucrose solution.

8



9. Centrifuge in a swinging bucket rotor at 150,000xg for 2hr at 4°C. Use 1ml syringe to puncture the tube at the interphase between 1.0M and 1.2M HEPES-buffered sucrose solution to withdraw the synaptic plasma membrane layer (SPM)
10. Collect the SPM layer in 3.5ml thick-wall ultracentrifuge tubes, and add exactly 2.5volumes of 4mM HEPES to adjust the sucrose concentration from 1.2M to 0.32M.

11. Ultracentrifuge the collected sample (adjusted concentration for sucrose) at 200,000xg for 30min at 4°C to remove the supernatant. Resuspend the synaptic plasma membrane pellet(SPM).

Solution used in the above procedures:

1. 0.32M HEPES buffered sucrose solution (4mM HEPES buffer pH 7.4)
2. 1.0M HEPES buffered sucrose solution (4mM HEPES buffer pH 7.4)
3. 1.2M HEPES buffered sucrose solution (4mM HEPES buffer pH 7.4)
4. 4mM HEPES
5. 1M HEPES
6. >225ul Halt protease inhibitor cocktail (don't know how much SPM can be collected in Steps 9 & 10)

Equipment used:

1. 15ml tapered glass-Teflon tissue grinder/homogenizer.
2. Centrifuges (900xg, 10,000xg, 25,000xg, 150,000xg and 200,000xg)
3. Glass Pasteur pipet.
4. 13ml polypropylene tube(x2)
5. 6ml snap cap tubes(x3)
6. 1ml syringe and 18G needle
7. 3.5ml thick-wall ultracentrifuge tubes.
8. 12ml polyallomer ultracentrifuge tube.

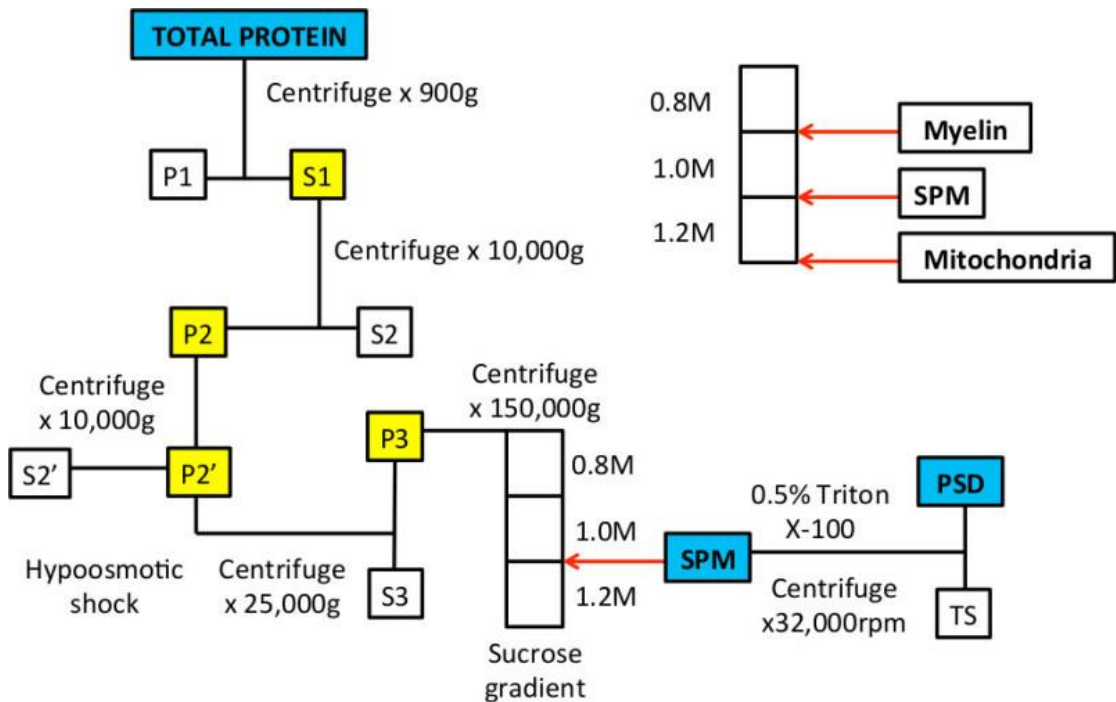
Table 1 list of subcellular fractions

Fraction	Protein fraction
P1	Nuclear
S1	Cytosol/membranes
P2&P2'	Crude synaptosomes
S2&S2'	Cytosol/light membranes
P3	Synaptosome/mitochondria
S3	Synaptic vesicle
0.8M/1.0M	myeline
1.0M/1.2M,	SPM
1.2M	mitochondria

Note:

1. it is important that a consistent degree of homogenization is achieved for each sample.
2. Another critical step is in the preparation of reagents, especially the sucrose solutions; if the molarity of the sucrose solution is incorrect the procedure will not work. Therefore, sucrose solutions should be prepared by weighing sucrose, dissolving in 4 mM HEPES solution then adding 4 mM HEPES to **the precise final volume**. Troubleshooting tip: build a test gradient with the prepared sucrose solutions to ensure that the gradient is properly assembled. Add varying concentrations of bromophenol blue (for example, final concentration of 0.005 % - 0.02 % w / v) to the two of the three sucrose solutions to assist in the visualization of three distinct layers.
3. It is important to limit the amount of time between when the gradient is assembled and when the tubes are centrifuged.
4. Finally, it is important to collect the SPM sample in as small a volume as possible, since it is necessary to subsequently dilute the sample with 2.5 volumes of water.

Ideally the sample should be collected in a volume of 0.4-0.7 ml using a 1 cc syringe.



Convert between times gravity (xg) and centrifuge rotor speed (RPM)

Certain procedures necessitate precise centrifugation conditions, which must be specified in terms of relative centrifugal force (RCF) expressed in units of gravity (times gravity or x g). Many microcentrifuges only have settings for speed (revolutions per minute, RPM), not relative centrifugal force. Consequently, a formula for conversion is required to ensure that the appropriate setting is used in an experiment. The relationship between RPM and RCF is as follows:

$$g = (1.118 \times 10^{-5}) R S^2$$

Where g is the relative centrifugal force, R is the radius of the rotor in centimeters (cm), and S is the speed of the centrifuge in revolutions per minute (rpm).

Appendix 2

A brief overview of the steps involved in a d-DNP experiment using the Nottingham dual isocentre magnet are provided.

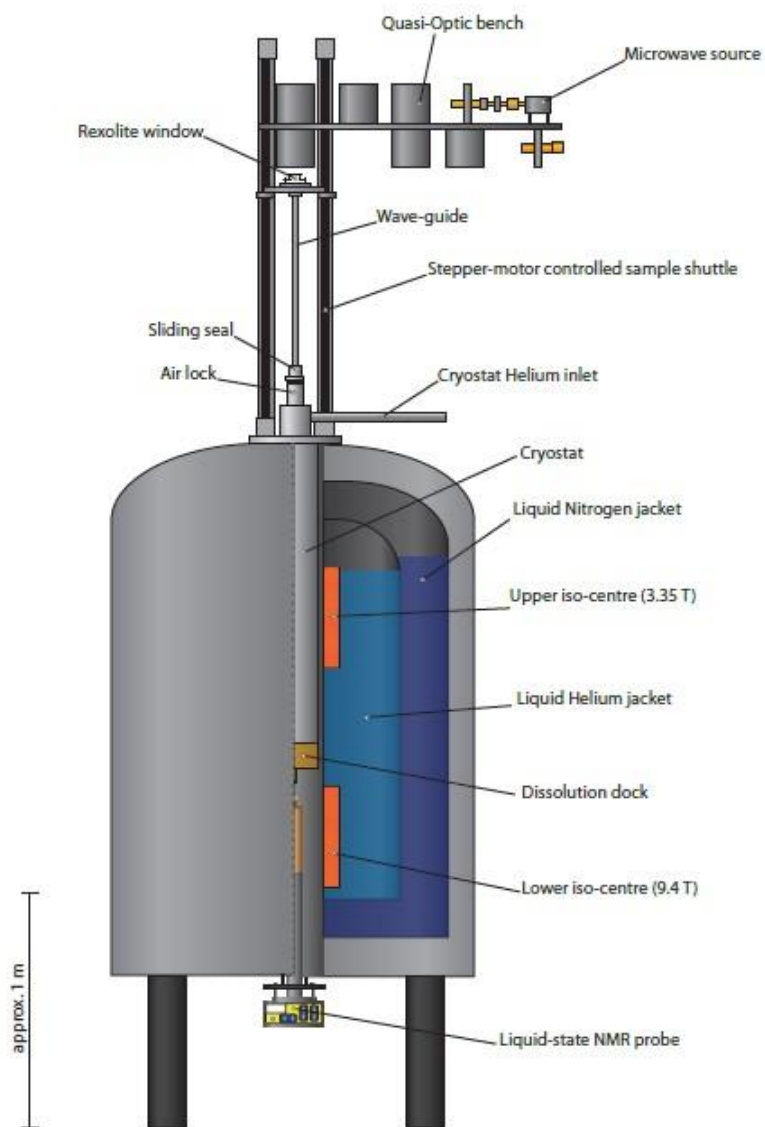


Figure 1

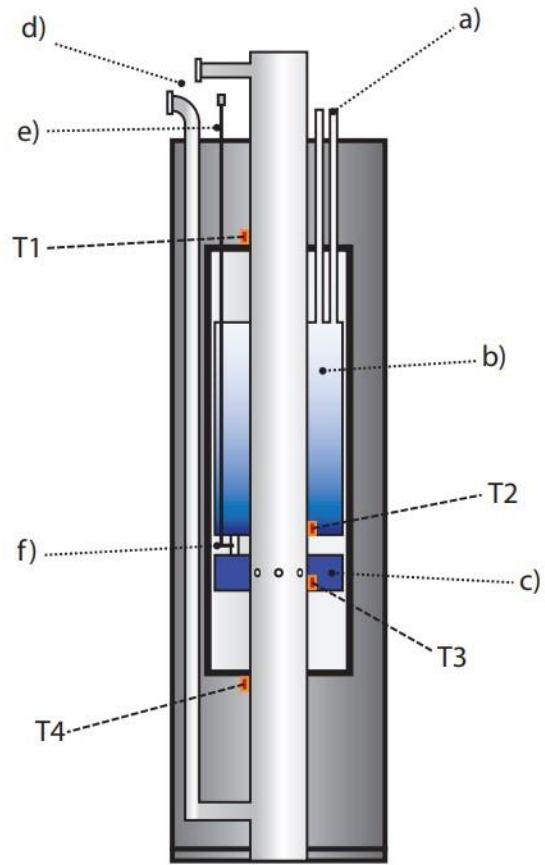


Figure 2

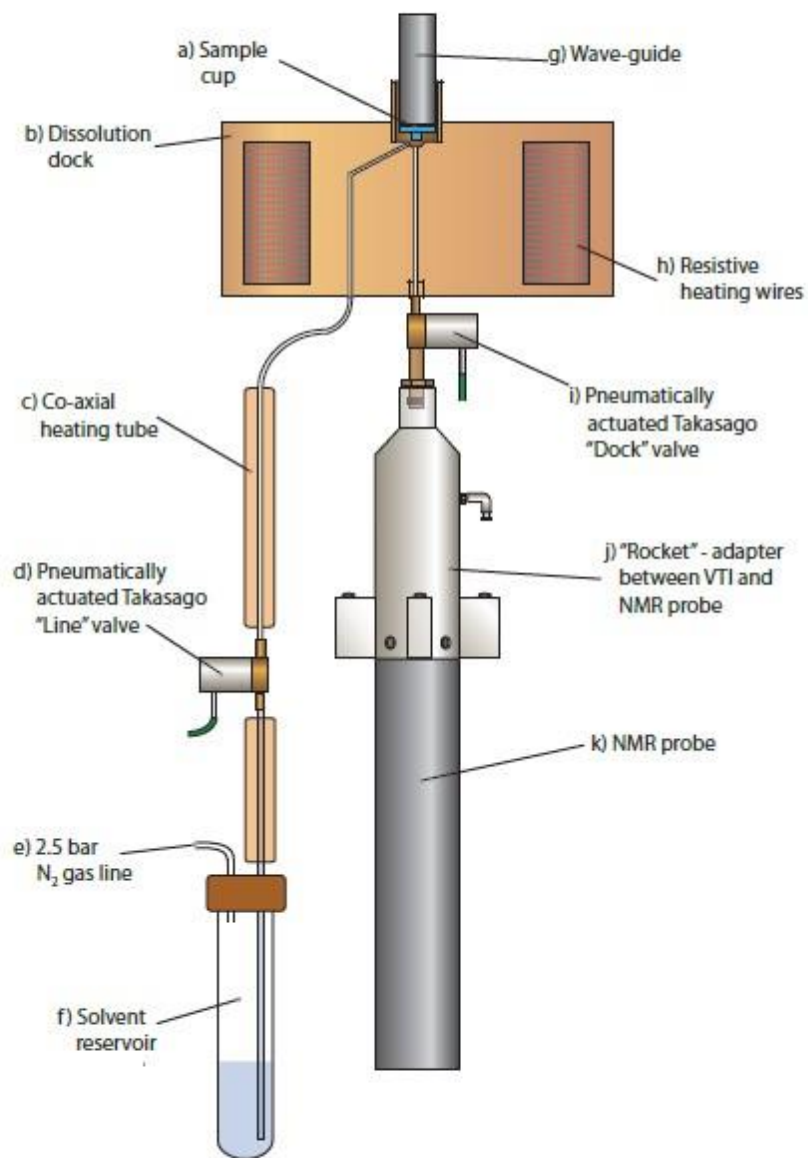


Figure 3

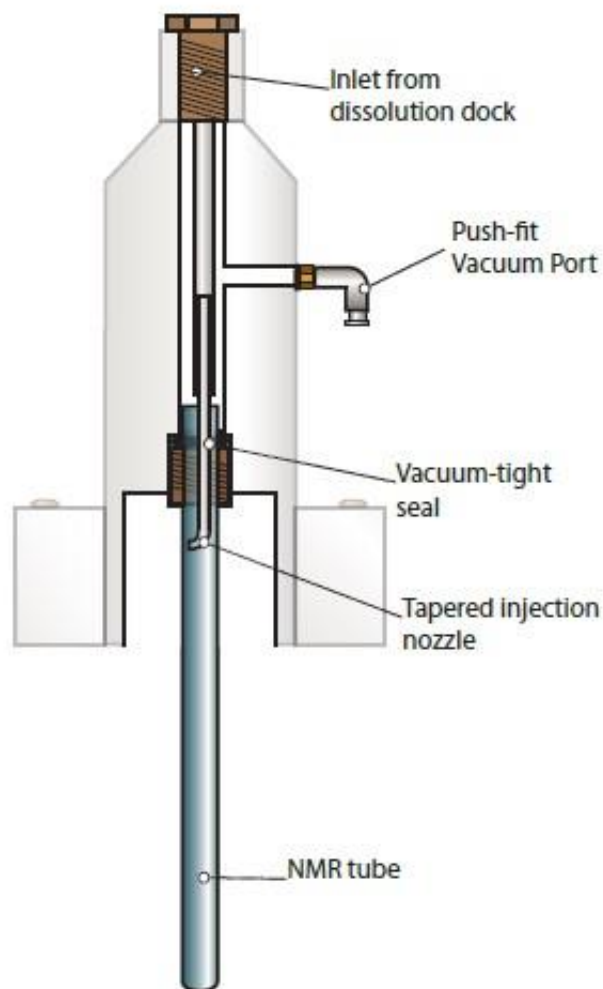


Figure 4

- 1) Low pressure is generated in a vacuum chamber surrounding the variable temperature insert (Figure 2) using a Pfeiffer TC-400 turbo pump overnight before carrying out the experiment.
- 2) On the day of the experiment, the bore (Figure 2d) is flushed with helium gas, the cryostat (Figure 2b) and liquid helium siphon (attached to Figure 2a) are flushed with helium gas and pumped on with a Pfeiffer DUO 65 M vacuum pump to cycle from low pressure to atmospheric pressure then flushed with helium gas for a further 30 mins at atmospheric pressure. This removes air and other impurities from the system before introducing liquid helium.
- 3) The liquid helium siphon, attached to the inlet labelled Figure 2a, is lowered into a dewar containing liquid helium. The cryostat is de-pressurized using a

small vacuum pump and the dewar is pressurized using a compressed helium gas bottle causing a liquid helium flow down the pressure gradient and into the cryostat.

- 4) When the temperature in the cryostat reaches ~100 K, measured using the ceramic temperature sensor labelled T2 in Figure 2, the waveguide (Figure 1) with the sample attached to the bottom is pneumatically moved into the bore to below the centre of the 3.4 T top magnet.
- 5) The quasi-optic microwave bench is moved into position such that microwaves are directed vertically down the waveguide and can irradiate the attached sample. The waveguide is moved upwards so the sample sits in the centre of the top 3.4 T magnet and the hole at the top is almost touching the quasi-optic bench where microwaves are emitted.
- 6) When the temperature in the bore reaches ~20 K, the vacuum pump attached to the bottom of the bore is opened leading to low pressure in the bore. The needle valve (Figure 2f) is opened, resulting in a flow of liquid helium into the '1 K pot' (Figure 2c). The CTC labelled T3 in Figure 2 is measures the temperature at this position.
- 7) A second vacuum pump, attached to the top of the bore, is activated when the T3 temperature is ~2-3 K. The needle valve is adjusted such that only a slight flow of helium occurs in the '1 K' pot- this causes the 'bore flow' display to drop from the maximum reading of 10.8 l / m to ~3.5 l / m. These conditions result in optimal Joule-Thompson expansion, and a minimum temperature of ~1.8 K is achieved in the '1 K pot'.
- 8) The microwave source is turned on us for a defined polarisation time, controlled using LabView software.
- 9) During the polarisation time, an empty NMR tube is screwed into the 'rocket' adapter (Figure 4) which is attached to the top of the NMR probe (Figure 3k). A tube connected to a vacuum pump is attached to the push-fit vacuum port (Figure 4), and the NMR probe is inserted into the bore of the bottom 9.4 T magnet.
- 10) Solvent is loaded in the solvent reservoir (Figure 3f) and is pressurized to 2.5 bar using compressed nitrogen gas. An oil heater is turned on, which heats in the co-axial heating tube (Figure 3c) to 100°C.
- 11) At the end of the polarisation time, the small pump connected to the 'rocket' is turned on, creating low pressure above the NMR tube.
- 12) One operator clicks the 'arm' and 'fire' buttons on the LabView display, which initialises the dissolution process. The other operator quickly closes

both bore vacuum ports (Figure 2d) and brings the bore to atmospheric pressure. The waveguide descends rapidly so that the to sit just above the 'rocket', as show in Figure 3.

- 13) The 'Dock' takasgo valve is activated (Figure 3i), quickly followed by the 'line' valve (Figure 3d), causing pressurized hot solvent into the cavity where the frozen sample sits, resulting in dissolution. The melted sample is drawn down the pressure gradient and into the NMR tube.
- 14) The movement of the waveguide into the bottom position automatically triggers NMR acquisition using a pseudo-2D pulse program (shown in chapter 6, Figure 6.17).
- 15) Following the dissolution, all vacuum pumps are turned off, the siphon is removed from the helium dewar and the remaining helium in the cryostat is allowed to boil off. The dock heater (Figure 3h) is turned on to melt any solvent that froze on contact with the waveguide and the system is washed by opening the 'line' and 'dock' valves and flushing cleaning solvent through the system.

Appendix 3

T₁ measurements-

An inversion recovery pulse sequence for presented T₁ data, shown below

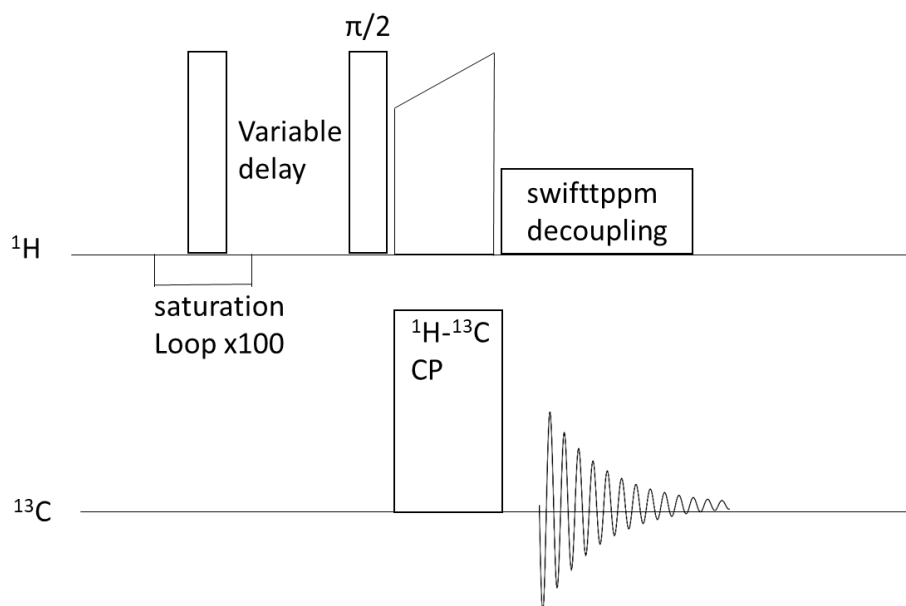


Figure 1: pulse sequence for a saturation recovery experiment to determine the build-up time required for spins to relax to Boltzmann polarisation. A saturation loop is followed by a variable delay, which is incremented after each experiment. Signal intensity is plotted against the delay time and the build-up curve is fitted to $I(t) = I(0)\exp(-t/T_{sr})$, where t is the variable delay time, $I(t)$ is intensity after time t and T_{sr} is the saturation recovery time.

Spectra were recorded with the following delays-

Spectrum	Time / s
1	0.2
2	0.8
3	1
4	2
5	4
6	6
7	8
8	16
9	32
10	48
11	64

T₂ measurements-

T₂ measurements were made using a spin echo experiment, shown below

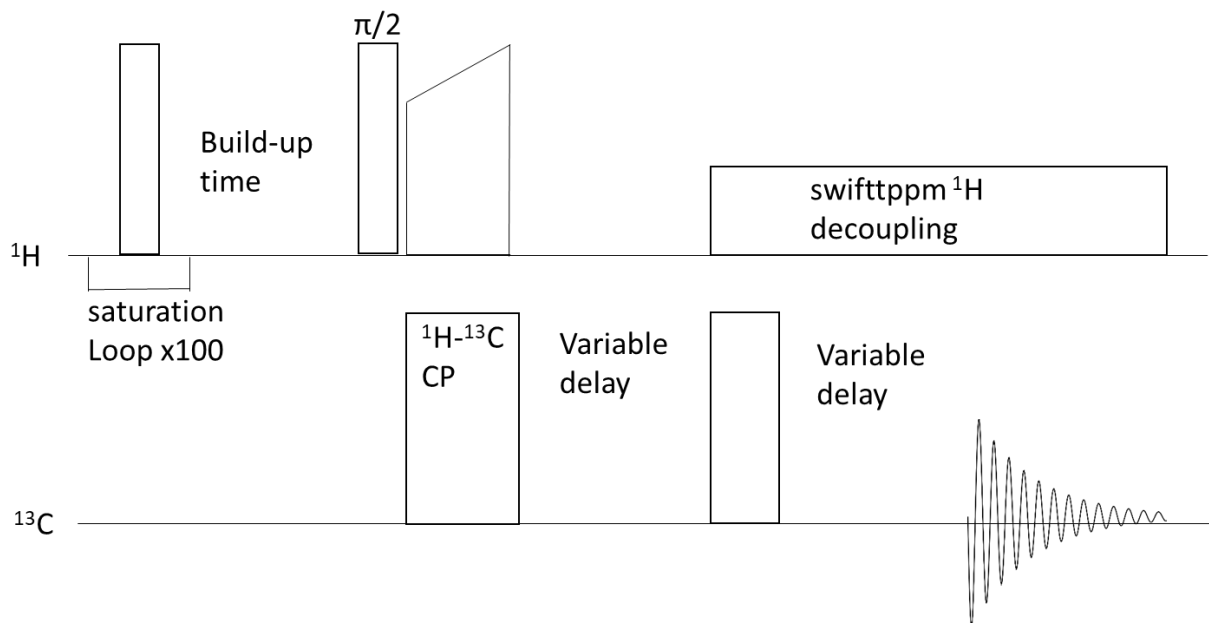


Figure 2 pulse sequence for T₂* measurement. A CP pulse is followed by two variable delays of equal length with a π pulse separating them. The π pulse refocuses the dephasing of magnetization vectors that occurs during the first delay such that after the second delay the magnetization vectors all have their original geometries after CP.

Spectra were recorded with the following delays-

Spectrum	Time / s
1	0.1
2	0.2
3	0.4
4	0.5
5	0.8
6	1
7	2
8	4
9	5
10	6
11	8
12	10

2D ^{13}C - ^{13}C experimental parameters

Sample	Experiment	MAS frequency / Hz	Mixing / excitation time / μS	Recycle delay / s	ns	Number of points
20 : 1 POPC / POPG + A β (1-40)	POST-C7	8000	471	8.0	32	256
20 : 1 POPC / POPG + A β (1-40)	DARR	8000	2.5×10^5	8.0	32	300
20 : 1 POPC / POPG + A β (1-40)	DARR	8000	1×10^6	8.0	32	200
100 : 1 POPC / POPG + A β (1-40)	POST-C7	8500	471	6.3	80	128
100 : 1 POPC / POPG + A β (1-40)	POST-C7	8500	471	8.3	64	128
30 : 1 complex lipid mixture + A β (1-40)	POST-C7	8500	471	9.0	32	256
150 : 1 complex lipid mixture + A β (1-40)	POST-C7	8000	500	12.0	64	128
10 : 1 Synaptic rat membrane + A β (1-40)	POST-C7	8000	500	6.0	512	64
10 : 1 Synaptic rat membrane + A β (1-40)	R20 ₂ ⁹	9000	444	7.0	256	64
40 : 1 POPG + A β (1-40) no incubation	POST-C7	8500	471	4.5	128	141
40 : 1 POPG + A β (1-40) no incubation	DARR	8500	2.5×10^5	4.5	16	300
40 : 1 POPG + A β (1-40) no incubation	PDSD	8500	2×10^6	4.5	28	300
40 : 1 POPG + A β (1-40) 8 hr incubation	POST-C7	8500	471	3.5	160	120

40 : 1 POPG + A β (1-40) 8 hr incubation	DARR	8500	2.5×10^5	3.5	28	300
40 : 1 POPG + A β (1-40) 8 hr incubation	PDSD	8500	2×10^6	3.5	28	300

2D ^{13}C - ^{15}N experimental parameters

Sample	Experiment	MAS frequency / Hz	SPECIFIC CP pulse length / μS	DARR mixing time / mS	Recycle delay / s	ns	Number of points
20 : 1 POPG + A β (1-40) 8 hr incubation	NCA	8000	9000	N / A	8.0	8	128
20 : 1 POPG + A β (1-40) 8 hr incubation	NCACX	8000	9000	25	8.0	8	128